Southampton

University of Southampton Research Repository

Copyright © and Moral Rights for this thesis and, where applicable, any accompanying data are

retained by the author and/or other copyright owners. A copy can be downloaded for personal non-

commercial research or study, without prior permission or charge. This thesis and the accompanying

data cannot be reproduced or quoted extensively from without first obtaining permission in writing

from the copyright holder/s. The content of the thesis and accompanying research data (where appli-

cable) must not be changed in any way or sold commercially in any format or medium without the

formal permission of the copyright holder/s.

When referring to this thesis and any accompanying data, full bibliographic details must be given, e.g.

Thesis: Author (Year of Submission) "Full thesis title", University of Southampton, name of the

University Faculty or School or Department, PhD Thesis, pagination.

Data: Author (Year) Title. URI [dataset]

University of Southampton

Faculty of Engineering and Physical Sciences
School of Chemistry

Strain induced Layered to Spinel phase transformation in metal oxide cathodes

by

Bud Macaulay

Master of Chemistry

A thesis for the degree of Doctor of Philosophy

May 2024

University of Southampton

Abstract

Faculty of Engineering and Physical Sciences
School of Chemistry

Doctor of Philosophy

Strain induced Layered to Spinel phase transformation in metal oxide cathodes

by Bud Macaulay

Battery materials are at the fore-front of the fight against climate change with industry standard battery materials seeing significant degradation after prolonged cycling. This study utilises ab initio Density Functional Theory to explore the driving forces governing phase transformation of layered metal oxides in the context of battery materials. Investigating known degradation routes under lattice strain closely models the conditions seen during typical battery operation and elucidates methods for inhibiting degradation.

Contents

Li	st of	Figures	3	vii
Li	st of	Tables		xiii
D	eclara	ation of	f Authorship	XV
A	ckno	wledge	ments	xvii
1	Intr	oductio	on and Background	1
	1.1	The H	listory of the Battery	. 2
		1.1.1	Batteries predating Li-Ion	. 2
		1.1.2	The Lithium Ion battery	. 4
	1.2	Lithiu	ım-Ion today	
		1.2.1	Issues with NMC	. 7
	1.3	_	ground degradation of layered cathodes	
	1.4	Motiv	ration	. 13
2	Firs	t-Princ	iples methods for modelling battery materials	15
	2.1	The q	uantum many body problem and the wavefunction	. 16
	2.2	Hartr	ee Fock	. 18
		2.2.1	Slater determinants	. 18
		2.2.2	The Variational Principle	. 19
	2.3	Densi	ty Functional Theory	. 21
		2.3.1	LDA and GGA	. 24
		2.3.2	The Hubbard U for localising metal orbitals	
	2.4	Plane	wave basis sets	
		2.4.1	The pseudopotential method	
		2.4.2	Reciprocal space and the Brillouin Zone	
		2.4.3	Kinetic energy cutoffs	
	2.5	Nudg	ged elastic band theory	. 34
3	Cry	stal Str	ructures of relevant metal oxides	39
	3.1	Typica	al oxides in nature	. 40
		3.1.1	Generation of benchmark systems	. 41
		3.1.2	Convergence and structure of benchmark systems	. 43
	3.2	Forma	ation energy of transition metal oxides	. 44
		3.2.1	Elemental crystal structures	. 46

iv CONTENTS

		3.2.2		hull and formation energies at the end member Li_0M_xOy	47
	3.3	Stabili		ructure of Lithium metal oxides	52
		3.3.1	•	nal choice and its effect on calculating end-member of	
				metal oxides	54
			3.3.1.1	Calculated structures of Li_1MO_2	55
			3.3.1.2		62
		3.3.2		of partially lithiated layered oxides	65
			-	Generation of partially lithiated superstructures	67
			3.3.2.2	1 , 1	68
	3.4	Summ	ary		73
4	Ion	migrati	on in bu	lk cathode materials	77
	4.1	•		e of layered cathode materials	78
	4.2			analysis of the end-member $Li_0MO_2 \dots \dots$	80
		4.2.1		ion and structure of initial and final states	80
				Electronic structure of states A, E and F	82
		4.2.2		ted minimum energy pathways for metal migration in	
		1,_,_			87
	4.3	Transi		analysis at the dilute limit of lithiation	90
		4.3.1		e of intermediates at the dilute limit	91
		4.3.2		ic structure and calculated minimum energy pathway at	
		1.0.2		te limit of delithiation	95
	4.4	Transi		analysis at half lithiation	101
		4.4.1		res of intermediates across pathway	102
		4.4.2		ted minimum energy pathway under equilibrium condi-	
		1, 1, _		· · · · · · · · · · · · · · · · · · ·	112
		4.4.3		strain and its impact on ion migration	116
			4.4.3.1	Strain-sensitivity of lattice parameters	118
			4.4.3.2	Strain and its effect on key intermediates across the pri-	110
			1.1.0.2	mary degradation pathway	121
			4.4.3.3	Strain and its effect on the transition states for dumbbell	
			1, 1,0,0	formation	124
	4.5	Summ	ary of fac	ctors influencing layered to spinel transformation	
	_		•		
5	lon	_		rface cathode materials	135
		5.0.1		ration of low energy surfaces for layered cathodes	137
			5.0.1.1	Tasker type surface cleavage	138
			5.0.1.2	Convergence of energy cut-off vacuum size and slab size	
			5.0.1.3	Generation of surface slabs	143
			5.0.1.4	Surface energies of layered metal oxides	145
	5.1		0 0	tion energies in layered mixed metal oxides	151
	5.2		_	or key metal surfaces	154
	5.3	Transi		analysis of surfaces at and near the end-member $\mathrm{Li}_0\mathrm{MO}_2$	154
		5.3.1		ion of initial and final states	155
		5.3.2		nergies and minimum energy pathways at the surface of	
		_		i crystallite	156
	5.4	Summ	arv		158

CONTENTS		•

6	Conclusions 6.1 Future work	161 163
Re	eferences	165
7	Appendices A Energy differences of the high and low-spin O3-type structures	207 207

List of Figures

1.1	The Daniell cell	3
1.2	Diagram of the Goodenough Li-ion battery	5
1.3	Practical specific energies for some rechargeable batteries	7
1.4	Common routes of degradation in battery materials	8
1.5	The O3-type $R\overline{3}$ m layered crystal structure	9
1.6	Proposed mechanism for metal segregation at the surfaces of cathode crystallites	11
1.7	Layered cathode nanoparticles favor a hexagonal platelet shape	12
2.1	Equilibrium bond lengths under the Born Oppenheimer approximation.	17
2.2	Flowchart diagram for finding the wavefunction within Hartree Fock theory	21
2.3	Potential and wavefunction of a pseudopotential as a function of dis-	
	tance from the nucleus	31
2.4	Brillouin zones of a 2d lattice	31
2.5	Plane waves within reciprocal space	33
2.6	Contour plot showing a potential energy diagram of an ionic migration between two states	35
2.7	The nudged elastic band method implements spring forces between images	36
3.1	Layered metal oxides with formula AMO ₂	40
3.2	Connectivity of metal oxide polyhedra within ordered crystals	41
3.3	Derivation of the Layered Goodenough structure	42
3.4	Plane wave kinetic energy cut-off convergences (linear and logarithmic) for 3d transition metals	44
3.5		
3.6	High density packing of hard-spheres into a crystal structure	48
3.7	Two key structures when discussing battery cathodes. The layered MO_2 and the Zero Li spinel-like structure	49
3.8	1	50
3.9	Convex hulls for Mn_xO_y , Co_xO_y and Ni_xO_y	51
	Convex hulls for other 3d metals	31
3.10	Transformation between Prismatic and Octahedral occupation of the vacuum layer in layered metal oxides	55
3.11	Jahn Teller distortion of Mn systems results in a D_{4h} geometry MO6 polyhedra	55
3.12	The LT-LiMO ₂ structure	56
	Calculated lattice parameters for layered Li_1MO_2 (M = Co, Ni and Mn).	
	a axis is a	58

viii LIST OF FIGURES

3.14	Calculated lattice parameter for $LT - LiMO_2$ using various functionals	59
3.15	The Li layer spacing and M layer spacing is defined by the planar dis-	
	tance between subsequent layers in the oxygen sub-lattice (i.e. d-spacing	
	in [0,0,1] plane)	60
3.16	Calculated energies of the investigated structures using different func-	
0.10	tionals (normalised to the O3-type structure).	61
3 17	Identified candidate structures at the delithiated end-member Li_0MO_2 .	62
	Calculated lattice parameters for O1, O3, O2, P2-type Li ₀ MO ₂ using var-	02
5.10	ious functionals	64
2 10		03
3.19	Calculated Li and M layer spacing for O1, O3, O2, P2-type Li ₀ MO ₂ using	65
2.20	various functionals	65
3.20	Calculated lattice parameters for the Zero-Li Spinel structure using var-	
2.21	ious functionals.	66
3.21	Formation energies (relative to O3-type) of the Zero-Li spinel, O2, O1	
	and P2 type structures	66
3.22	Calculated convex hulls for Li _x MO ₂ (M=Co, Ni and Mn) using various	
	functionals	69
3.23	Stable Li/ V_{Li} configurations are those that maintain equal distribution	
	of Li across layers	70
3.24	i) The in plane Li arrangement investigated by Van der Ven et al ¹ can	
	yield numerous structures when stacked across layers. ii) The $P2/m$	
	structure has vacancies that run planar across the b-axis. iii) The off-	
	set stacking sequence results in a reduction of the space-group to $P2/c$	
	and a breaking of the co-operative Jahn Teller effect	71
3.25	Energy penalties for breaking the Li-O-M-O-Li connectivity for the or-	
	dered structure seen in Figure 3.24	71
3.26	Comparison of calculated c-axis lattice parameters in the literature and	
	this work.	7 3
4.1	The Goodenough structure can be thought to operate between two ex-	
	treme states of lithiation	78
4.2	Migration from the P2/m structure to the Spinel structure requires nu-	
	merous steps. Adapted from Ceder and Reed. ²	80
4.3	Pathways for O_h to O_h migration	81
4.4	Potential pathways for metal migration at zero-Lithiation	82
4.5	Structure E results in moderate displacement of the metal-bound oxygen	
	across the Li layer. This displacement is increased in the large layer spac-	
	ing structure predicted by PBE+U. Despite this increased displacement	
	the $M_{Td}-O$ bond is longer than that seen in the PBE+U+D3 structure.	83
4.6	In an octahedral coordination, the d orbitals (quantum number $\ell = 2$) are	
	split such that the the orbitals directed at the ligands (e_g) are higher in	
	energy than the orbitals directed away (t_{2g})	83
4.7	Occupation of the d-orbitals for M^{4+} (M = Co, Ni and Mn) can be either	
	be low-spin or high-spin and is the result of the relative sizes of Δ_o (the	
	d orbital splitting) and Δ_s (the spin-pairing energy)	85
4.8	Calculated d orbital occupation of a migrating M^{4+} ion (M = Co, Ni and	
	Mn) at stable intermediates A, E and F	86

LIST OF FIGURES ix

4.9	Qualitative molecular orbital diagram for a ML ₆ octahedra. This diagram only illustrates σ bending interactions. Typically to * and a * bayes	
	gram only illustrates σ bonding interactions. Typically t_{2g}^* and e_g^* have	
	their superscript dropped when discussing transition metals. Left) ML ₆	87
4 10	with strong orbital overlap. Right) ML_6 with poor orbital overlap	0/
4.10	Calculated minimum energy pathways under various functionals as a	
	metal migrates from an O_h site in the metal layer (State A) to an O_h site	
	in the Li layer (State F). The open pathway features a relatively low lying	
	intermediate as the metal occupies a T_d site in the Li layer (State E)	89
4.11	Suggest pathways for dumbbell formation at the dilute limit. Pathway	
	$A \rightarrow D^a \rightarrow E^3$ is Li migration followed by M migration. While Pathway	
	$A \to D^b \to E^4$ is the reverse pathway	91
4.12	Expected distortion of a octahedron that spans an enlarged Li layer	92
4.13	i) Initialised structure for a near-zero Li metal oxide, the Li is placed	
	in the center of the pseudo-octahedral site. ii) Relaxed geometry for a	
	near-zero lithiated metal oxide. The Li ion has migrated towards the	
	octahedral face. iii) Resulting spin density of the close (edge-shared)	
	metal site at initialisation and relaxation of the structure	93
4.14	The Li ion in State D_{1Li}^a can lie between one of the two extreme states, i)	
	the Li ion relaxes toward the MO ₂ sheet. ii) the Li ion relaxes away from	
	the MO_2 sheet	94
4 15	The change in d occupation for a Co ion in various states. The change	, -
1.10	in chemical environment/geometry can often have an associated spin	
	moment change.	97
116	Calculated minimum energy pathway from the undefected structure struc-)1
4.10		
	ture (A) through intermediate D^a to the dumbbell structure formation at	
	the dilute limit of lithiation for Co, Ni and Mn systems. This pathway is	
	characterized by a $O_h \rightarrow T_d$ Li migration followed by a $O_h \rightarrow T_d$ Metal	99
4 1 17	migration.	99
4.17	Calculated minimum energy pathway from the undefected structure struc-	
	ture (A) through intermediate D^b to dumbbell formation at the dilute	
	limit of lithiation for Co, Ni and Mn systems. This pathway is character-	100
		100
4.18	Metal Oxide cathode as as seen looking down the c-axis. $O_h \rightarrow T_d$ metal	
	migration into the Li layer is only possible when the T_d site has no O_h	
		102
4.19	The P2/m structure of Li _{1/2} MO ₂ has been previously identified as low	
	energy, Li ⁺ and V _{Li} alternate across the a-axis of the structure, resulting	
	in vacancy channels across the b-axis. With a charge ordering of Mn ⁴⁺	
	and Mn^{3+} ions running parallel to these channels	103
4.20	The principle pathway for dumbbell formation, is a multi-step process	
	featuring many O_h - T_d 'hops'. Starting from the P2/m a lithium mi-	
	gration is required to free the dumbbell site of neighbouring lithium.	
	Migrating ions are indicated via shaded polyhedra. Adapted from Sey-	
		104
4.21	States B and C are related by an $T_d \rightarrow O_h$ Li migration. The T_d Li in state	
	B induces a significant displacement of the metal site in the layer below.	
	,	106
	ı ı ı ı ı ı ı ı ı ı ı ı ı ı ı ı ı ı ı	

x LIST OF FIGURES

4.22	Integrated net spin around the metals sites for Li migration steps across the pathway (A through D). The retention of on-site spin density sug-	
	gests the charge ordering is maintained despite Li rearrangement	108
4.23	Possible changes in d occupation for Co during the metal migrating to the T_d in dumbbell structure step D \rightarrow E. For the spectating pathway there is no redox activity, while the participating pathway involves a	
	charge disproportionation reaction	110
4.24	Possible changes in d occupation for Ni during the metal migrating to the T_d in dumbbell structure step D \rightarrow E. For the spectating pathway there is no redox activity, while the participating pathway involves a charge	
	disproportionation reaction	111
4.25	Possible changes in d occupation for Mn during the metal migrating to the T_d in dumbbell structure step D \rightarrow E. For the spectating pathway there is no redox activity, while the participating pathway involves a	
	charge disproportionation reaction	111
4.26	The normalised minimum energy pathways at equilibrium for dumbbell	
	formation for Co, Ni and Mn. States A through D are Li rearrangements	
	of one another and thus have low energy transition states. State E is the	
4.07	Li-M dumbbell	114
4.27	i/ii) State D and E as viewed down the c axis. State D shows a M^{4+}/M^{3+} charge ordering with the migrating ion lying within the vacancy chain.	
	Li is removed for clarity, colors match those seen in iii. iii) Integrated	
	spin densities of metal sites across the $O_h \to T_d$ metal migration step	115
4.28	At high rates of delithiation, surface state delithiate rapidly, resulting in	
	a mismatch of local and global lithiation and induced lattice strain	117
	The response of Li layer spacing (Oxygen-Oxygen dspacing	119
4.30	The response of other key lattice parameters under varying isotropic stress for half lithiated Co, Ni and Mn oxides	120
4 31	top) The response of M-O bond lengths as a function of applied stress,	120
1.01	both Ni and Mn show a 4:2 split in the M ⁴⁺ -O bonds indicating Jahn	
	Teller distortion (which are more susceptible to stress). bottom) The re-	
	sponse of Li-O bond lengths as a function of applied stress, the elongated	
	Li layer results in LiO ₆ polyhedra being distorted (and thus having dif-	100
1 22	ferent bond lengths.)	120
4.32	vestigated at strained lattice parameters. Figure Repeated for clarity	121
4.33	Harmonic relationship of key steps in the layered to spinel transforma-	
	tion for (i) $\text{Li}_{0.5}\text{CoO}_2$, (ii) $\text{Li}_{0.5}\text{NiO}_2$ Ni and (iii) $\text{Li}_{0.5}\text{MnO}_2$	123
4.34	Scheme for calculating the minimum energy pathway with respect to	
	strain state	125
4.35	Calculated MEP's under varying compression/tension, normalized to	
	state A at it's given stress. Pathway steps correspond to those seen in Figure 4.32, in which the dumbbell structure E is noted to be a precursor	
	in spinel formation	127
4.36	Transition state barriers for $O_h \rightarrow T_d$ metal migration under equilibrium	
	lattice parameters. The green line represents a typical migration barrier	
	for Li diffusion ⁵ . *Ceder and Reed's ^{4,6} work differs from the work here	
	and by Seymour et al ³ , in that no on-site interaction was include (i.e $U = 0$ in the Hubbard model)	131
	oni die massara moder,	101

LIST OF FIGURES xi

4.37	Transition state barriers and dumbbell defect energies for $O_h \to T_d$ metal migration seen in the literature and in this work. Seymour et al ⁷ investigated dopant effects	133
5.1	Proposed mechanism for metal segregation at the surfaces of cathode	100
5.2	crystallites	136 139
5.3	Slab models of surfaces need to be large enough to not collapse but small enough to be computationally feasible	140
5.4	Convergence of plane wave energy cut-off of a $[1, 0, \overline{1}, 4]$ slab	141
5.5	Convergence of necessary slab parameters. top) Surface energy convergence of slab size per number of mono-layers. bottom) Surface energy	
	convergence of size of vacuum in simulation cell in Å	142
5.6	Cleavage of the $[0, 0, 0, 1]$ surface is impossible without slabs being either	1 4 5
F 7	polar (ii) or non-stiochiometric (iii).	145
5.7	The generated surface slabs for LiMO ₂ . When applicable they have been reconstructed to be non-polar.	146
5.8	Relaxation of the $[1, 0, \overline{1}, 4]$ LiCoO ₂ surface results in a small migration	140
5.0	of the surface oxygen into the vacuum, this is further pronounced in the	
	delithiated surface slab. Light colors represent the initial slab, darker colors	
	the relaxed slab	149
5.9	The surface geometry of a LiMnO ₂ [1, 0, $\overline{1}$, 4] slab. Relaxation a reduction	11/
0.,	of the Jahn Teller distorted Mn-O bonds. <i>Light colors represent the initial</i>	
	slab, darker colors the relaxed slab	149
5.10	2	
	pyramidal geometry. the destabilised z^2 orbital allowing an intermedi-	
	ate spin state	150
5.11	Slabs used for calculation of surface segregation energies. i/ii) The slabs as viewed down the a axis, M^{\dagger} is located in the bulk and at the surface respectively. iii/iv) The slab as viewed down the c axis, when M^{\dagger} is at the	
	surface the unit-cell needs to be twice as big to maintain stiochiometry.	153
5.12	i) The undefected $[1, 0, \overline{1}, 4]$ slab of a zero-lithiated system. ii) symmetri-	
	cal defects can either migrate toward (yellow) or away (green) from the	
= 40	surface	155
5.13	Unique T_d sites within the Li layer in which a metal can migrate into. Since each defect has a different distance from the surface they are non-equivalent	156
511	equivalent	156
J.14	the surface oxygen and this oxygen is pulled back into the plane	157
5.15	Tetrahedral defect energies as a function of depth for the delithiated [1,	107
0.10	0, $\bar{1}$, 4] surface slabs (MO ₂ where M = Co, Ni and Mn). Filled circles	
	indicate the bulk calculations	158
7.1	The Daniell cell	209

List of Tables

2.1	Chosen U values, based on work by Jain et al. 9	27
3.1 3.2	Calculated and reference lattice parameters of halite metal oxides The calculated crystal structures of the 3d transition metals	45 47
4.1 4.2	Calculated lattice parameters in the $C2/m$ basis using a PBE+U functional. Calculated lattice parameters in the $C2/m$ basis using a PBE+U+D3 func-	
4.3	tional	79 84
4.4	Defect energies at zero lithiation. state E is a Tetrahedral M defect in the Li layer. state F is a Octahedral M defect in the Li layer	88
4.5	Calculated Li-O bonds near the dilute limit for the tetrahedral Li system	95
4.6	(D_{1Li}^a)	
4.7	Relaxed lattice parameters of $\text{Li}_{\frac{1}{2}}\text{MO}_2$ within the P2/m framework	103
4.8	Displacement of face-shared metal ion for state B and state C	105
4.9	Defect energies for Li migration steps B (T_d) and C (O_h)	107
4.10	Displacement of face shared metal ion and Expected/Calculated defected energies of state D	107
5.1	The Miller planes in the C2/m lattice and their equivalents when converted to the $R\overline{3}m$ lattice	143
5.2	Calculated surface energies in mJ m ⁻² in comparison to those found in	
	the literature	147
5.3	Calculated surface energies in mJ m^{-2} for delithaited surface slabs. The	1 117
5.4	$[1, 0, \overline{1}, 4]$ surface remains low energy for these surfaces Segregation energies of LiM [†] M*O ₂ . Positive energies show a enthalpy to be located within the bulk while negative energies show enthalpy to-	147
	ward the surface	154
7.1	Metal d electron and spin state configurations of Goodenough analogue systems.	207
7.2	Calculated on-site magnetic moments of species within the O3-type structure after geometry optimization. Magnetic moments were initialised at	4 07
	their expected d-configuration	208

Declaration of Authorship

I declare that this thesis and the work presented in it is my own and has been generated by me as the result of my own original research.

I confirm that:

- 1. This work was done wholly or mainly while in candidature for a research degree at this University;
- Where any part of this thesis has previously been submitted for a degree or any other qualification at this University or any other institution, this has been clearly stated;
- 3. Where I have consulted the published work of others, this is always clearly attributed;
- 4. Where I have quoted from the work of others, the source is always given. With the exception of such quotations, this thesis is entirely my own work;
- 5. I have acknowledged all main sources of help;
- 6. Where the thesis is based on work done by myself jointly with others, I have made clear exactly what was done by others and what I have contributed myself;

Signed:	Datos
Signed:	Date

Acknowledgements

First and foremost, I would like to express my deepest gratitude and respect to my supervisor, Dr Denis Kramer. The research could not have been accomplished without his guidance, encouragement and time. Additionally the many thanks have to be given to the rest the Kramer group with support and guidance throughout my research.

This work was supported by the Faraday Institution FITG 014, FITG 014B.

Chapter 1

Introduction and Background

The advent of the battery largely predates the industrial revolution, having been a point of fascination and wonder of the 18th century scientists Galvani, Volta and Faraday. However, the science had laid stagnant and unexplored for around 200 years after the initial studies. Placed on the back-burner, as a forgotten piece of history while coal and the combustion engine powered most scientific research and the industrial revolution of the 19th and early 20th century.

With the birth of modern computing and from it consumer electronics a small spotlight was placed back onto battery materials. The old Zinc-Carbon or Zinc-Chlorine batteries archaically designed in the 18th century while initially adequate for powering handhelds of any sort, quickly showed some deep flaws. More computational power was crammed into a smaller and smaller area and thus the battery was also required to shrink. While these alkaline batteries have firmly grasped a place in every day life within low wattage television remotes and smoke alarms, the task of powering anything more demanding has generally fallen onto 'Lithium-ion' battery materials.

1.1 The History of the Battery

The world of electrochemistry was born under Luigi Galvani in the middle of the 18th century, although largely by accident. ¹⁰ While researching the field of 'medical electricity' a charged metal scalpel came in contact with the leg of a partially-dissected frog, in which the frog leg was observed to twitch. Galvani postulated that all muscles are moved by a liquid that runs through them and coined the term 'animal electricity'. While a somewhat astute observation considering the era, it was his contemporary Volta that showed that this electricity was not an intrinsic property of life but of the metals from the scalpel. He did so with what can be considered the first battery, the voltaic pile.

1.1.1 Batteries predating Li-Ion

The voltaic pile 11 was a stack of alternating Zinc and Copper plates separated by a brine electrolyte. Volta theorized that just the mere contact of differing metals resulted in a electromotive force. Clearly science of today shows a chemical reaction is taking place, (See Reaction 1.1). The Zinc plate acts as the anode, being oxidised into Zn^{2+} ions into solution. While it would be expected that Copper would act as the opposite active species, instead it's found that the Copper electrode is inert, and any inert conductor would have proved sufficient. Instead the active specie is from the electrolyte solution, with Hydrogen ions being electrolyzed into H_2 gas. This results in a poor-performing battery as hydrogen bubbles would become trapped on the copper surface inhibiting further electrolysis and increasing the internal resistance of the battery. This phenomenon broadly falls under 'polarization effects' at electrode surfaces.

anode (oxidation) Zn
$$\rightarrow$$
 Zn²⁺ + 2e⁻ (1.1) cathode (reduction) 2H⁺ + 2e⁻ \rightarrow H₂

It was work half a century later by Michael Faraday and John Daniell ^{12,13} that disproved Volta's misguided 'contact electricity'. Their invention is called the Daniell cell (see Figure 1.1), perhaps the first cell that could be reasonably called an ancestor of those of today. Depositing a Zinc anode within a zinc sulphate electrolyte and a copper cathode in a copper sulphate electrolyte the basic framework for electrochemistry is possible. Addition of a salt-bridge allows ionic flow between solutions without direct mixing (as that would short the circuit). This discovery found its footing in industry, becoming the standard for the newly invented telegraph, paving the way for the future of battery technology.

Batteries once drained of their chemical reaction are fully discharged. If this battery is then considered unusable or spent (i.e. non-rechargeable) it is a primary battery. The inconvenience of replacing primary batteries has largely relegated them to low wattage use cases. On the other hand rechargeable batteries have found a much wider range of use, from handheld electronics to electric vehicles and national grid balancing. With such a broad application range, the exact chemistries varies significantly from battery to battery.

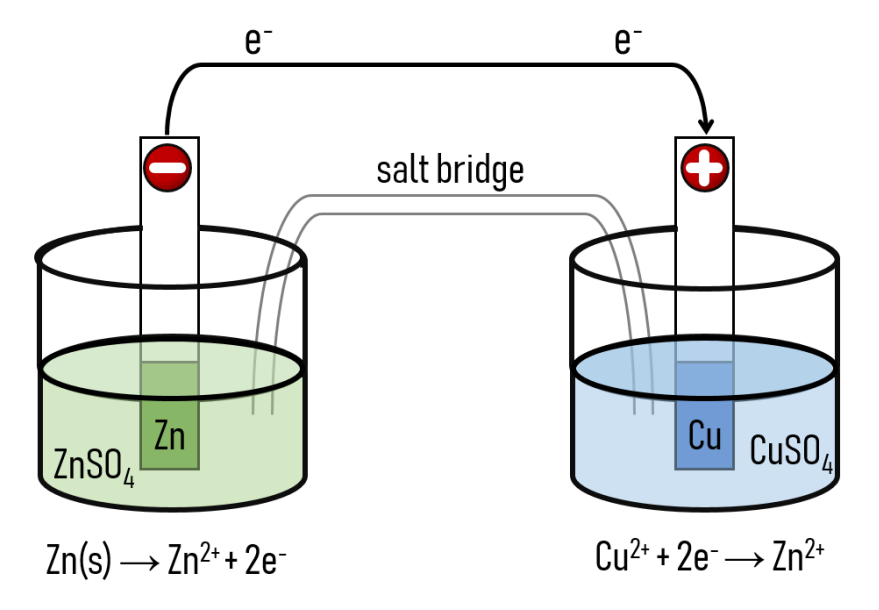


FIGURE 1.1: The Daniell cell is one of the first batteries. Comprised of a Zn electrode and a Cu electrode. Ionic exchange is facilitated through the salt-bridge.

The first rechargeable batteries were first invented less than 50 years after the birth of electrochemistry. The lead-acid battery consists of a lead anode and a lead-dioxide

cathode immersed in sulphuric acid. Lead sulphate is formed at both electrodes and the flow of electrons are from anode to cathode as shown in Equation 1.2. Passing a current across the electrodes in reverse, yields the reverse reaction, recharging the battery. In the modern era lead-acid batteries are abundantly found in vehicles, used to power lights, dashboard electronics and spark-plugs that kick-start the combustion process. The use of an alternator when the vehicle is running ensures the battery remains charged. Unfortunately, these lead-acid batteries are heavy and are undesirable for use in handhelds or supplying the driving force to operate the vehicle itself.

anode (oxidation):
$$Pb \rightarrow Pb^{2+} + 2e^{-}$$

$$Pb^{2+} + SO_4^{2-} \rightarrow PbSO_4$$
 (1.2)
$$PbO_2 + 4H^+ + 2e^{-}$$

$$Pb^{2+} + SO_4^{2-} \rightarrow PbSO_4$$

1.1.2 The Lithium Ion battery

Differing chemistries for battery materials have emerged during the 20th century yet none have close to the impact of the research by Goodenough, Whittingham and Yoshino. ^{14–16} Their discovery of the Lithium ion battery (see Figure 1.2) has been award a Nobel prize. Initially the choice of lithium for the electrochemical reaction was clear, it has the lowest reduction potential and a small ionic radius. As a result Lithium is often viewed as the most promising battery system to achieve high gravimetric and volumetric energy densities. ¹⁷ Research around Lithium intercalation in the context of electrical energy storage was first noted by Whittingham, ¹⁸ where it was shown that Lithium could intercalate into numerous sulphides (notably TiS₂) and could act as storage for energy. ¹⁹ Further refinement by Goodenough, Mizushima and Yoshino, ²⁰ lead to the choice of material being a layered Cobalt oxide system with Lithium intercalating between the MO₂ sheets (commonly denoted LCO). This cathode material is stable and has a very large cell potential of 3.70V. On the other side of the battery, numerous anode materials have been suggested in the past 40 years.

Whittingham suggested Li metal for its large energy density but dendrite formation has often kept that material shelved.²¹ Anode materials featuring layered graphite are widely found in industry, this layered system eases Li intercalation between the sparse sheets. Doped Silicon variants²² of this material as well as more exotic materials²³ are still contested areas of research.

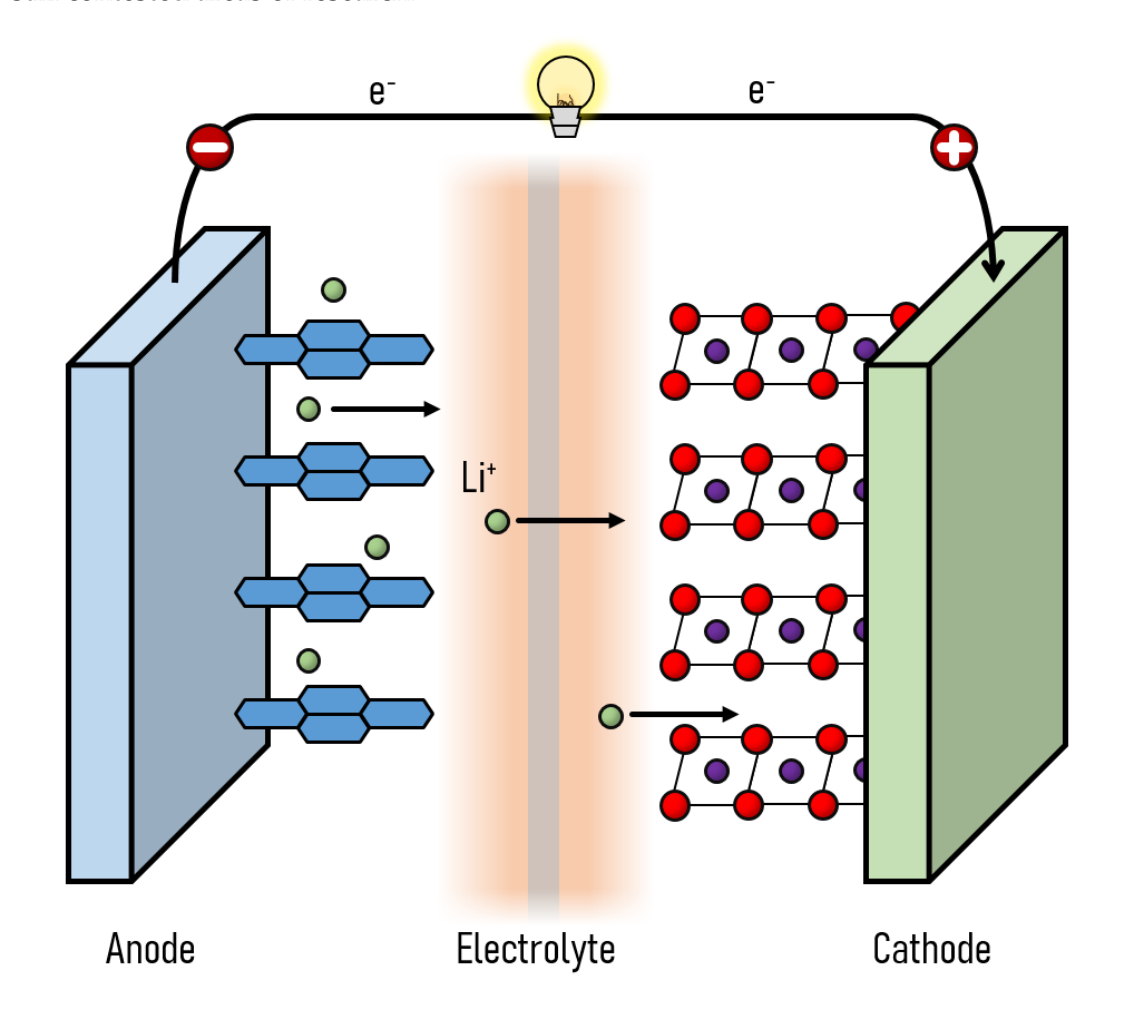


FIGURE 1.2: Diagram for the Li-ion battery, under load, Li flow from one electrode to another across the electrolyte and electrons pass through the external circuit. $Adapted\ from\ Goodenough\ et\ al.$ ¹⁴

It wasn't long until the industry adopted the LCO battery with Sony first commercializing the technology in 1991, spawning the birth of the handheld devices we see in the palm of everyone's hands today. However, the ever looming threat of climate change has pushed these batteries to their absolute limits as they approach their theoretical maximum potential. While even today, there is still some research trying to further increase power and energy densities of these materials further, many current targets for these batteries are focuses on environmental and social impact

factors. In particular, low Cobalt analogs of the LCO material have been a point of fascination within the battery research world. Cobalt has long had social issues, with the mining of Cobalt dominated by a small geographic region. As a result politics and ethics have tipped the scales away from relying on a singular metal oxide system. ²⁴ Instead, a wide range of structures and compositions are in active development, most commonly seen in the industry is Nickel, Manganese Cobalt (NMC) mixed metal oxides in varying ratios. ²⁵

1.2 Lithium-Ion today

In today's climate and with government pledges to switch toward net-zero, promising technologies such as fuel-cells, ²⁶ Hybrid engine vehicles and even fully electric vehicles ²⁷ have crept into the discussion as potential alternatives to the internal combustion engine. Of course, the complexities that the auto-motive industry faced during its infancy, from logistical, technological and public perception are once again rearing their ugly head and are being carefully tackled on a wide range of fronts. Although more ambitious options for powering the future are becoming available they often come with the caveat of unexplored research/implementation and thus higher risk. As seen with fuel cells, this often leaves investors hesitant to make the economic contributions necessary to iron out the kinks seen in development. The general public are also hesitant with embracing battery powered vehicles in their every day life. However, difficult questions such as range, roadside charging, cost and the second-hand market are becoming active conversations suggesting that public perception may be shifting. Many of these issues are thought to be manageable as more wide spread adoption takes place. However, this unfortunately has yielded a chicken or the egg situation, with electric vehicles not yet finding stable footing, there is no incentive to build the infrastructure to support widespread adoption which in turn further impacts the public perception. nonetheless Li-Ion has found a firm and solid place in the automotive industry with numerous top automakers launching their own branded electric vehicles.

While this is good news for a greener world, there is still a thriving and active community of ongoing research around Li-ion technology, largely in a bid to cram more energy into a smaller area or more importantly improve the longevity of these batteries. Both cost (\$/kWh) and energy density have vastly improved since the 90s and range is near rivalling petrol engines. ^{28,29} Despite these energy densities being just a fraction of those batteries still in R&D as seen by Figure 1.3, Li-ion is expected to be common place in both the automotive and the cellular phone industry for the foreseeable future. ³⁰

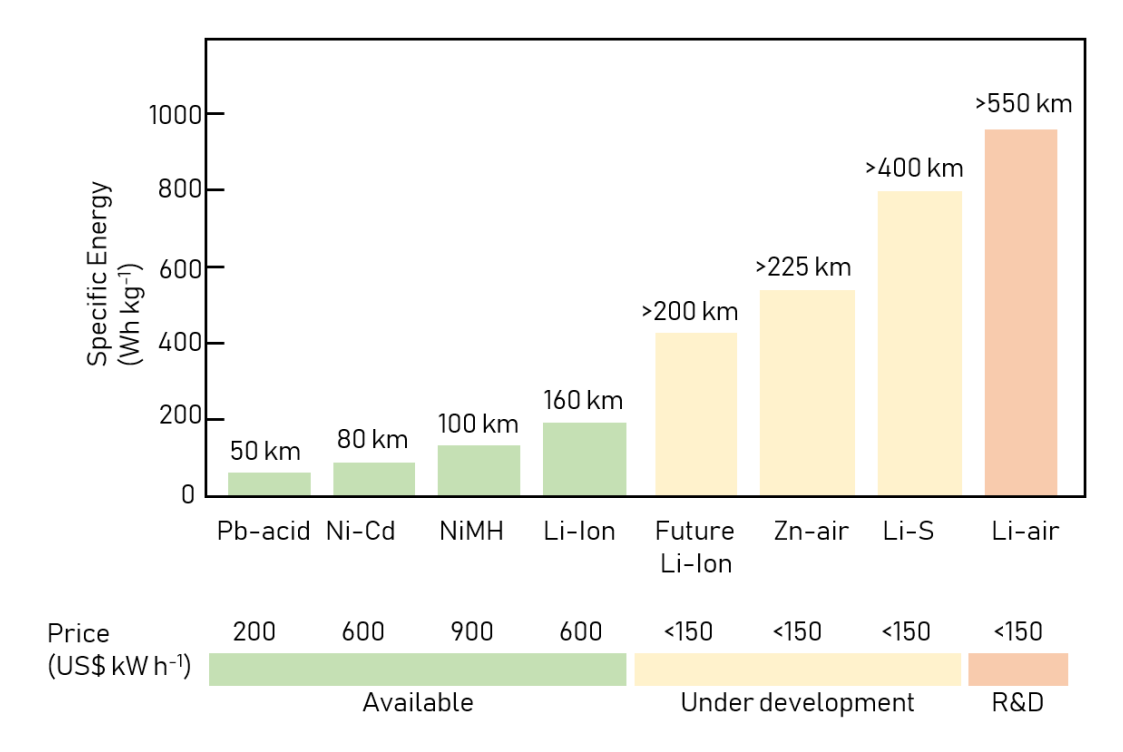


FIGURE 1.3: Practical specific energies for some rechargeable batteries, and their estimated driving ranges. Current Li-ion is near the theoretical maximum capacity. *Adapted from Li et al.* 30

1.2.1 Issues with NMC

Li-ion has seen a modern boom, with large-scale industrial expansion globally by Companies like Tesla and Nissan. It can expected that electric vehicles will play a significant role in the future of the automotive industry. However the rapid growth has left some questions of the lifespan of these materials. Upon synthesis some capacity is expected to be lost after the first few cycles as the surface layers are exposed to the electrolyte. These surface layers reconstruct becoming sacrificial to

protect the bulk from the high charge. 31 However, this loss of capacitance is continued over many cycles (>100) and the exact nature of this process complex, environment dependent and multi-pathed. Empirically measuring such processes is challenging and instead modelling methods are often used. 32,33

The NMC oxide system is often thought of as the *de facto* cathode material for Li ion. However, for batteries to see a prolonged life within automotive industry they will need to last as long as the current internal combustion engine vehicles. As such a plethora of investigations into battery breakdown and their influencing factors have been undertaken. ^{34,35} These routes to degradation are plenty and summarised in Figure 1.4. Perhaps the most challenging task when investigating these degradation processes as a whole is the scale on which they occur. Particle cracking and dendrite formation occur on the macro-scale, while phase transformations and point defects are isolated atomistic processes. ³⁶ Additionally, it's unlikely these process are uncoupled, high strains can be due to interactions on the atomistic level and particle cracking may enable particular atomistic migrations.

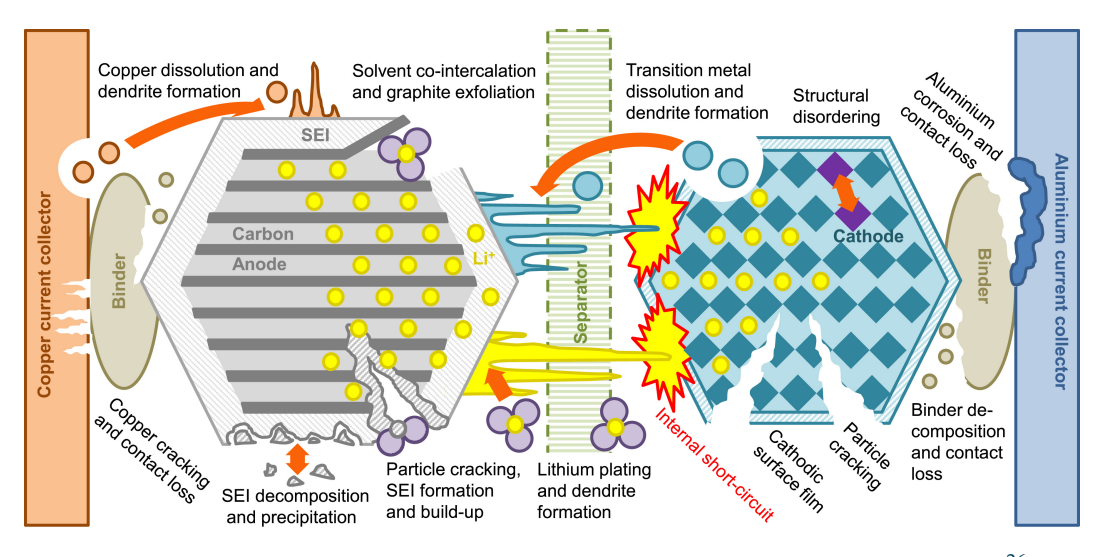


FIGURE 1.4: Common route of degradation in battery materials. From Birkl et al³⁶

The NMC structure is inherited from the LCO structure described by Goodenough (see Figure 1.5) and belongs to a class of materials broadly labelled as "layered metal oxides". At certain Li concentrations or within 5 nm of the surface of the cathode a phase transformation occurs in which the layered structure rapidly converts to Spinel and eventually proceeds to a Fm3m rock-salt structure. This surface is noted as highly

reduced. Additionally, contact with the electrolyte results in a build up of a complex surface reaction layer consisting of LiF (and organic compounds has been observed.³⁷ This process has been noted to be anistropic and occur predominantly across the pathway that Li migrates through. In this Spinel structure Li is still able to diffuse in and out of the structure but with metals occupying the Li sites diffusion is severely hindered.³⁸ This reduced lithium mobility (as-well as the nature of lithium mobility in general) has been observed through the use of optical scattering microscopy.³⁹

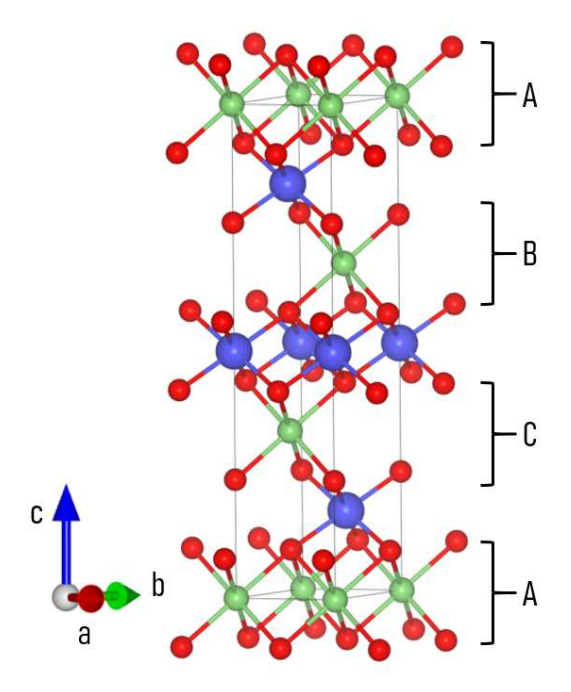


FIGURE 1.5: The O3-type R3m layered crystal structure a=b. Is analogous to the α -NaFeO₂ structure. The oxygen sub-lattice shifts along the c axis such that the fourth layer MO₂ sheet is directly above the first MO₂ sheet.

Some work has been done to inhibit or even incorporate this layered-to-Spinel transformation in a bid to maintain consistent battery performance over many years. One such method by Zhao et al⁴⁰ used a synthetic control to form hierarchical micro-structures to allow layered and Spinel structures to coexist harmoniously throughout the nanoparticles of NMC cathodes containing a small amount of Iron. The method results in a clean 3D channel in which lithium ions can transport without the same hindrance that is observed in deformed layered compounds.

Prior modelling work has shown that at low lithium concentrations the layered-to-Spinel transformation becomes thermodynamically favoured and kinetically feasible in a wide variety of metals. ^{2–4,7} The exact nature of this

layered-to-Spinel transformation is complex and multi-stepped and has been discussed in detail over many years. This phase transformation is the main focus of this body of text.

1.3 Background degradation of layered cathodes

Numerous modes of degradation have been observed experimentally in the literature for both the cathode and anode of these layered materials.³⁶ In particular, degradation of the cathode falls into two large areas, material loss (via dissolution) and material disorder.

As the mobile species loss of Li is of high importance. Typically, some Li loss is expected during the first cycles as the surface bound electrolyte decomposes and a stable solid electrolyte interface (SEI) is formed. ⁴¹ This process is exacerbated at the graphite anode and of less importance at the cathode. This SEI is composed of electrolyte decomposition products and as such are dependent on the composition of the electrolyte used. It has been reported in the literature that an electrolyte choice that aims to form a SEI that is stable and avoids the corrosive HF product can support electrolyte formation and reduce the SEI aging process. ^{42–44}

At the cathode, Vetter et al ⁴¹ characterize aging mechanisms under three large modes. Metal dissolution, phase transition and structural disordering. While the latter two are often treated as bulk processes, metal dissolution happens at the surface and can result in re-precipitation of new phases in the form of a surface film. ⁴⁵ This impacts battery performance without necessarily requiring permanent metal loss into the electrolyte. More recently, surface spectroscopy has determined that this surface reconstruction is occurs rapidly from upon cycling the pristine cathode material and within 20 cycles up to five 5 nm of cathode materials has reconstructed. This reconstructed surface is primarily the Fm3m rock-salt structure with a few bridging layers of Spinel. It was noted that this reconstruction is greatly influenced by the crystal orientation, in which reconstruction is dominant perpendicular to Li migration pathway.

Additionally, work by Boulineau ⁴⁶ identified that surface processes corresponds with a densification of Mn into the bulk of the cathode material and a Ni-rich surface layer. Figure 1.6 suggests the mechanism for this process. The pristine material undergoes a loss of surface oxygen at low levels of Lithiation. This results in under-coordinated metal ions which proceed to hop through the between Li vacancies penetrate deeper into the bulk. This yields an increased density of Mn in the bulk of materials as they hop more readily.

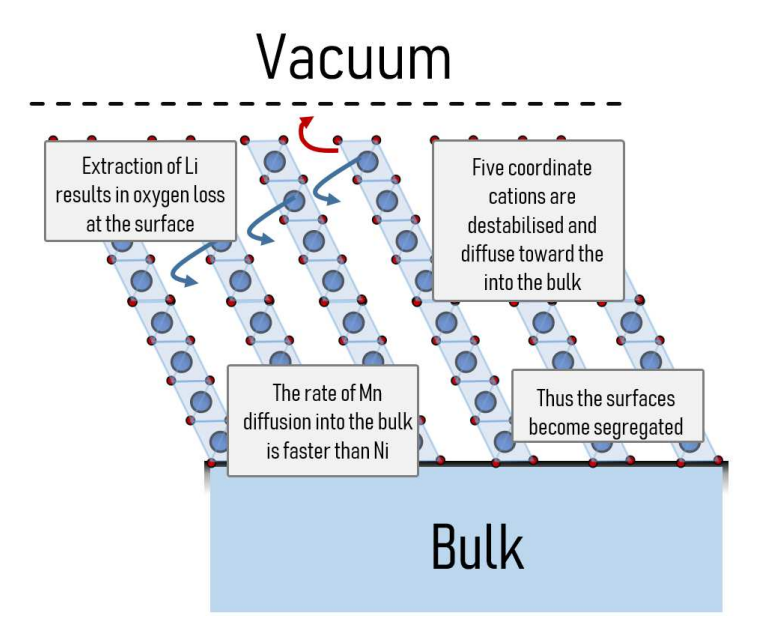


FIGURE 1.6: Proposed mechanism for metal segregation at the surfaces of cathode crystallites. *Adapted from Boulineau et al.* ⁴⁶

Modelling work $^{47-52}$ has identified that typical synthesis of layered cathode materials results in nanoparticles with equilibrium shapes that are hexagonal platelets due to the low energy (0001, $10\overline{1}4$ and $01\overline{1}2$) surfaces. This surfaces compose a large fraction of the total surface area (see Figure 1.7). More recently, Garcia et al 53,54 modeled a reconstruction of the $10\overline{1}4$ and the $01\overline{1}2$ surfaces using an ordered NMC model system and demonstrated that lattice stress is a key driving force in the Ni segregation suggesting that global composition and strain effect the chemical stability of the cathode/electrolyte interface. It's also observed that the distribution of Ni is non-uniform with a preference for grain boundaries and surface regions 55,56

Phase transformation has also been noted to occur within the bulk of these materials. In particular the Spinel phase is energetically favored for at half lithation for all 3d

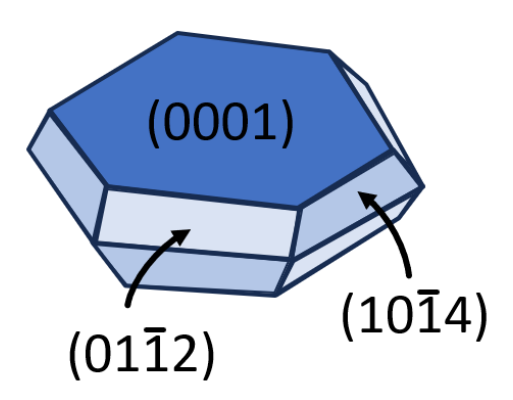


FIGURE 1.7: Layered cathode nanoparticles favor a hexagonal platelet shape. *Adapted from Kramer and Ceder.* ⁴⁷

transition metals from Ti to Cu. 2 This transformation has been noted to occur rapidly for Li $_x$ MnO $_2$ cathodes, require moderate heating for Li $_x$ NiO $_2$ cathodes, 57 while Li $_x$ CoO $_2$ cathodes appear resistant. 58 This new phase shares the same close cubic packing oxygen sub-lattice as the layered materials and thus transformation can occur without requiring deoxygenation or oxygen diffusion altogether. While in this phase, there is a noted reduction in capacity and thus potential materials that avoid this transformation are of high interest. 59

DFT calculations by Reed and Ceder ^{2,4,6} calculate two potential pathways for this transformation and suggest that metal migration is facilitated by metal 'hops' through tetrahedral sites in the Li layer. This process requires moderate delithiation to both free vacancies within the Li layer but also because at high lithiation the metals occupy the +4 oxidation state and are resistant to migration. A common approach in the literature to discern the viability of this phase transformations is to use a crystal field theory. ⁶⁰ It's argued that a metal ion with a low energy d-occupation when tetrahedral (relative to it's octahedral d occupation) is likely to migrate into tetrahedral sites and thus proceed to Spinel. The Manganese system is an interesting case as neither the 4+ or 3+ oxidation states are particularly favored for this process. However, the Mn³⁺ species undergoes a charge disproportionation reaction into a highly labile Mn²⁺ ion, with a neighboring ion being oxidized to 4+.

There is some evidence suggesting that high Nickel NMC is resistance to rapid spinel formation as Mn³⁺ is avoided regardless of the state of charge. The metal ions for a

1.4. Motivation

single metal layered oxide are typically between +3 and +4 dependent on degree of lithiation. However, for NMC materials the Nickel is preferentially reduced and the Mn oxidized, with the composition at full lithiation being $\text{LiNi}_{1/3}^{2+} \text{Mn}_{1/3}^{4+} \text{Co}_{1/3}^{3+} \text{O}_2$. ⁶¹ While avoiding rapid spinel formation NMC has shown a differing issue, both at synthesis and under consistent cycling Ni/Li disorder has been noted to occur. Zheng et al ⁶² suggest that the similar sizes of Ni²⁺ and Li⁺ driving this disorder and that introducing a greater steric barrier would inhibit this process at synthesis. Kang et al ³⁸ propose that preparation of of high Nickel cathodes via an ion exchange from a sodium manganese oxide (NaMnO₂) inhibits the disorder at synthesis and improves battery performance.

Despite the promising future of mixed metal cathodes, there is still plenty of desire to pursue layered-LiMnO₂, with Manganese Oxide as a host lattice these materials have nominal voltages upward of 4.0 V (vs Li⁺/Li⁰)¹⁴ while not having the ethical issues often seen for cathodes containing Cobalt. ²⁴ As a result, much work on avoiding this layered to Spinel transformation is still undertaken, recently modelling work by Seymour et al³ investigated the electronic structure of the layered-LiMnO₂ during the the initial steps of this degradation mode. A low energy defect that features a locked Li-Mn pair held in the tetrahedral sites across a vacancy in the metal layer as a 'dumbbell'. Corroborating work by Ceder and Reed,² this dumbbell structure was found to be low energy and due to a charge disproportionation reaction. In a follow-up publication Seymour et al⁷ suggest that dopants can inhibit the formation of the defect where it's suggested that small dopants such as Al³⁺ and Cr³⁺ can increase the barrier to this migration and prolong battery life. A methodology that completely inhibits Spinel formation may revitalize this material as a alternative cathode option.

1.4 Motivation

With low Co cathodes becoming common place in the industry it's essential to understand the routes of battery breakdown and the factors that influence them within NMC cathodes. These materials have been explored at depth^{2,3,63} and

atomistic modelling has identified that phase transformation is governed by an atomistic process.

In particular layered $\text{Li}_x \text{MnO}_2$ has long been identified as an unsuitable cathode material despite its high energy densities, low cost and low toxicity. This material undergoes a rapid phase transformation to Spinel at room temperature. While it's known that all of the layered 3d metal oxides are thermodynamically favoured to transform into Spinel, Co and Ni are resistant while Mn is not. ⁶⁴ This indicates that this phase transformation is governed by kinetics, therefore processes that can affect the rate of this transformation may revitalise Mn as a pure metal cathode.

Additionally attempting to investigate the extent to which degradation processes are coupled with one another will shed insight into potential feedback loops and the strategies to avoid them. In particular chemical modelling of surface degradation atomistically may produce results applicable to larger scale models and allow further understanding of surface bound degradation on a macro-scale.

There has been a plethora of recent publications looking to elucidate the electronic structure for the class of materials broadly labelled 'metal oxides' in the context of cathode materials. In particular, the layered metal oxides and their phase stability has been studied in detail. However modelling such materials allows quite a bit of user-flexibility with a wide range of reported structures and parameters. In particular there is evidence that parameters that are often considered a "user-adjustable dial" 65 can significantly distort results and may lead to incorrect conclusions being drawn 3. Investigating numerous modelling practices will hopefully yield guiding principles when investigating cathode systems.

Chapter 2

First-Principles methods for modelling battery materials

The findings throughout this thesis have been drawn from first principle (*ab initio*) calculations. These calculations are distinguished from empirical methods in that all input parameters are based on physical constants, and there are 'no' user-determined parameters. This in theory separates results from bias, as the models are 'a complete picture' of the electrons within a molecular system with the relevant physics and chemistry's being the only influencing factors on the nature of the results. In general, the resulting accuracy of first principle methods should be a function of computational power and calculation time. In practice however, such processes use numerous approximations, have user-defined parameters based on empirical results or yield results that are 'open to interpretation'.

When modelling a new system, benchmark calculations are important to understand exactly where the interplay between accuracy and computational cost lies, cheap calculations which fail to grasp the important chemistry's will result in erroneously drawn conclusions. While utilising hours of compute time on a result that could have been acquired with a tenth of the cost wastes compute resources and time. These bench-marking methods are discussed at detail in Chapter 3, using the bench-marking framework from the MaterialsProject. ^{66–69}

2.1 The quantum many body problem and the wavefunction

With the exception of machine learned methods $^{70-72}$ modelling of chemical systems is typically mathematically rigorous and can branch a plethora of time and length scales. On the macro-scale, statistical thermodynamics 73,74 or coarse grain Newtonian mechanics $^{75-77}$ are often sufficient at predicting the large bulk properties of a chemical system. On the nanometer scales however, quantum mechanics rears its ugly head, $^{78-80}$ which explicitly requires finding the (*approx. non-relative*) wavefunction Φ of a system through solving the Schrödinger equation (see equation 2.1). $^{81-84}$

$$i\hbar \frac{d}{dt}\Phi(t) = \hat{H}\Phi(t) \tag{2.1}$$

The time independent Schrödinger Equation is much more applicable since most chemical processes happen 'slowly'.

$$\hat{H}\Psi = E\Psi \tag{2.2}$$

 \hat{H} denotes the Hamiltonian operator and E is the energy of the systems wavefunction Ψ . In expanded form, \hat{H} is the sum of kinetic and potential energies of all particles in addition to their Coulombic interactions.

$$\hat{H} = -\frac{\bar{h}^2}{2m} \sum_{i} \nabla_i^2 - \sum_{A} \frac{\bar{h}^2}{2M_A} \nabla_A^2 - \sum_{A,i} \frac{Z_A e^2}{4\pi\epsilon_0 r_{A,i}} + \sum_{A>B} \frac{Z_A Z_B e^2}{4\pi\epsilon_0 R_{A,B}} + \sum_{i>j} \frac{e^2}{4\pi\epsilon_0 r_{i,j}}$$
(2.3)

Where i, j are electron indices and A, B are nuclei indices. This equation is often expressed in atomic units (i.e. normalised to $4\pi\epsilon_0$, and Planck's constant).

This equation cannot strictly be separated into the nuclear and electronic components due to the coulombic interaction term between nuclei and electrons. However, the adiabatic Born-Oppenheimer^{85,86} approximation assumes that nuclei motion is orders of magnitude slower than electronic motion and thus can be uncoupled, yielding the electronic wavefunction.

$$\hat{H}_e(r,R)\psi_e(r,R) = E_e\psi_e(r,R) \tag{2.4}$$

$$\psi_{n,e}(r,R) = \chi_n(R)\psi_e(r,R) \tag{2.5}$$

 χ_n is the nuclear vibrational wavefunction that depends on the nuclear coordinates R and is index by the vibrational quantum state n. The electronic wavefunction ψ_e is a function of both the electronic and nuclear coordinates (r and R). The total wavefunction $\psi_{n,e}$ is approximated as the product of these decoupled wavefunctions simplifying the Schrödinger equation for molecules.

For instance when applying the Born-Oppenheimer approximation to a diatomic, the nuclear and electronic motion is decoupled and as such at any given inter-nuclear distance (R) the electronic Schrödinger equation can be solved and the potential energy found. A potential energy curve can be obtained (see Figure 2.1) where the minima energy indicates the equilibrium bond length.

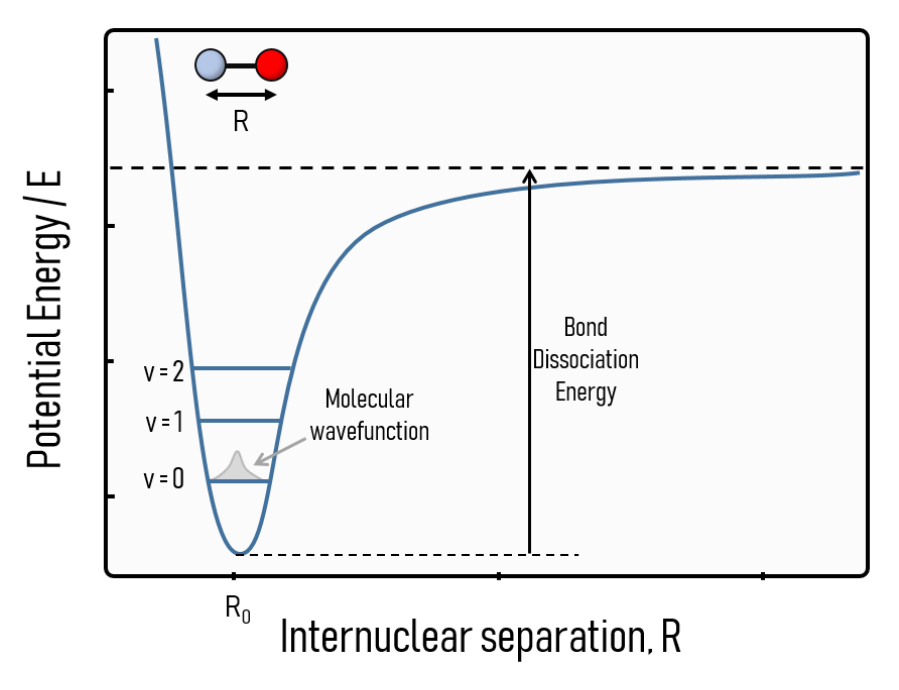


FIGURE 2.1: The Born Oppenheimer approximation assumes that electron motion is much faster than nuclear motion and as such they can be uncoupled and equilibrium bond lengths can be determined. For asymmetric larger systems, the dimensionality of R is 3N-6.

2.2 Hartree Fock

The resulting wavefunction, being a descriptor of all electrons $\Psi(x_1, x_2, x_3, ..., x_N)$, is formally a many-body object with a dimensionality of 3N. As a result, often the Hartree product is employed; in which the complete Schrödinger equation for a system is approximated to be a combination of it's single-electron solutions in a mean field. 87

$$\left[\frac{-\hbar^2}{2m} \nabla_i^2 - \frac{Ze^2}{r_i} + e^2 \sum_{j \neq i} \int d^3 r_j \frac{|\phi_j(\vec{r}_j)|^2}{|\vec{r}_i - \vec{r}_j|} \right] \phi_i(\vec{r}_i) = \varepsilon_i \phi_i(\vec{r}_i)$$
(2.6)

$$\psi \approx \phi_1(\vec{r_1})\phi_2(\vec{r_2})\phi_3(\vec{r_3})\dots\phi_Z(\vec{r_Z}) \tag{2.7}$$

 ϵ_i is the energy contribution of electron i. The first two terms of Equation 2.6 are the kinetic and potential energy for electron i and the third term represents the potential due to all other electrons. This assumption places every particle within a dielectric medium (generated from the coulombic terms of all other particles), reducing the 3N dimensional matrix to N 3 dimensional matrices.

2.2.1 Slater determinants

With quantum mechanics developing, a fundamental component was missing in Hartree's approximation to the valid wavefunctions of fermions, anti-symmetry. One such methodology was that by Fock (See equations 2.8, 2.9), ⁸⁸ that can find solutions to the wave function by constructing the Fock operator.

$$\hat{F}\psi_i = \epsilon_i \psi_i \tag{2.8}$$

Where:

$$\hat{F} = \hat{H}_{core} + \sum_{j=1}^{n/2} |2\hat{J}_{j}(i) - \hat{K}_{j}(i)|$$
 (2.9)

This formalism introduces the Fock operator \hat{F} . This operator consists of the one-electron terms bundled into \hat{H}_{core} , and the electron-electron operators between electron i and electron j for Coulombic and exchange interactions, \hat{J} and \hat{K} respectively.

2.2. Hartree Fock

It was found that the use of Slater determinants ^{89,90} within the Fock formulation trivially satisfies the anti-symmetric necessity of electron exchange, which in combination with an approximation to the Schrödinger equation being composed of one-electron wave-functions can be utilised to propose 'solutions' to the wavefunction (see Equation 2.10) that account for Pauli exclusion and electron exchange. ^{91,92}

$$\psi_{HF} = \frac{1}{\sqrt{N!}} \begin{vmatrix} \chi_1(\mathbf{r_1}) & \chi_2(\mathbf{r_1}) & \dots & \chi_n(\mathbf{r_1}) \\ \chi_1(\mathbf{r_2}) & \chi_2(\mathbf{r_2}) & \dots & \dots \\ \vdots & \vdots & \ddots & \dots \\ \chi_1(\mathbf{r_n}) & \dots & \dots & \chi_n(\mathbf{r_n}) \end{vmatrix}$$
(2.10)

2.2.2 The Variational Principle

For any valid trial wavefunction Ψ_T , the expectation of the energy can be determined. This expectation energy must be equal or greater than the true ground-state energy of the system.

$$E_{gs} \le \langle \Psi_T | \hat{H} | \Psi_T \rangle \equiv E[\Psi_T] \tag{2.11}$$

The Rayleigh-Ritz variational principle, 93 yields an approach to finding this ground state wavefunction from a trial wavefunction Ψ_T . Typically, this is achieved by introducing a small variation to this trial wavefunction such that $\Psi_T \to \Psi_T + \delta \Psi_T$. Thus the energy of this wavefunction is:

$$E[\Psi_{T} + \delta \Psi_{T}] = \langle (\Psi_{T} + \delta \Psi_{T}) | \hat{H} | (\Psi_{T} + \delta \Psi_{T}) \rangle$$
 (2.12)

$$E[\Psi_{T} + \delta \Psi_{T}] = E[\Psi_{T}] + \langle \delta \Psi_{T} | \hat{H} | \Psi_{T} \rangle + \langle \Psi_{T} | \hat{H} | \delta \Psi_{T} \rangle + \dots$$
 (2.13)

Where the first term in equation 2.13 yields the unchanged energy $E[\Psi_T]$ the second and third terms are first order and higher order terms are omitted. The ground state energy must lie at a minima and therefore be found when $\delta E = 0$. Typically, with modern computing this variation is calculated through the Roothaan Equations,

which are a matrix formalism and can be derived using:

$$|\Psi_T\rangle = \sum_{i=1}^k c_i |\psi_i\rangle \tag{2.14}$$

in which the energy is derived as:

$$E = \langle \Psi_T | \hat{H} | \Psi_T \rangle = \sum_{i=1}^k \sum_{j=1}^k c_i^* c_j \langle \psi_i | \hat{H} | \psi_j \rangle$$
 (2.15)

When using the orthonormal constraint $\langle \Psi_T | | \Psi_T \rangle = 1$ is minimised when:

$$\sum_{j} \hat{H}_{i,j} c_{j} = E \sum_{j} j S_{i,j} c_{j}$$
 (2.16)

Which in matrix form:

$$\underline{H}\ \underline{c} = E\ \underline{S}\ \underline{c} \tag{2.17}$$

Where $\underline{\underline{H}}$ is the Hamiltonian matrix, \underline{c} is the coefficient vector of the one-electron orbitals, $\underline{\underline{S}}$ is the overlap matrix. In the special case in which orthonormality is preserved this overlap matrix is the Identity matrix yielding the matrix representation of the Schrödinger equation.

Figure 2.2 shows a typical flowchart for iteratively calculating the wavefunction within Hartree-Fock theory. Using a linear combination of 'Hydrogen-like' atomic orbitals as an ansatz (initial guess) wavefunction. The Fock matrix and its coefficients can be formulated from the Coulombic and Kinetic interactions from this initial guess (as seen in Equation 2.6), which in turn can be used to reform the Fock matrix and coefficients until a convergence criteria is reached. However, it wasn't until the 1950's in which computational power improved and the Hartree-Fock method saw implementation in modern computing. Hartree-Fock, however, is fundamentally flawed in approach, by isolating each electron within a mean-field. As a result, electron-electron correlation effects are ignored, resulting in inaccuracy. 94

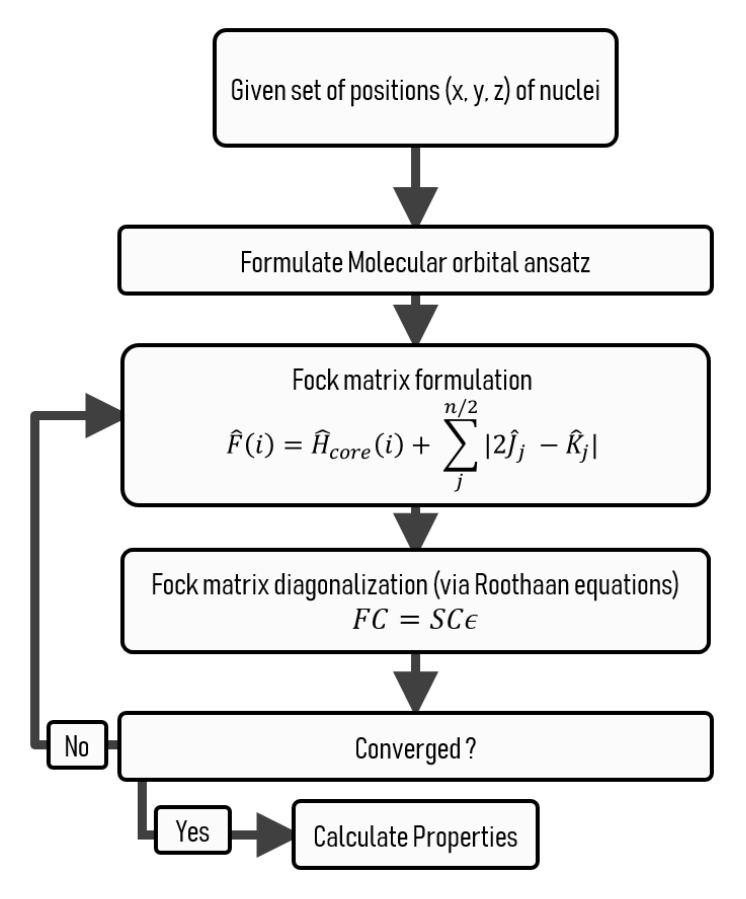


FIGURE 2.2: Flowchart diagram for iteratively calculating the wavefunction within Hartree-Fock theory.

2.3 Density Functional Theory

With electron correlation effects often proving necessary to capture the details of a system, most quantum mechanical modelling has shifted away from pure Hartree-Fock. One such approach is Density Functional Theory (DFT). By approaching the problem away from the wavefunction and instead from the electron density $\rho(\mathbf{r})$ where the electron density is defined as:

$$\rho(\mathbf{r}) = \sum_{i=1} \psi_i^*(\mathbf{r}) \psi_i(\mathbf{r}), \tag{2.18}$$

Where this summation is over the occupied orbitals. This is valid as the first Hohnenberg-Kohm theorem states that "the external potential of a system is a unique functional of the electron density, $\rho(\mathbf{r})$. Therefore the full many particle ground state is a unique functional of this electron density.

The second Hohnenberg-Kohm theorem is a reformulation of the variational principle, stating that for a trial density $\rho(\mathbf{r})$ the ground-state energy is less than or equal to the energy of the trial electron density:

$$E_{gs} \le E[\rho], \tag{2.19}$$

Where this energy functional is given by:

$$E = T[\rho] + V_{ext}[\rho] + U[\rho].$$
 (2.20)

Here $T[\rho]$ is the kinetic energy operator, $V_{ext}[\$rho]$ is the operator for the external potential and $U[\rho]$ is the electron-electron repulsion operator. The kinetic energy operator for a system of non-interacting electrons is:

$$T_s[\rho] = \frac{1}{2} \int \nabla \psi^*(\mathbf{r}) \nabla \psi^*(\mathbf{r}) d\mathbf{r}, \qquad (2.21)$$

The external potential energy operator is:

$$V_{ext}[\rho] = \int v(\mathbf{r})\rho(\mathbf{r})d\mathbf{r}, \qquad (2.22)$$

The electron-electron interaction energy operator is:

$$\hat{U} = \frac{1}{2} \int \int \frac{\rho(\mathbf{r})\rho(\mathbf{r}')}{|\mathbf{r} - \mathbf{r}'|} d\mathbf{r} d\mathbf{r}'.$$
 (2.23)

The kinetic energy and electron-electron operators are typically bundled into the 'unknown' functional $F[\rho(\mathbf{r})]$: ⁹⁵

$$F[\rho(\mathbf{r})] = T[\rho] + U[\rho], \tag{2.24}$$

which yields:

$$E[\rho] = \int v(\mathbf{r})\rho(\mathbf{r})d\mathbf{r} + F[\rho]$$
 (2.25)

This 'unknown' functional is universally valid and inherently incorporate this elusive correlation energy that Hartree-Fock misses. Therefore for the correct charge density

 $\rho(\mathbf{r})$, $E[\rho]$ is equal to the ground-state energy.

Kohm and Sham define this unknown functional via the Kohm-Sham equations upon the one electron states. 96 This unknown functional $F[\rho]$ is re-framed such that it is the *difference* between a system of N interacting electrons and a fictitious system of N non-interacting electrons:

$$F[\rho] = T_s[\rho] + E'_{xc}[\rho], \qquad (2.26)$$

where $T_s[\rho]$ is the kinetic energy of a system of non-interacting electrons with density ρ , and $E_{xc}[\rho]$ contains both the exchange and correlation energy aswell as the difference in kinetic energy between interacting and non-interacting systems.

The electron-correlation energy can be detailed as:

$$E'_{xc} = \left(T[\rho] - T_s[\rho]\right) + E_H[\rho] + E_{xc}[\rho],$$
 (2.27)

where $T[\rho] - T_s[\rho]$ is the difference in kinetic energies, E_H is the Functional for the Hartree potential that arises from electrostatic repulsion of electrons and E_{xc} is this exchange-correlation functional.

This leads to the Kohm-Sham equations, which are a set of one-electron equations:

$$H\psi_i(\mathbf{r}) = \left(-\frac{\hbar^2}{2m}\nabla^2 + v_{eff}(\mathbf{r})\right)\psi_i(\mathbf{r}) = \epsilon_i\psi_i(\mathbf{r}), \tag{2.28}$$

where this Kohn-Sham effective potential $v_{eff}(\mathbf{r})$ is composed of the external potential, the Hartree potential and the potential due to exchange-correlation: ⁹⁶

$$v_{eff}(\mathbf{r}) = V_{ext}[\rho] + \frac{\delta E_H[\rho]}{\delta \rho} + \frac{\delta E_{xc}[\rho]}{\delta \rho}.$$
 (2.29)

In which the electron density can be derived from a set of N orbital solutions to the one electron equations:

$$\rho(\mathbf{r}) = \sum_{i=1}^{N} \sum_{s} |\psi_i(\mathbf{r}, s)|^2, \qquad (2.30)$$

where the sum is over the occupied Kohm-Sham orbitals. This yields a self-consistent determination of the electron density. In which an initial guess electron density yields a potential via equation 2.28 that updates the electron density through equation 2.30. Offering an iterative approach to calculate the electron density $\rho(\mathbf{r})$ to a desired degree of convergence.

2.3.1 LDA and GGA

With the groundwork for solving these series of equations iteratively laid, the only remaining task is finding sufficiently accurate approximations of the unknown E_{xc} and thus $v_{eff}(\mathbf{r})$ in ensuring accurate calculations. Kohn and Sham suggested using a simple Local Density Approximation (LDA) described by Enrico Fermi, ⁹⁶ where the exchange correlation energy is modelled as uniform electron gas:

$$E_{xc}^{LDA} = \int d^3 \mathbf{r} \rho(\mathbf{r}) \epsilon_{xc}(\rho(\mathbf{r}))$$
 (2.31)

This assumes that the exchange correlation energy for a system at a given point in space is equal to that of a homogeneous electron gas with equivalent density. For electron densities that are smooth and not correlated, this performs exceedingly well (i.e. those with high delocalisation). However, systems with highly localized states tend to perform poorly. Numerous case studies show that LDA has a tendency to over-bind atoms resulting in underestimated bond lengths and cell volumes. ^{97,98}

More recently, the Generalized Gradient Approximation (GGA)^{99–101} has been shown as an effective functional in Kohn-Sham DFT. This method assumes that the elusive exchange correlation energy at a point in space is dependant on both the electron density and the gradient of this density.

$$E_{xc}^{GGA} = \int d^3 \mathbf{r} f(\rho(\mathbf{r}), |\nabla \rho(\mathbf{r})|)$$
 (2.32)

Which in practice often is as a correction term added to the LDA functional:

$$E_{xc}^{GGA} = E_{xc}^{LDA} + \Delta F_{xc} \tag{2.33}$$

With F_{xc} being often labelled the 'enhancement factor' typically with the form:

$$F = k \frac{|\nabla \rho(\mathbf{r})|}{n^{4/3}(\mathbf{r})} \tag{2.34}$$

Practically, for both LDA and GGA, the functional that governs the exchange-correlation interaction are parameterized, with the nature of the uniform electron gas being well established in LDA. However for GGA, some choice is available. During the 90's numerous descriptions of this functional were developed semi-empirically. Some functionals were derived from analytically fitting specific conditions ^{99,102–104} (CAM, PW, B88, G96), allowing accurate results for 'poorly-behaved' systems at the expense of some of the physical reasoning. While other functionals are derived ab-initio and thus should model reality (B86, PBE, PW91). ¹⁰⁵

All of the work in this text has utilised the Plane wave implementation of the hubbard U variant of a pure PBE functional (often denoted PBE+U). In pure PBE this enhancement factor is derived non-empirically as:

$$F_{xc}^{PBE} = 1 + \kappa - \left(\frac{k}{1 + \mu s^2/k}\right)$$
 (2.35)

where μ is set to 0.21951 and κ is set to 0.804 and s is the dimensionless density gradient ($|\nabla n|/6\pi n^{4/3}$). These are chosen to satisfy a second order gradient expansion for correlation and a linear response for an electron gas (i.e. LDA-like). This functional performs well for 3d metals, however has a tendency to over delocalise metal oxide systems. 106,107

*It should be noted, that for magnetic systems, the Spin-density is used instead of the electron density, this has been omitted from all equations prior for simplicity. For GGA the spin-polarised exchange energy is:

$$E_{xc}^{GGA} = \int d^3 \mathbf{r} f(\rho(\mathbf{r})_{\uparrow}, \nabla \rho(\mathbf{r})_{\downarrow})$$
 (2.36)

2.3.2 The Hubbard U for localising metal orbitals

Much of the body of this work studies transition metal oxides. PBE (and GGA in general) has a tendency to over-delocalise electrons within metal oxides. Which while useful for simple metallic systems, many of the oxides exhibit Mott-insulating properties. ^{108–112}

The electronic structure for a spin pairs system abides to the same symmetry constraint as the crystal:

$$V(r) = V(r+L) \to n(r) = n(r+L)$$
 (2.37)

While a sensible conclusion, this leads to systems with partially filled d-bands always being metallic. However for some oxides, such as CoO and NiO, conventional orbital suggests a half occupied d-band despite being known insulators. The electrons in these materials are 'highly-correlated' resulting in symmetry breaking across the unit cell. ^{108,112}

$$(Ni^{2+}O^{2-})_2 \rightarrow Ni^{3+}O^{2-} + Ni^+O^{2-}$$
 (2.38)

One approach to handling this is the Hubbard Model. ^{110,113–116} Simply stated, the Hubbard model considers the wavefunction for an electron to consist of two parts; a kinetic ('hopping') term and a potential term that acts as the on-site interaction (see Equations 2.40 and 2.41). In the context of pure GGA, no such on-site interaction is present and thus on-site occupation of electrons are typically under-represented.

Numerous implementations of the Hubbard model are found throughout the literature, with various additional terms or symmetry considerations. ^{65,67} Simply described most implementations of this model take the form:

$$E_{DFT+U} = E_{DFT} + E_{nonint.} - E_{int} (2.39)$$

Which states that the energy calculated via DFT+U is equal to pure DFT + the energy from the coulombic and exchange interactions of non-integer orbital occupancies ($E_{nonint.}$) and subtracting the the same kind of interactions for integer occupancies. ¹¹⁷

The implementation used throughout this thesis is the rotationally invariant implementation by Dudarev et al. 118,119

$$E_{PBE+U} = E_{PBE} + \sum_{I} \frac{U^{I} - J^{I}}{2} \sum_{m,\sigma} \left(n_{mm}^{l\sigma\sigma} - \sum_{m'\sigma'} n_{mm'}^{l\sigma\sigma'} n_{m'm}^{l\sigma'\sigma} \right)$$
(2.40)

Where U and J are often user defined and are the spherically averaged matrix elements of the Coulombic electron-electron interaction. I, is the label of atomic site within the unit cell, m and σ are the atomic magnetic quantum number and spin index respectively. n is the system occupation matrix and therefore the first term within the brackets is the on-site occupancy and the second the delocalised interaction ($0 \le 0$) occupancy $0 \le 1$). Since the U and J values are user defined they can be used as a means to control the extent of delocalisation within a model. Typically this interaction is defined via a 'U' parameter in units of energy (2-7 eV)

$$E_{PBE+U}[n(r)] = E_{PBE}[n(r)] + E_{U}[n_{m}^{l,\sigma}]$$
 (2.41)

This parameter has been studied extensively with both empirical U values found in the literature, ⁹ via tailoring expected band-gaps of known insulating materials. There are *ab initio* methods for determining this Hubbard U interaction via a linear response, ⁶⁵ however there is little evidence this provides any improvements over being user-defined. Some care has to be taken when utilising the Hubbard U, with work being shown that metal migration energy barriers can be heavily impacted by this choice.

Table 2.1 shows the Hubbard U values used throughout this body of work. While oxidation state is likely to impact the extent of delocalization, the values chosen have been shown to be effective at predicting band-gaps for metal oxides⁹.

	Ti	V	Cr	Mn	Fe	Co	Ni	Zn	Li	О
U value	0.0	3.2	3.7	3.9	5.3	3.2	5.3	0.0	0.0	0.0

TABLE 2.1: Chosen U values, based on work by Jain et al.⁹

2.4 Plane wave basis sets

All of the modelling work here has utilised the Vienna Ab Initio Software Package (VASP). The Kohn-Sham equations have been solved in VASP using norm-conserving Vanderbilt pseudopotentials 120,121 determined from first principles in an iterative fashion. Traditional DFT scales with N^3 where is N is the number of atoms, this presents a hard limit on what can be reasonably modelled within the confines of a finite cell. Fortunately, VASP utilises translational symmetry to implement periodicity and can model crystal systems.

Accurately modelling the wavefunction, that is the Bloch functions of the Kohn-Sham orbitals, of any periodic system requires a sufficient basis set representation and as such is a careful balancing act of efficiency and accuracy. Numerous such schemes have been derived with varying complexities and computational cost. For instance, Gaussian's ^{122,123} (see Equation 2.43) yield analytic integrals, in which orbitals often directly correspond to bonding modes. However, these are particularly expensive and usually reserved for non-periodic systems (i.e. organic calculations). Alternatively there are Plane waves, ^{121,124–126} these are readily incorporated into periodic crystals using Bloch's theorem.

This body of work has utilised Plane Waves (see Equations 2.44, 2.45), these are prevalent throughout solid state modelling as they scale well computationally $(O(N^2))$ utilising Fourier transformations. The general form of the expansion of wavefunctions into a basis set is:

$$\psi_i(r) = \sum_{a=1}^{N_b} c_{i,a} f_a(r)$$
 (2.42)

Which as a Gaussian:

$$\psi_i(r) = \sum_{ilm} C_{ij,lm} e^{-a_i r^2} Y_{lm}(\hat{r})$$
 (2.43)

and as a plane wave in a periodic system (Ω is the total volume of the primitive cell):

$$\psi_{i,k}(r) = \frac{1}{\Omega} \sum_{G} C_{ik,G} e^{i(k+G)\cdot r}$$
(2.44)

and to ensure the periodicity of the lattice:

$$e^{iG\cdot(r+R)} = e^{iG\cdot r} \tag{2.45}$$

In which only some wave-vectors (G) are valid (see Section 2.4.3)

While with a complete plane wave basis set the wavefunction for a periodic system can be calculated in principle, the computational cost is often prohibitive. As such some approximations are taken, which are discussed briefly in sections 2.4.1 - 2.4.3.

2.4.1 The pseudopotential method

While it can be demonstrated that a complete basis set defines the wavefunction of a periodic system completely, the cost is often prohibitively expensive to describe the interactions of every electron. In particular for heavy metals, the tight-boundness of core electrons result in them requiring exceedingly high kinetic energy plane waves to accurately model the wavefunction and charge density of a system. ¹²⁷ This is all while contributing very little to chemical bonding and being largely impervious to the chemical environment. Instead, common practice is to 'remove' the core electrons and the strong Coulombic potential instead representing them by a pseudopotential which can be represented by low node plane waves and thus a small basis set. This should have minimal impact on calculation results provided the following assumptions hold true:

- Bonding/Valence electron density lies far outside of the core radius.
- The valance wavefunction remains unchanged outside of the core-region
- The frozen pseudo wave function matches at the edge of the core region
- pseudopotentials are norm-conserving (Total Charge density is maintained)
- pseudopotentials maintain scattering properties (non-local)

The general form for these pseudopotentials is:

$$\hat{V}_{ps}(r) = \sum_{l} \sum_{m} \langle Y_{lm} | V_{lm}(r) | Y_{lm} \rangle$$
(2.46)

In which Y is necessary to generate a projector for each angular momentum component.

These pseudopotentials can be calculated from an isolated atom using an all-electron DFT approach. The resulting valance wavefunctions are modified in the core region to remove oscillations while obeying norm-conservation. Inversion of the Schrödinger equation yields the pseudopotential, this procedure yields atomic pseudopotentials that can be transferred between widely varying systems. ^{128,129} Both the norm and scattering conserving properties can be relaxed and typically is done to generate 'ultra-soft' pseudopotentials. ¹³⁰ Typically, these are system dependent but offer reduced energy cut-off (i.e. a smaller basis set) which may be necessary when running into memory constraints (see section 2.4.3).

Figure 2.3 describes the resulting wavefunctions and potentials for both the 'all-electron' and the 'frozen-core psuedopotential' methods. After a certain radius away from the core both the potential and wavefunction (V_{PS} and Ψ_{PS}) become equivalent to the all-electron method.

Numerous pseudopotentials have been derived and pre-calculated with varying optimizations ^{132,133} and as such the choice in pseudopotential is largely to the users discretion and a measure of the desired accuracy. The study by Jain et al ^{66,134} has calculated the errors for numerous pseudopotentials available within VASP. The guidance given by Jain et al has been followed here ^{9,134,135}.

2.4.2 Reciprocal space and the Brillouin Zone

In dealing with plane waves, it's often convenient to use reciprocal space, as such every Bravais lattice has a corresponding reciprocal lattice (in 'k space'). In this k space, the first Brillouin zone is the locus of points that are closer to the origin than

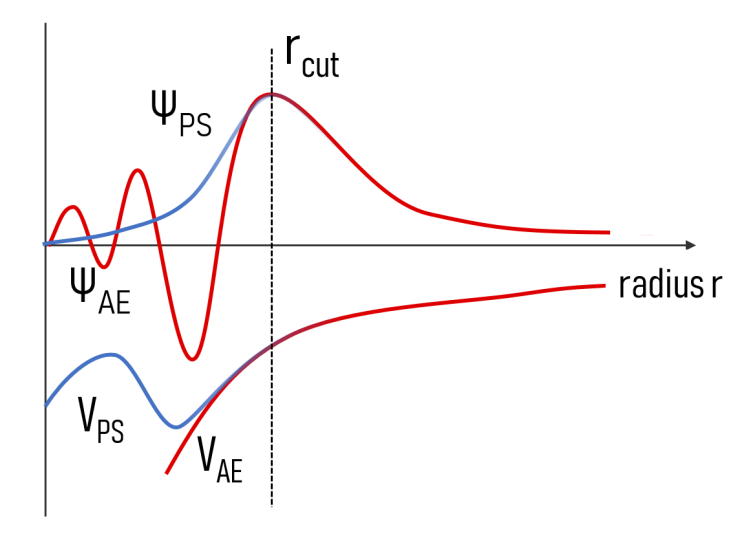


FIGURE 2.3: Potential and wavefunction of a pseudopotential as a function of distance from the nucleus. The all electron (red) and pseudo wave function (blue) and their corresponding potentials. r_{cut} represents the distance after which the pseudopotential is similar to the all electron potential. *Adapted from Payne et al.* ¹³¹

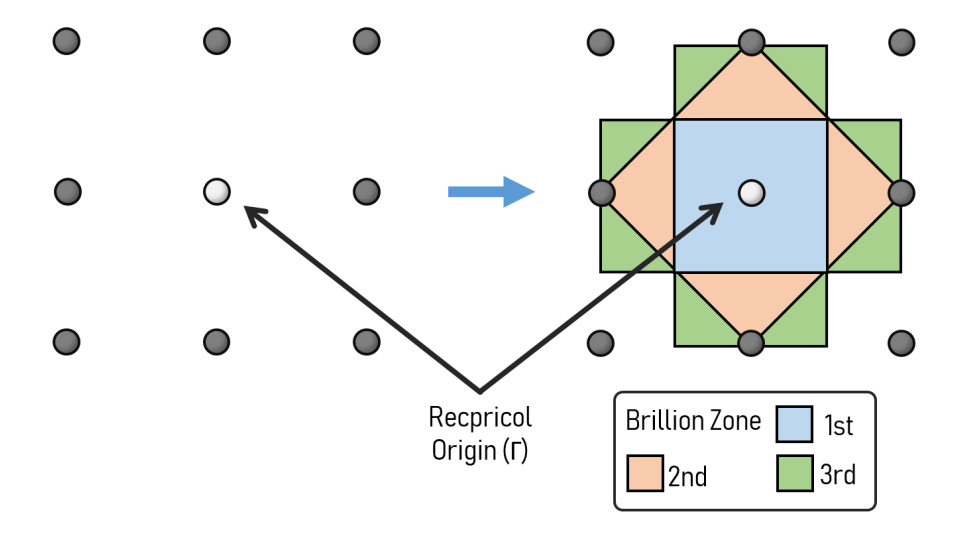


FIGURE 2.4: Brillouin zones of a 2d lattice. This is defined as the area that lies closer to the origin than any other lattice point within reciprocal space

that of any other reciprocal lattice point the Voronio diagram about the origin. ^{136,137} That is, the area that can be reached from the origin without crossing a singular Bragg plane. This region is of high importance, since Bloch's theorem states that a periodic system can be uniquely defined with just wave-vectors lying within this region.

Figure 2.4 depicts such Brillouin zones, in which accurate modelling of the wavefunction only sampling the first Brillouin zone is required.

Often, this Brillouin zone belongs to a high symmetry group and the region that needs to be sampled can be reduced (into the irreducible Brillouin zone). Many schemes in doing so are available in the literature and readily incorporated into most simulation packages. 138-141 However, while yielding a bound region in k space, there is no immediate indication as to how densely this region needs to be sampled to produce accurate results. Since both the wavefunction and charge densities are periodic, a insufficient sampling of the brillioun zone in k-space would yield spurious interactions and a poor description of the electronic structure. Computationally, this region is typically sampled through a regular equidistant mesh (k grid) and a simple convergence study is required to determine the density of k grid required for accurate results. Best practice generation of k grids is debated in literature (such as those that pass through the origin) or other high symmetry regions, ^{139,142,143} with different trade-offs depending on the Bravais lattice of the host system. Typically, in modern modelling the density of the k grid can be considered a user-controlled dial that controls accuracy and speed. Band structure calculations and other fine-electronic measurements often require dense k grids, whereas simple total energy calculations can suffice with sparser k grids (and reduced computational cost).

2.4.3 Kinetic energy cutoffs

Since the system has a set volume, expansion of the plane waves must consist of only those with the same periodicity as the lattice. Where the reciprocal lattice vectors are defined as:

$$\vec{b}_1 = 2\pi \frac{\vec{a}_2 \times \vec{a}_3}{\Omega} \tag{2.47}$$

$$\vec{b}_2 = 2\pi \frac{\vec{a}_3 \times \vec{a}_1}{\Omega} \tag{2.48}$$

$$\vec{b}_3 = 2\pi \frac{\vec{a}_1 \times \vec{a}_2}{\Omega} \tag{2.49}$$

Which yields the wave-vectors that satisfy the periodicity of the lattice as:

$$\vec{G}_{i_1 i_2 i_3} = \left(i_1 - \frac{N_1}{2}\right) \vec{b}_1 + \left(i_2 - \frac{N_2}{2}\right) \vec{b}_2 + \left(i_3 - \frac{N_3}{2}\right) \vec{b}_3 \tag{2.50}$$

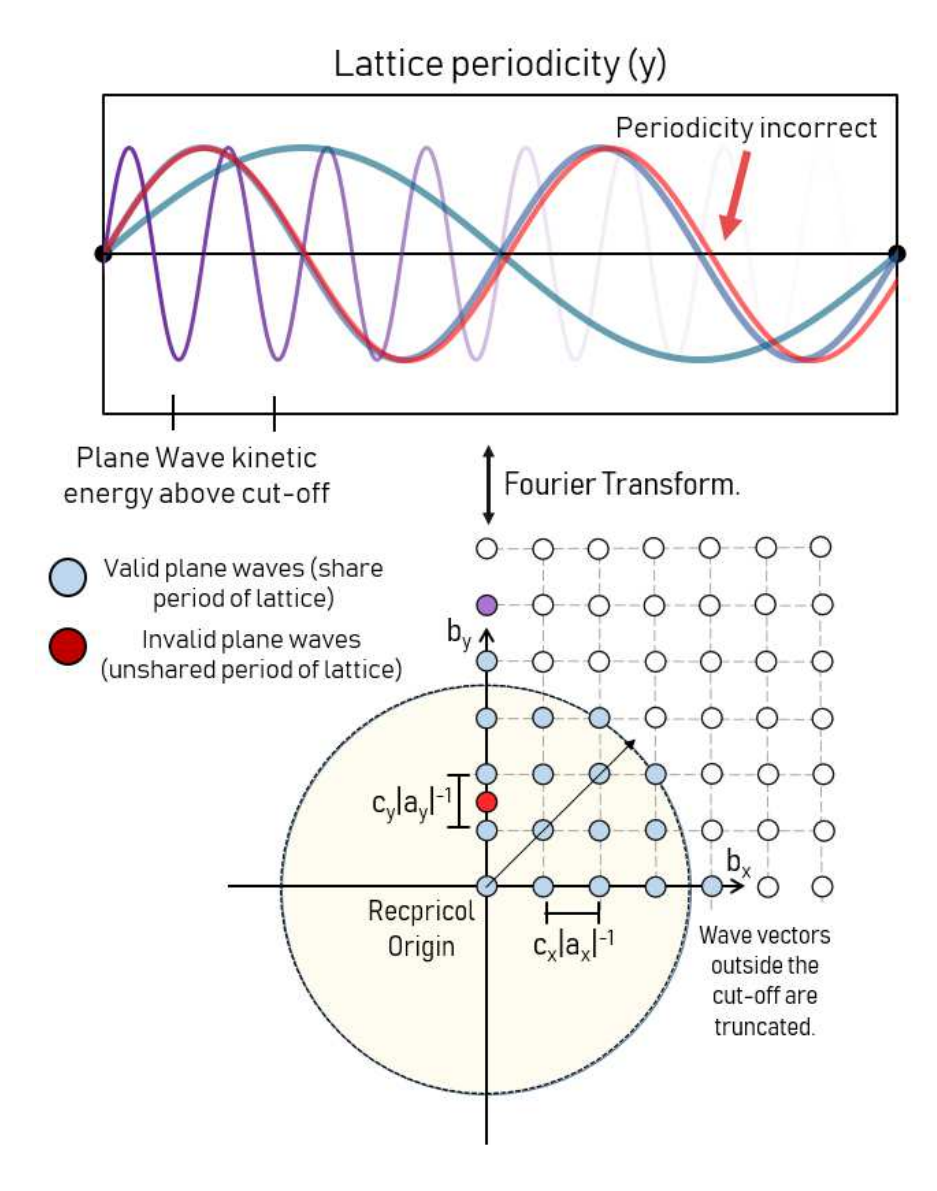


FIGURE 2.5: Plane waves within reciprocal space. Valid plane waves are such that they share the periodicity of the lattice. The plane wave cutoff condition E_{cut} truncates the summation such that exceedingly high energy plane waves are not included in the calculation.

In reciprocal space, this corresponds to discrete values in which the wave vectors fit this condition (see Figure 2.5). In principle, this summation of valid plane waves is infinite. In practice, however, (with the removal of high energy interaction through the use of a pseudopotential), plane waves with large kinetic energies contribute less to the overall wavefunction and can be truncated through the use of a 'kinetic energy

cutoff'.

$$\psi_{i,k}(r) = \frac{1}{\Omega} \sum_{G} C_{ik,G} e^{i(k+G)\cdot r} \approx \frac{1}{\Omega} \sum_{G}^{G_{max}} C_{ik,G} e^{i(k+G)\cdot r}$$
(2.51)

Where this cutoff G_{max} is related to the kinetic energy of the plane wave as:

$$E_{cut} = \frac{1}{2}G_{max}^2 (2.52)$$

As a result, DFT calculations on periodic systems can be performed with a discrete number of plane waves, in which the accuracy and cost of the calculation is a function of this number of plane waves.

2.5 Nudged elastic band theory

The task of determining the transition state energy for a chemical reaction or a solid-state deformation process has been discussed in detail with numerous methodologies found throughout literature. 144–147 Most of the schemes can be loosely described as 'restricted relaxation methods', in which the transition state (or the whole minimum energy pathway) is 'guessed' (either through chemical intuition or gradient ascent) and is geometry optimized such as to find the local saddle point while inhibiting relaxation onto either stable state (I or F) (see Figure 2.6). Much of the intricacies between these methods focus on the nature of this 'restriction', with varying trade-offs between cost, stability accuracy and human intervention.

One simple method is that of the nudged elastic band method (NEB). ^{146,148–151} This method attempts to find the minimum energy pathway for a chemical process by linking a series of "images" between initial (I) and final (F) states with a spring-force between them. By minimising these images w.r.t both the spring force and the forces acting perpendicular to the band. This results in only requiring evaluation of the interaction energy between images and the first derivative of the energy with respect to coordinates. Additionally, since images are connected sequentially, the resulting traced pathway is continuous (see Figure 2.7).

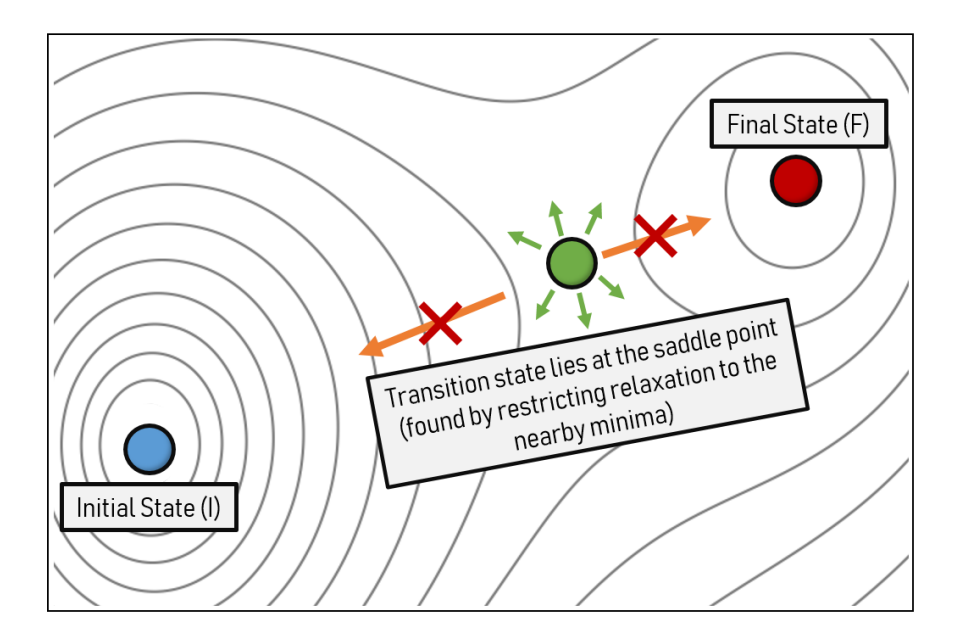


FIGURE 2.6: Contour plot showing a potential energy diagram of an ionic migration between two states. Transition state theory assumes that the transition state (green) lies on the saddle point across the minimum energy pathway, with "stable intermediates" lying a local minima (blue/red).

This band is denoted as a series of N+1 images $[R_0, R_1, R_2, ..., R_N]$ where the endpoints R_0 and R_N are fixed and the initial and final state of a transition. The tangent at image i can be constructed from adjacent images R_{i+1} and R_{i-1} :

$$\tau_{i} = \frac{R_{i} - R_{i-1}}{|R_{i} - R_{i-1}|} + \frac{R_{i+1} - R_{i}}{|R_{i+1} - R_{i}|}$$
(2.53)

By normalizing this tangent $\hat{\tau} = \tau / |\tau|$, the spring constant remains the same throughout all images across the NEB. The total force acting on a given image is the fictitious spring force along the tangent and the true force acting perpendicular to this tangent:

$$F_i = -\nabla V(R_i)|_{\perp} + F_i^s \cdot \hat{\boldsymbol{\tau}}_{\parallel} \hat{\boldsymbol{\tau}}_{\parallel}$$
 (2.54)

Where this spring force is given by:

$$F_i^s|_{\parallel} = k(R_{i+1} - R_i) - k(R_i - R_{i-1})$$
(2.55)

When the tangential force acting on a given image $\nabla V(R_i)|_{\perp}$ reaches 0, it lies upon the MEP and the spring force acts between images to restrict relaxation onto the local minima. Iterative updating of the images across the elastic band (in a similar fashion

to geometry optimization) yields a distinct continuous set of images that lie across the MEP.

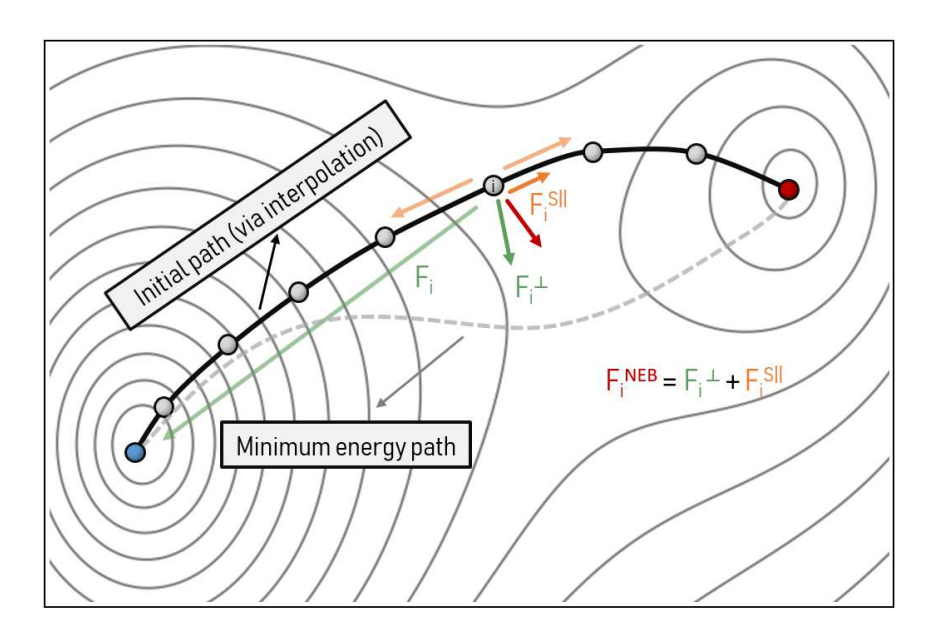


FIGURE 2.7: The nudged elastic band method implements spring forces between images. These two co-operative forces to drive 'images' toward the MEP. The tangential spring force acts between images and restricts free relaxation while the perpendicular force is calculated after electronic optimization convergence procedure and drives the 'images' lower in energy.

At first implementation, the method saw some issues. 148 The lack of a penalty for when the parallel force is orders of magnitude larger than the perpendicular force, often resulted in kinks to form across the band. With continued iteration, these kinks would cause poor convergence as the kinks in the band would straighten and re-kink in a cyclic equilibrium. This however can be mitigated by redefining the tangent τ such to be dependent on the energies of its images (see Equation 2.56).

$$\tau_{i} = \begin{cases} \tau^{+} & \text{if } V_{i+1} > V_{i} > V_{i-1} \\ \tau^{-} & \text{if } V_{i+1} < V_{i} < V_{i-1} \end{cases}$$
(2.56)

where:

$$\boldsymbol{\tau}_{i}^{+} = \mathbf{R}_{i+1} - \mathbf{R}_{i} \quad \text{and} \quad \boldsymbol{\tau}_{i}^{-} = \mathbf{R}_{i} - \mathbf{R}_{i-1}$$
 (2.57)

Additionally convergence is slow near the transition state. Improvements on this end were achieved by Henkelman et al, ¹⁴⁸ by adding a central 'climbing' image, the

transition state is found with fewer iterative steps. ^{148,149} This climbing image is managed by inverting the direction of the tangential force on the central image.

Chapter 3

Crystal Structures of relevant metal oxides

While XRD and other crystallographic methods have determined the crystal structures of a plethora of Li_xMO_2 materials, it's noted that both the oxygen stacking and space-group of layered metal oxides is dynamic, synthesis dependent and sensitive to environment. $^{152-154}$ With numerous similar materials being noted in the literature, a naming convention has been developed 155 to ease the comparison between similar materials with formula unit A_xMO_2 . This class of materials is typically characterised by edge shared octahedra to form $(MO_2)_n$ sheets, in which an Alkali metal or Vacancy (A, V respectively) lies between these sheets. Due to symmetry constrains, the layers of the oxygen sub-lattice can adopt one of three arrangements relative to the prior layer, labelled 'a', 'b' or 'c'. The choice of stacking that sequential oxygens layers occupy effectively determines the coordination of the inter-layered alkali ion, (where it typically lies in an octahedral (O), tetrahedral (T) or prismatic (P) site) and the repeat unit of the crystal. For example, the structure discovered by Goodenough (see Figure 3.1) is O3-type, the Li lies in the O_h sites with the Co-O sheets having a repeat unit of three (in an ABCA/abcabca pattern).

Due to the relative similarities of these structures and no clear indication into best practices in modelling these materials, ^{2,134,157–159} this chapter serves to benchmark

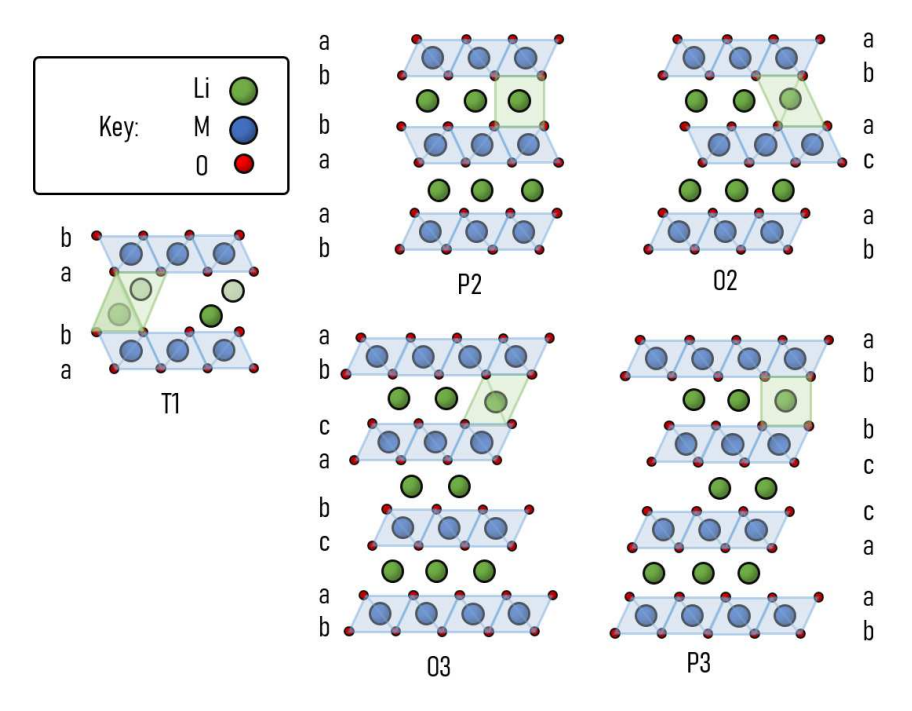


FIGURE 3.1: Layered metal systems with formula AMO₂. These systems are closely related via glide planes of the metal oxide layers and as a result many crystals may undergo phase transformation. ¹⁵⁶ Adapted from Delmas et al. ¹⁵⁵

multiple modelling parameters and identify the relative thermodynamic trends of this class of materials determining valid model systems for metal migration investigations.

3.1 Typical oxides in nature

Its a rarity to find pure metals as a native mineral, largely due to the abundance of Oxygen in the atmosphere in conjunction with its reactivity to much of the d-block metals. Other than notable exceptions of Cu, Ag and Au, the majority of all mined minerals are classified as oxides, sulphides or hydrates. 160,161 Despite this, layered oxides (formula unit MO_2) are uncommon minerals and are typically the result of synthetic methods. This is largely due to their low density and poor Metal-Oxygen connectivity (with a large vacuum spacing between MO_2 sheets). As such their lifespans are thermodynamically short on a geological scale 162,163 often with degradation routes consisting of metal migration into the vacuum spacing. Instead binary metal oxides (MO_x) are typical found in higher densities where crystallographic unit cells feature a high density of polyhedra that are corner, edge, or

face shared (see Figure 3.2), with some minerals featuring numerous types of connectivity. ^{164,165}

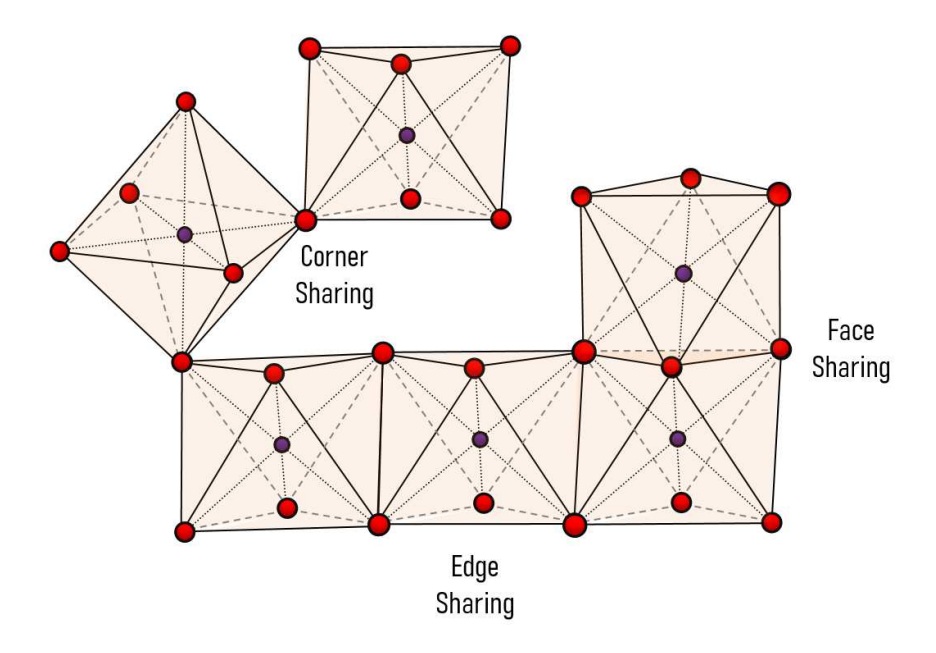


FIGURE 3.2: Connectivity of metal oxide polyhedra within ordered crystals. Polyhedra are often, corner, face or edge shared. *Adapted from Rao et al.* ¹⁶⁴

Many of these binary systems can be derived from one-another or directly from an optimal body-centered or face-centered cubic packing. Defining a starting lattice directly from a high packing density of 'hard spherical' oxygen with the inter-anion spacing or 'holes' occupied by a cation yields the halite (rock-salt) structure. Further site or plane specific substitutions or defects further lower the symmetry/connectivity. An example can be found in Figure 3.3. While thorough analysis of the metal oxide minerals is outside of the scope of this body of work, there lies a large amount of readily available crystal structures (both experimentally and modelling data) for the simple metal oxides which serves as a dataset to validate methods and benchmark key parameters to.

3.1.1 Generation of benchmark systems

While not a layered material, the ubiquitous research on the halite structure (both experimental and modelling) serves as a crystal system to converge the key parameters discussed in Section 2.4. A similar methodology (albeit with a larger

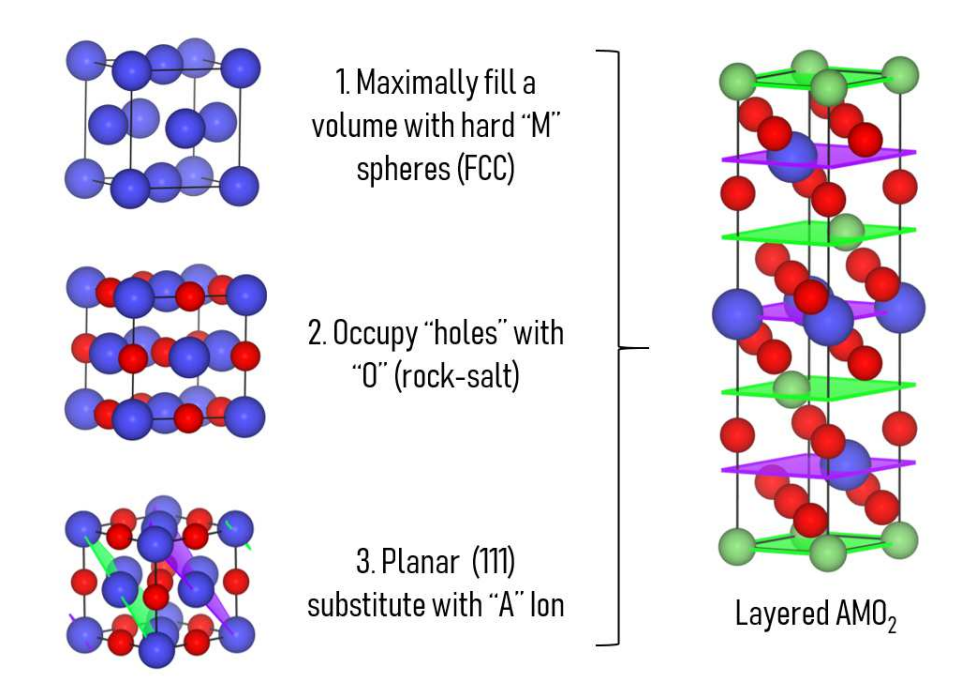


FIGURE 3.3: The layered Goodenough structure can be derived from a series of transformations from a "optimally packed" FCC structure.

sample of structures) has been employed by The MaterialsProject and is actively used as a framework for autonomous materials discovery. ¹³⁵ Using ICSD (Inorganic Crystal Structure Database), ¹⁶⁶ the conventional standard cell for a metal oxide adopting the halite structure was generated.

To calculate the convergence criteria of the 3d metals, density functional calculations were performed using the Vienna Ab Initio Simulation Package (VASP). The spin-polarized generalized gradient approximation Perdew, Burke and Ernzerhof with Hubbard U corrections (PBE+U) applied to metal sites (using U values found in Table 2.1). Effective Magnetic moments were initialised to 3 μ_B . Full ionic and lattice relaxation was utilised such to find the optimised geometry (convergence criteria: forces $\leq 0.01 \text{ eV/Å}$ on all ions). Both the plane wave kinetic energy cut-off and k-grid density was increased to determine sufficient values in which calculations are accurate via Equation 3.1. The generation of k-grids was handled using the Monkhorst-Pack algorithm ¹³⁹ as implemented in VASP.

$$|X_n - X_{n+1}| \le 0.010 \,\text{eV/atom}$$
 (3.1)

As K-points are discrete and their domain is bound within reciprocal space, the number of k-points required to accurately model a system is dependent on the crystal lattice. For instance, a lone k-point would produce an accurate result in a sufficiently large cell as this would correspond to a high k-grid density in k-space. Instead, common practice is to normalise the k-grid to the lattice dimensions of which it is bound via the metric termed "K-SPACING", which is the maximum allowed distance between two neighbouring k-points in k-space, which while is being a discrete variable is lattice independent. (See Equation 3.2).

$$N_i = \max(1, \text{ceiling}(|\mathbf{b}_i| \cdot 2\pi/\text{KSPACING})) \tag{3.2}$$

Where N_i is the number of k-points across lattice vector i and b_i is the vector length/

3.1.2 Convergence and structure of benchmark systems

For all third row transition metals, convergence of the total energy ≤ 0.010 meV/atom was achieved at a plane wave kinetic energy cutoff of 500 eV and a tighter bound of convergence (0.002 meV/atom) was found at 575 eV (see Figure 3.4), therefore a plane wave cutoff of 500 eV should be sufficient for all reasonable metal oxide systems. For these halite systems, it's found that utilising just the Gamma-point for small cells (*i.e* K-SPACING $> 1~\rm{\AA}^{-1}$) is insufficient at calculating the total energy of these systems and as such tighter K-SPACING is required. K-grid convergence was found for all metals with using a $7\times7\times7$ k-grid which corresponds to a K-SPACING value larger than of 0.40 $\rm{\AA}^{-1}$ and as such K-SPACING values of 0.4 will suffice (Figure 3.5). While the electronics (and thus required k-grids) will vary between halite and layered materials, a K-SPACING of 0.4 has been shown to be effective for layered structures aswell. 3,7

Using this convergence criteria (plane wave cutoff: 550 eV, K-SPACING: 0.4), the calculated lattice parameters of MO_2 halite structures can be found in Table 3.1. These are similar to experimentally observed lattice dimensions ($\pm 2\%$) and as such indicate the functional and convergence parameters are sufficient for these metal oxides.

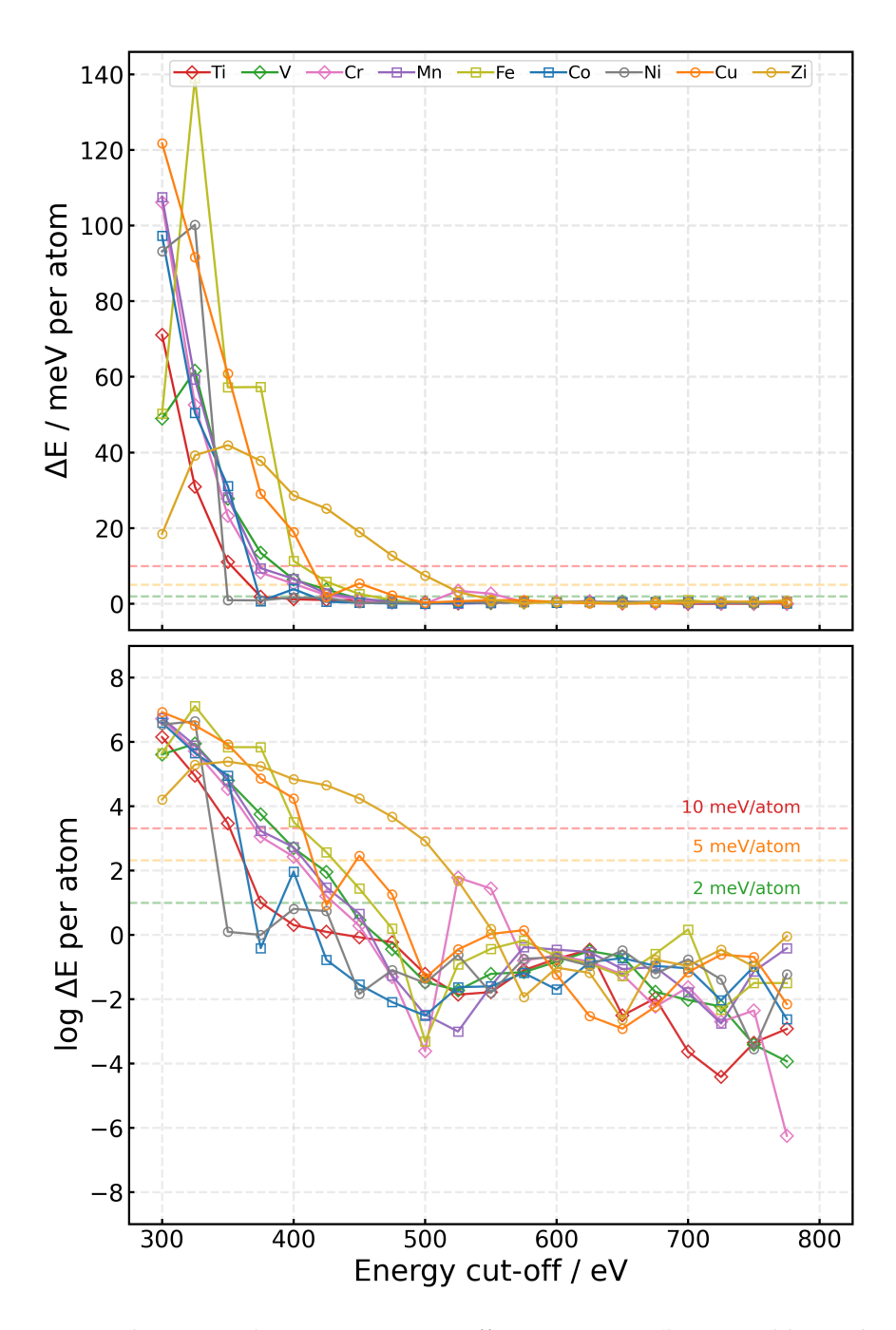


FIGURE 3.4: Plane wave kinetic energy cut-off convergences (linear and logarithmic) for 3d transition metals. Convergence is reached for all metals when cut-off > 500 eV.

3.2 Formation energy of transition metal oxides

With reasonable convergence parameters known, calculations of the Lithium-Metal-Oxygen ($\text{Li}_x\text{M}_y\text{O}_z$) series can be performed to determine stable oxides. Prior work has demonstrated that stable structures within the metal-oxygen series is typically composed of just a few different crystal systems (rutile, halite, spinel etc.),

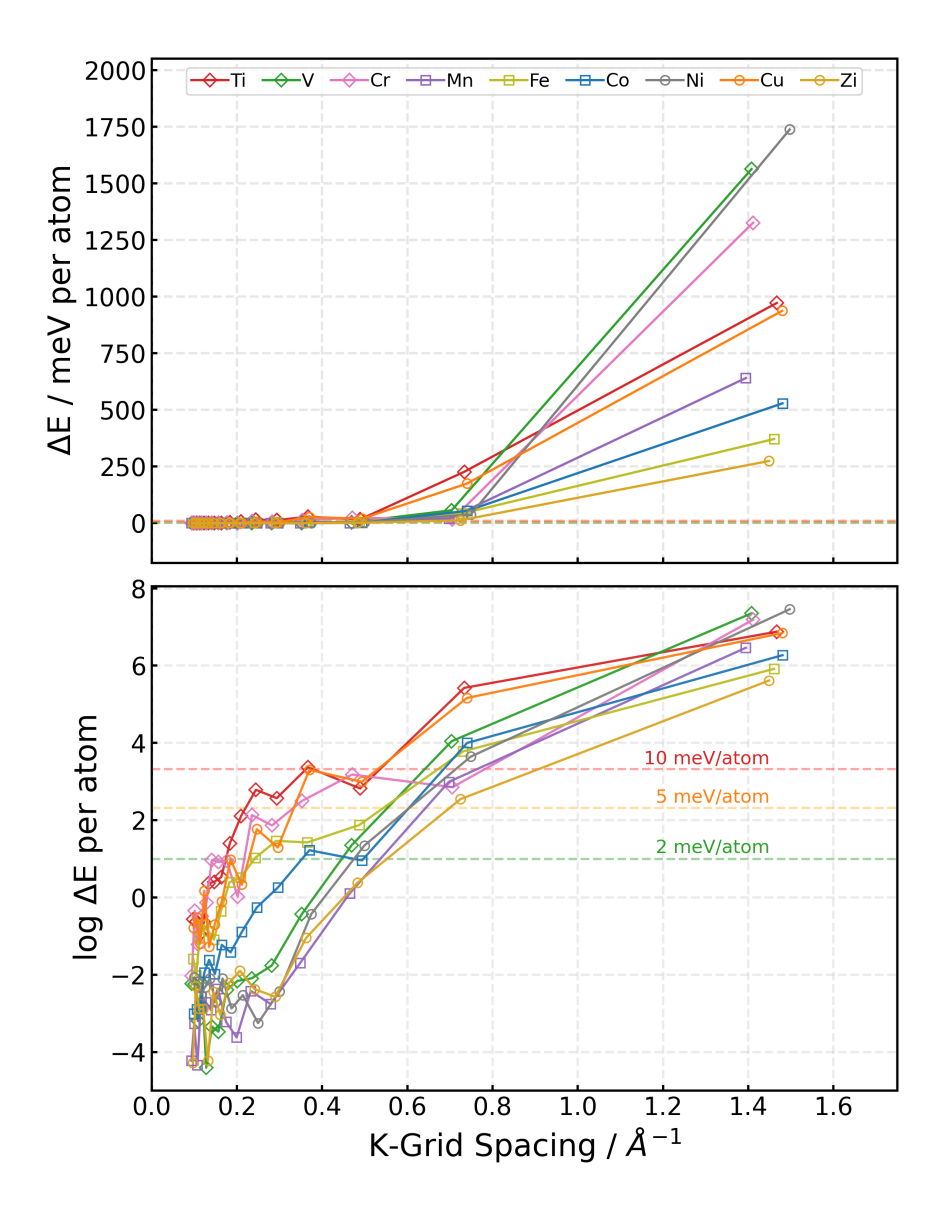


FIGURE 3.5: K-Grid spacing convergence (linear and logarithmic) for 3d transition metal. Convergence is reached for all metals when K-Spacing $< 0.4 \, \text{Å}^{-1}$.

	TiO	VO	CrO	MnO	FeO	CoO	NiO	CuO
A (calc.) / A	4.202	4.459	4.450	4.506	4.301	4.244	4.196	4.246
A (ref.) / A	4.181	4.393	n/a*	4.435	4.31	4.260	4.195	4.245
ref.	b	c	c	a	С	a	a	d

Table 3.1: Calculated and reference lattice parameters of halite Metal Oxides. ref a-e: $^{167-170}$ *The Chromium oxide is not synthesised under normal conditions.

few of which are layered. ^{160,162,163} It's known that the layered structures of binary metal oxides are subject to degradation toward spinel and rock-salt via a simple metal migration and oxygen loss. ⁴ Determining the formation energies of the layered structures with respect to these more ubiquitous oxides will allow inference of the

long-term stability and likelihood of specific crystal structures along the degradation pathway.

It can be shown that for an isobaric, isothermal closed system, the Gibbs free energy of said system is the correct thermodynamic potential for the formation energy (See Equations 3.3 - 3.6). Construction of a convex hull from the formation energies of investigated structures yields the set of structures that are thermodynamically stable.

$$\Delta G = \Delta H - T \Delta S \tag{3.3}$$

The Gibb's free energy is given by:

$$G(T, P, N_A, N_B, N_C) = H(T, P, N_A, N_B, N_C) - TS(T, P, N_A, N_B, N_C)$$
(3.4)

Expressed as a Legendre transform of the enthalpy H, and internal energy E is as follows:

$$G(T, P, N_{A}, N_{B}, N_{C}) = E(T, P, N_{A}, N_{B}, N_{C}) + PV(T, P, N_{A}, N_{B}, N_{C}) - TS(T, P, N_{A}, N_{B}, N_{C})$$
(3.5)

With the assumption that $P\Delta V$ is small, T=0K and normalising with respect to the stoichiometry of a given system this equation simplifies to:

$$G(0, P, \chi_{A}, \chi_{B}, \chi_{C}) = E(0, P, \chi_{A}, \chi_{B}, \chi_{C})$$
 (3.6)

where T is the temperature of the system, S is the entropy of the system, P is the pressure of the system, V is the volume of the system, N_i is the number of atoms of species i in the system and $\chi_i = N_i/(N_A + N_B + N_C)$

3.2.1 Elemental crystal structures

In determining formation energies of a material it's necessary to determine the energy of edge members the series ${\rm Li_xM_yO_z}$ and as such total energy calculations have to be performed on the pure elemental crystals. It should be noted that the prior used PBE +

	Ti	V	Cr	Mn	Fe	Co	Ni	Cu
Structure	hcp	bcc	bcc	bcc*	hcp	fcc	fcc	fcc

TABLE 3.2: The calculated crystal structures of the 3d transition metals. *Mn forms a low symmetry (A12, space-group: I43m) cubic structure consisting of 58 atoms/unit cell of interlinking Fraif polyhedra. 178

U methodology is inapplicable for pure metal systems and as such should not be directly compared to PBE + U calculations. There are numerous discussions in the literature regarding mixing of DFT and DFT + U results ^{66,69,134}. The scheme devised by Jain et al applies a U-value bias to calculations and has been shown to be adequate at producing correct phase diagrams. ^{68,78}

Across the d-block all metals exist as ordered crystals upon solidification. 171 Abiding to the Kepler conjecture of hard-sphere packing 172,173 most metals occupy high density lattices, typically, face-centered cubic (fcc), hexagonal-close packed (hcp) or body centered cubic (bcc) (see Figure 3.6). The reasoning's for specific ground-state stable crystal structure is complex and generally understood as a balance between Madelung interactions (which favour high symmetry and densities) and Peierls distortion (which breaks symmetry). 171,174 Using the ICSD, crystal structures for the 3d transition metals were found, while numerous allotropes are known for the transition metals (in particular, Fe and Mn) 175,176 those found to be meta-stable were removed. 174,177 A summary of the stable crystal structures for pure metals can be found in Table 3.2. All metals were found to occupy one of the three prior mentioned crystal structures with the exception of Mn, which adopts a complex 58 atom/cell crystal within the $\overline{143}$ m space-group. Commonly referred to as α -Mn.

3.2.2 Convex hull and formation energies at the end member ${\rm Li_0M_xOy}$ domain

At the state of complete delithiation, the Goodenough structure is a binary oxide with formula unit Li_0MO_2 . The structure is comprised of MO_2 sheets that are seperated by a Vacancy layer (in which none of the sites are filled), with the spacing of sheets being dependent of van der Waals interactions between sheets ^{179,180} (See 3.7a). Typically for the 3d transition metals, this structure is meta-stable, with the higher density oxides

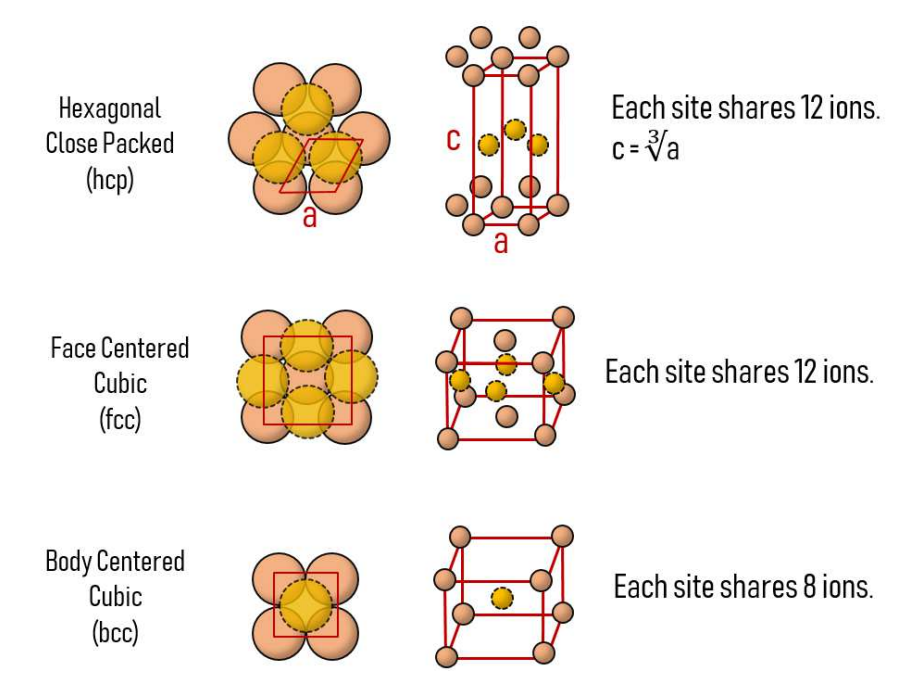


FIGURE 3.6: High density packing of hard-spheres into a crystal structure. Most elemental metal crystal belong to one of these three lattices.

(Rutile, Spinel, Wurtzite etc.) being thermodynamically favoured crystal morphologies. In reality, complete delithiation of cathode materials is both avoided and exceedingly difficult during normal battery operation (with most batteries operating at > 25% state of charge). The publication by Reed and Ceder, ² discuss this end-member structure (and higher lithium concentration structures) in the context of meta-stability and transformation pathways. Within their publication its noted that the both this structure and the 'Zero Li Spinel-like Structure' (ZLS) (See 3.7b) are unstable and have similar formation energies. Typically metal migration is only feasible when the end tetrahedral site is not neighboured by a cation and thus is often prefaced by Lithium migration. However, with zero lithium within the structures, no Lithium migration is necessary; instead, the two structures are related simply via a migration of 1/4 of the Metal ions into the "Vacancy layer in a checkerboard pattern". This is typically accustomed by relaxation the vacancy layer such that each octahedra are equivalent.

Investigating the formation energy and stability of a specific structure across the metal oxide series is not a trivial task, with over sixty known crystal structures that are binary oxides across a wide range of complexity and connectivities. Systematic

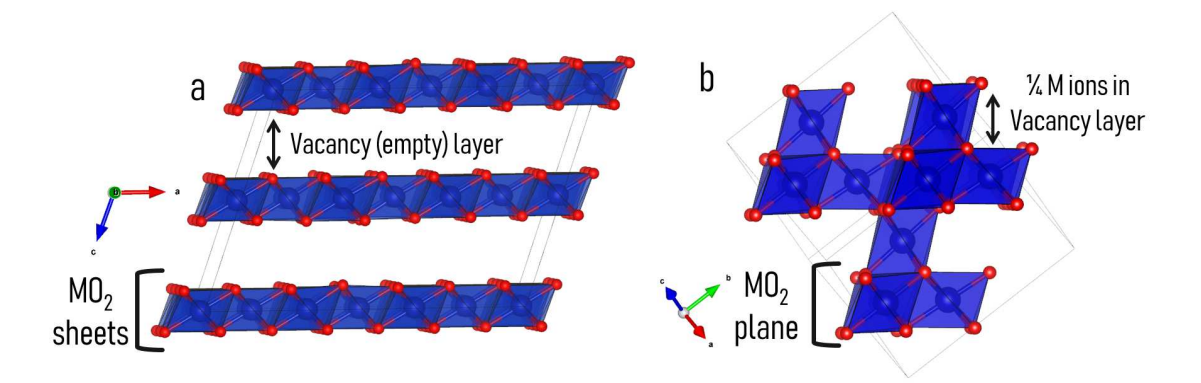


FIGURE 3.7: Two key structures when discussing battery cathodes. The layered MO_2 and the Zero Li spinel-like structure. a) The delithiated layered structure is planar MO_2 sheets separated by a vacuum spacing. b) The Zero Li Spinel-like structure is related by a $\frac{1}{4}$ Metal migration into the Lithium layer.⁴

generation of all possible metal oxide orderings would yield an insurmountable number of potential structures, most of which have little to no chemical basis. Instead determination of the relative stability of the delithiated Goodenough structure in respect to other binary oxides was handled via existing databases of known metal oxide crystals. Both the ICSD and MaterialsProject was utilised to generate all observed binary oxides across the 3d transition metals. A symmetry search was performed (via PyMatGen) to identify if all sites within a given structure A map uniquely to sites in another structure B. Equivalent structures were removed from dataset as to reduce computational cost. The collective data-set (70 unique structures with formula M_xO_v) alongside both Structures in Figure 3.7 were geometry relaxed using the convergence criteria discussed prior for all 3d transition metals (Ti - Cu). Metal sites were initialised at their high spin configuration but this magnetization is allowed to relax into alternate states. This data-set consists of both exotic and well-investigated oxides such as Binary spinel, halite and Rutile and as such many of the resulting structures have small or positive formation energies. The formation energies for each structure was calculated as per Equations 3.3 - 3.6. The resulting convex hull as a function of oxygen content for 3d transition metals can be found in Figures 3.8 and 3.9. Structures with large positive formation energies were removed from the resulting plots.

The phase diagrams for key battery oxides (see Figure 3.8) are largely in agreement with those calculated by the MaterialsProject. The MaterialsProject utilise both DFT+U

and restored regularized strongly constrained and appropriately normed (r2SCAN) calculations. Similarly to Ceder and Reed both the Zero-Li layered Structure and the Zero-Li Spinel structure have large negative formation energies yet are meta-stable. The Mn-O convex-hull indicates stable structures at a plethora of compositions (MnO, Mn₂O₃, Mn₃O₄ and MnO₂) all of which are observed experimentally. ^{181–183} Both the Zero-Li Spinel structure and the Zero-Li Goodenough Structure, lie above the hull (+42 and +17 meV/atom respectively) with the Rutile structure calculated as stable. Reed and Ceder calculated that the Zero-Li Spinel structure lies < 50 meV higher than the layered structure. The Co-O convex-hull paints a similar picture to the Mn, with stable compositions found: CoO, CoO₂ and Co₂O₃. The Zero-Li Spinel and Goodenough Structures lie above the hull (+60 and +8 meV respectively), with the Rutile structure being found as stable. However, the Ni-O convex-hull varies somewhat with only Halite NiO, Metal-rich Spinel Ni₃O₄ and an exotic NiO₂ structure being stable compositions with the Rutile structure being meta-stable. The Zero-Li Spinel and Goodenough Structures lie similarly far above the convex hull at +160 and +143 meV respectively.

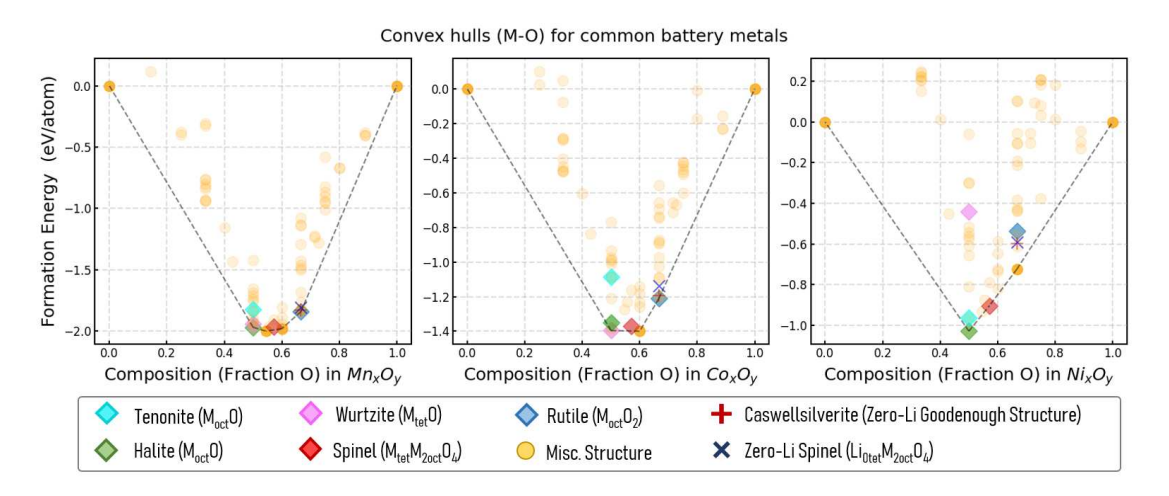


FIGURE 3.8: Convex hulls for Mn_xO_y , Co_xO_y and Ni_xO_y . Structures lying on the hull (dashed grey line) are stable.

Ceder and Reed discuss the relative energetics of metal O_h vs T_d occupation of the Vacancy/Li layer in half-lithiated layered structures. There it's concluded that thermodynamic stability is achieved upon Vacancy/Metal exchange, with 1/4 migration resulting in spinel formation. Interestingly, here a similar structure is found to be low energy. A "Metal-rich" analogous Spinel structure (Mn_{tet}Mn_{2oct}O₄) shows

small thermodynamic penalties for occupation of tetrahedral sites lying near the convex hull with formation energies of -1.96, -1.37 and -0.92 meV for Mn, Co and Ni respectively. This "Metal-rich" Spinel structure is features metal occupying the 16d O_h sites aswell as the 8a T_d sites that are typically reserved for Li in LiM_2O_4 resulting in the M_3O_4 composition. This structure has been discussed in detail as a midpoint of a complex degradation process of the Goodenough structure to rock-salt, involving numerous metal migrations (both $O_h \rightarrow O_h$ and $O_h \rightarrow T_d$), oxygen loss and significant lattice restructuring. Formation of this material during normal battery operation is undesired 184–186 resulting in decreased Li diffusion. The convex hulls for the other 3d transition metals can be found in Figure 3.9 and show that the layered structure is typically meta-stable to metal migration toward the Zero-Li Spinel structure.

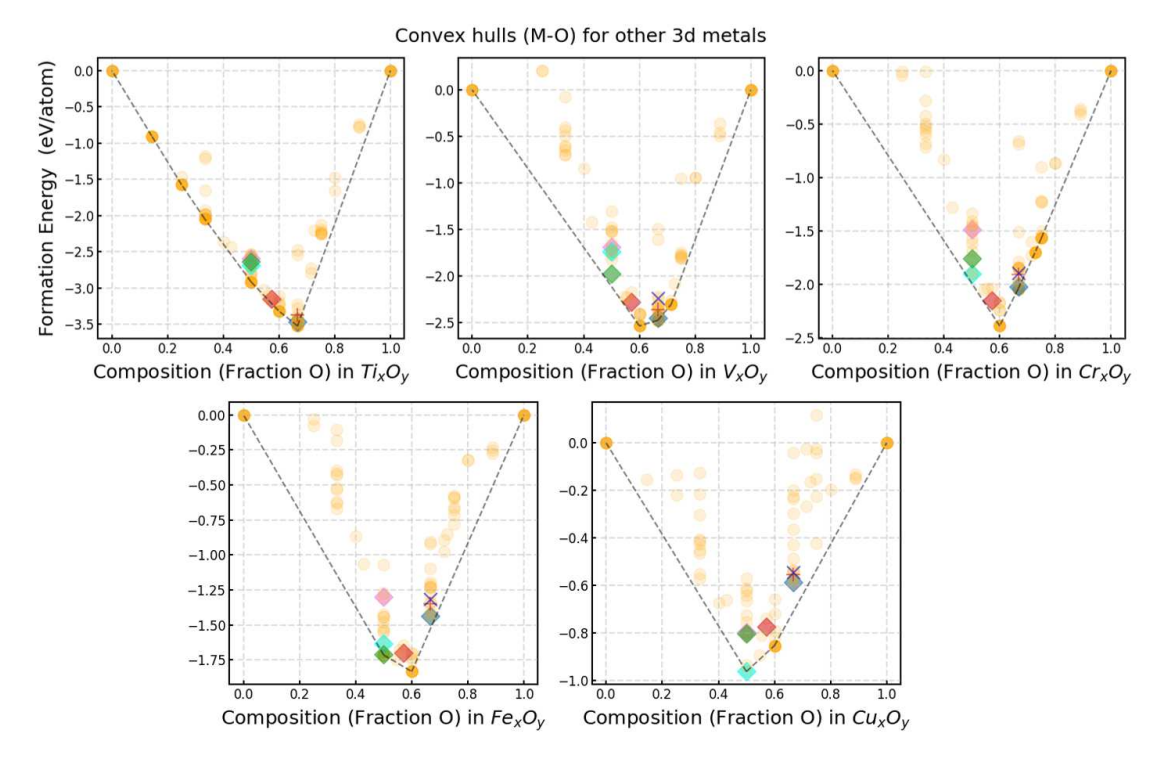


FIGURE 3.9: Convex hulls for other 3d metals. Structures lying on the hull (dashed grey line) are stable.

While important, normal battery operation typically avoids complete delithiation of the cathode, with operating ranges between 15-85% lithiation. As such much of the batteries life-span is at half occupation of the cathode thus degradation routes around near half lithiation are crucial in predicting battery life-cycles. ^{2,4,31}

3.3 Stability and Structure of Lithium metal oxides

With much discussion in the literature regarding lithium metal oxide stability, in particular a tendency for metal ions to migrate into the lithium toward the Spinel structure ($Li_{1/2}MO_2$) at and around half lithiation, investigation of the thermodynamics of layered Li_xMO_2 yields insight into stable phases during cycling. This, however poses a difficult question of the structure of partially lithiated battery cathodes. There in principle lies an infinite number of superstructures for a disordered Li^+/V_{Li} composition. Typically, methods to perform calculations on such disordered structures are inherently a statistical approach, often through the use of a mean-field approximation (such as Virtual Crystal Approximation). This however, fails to yield specific low energy structures thus are difficult to incorporate into migration pathway studies. This issue, in conjunction with the variety of known layered $LiMO_2$ systems (P2, O2, O3 etc.) requires careful consideration into determining reasonable models for specific lithium concentrations.

Some work has investigated the relative stability of different layered metal oxides, ^{154,158,187–189} other work has investigated stable structures under delithiation ^{1,190,191}. There is considerable disagreement between publications regarding both lattice parameters of these structures aswell as the energetics between O2, O3 and P2 structures. Transition state energies of defects depend heavily on c-axis parameter ³⁷ and thus correctly calculating the lattice parameter is of high importance. Interestingly, it is noted that these differences are likely due to the disparity within the literature regarding functional choice, in particular whether to utilise the Hubbard U model and/or dispersion corrections. Due to the large vacuum spacing of subsequent MO₂ sheets, it's fundamental to understand the extent that dispersion interactions play, particularly at zero-lithiation. Prior work has demonstrated that poor or no dispersion corrections can grossly miscalculate lattice dimensions ¹⁵⁸. By default these interactions are disabled within *VASP* and numerous varying implementations exist.

Fundamentally, Fritz London¹⁹² used quantum mechanical theory to demonstrate the dispersion interaction between two atoms is:

$$E_{AB}^{disp} \approx -\frac{3}{2} \frac{I_A I_B}{I_A + I_B} \frac{a_A' a_B'}{R^6}$$
 (3.7)

Where I is the first ionisation energy, a' is the polarisability and R is the distance between the two atoms.

Within VASP the DFT-D2 implementation by Grimme ¹⁹³ is such that long range interactions are weak (6th power dependence) yet at near-bonding ranges are zero. This is achieved via a set of pre-calculated and chemically independent dispersion coefficients C_{6ij} and a dampening function $f_{d,6}$. This modifies the Hamiltonian as such:

$$E_{\rm DFT-D2} = E_{\rm DFT} + E_{\rm disp}^{\rm D2} \tag{3.8}$$

Where:

$$E_{\text{disp}}^{D2} = -\frac{1}{2} \sum_{i}^{N} \sum_{j \neq i}^{N} \frac{C_{6ij}}{r_{ij}^{6}} f_{\text{damp}}^{D2}(r_{ij})$$
(3.9)

Where: $C_{6ij} = \sqrt{C_{6ii}C_{6jj}}$ and $R_{0ij} = R_{0i} + R_{0j}$. The damping function $f_{d,6}$ is:

$$f_{\text{damp}}^{D2}(r_{ij}) = \frac{s_6}{1 + e^{-d((r_{ij}/s_R R_{eq}) - 1)}}$$
(3.10)

Alternatively there is the more "modern" DFT-D3 implementation which introduces local geometry of the ions i and j into the dispersion coefficient C_{6ij} and is often cited as an improvement ¹⁹⁴. The study by Aykol and Kim ¹⁵⁸ noted a stark variance in calculated lattice parameters under varied correction functionals including opt-B88 and D4 where it has been demonstrated that the lattice parameters of the Zero-Li Goodenough Structure discussed in Section 3.2.2 can vary by upwards of 50%.

3.3.1 Functional choice and its effect on calculating end-member of Lithium metal oxides

As introduced at the beginning of this Chapter (Chapter 3), layered lithium metal oxides can adopt various stacking sequences and alkali ion coordination ¹⁵⁵. Investigation of the literature identified three similar structures within the R3m space-group for LiCoO₂ that have been discussed in detail prior ^{187,188,195–198}. The O3-type (Goodenough) structure where stacking repeats every three MO2 sheets and oxygen layers are stacked in alternate sites (abcabca) with Li lying between MO₂ sheets in octahedral sites. The O2-type structure with a stacking sequence that repeats every two MO₂ sheets with oxygen layers stacked in a alternating pattern (abaca) and Li lying in octahedral sites. Finally, the P2-type structure with a stacking sequence that repeats every two MO₂ sheets with the oxygen layers stacked in a flipped pattern (abbaa) and Li lying in prismatic sites. These structures have been discussed in detail as viable routes for phase transformation, in particular for Sodium-Ion batteries where the Octahedral and Prismatic occupation of Na have been shown benefits of capacity and power-draw respectively ¹⁵⁴. The O2 and P2-type structures are related via a glide plane transformation of the oxygen sub-lattice (see Figure 3.10). Prior work has found that type-2 to type-3 transformation is not observed under normal cycling conditions. 197 Additionally the sodium equivalent O3-type system NaCoO₂ has been shown to convert to the P3-type structure has been shown to form from O3-type via a similar glide plane. However this material was shown to not be thermodynamically competitive for Li-ion.

At full lithiation with the metal sites being formally +3, both the crystal structures for the single metal Goodenough equivalent LiNiO₂ and LiMnO₂ materials should be Jahn Teller distorted. This would break the a/b symmetry of the hexagonal crystal with the resulting structures lying in a lower symmetry space-group (C2/m). While synthetic routes exist that seem to form non-distorted $R\overline{3}m$ LiMnO2 and LiNiO2, these seem to be short lived ¹⁹⁹. Typically the extent of distortion for the Nickel systems is small and it is often categorised as a O3-type $R\overline{3}m$ structure similar to Cobalt. Constrastingly, the distortion of high-spin Mn-O bond lengths can be upward of 10%

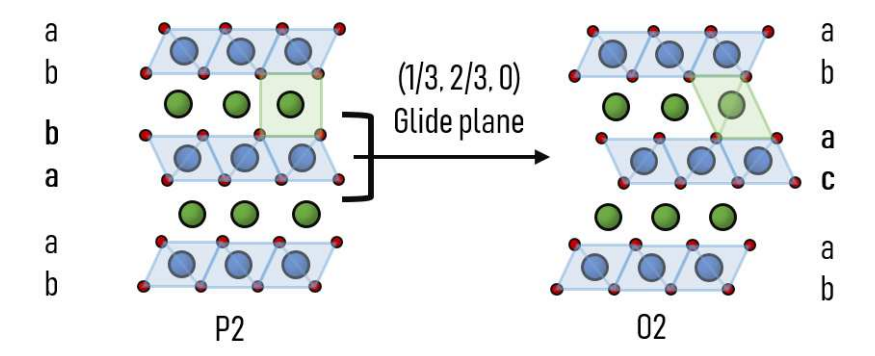


FIGURE 3.10: Transformation between Prismatic and Octahedral occupation of the vacuum layer in layered metal oxides. the P2-type structure converts to the O2-type structure via a glide plane transformation $(\frac{1}{3}, \frac{2}{3}, 0)$ of the oxygen sub-lattice.

and as such this material is commonly referred to as m-LiMnO₂ or O'3-type with the prime denoting the breaking of the a/b axial symmetry. (see Figure 3.11).

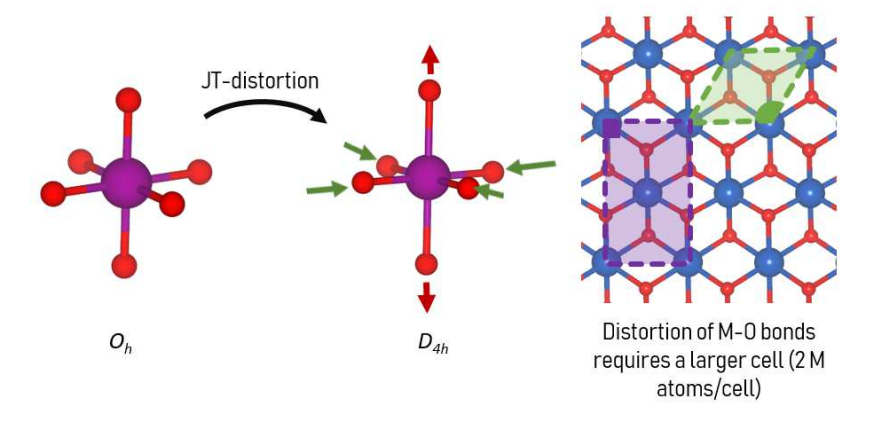


FIGURE 3.11: Jahn Teller distortion of Mn systems results in a D4h geometry MO6 polyhedra. This arises from the uneven occupation of the d orbitals for high spin Mn and results in a reduction of the symmetry of the parent lattice (O3-type to O'3-type.)

3.3.1.1 Calculated structures of Li₁MO₂

Experimental data often cites the Goodenough structure to have lattice parameters of a = b = 2.83 and $c = 14.11^{161}$. These lattice parameters were used to initialise crystal structures of the O3-type, O2-type and P2-type lattices for Co, Mn and Ni. The magnetic moments of the metal ions of each structure was initialised at $3\mu_B$ (with literature references citing ground state Co and Ni as typically low-spin and Mn as high-spin for these systems). For all 3 metals, full lattice relaxation was allowed in conjunction with a small distortion on both lattice and sites to capture Jahn Teller

effects when applicable. Geometry optimization was achieved for all model systems within VASP to a force tolerance of < 0.005 meV/Å on each atom. Additionally literature sources reference a peculiar structure formed at low temperature that has been demonstrated to be thermodynamically low lying ²⁰⁰. The structure lies within the Fd $\bar{3}$ m space-group with a M₂O₄ frame-work. Typically such framework is associated with spinel cathodes (LiM2O4) in which Li is tetrahedral and located in the 8a sites and the M ions are located in 16d sites. This structure has double the degree of lithiation however, Li occupying the 16c sites forming an interconnected double-spinel framework. This structure is similar to the Goodenough structure, however featuring a M-Li exchange of 1/4 of the ions (see Figure 3.12). Such structure has been a synthesis candidate for sometime, boasting the stability of the M₂O₄ framework with the same active ion count as the layered structures. With XRD data for Cobalt 200,201 and Manganese showing a cubic lattice (a=8.00 Å and 8.2 Å respectively) the structure has long been abandoned for its difficulty during cycling (with a tendency for Li to migration to 8a sites)²⁰². This structure was also geometry optimized using the same methods.

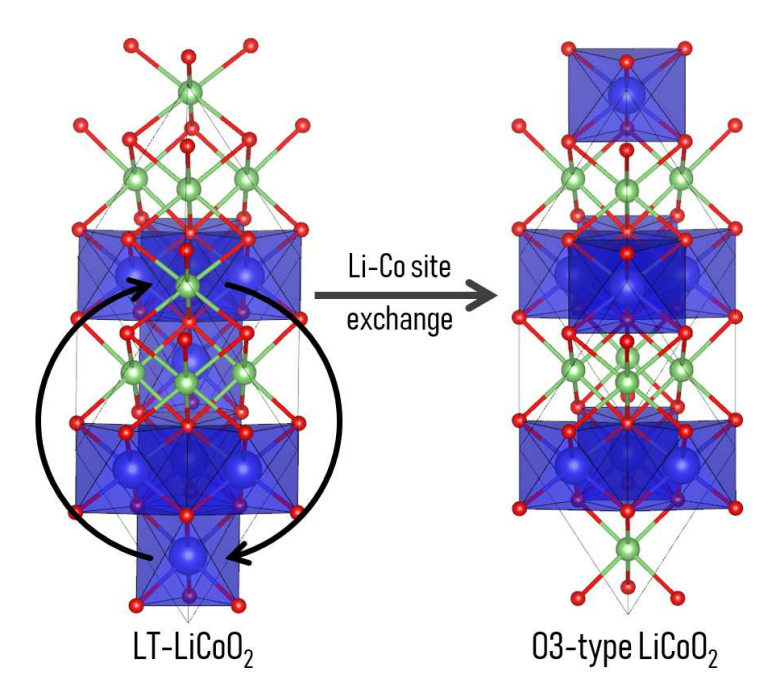


FIGURE 3.12: The LT-LiMO₂ structure 200 . This structure is related to the Goodenough structure via Li-M exchange forming the M_2O_4 framework and lithium occupying the octahedral sites. This structure is similar to normal LiM₂O₄ spinel, except Li occupies the O_h sites rather than T_d sites.

$$A_{O3-type} \approx (A_{O'3-type} + B_{O'3-type})/2$$
 (3.11)

$$C_{O3-type} \approx \frac{3}{2}C_{O2-type} = \frac{3}{2}C_{P2-type}$$
 (3.12)

Analysis of relaxed lattice parameters of the layered structures can be found in Figure 3.13, to ease comparison between these similar structures Jahn Teller distorted lattice parameters have been approximated to that of the equivalent O3-type structures (equation 3.11) and O2/P2-type structures are approximated to their O3-type equivalent (equation 3.12). While an abundance of experimentally measured lattice parameters for O3-type structures are found throughout the literature the P2-type and O2-type crystal have limited experimental data for Li-ion. Across all three metals, the c-axis lattice parameter was calculated to be between 13.5 - 14.6 Å for the O3-type system with their equivalent O2-type and P2-type structures being calculated to be comparatively larger. Generally, all functionals are aligned with experimental data (<5% error in c-axis). However it should be noted that the D2 dispersion correction consistently under-estimates c-axis lattice parameters indicating van der Waals interactions are over-estimated within this functional. Mn is found to have larger lattice constants (and similarly large polyhedra) due to Mn³⁺ being a high-spin ion. In contrast to the flexible c-axis, the a and b -axis is comparatively rigid across metals varying by 0.2 Å with all methods predicting a-axis lengths o between 2.8-3.0 for O3-type structure regardless of metal. Due to the Jahn-Teller effect, measured lattice lengths aligned parallel to the MO₂ sheets (a/b) were averaged such to be easily compared to the R3m Goodenough structure. While having better alignment with the literature, the PBE functional comparatively under-estimates the a-axis lengths for the Mn systems, analysis of magnetic moments of the relaxed structures indicates that the PBE functional predicts the layered LiMnO₂ to be low-spin ($2\mu_B$ rather than $4\mu_B$). While there has been some discussion around inhibiting high-spin Mn³⁺ to reduce the Jahn Teller effect and resulting structural instability through the use of various dopants, pure LiMnO₂ is typically understood to be high-spin ¹⁹⁹. Experimental data ²⁰³ for the O3-type Mn system show significant (10%) Li/Mn exchange indicating a tendency to form the LT – LiMO₂ seen in Figure 3.12 this would explain the reduced experimental a-axis lattice constant (compared to the modelling data here). A detailed analysis of the spin states for the O3-type systems can be found in Appendix A.

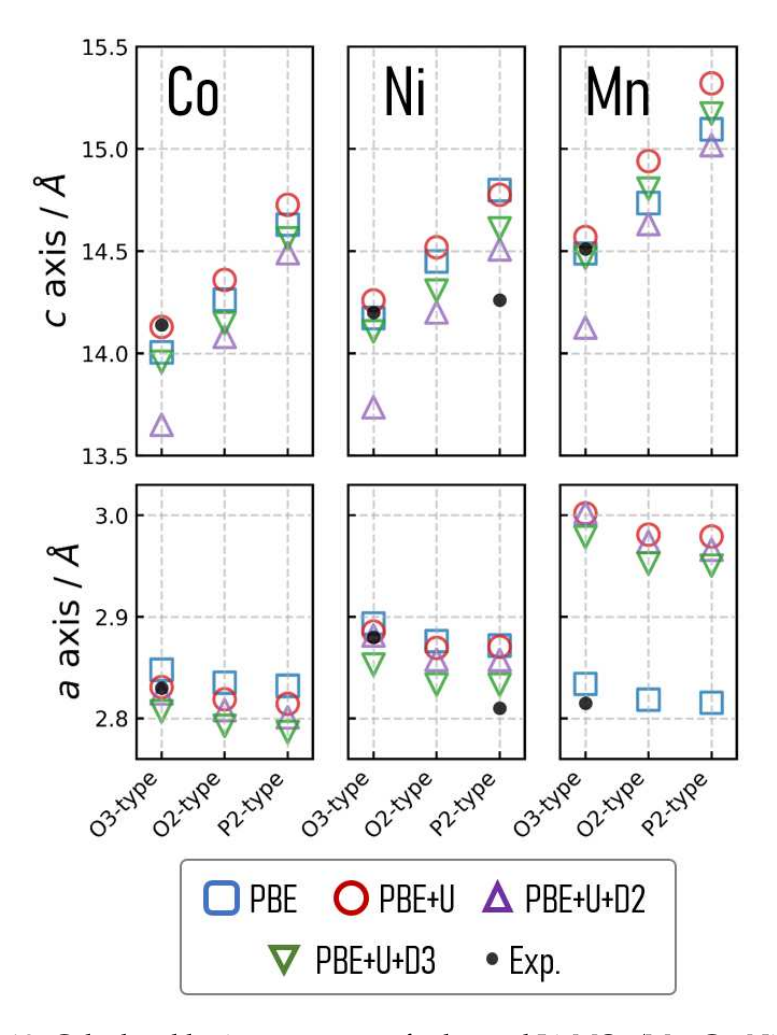


FIGURE 3.13: Calculated lattice parameters for layered Li_1MO_2 (M = Co, Ni and Mn). a axis is a

The Li layer spacing (see Figure 3.15) is defined as the planar distance between layers in the oxygen sub-lattice that span the Li layer. This parameter is a frequent talking point in literature having been shown to depend on the degree of lithiation and directly impact Li migration energy ¹⁵⁹. As such functional choice needs to accurate predict this parameter to avoid erroneous migration energies. Literature references cite this layer spacing as 2.58 for O3-type LiCoO₂ and state that an increase of this spacing by 5% results reducing the energy barrier for Lithium diffusion threefold. Both Li and M layer spacing values can be found in Figure 3.15 in which there is large agreement between functionals (with the notable exception of the D2 dispersion method). Layer spacing's are calculated to be between 2.45 and 2.6 for the O3-type

structures and largely align with experimental data with the exception of the O3-type Mn structure. This structure once again differs from the experimental data as it has a high proportion of Li/Mn exchange and as such is affected by the same artifact as discussed prior.

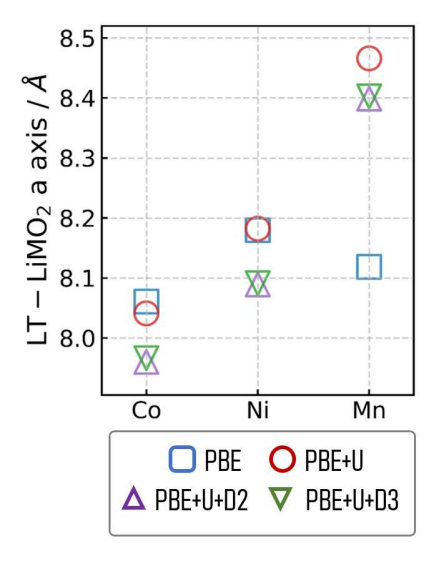


Figure 3.14: Calculated lattice parameter for $LT - LiMO_2$. PBE predicts the wrong spin-state for the Mn system.

In general these lattice parameters are largely aligned with the prior work by Aykol and Kim 158 and as such similar conclusions can be drawn. Largely that for both Nickel and Cobalt, the inclusion of a Hubbard U model and/or dispersion corrections yields marginal benefits over PBE. This is observed for the O3-type structure (which they investigated) aswell as the larger O2/P2-type systems. Interestingly, the O'3-type LiMnO2 structure is grossly miscalculated by PBE, predicting Mn³⁺ to be low-spin. While the c-axis parameter aligns with experimental, the O^{2-} ions lie closer to low-spin Mn³⁺. This reduces the stress induced via planar Li migration and would grossly miscalculate migration energies and thus battery performance/degradation. For the LT - LiMO2 structures PBE once again predicts the Mn system to be low-spin reducing the M-O bond length (2.1, 1.92 for PBE+U and PBE respectively) with a similar reduction in the lattice constant (see Figure 3.14). As such the data-point can be considered erroneous. The introduction of dispersion corrections has marginal effect on the observed lattice constant for all three metals resulting in a reduction of bond lengths of less than 1%.

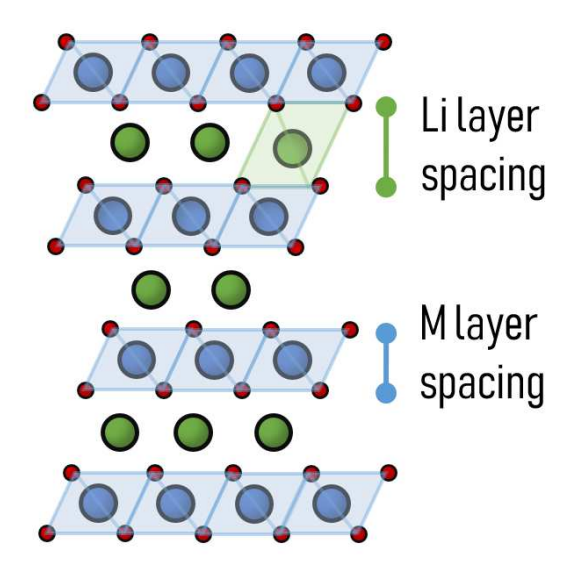


FIGURE 3.15: The Li layer spacing and M layer spacing is defined by the planar distance between subsequent layers in the oxygen sub-lattice (i.e. d-spacing in [0,0,1] plane).

The thermodynamic stability's of these structures can be found in Figure 3.16. For all metals the relative order of stability is O3, LT, O2 and finally P2. With all structures lying calculated to be within 100 meV/atom of each other. The site-exchanged structure (LT – LiMO₂) is thermodynamically competitive with the O3-type structure (> 10 meV except for the erroneous result) such trend is found in the literature 204 . Since the two structures are related via a 1/4 M-Li site exchange it's clear that there will always be synthetic challenges in producing unmixed layered cathodes (whether attempting to synthesise the spinel or layered framework structures). Fortunately, with the respective 16c/16d sites being filled at full lithiation, structures are unlikely to be in a dynamic equilibrium with one-another at rest. The alternate layered structures show a larger thermodynamic discrepancy, indicating synthetic challenges in manufacturing O2 or P2-type structures for Li-ion. With such structures being related via simple glide planes of the oxygen sub-lattice both the O2 and P2-type structures are likely to be sensitive to transformation onto the more-ubiquitous O3-type structure.

Overall, PBE alone is a poor predictor of the electronic structure and lattice parameters of lithiated metals oxides, this is particularly pronounced in Mn systems where ground state structures are wildly different from experimental. The band-gap derived

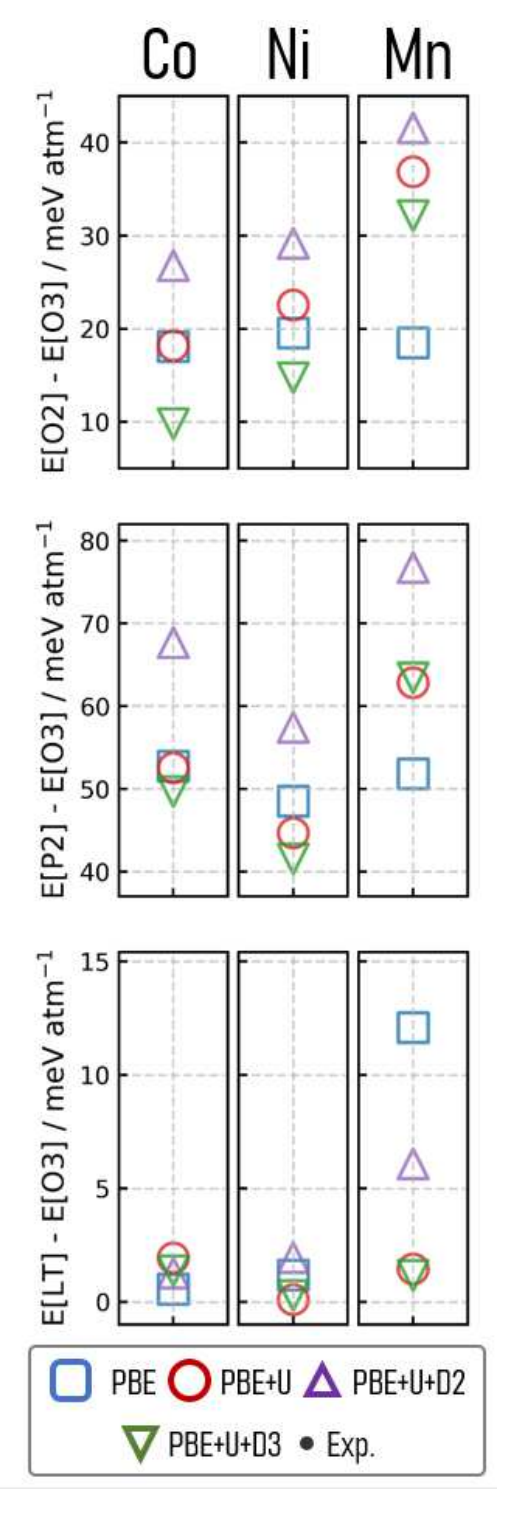


FIGURE 3.16: Calculated energies of the investigated structures using different functionals (normalised to the O3-type structure).

U values determined by Jain et al 9 nor the addition of dispersion correction don't massively impact the lattice parameters of these materials, this is likely due to the Li-O bonding being the dominating interaction between MO_2 sheets. The D2 dispersion correction 193 consistently overstates the extent of van der Waals interactions shrinking

lattice parameters accordingly.

3.3.1.2 Calculated structures of Li₀MO₂

In similar fashion to Section 3.3.1.1 four layered crystal structures (see Figure 3.17) were identified to be likely model candidates of the zero-lithiated end-member ${\rm Li_0MO_2}$. The O1-type O2, P2 and O3-type structures within $R\overline{3}m$ space-group (and their corresponding a/b symmetry broken equivalents for Jahn Teller active crystals). The O1 and O3-type structures are discussed in detail by Aykol et al ¹⁵⁸ and their relative energetics have been shown to be dependent on choice of U value. . Additionally the Zero-Li Spinel structure (ZLS) that was observed to be low-lying in Section 3.2 corresponds to the end-member structure of spinel-like cathodes (i.e ${\rm LT}-{\rm Li_xCoO_2}$ as x approaches 0) and as such is a candidate model for delithiated Spinel structures. All three structures were geometry optimized using the same methodology as the prior section. Since the layered structures (O3, O2, O1 and P2) are related by glide planes, there is to be small activation barriers to migration. Thus if there is a thermodynamic driving force to these glide transformations they will likely happen at ambient temperatures. ^{1,180,191,205}

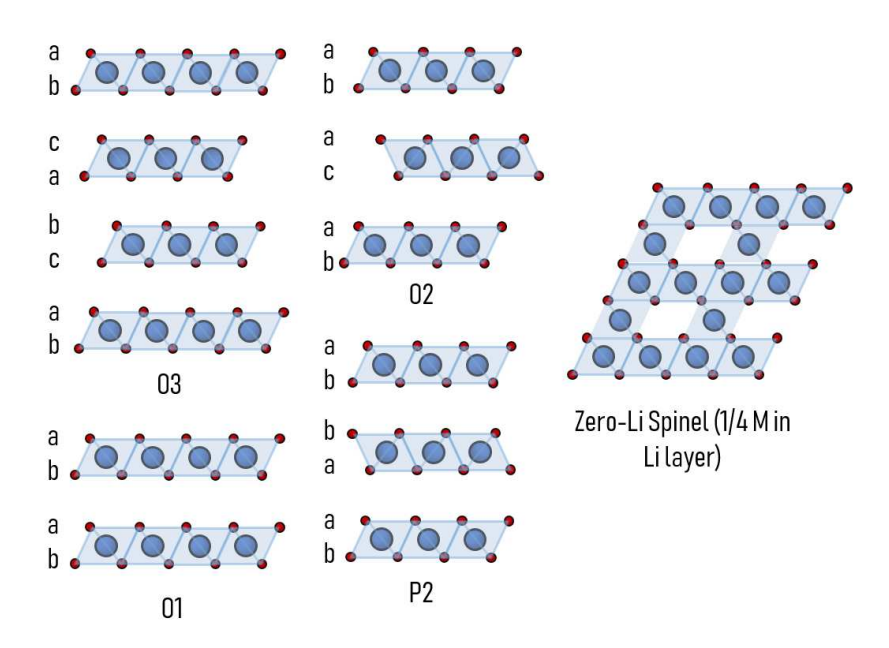


FIGURE 3.17: Identified candidate structures at the delithiated end-member Li₀MO₂.

Analysis of key lattice parameters of these structure can be found in Figure 3.18 and the Li layer spacing of these materials can be found in Figure 3.19. Aykol and Kim claim PBE and PBE+U calculate a c-lattice parameter of 17 Å for the O3-type structure. Such a large c-axis would indicate a Li layer spacing above 3.5 Å and would be sufficiently large to expect near-zero layer-to-layer interaction with MO₂ sheets being independent. The PBE/PBE+U work here similarly overstates the c lattice parameter albeit with a more reasonable value of 14.75 Å. It's likely the large discrepancy is due to a poor choice of geometry optimization process acting on a flat energy landscape. Once again, with the exception of PBE the a-axis lengths are largely undisturbed w.r.t to choice of functional indicating all functionals predict similar electronic structure. Once again while having little impact on the c-axis parameter the PBE functional miscalculates the spin-states of the Ni and Mn systems indicate the incorrect magnetic moment and a corresponding shift in the calculation of the a-axis parameter shows that M-O bond-lengths are deviating accordingly. The P2-type structure maintains its large Li layer-spacing even at zero-Li. This indicates that the extended lattice parameters is the result of interactions between the metal oxide sheets (and not solely prismatic occupation of Li). In particular the oxygen sub-lattice being comprised of sheet pairs (abbaa) results in reduced O-O distance across the vacuum. An equivalent Li layer spacing of the structures yields a $\sin(\pi/3)$ reduced O-O across the distance than the octahedral counterpart and as such the vacuum extends (and the MO polyhedra shrink) to compensate. The Zero-Li Spinel structure was calculated to have a lattice constant of 7.95, 7.80 and 8.15 Åfor Co, Ni and Mn. Once again PBE fails to predict the correct spin-state for both Ni and Mn and results in erroneous bond-lengths. These values are similar to the full lithiated lattice parameters indicating that occupation across the vacuum spacing by a metal ion aids to stabilize the lattice parameter between extreme states of charge.

The formation energies for these structures (normalised to the delithiated O3-type structure) can be found in Figure 3.21. It's observed that removal of Li from structures results in a competitive thermodynamic landscape between the O3 O1, and P2-type structures. with all of them lying within 20 meV/atom regardless of functional choice or metal. Interestingly, the O3-type structure is calculated to be meta-stable to the

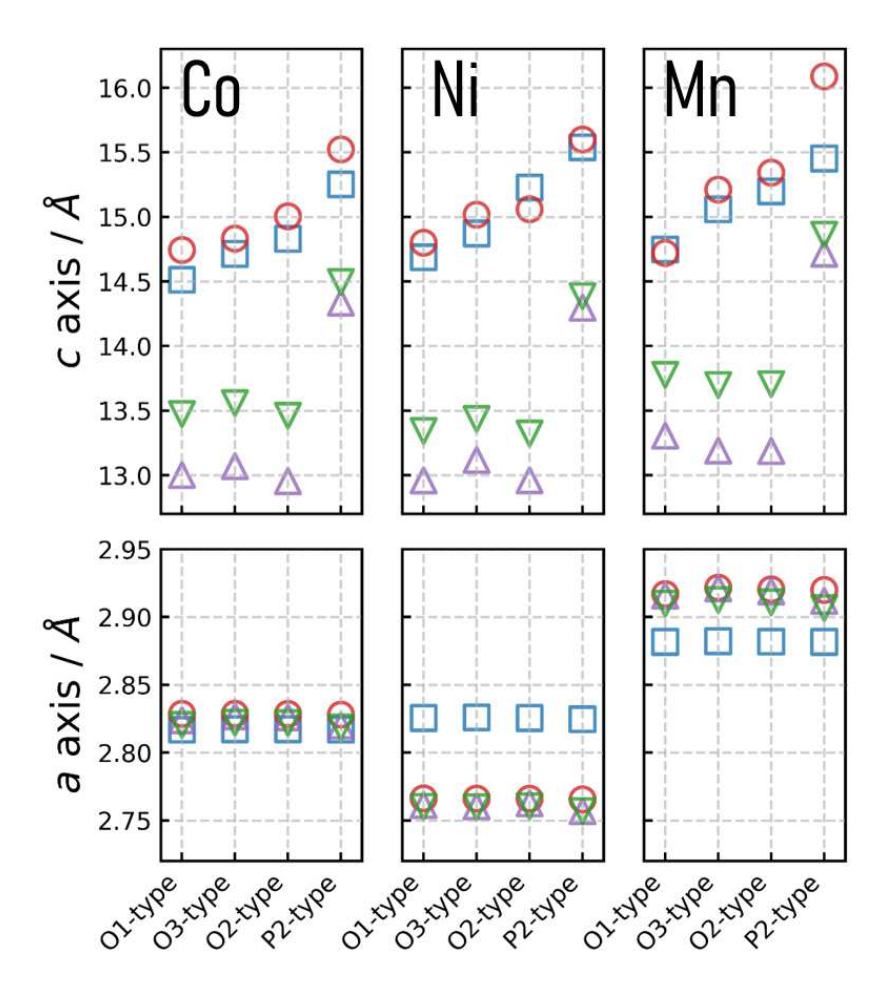


FIGURE 3.18: Calculated lattice parameters for O1, O3, O2, P2-type Li₀MO₂ using various functionals.

O1-type structure for both Ni and Co. This is observed throughout the literature with a phase transition predicted to occur at $x=\frac{1}{4}$ for LiCoO₂. ^{1,158}Interestingly the large P2-type structures show a disparity between functional and stability indicating that the lack of a dispersion interaction likely misrepresents the extent of the repulsive O-O force between layers.

The c-axis length for the delithiated end-member of these class of crystal is found to depend on van der Waals interactions between the MO₂ sheets. As evidenced by key lattice parameters (in particular Li layer spacing) being grossly miscalculated by functionals which lack dispersion corrections, with PBE failing to correctly calculate the electronic ground state of these systems. With a plethora of prior literature regarding these end-member structures care must be taken when drawing conclusions between publications as lattice parameter, electronic ground-state and thus battery

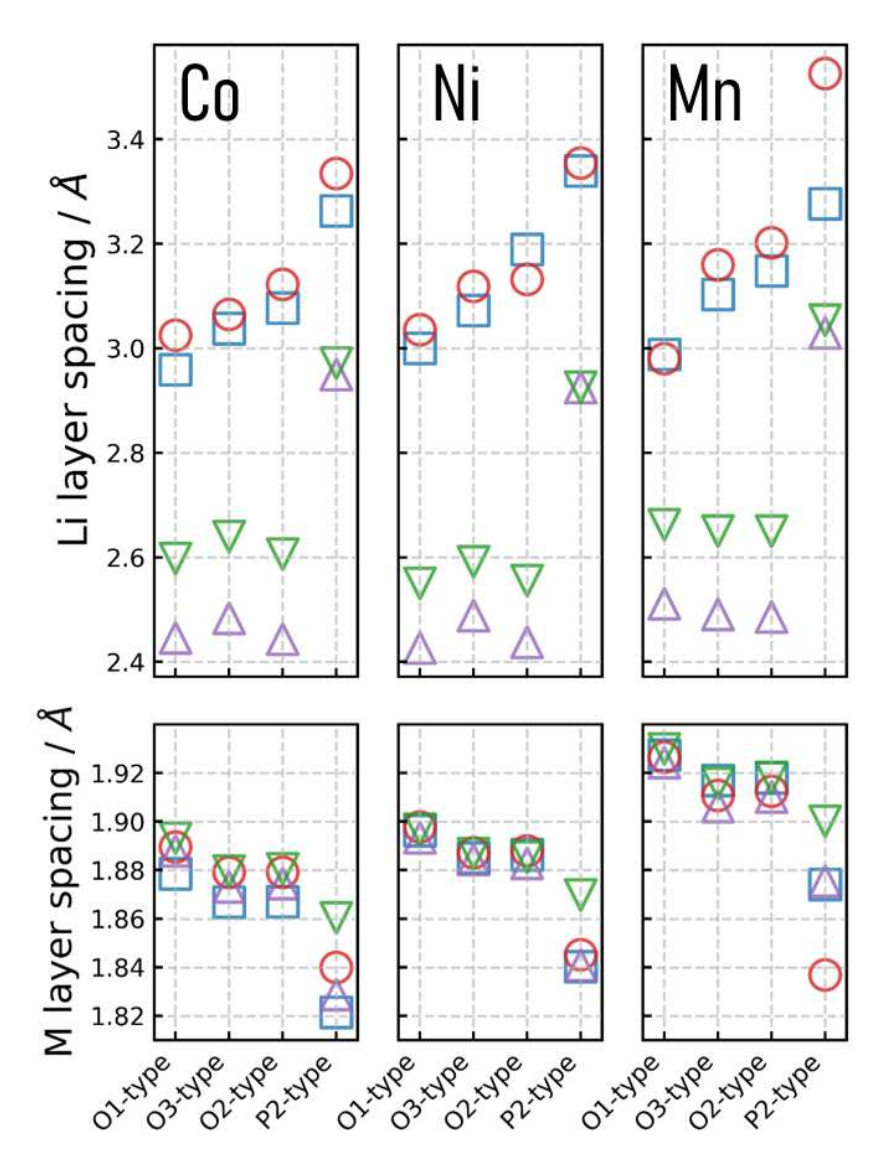


FIGURE 3.19: Calculated Li and M layer spacing for O1, O3, O2, P2-type Li₀MO₂ using various functionals.

performance may be subject to the methodology used. While only marginal gains are made when dispersion corrections are used for the fully lithiated end-member the delithiated structures require dispersion corrections as to avoid modelling these materials individual MO_2 sheets.

3.3.2 Stability of partially lithiated layered oxides

It is understood that these materials bend and flex during operation and the c-axis (and other corresponding parameters) are dependent on state of charge. More recently it's been demonstrated that rapid charge and discharge results in non-uniform

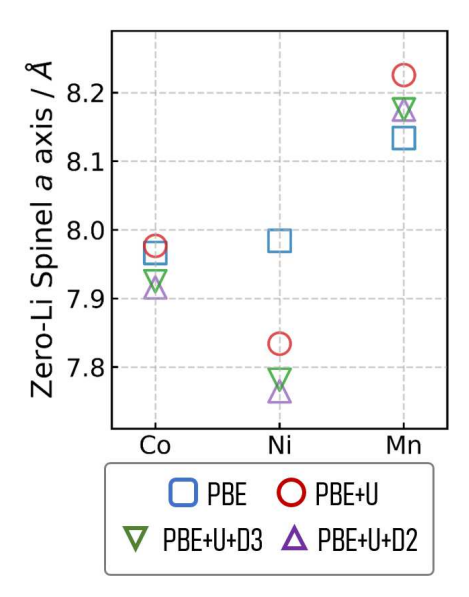


FIGURE 3.20: Calculated lattice parameters for the Zero-Li Spinel structure using various functionals.

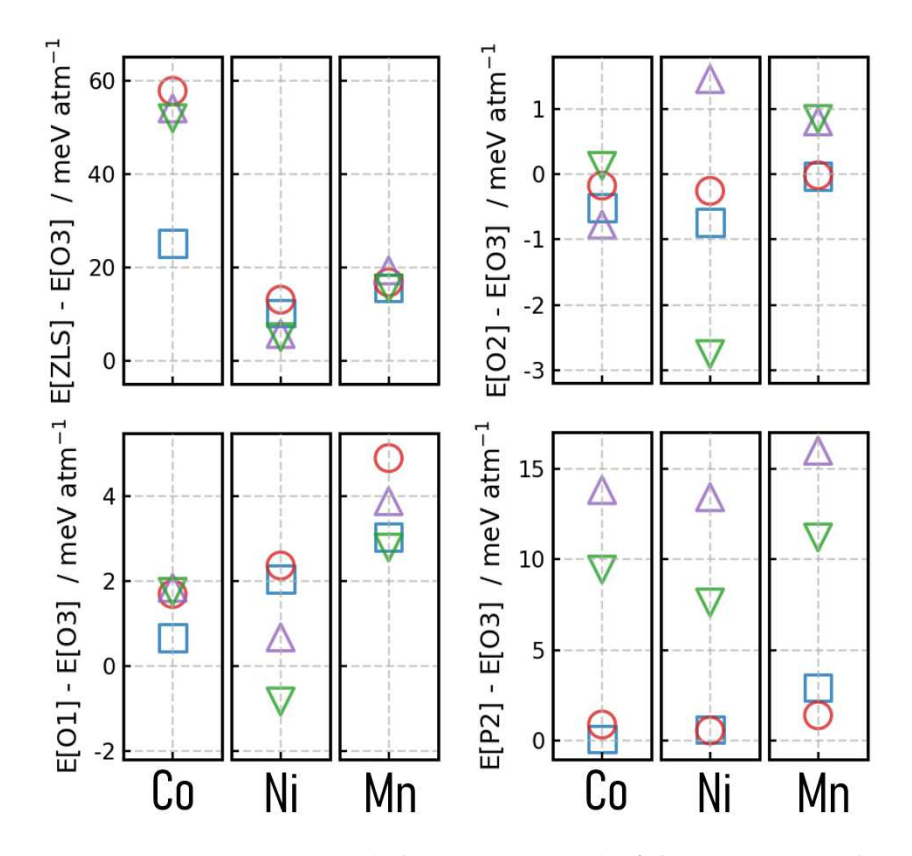


FIGURE 3.21: Formation energies (relative to O3-type) of the Zero-Li spinel, O2, O1 and P2 type structures.

delithiation across layered cathode nano-particles and a subsequent lattice strain. ²⁰⁶ Spectroscopic measurements claim this class of materials achieve a peak of c-axis value around half-lithiation. ²⁰⁷ Modelling work by Aykol and Kim states that this

effect is not observed without the inclusion of a dispersion correction (albeit this is mostly due to an erroneous delithated structure). Their work and work by others 208 however, has only investigated a singular model structure for the half-lithiated materials. While this structure is typically cited as the 'ground-state half lithiated structure' for layered systems 191,209 , there in principle lies an infinite number of Li/V_{Li} orderings for any non-trivial x in Li_xMO₂. Since ordered ground states in this class of materials determine the 0 K equilibrium voltage, understanding these phases is adapting these materials for specific electrochemical application.

Any methodology attempting to elucidate the ground-state for the non-trivial cases must tackle a configuration problem. In the literature, a common method is to search within several ad hoc supercells. However this has led to confusion within the literature 1,64,191,210 as numerous publications have used a variety of supercells. More recently, Ran and Zou applied a group-subgroup transformation method to determine formation energies of O3-type Li_xCoO_2 albeit with no investigation of alternate crystal phases no the effect of dispersion corrects.

3.3.2.1 Generation of partially lithiated superstructures

Rather than utilising just a singular model structure at half-lithiation, the methodology outlined by Hart et al^{211–214} was utilised to generate Li/V_{Li} orderings at various degrees of delithiation from the lithiated O3, O2 and P2-type structures. To truncate the total number of structures, the search was limited such that the maximum cell contained ≤ 12 metal ions. This yields a total of $\binom{12}{6} = 924$ derivative structures for each of the four crystals at half-lithiation. The majority of these structures will be symmetrically equivalent or be reducible to a smaller cell thus the total number of searched configurations is much smaller.

Although there has been some evidence to suggest that low-vacancy structures are stable (x=0.875, 0.833) in $\text{Li}_x\text{CoO}_2^{64,210}$ the degree of lithiation for this body of work was limited to x= $\left(0, \frac{1}{4}, \frac{1}{3}, \frac{1}{2}, \frac{2}{3}, \frac{3}{4}, 1\right)$ and a total of 1550 structures were investigated. Full lattice parameters and ionic relaxation was performed in *VASP* using the same

methodology as the end-members. While this method was attempted for the Spinel-like structure (LT - LiCoO₂) the delithiated states showed a tendency for partial migration of Li from the O_h to T_d sites, effectively becoming a co-crystal of Spinel (where Li is T_d and the some metal lies in the Li layer) and layered structures (where Li is O_h and no metal lies in the Li layer). Rather than further discerning energy barriers between tetrahedral and octahedral sites over a plethora of super-structures this data-set was removed from the results. Instead the known Spinel structure LiM₂O₄ in which Li occupies the T_d 8a sites was used as a reference for half lithiation where it's likely that similar structures with varied T_d/O_h occupancy are thermodynamically similar. The resulting formation energies if the different Li - V_{Li} configuration were calculated as per Equation 3.13 such to be normalised to the O3-type Li_xMO₂ structures with the end-members from the plots for clarity.

$$\Delta_f E_i = E_i - x E_{LiCoO_2} - (1 - x) E_{CoO_2} \tag{3.13}$$

where E is the total energy of configuration i per $\text{Li}_x V_{\text{Li}(1-x)} \text{CoO}_2$ formula unit. $\text{E}_{\text{LiCoO}_2}$ and E_{CoO_2} represent the end-member energies of the O3-type structure at full and zero lithiation respectively.

3.3.2.2 Stable structures at varying degrees of lithiation

Qualitatively (with the exception of PBE) the resulting convex hulls are similar to those found by both Ran and Zou^{209} , with the same O3-type structures found to lie on the hull for Co, Mn and Ni regardless of choice of functional (See figure 3.22). Across all three stacking sequences low energy delithiated structures tend to be high symmetry across the c-axis, maintaining an even distribution of Li or V_{Li} between layers while in contrast the structures that alternate between vacant and fully populated sheets are un-favoured (see Figure 3.23).

Despite being competitive (with structures < 10 mev above hull) both the P2 and O2-type stacked lattices were always higher in energy than the equivalent O3-type Li/ $V_{\rm Li}$ arrangement. This indicates that O2 and P2-type structures are spontaneous to

a glide plane reconstruction of the oxygen sub-lattice into the O3-type structure regardless of degree of lithiation for single metal layered cathodes. At half lithiation the high symmetry structure consisting of alternating Li and V_{Li} across the b-axis is consistently a low-energy structure regardless of metal and functional. This structure belongs to the P2/m space-group and has been discussed and utilised as a model half-lithation system in prior publications. 3,7,64,158 The PBE functional can largely be disregarded, it's incorrect description of the ground-state of the end-members introduces errors in the formation energies across the the compositional space, predicting stable compositions at $x = \frac{1}{4}$, $\frac{1}{3}$ and $\frac{2}{3}$ for Mn, Co and Ni respectively. Additionally, it predicts a formation energy of -223 meV /f.u for the P2/m structure for Cobalt a value three-fold PBE+U.

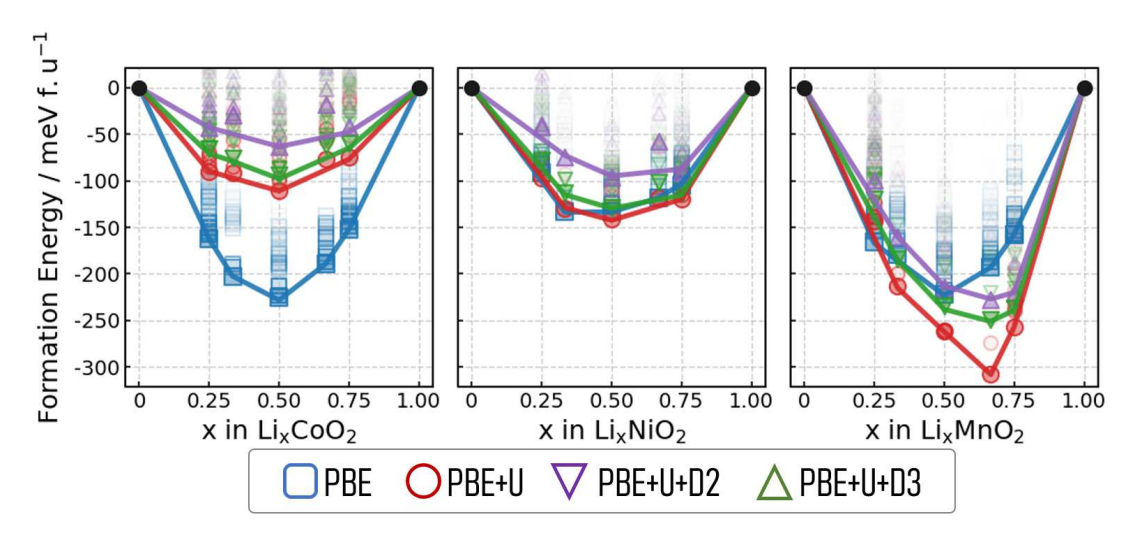


FIGURE 3.22: Calculated convex hulls for Li_xMO₂ (M=Co, Ni and Mn) using various functionals.

The prior publications by Van der Ven, Arroyo and Ceder 1,191 investigated orderings within Li_xMO_2 at detail. Their methodology utilised a PBE functional and showed similar convex hulls to those from the PBE method found here. In particular the earlier publications investigated both specific in plane lithium arrangements and Li stacking sequences. At half lithiation a low energy $\text{Li}/\text{V}_{\text{Li}}$ ordering features alternating linear chains of $\text{Li}/\text{V}_{\text{Li}}$ see Figure 3.24i). It has been demonstrated that such a $\text{Li}/\text{V}_{\text{Li}}$ arrangement can be offset from layer to layer across the c-axis and is typically a energy penalty associated with such processes. They postulate that maintaining a high symmetry Li/V arrangement across the c-axis (such that

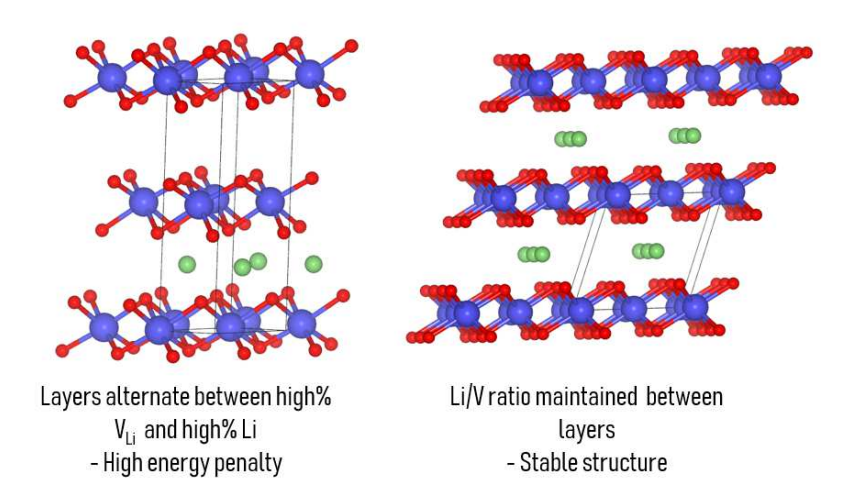


FIGURE 3.23: Stable Li/ V_{Li} configurations are those that maintain equal distribution of Li across layers.

 ${\rm Li_A}-{\rm O-M-O-Li_B}$ is 180°) results into a co-operative Jahn Teller effect and this ${\rm P2/m}$ structure having increased stability. Two such structures were investigated, the ordered low energy structure and it's alternating stacking sequence (see Figure 3.24ii, iii) respectively). Collaborating the prior conclusions it's found that With the exception of PBE. It's found the energy penalty associated with an alternate stacking is consistent between functionals (around 55, 35 and 30 mev for Co, Ni and Mn systems respectively) (see Figure 3.25A). In general, these energy barriers vary minutely and the overall trend is consistent thus it's concluded that functional choice doesn't greatly effect the relative thermodynamics of ${\rm Li/V_{Li}}$ arrangements nor the stability/electronics of specific stacking sequences.

Constrastingly the $Li_{Td}M_2O_4$ Spinel structure lies significantly below the hull for these layered materials, (-150, -200 and -300 for Co, Mn and Ni respectively). The overall conversion of layered LiCoO2 to this Spinel structure has been discussed at length in numerous publication under a variety of methods and functionals where it has been agreed that this process is spontaneous and facilitated at half-lithiation. As such the Spinel structure is often cited to be lower in energy than layered structure. However, it is of note that this relative energy difference does vary significantly with choice of functional. The functionals incorporating dispersion both predict lower formation energies than PBE/PBE+U methods (by around 75 meV/atom $^{-1}$). However, with the formation energy of the Spinel structure varying upward of 100 meV (in comparison

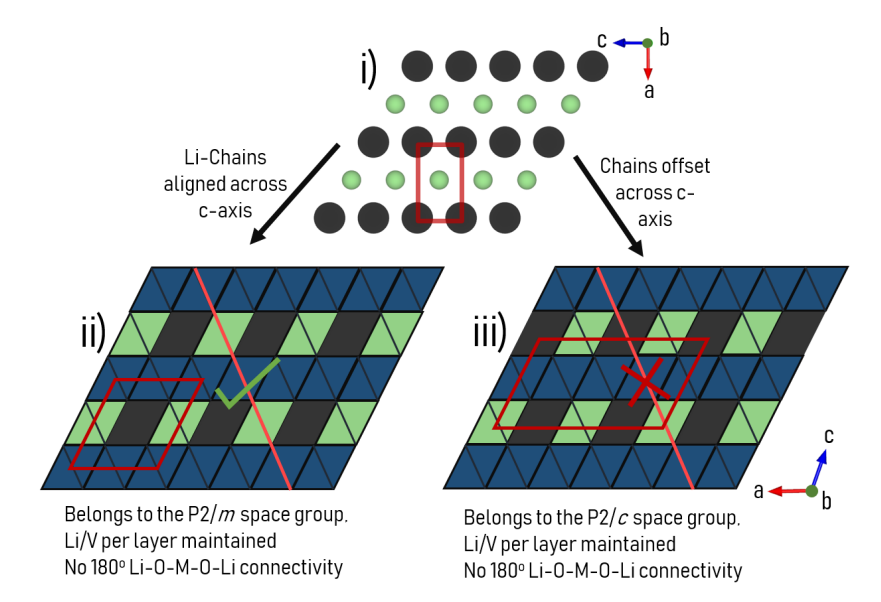


FIGURE 3.24: i) The in plane Li arrangement investigated by Van der Ven et al 1 can yield numerous structures when stacked across layers. ii) The P2/m structure has vacancies that run planar across the b-axis. iii) The off-set stacking sequence results in a reduction of the space-group to P2/c and a breaking of the co-operative Jahn Teller effect.

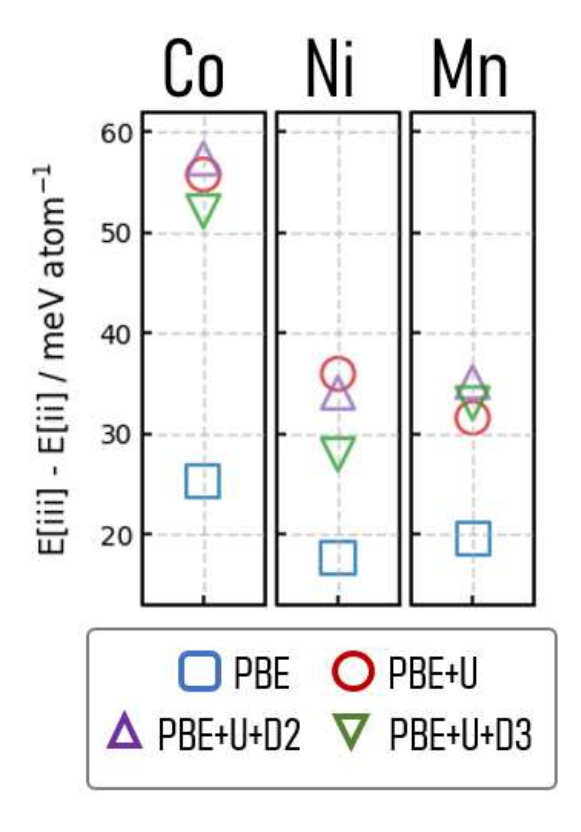


FIGURE 3.25: Energy penalties for breaking the Li-O-M-O-Li connectivity for the ordered structure seen in Figure 3.24.

to the half lithiated layered structure) depending on choice of functional it stands to reason that both the intermediates across this pathway as well as the overall rate of such process may also be subject to such variation. Such issues have plagued the literature consistently, Seymour et al³ demonstrated that choice of Hubbard U value drastically changes the energy landscape of a migrating metal ion from the MO₂ sheets within the layered structure into the Li layer. As such a energy barriers for metal migration should have the caveat that they may be functional dependent. Gathering experimental data for the energy differences of these two structures is not an easy task and as such there is no clear indication what functional performs best.

C-axis lengths at a given degree of lithiation for the O3-type structure was estimated through the use of configurational averaging, with contributions being derived from the partition function (See Equation 3.14). Thus, unstable and unlikely configurations do not contribute to the expect c-axis length.

$$C = C_i \frac{N_i}{N} = C_i e^{-(\epsilon_i/kT)}/Z$$
(3.14)

where

$$Z = \sum_{i} e^{-(\epsilon_i/kT)} \tag{3.15}$$

With the exception of PBE+U+D2 all methods predict reasonable values for the c-axis lattice parameter at full and half lithiation. PBE+U+D2 shows a tendency to over-estimate the extent of the van der Waals interactions in these materials, with resulting c-axis lattice parameters lying below those seen experimentally. The work by Aykol and Kim demonstrated that PBE and PBE+U is ineffective at calculating lattice parameters for the delithiated Cobalt Oxide system, however it's found that the extent they claimed (c=16.1, 16.6 for PBE and PBE+U respectively) seems egregious and is likely the result of a systematic error (likely a poor relaxation scheme). The publication by Chakraborty²⁰⁸ investigated similar functionals and c values (c=14.4 and 14.5 for PBE and PBE+U respectively), which align with those found here. With a lack of attraction force between MO₂, both PBE and PBE+U show a near-linear relationship between degree of lithiation and the c-axis for all three metals and as such

3.4. Summary 73

no "c-axis expansion" at half lithation is observed. Similarly to Chakraborty, it's found here that while PBE is clearly erroneous for the majority of the investigated systems, PBE+U performs exceedingly well provided the degree of lithiation ≥ 0.5 . Due to the flat energy energy landscape, geometry optimizations of the delithiated should utilise a force-based relaxation algorithm such that large unit cell volumes are penalised accordingly and even in these cases, the lack of a dispersion correct term will still over-estimate the lattice parameters.

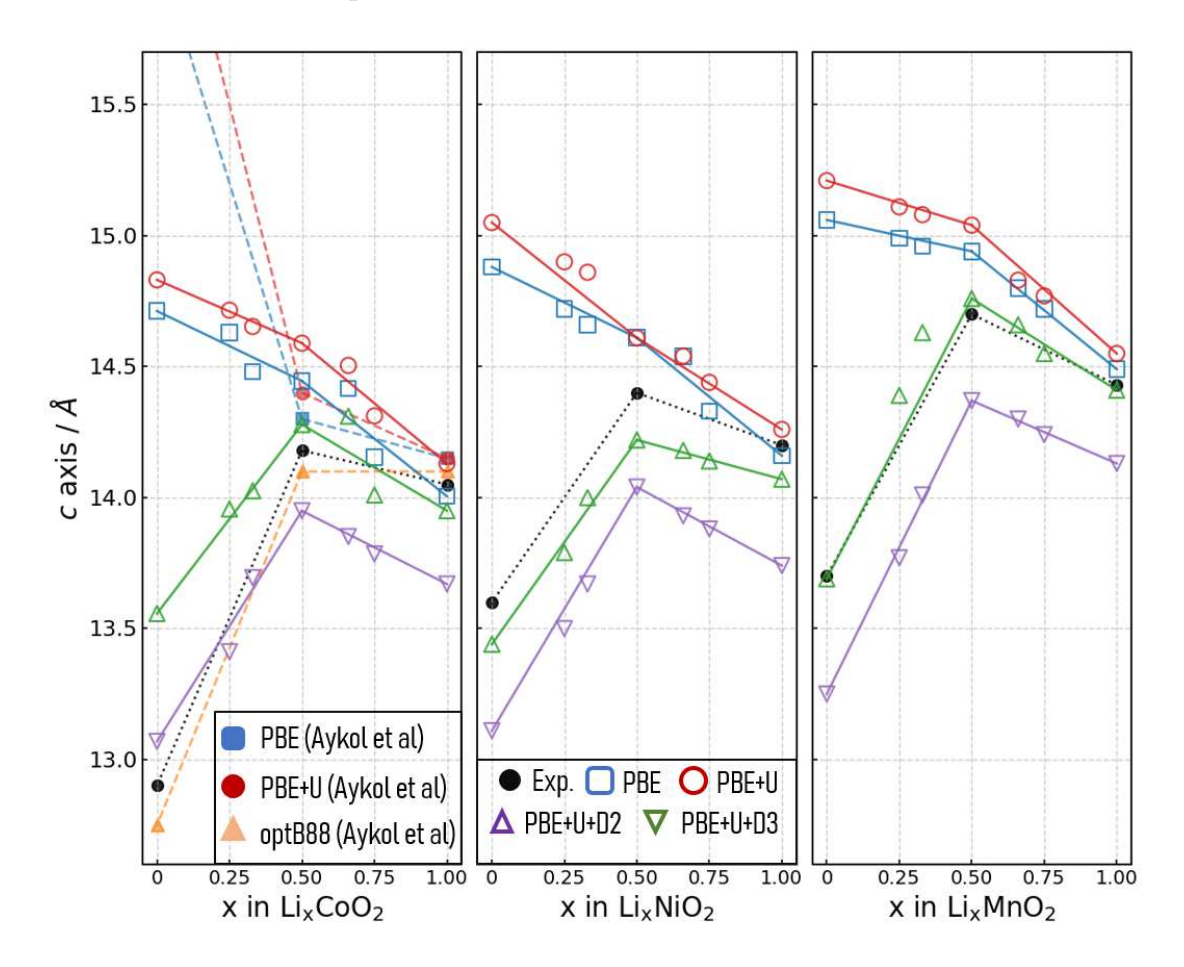


FIGURE 3.26: Comparison of calculated c-axis lattice parameters in the literature and this work. Dispersion correction are necessary to avoid c-lattice expansion at low lithiation.

3.4 Summary

A wide range of metal oxides have been investigated and key parameters have been bench-marked to. It's found that calculated lattice constants align with those seen of known materials provided the energy cut-off and kgrid-spacing is sufficiently dense. A plane wave cutoff energy of at least 550 eV and a k-grid spacing smaller than 0.4 $\rm \mathring{A}^{-1}$ yield an energy convergence > 10 meV / atom. It stands to reason that modelling of battery systems will require the same parameters thus these values have been followed to throughout the rest of this thesis.

The metal-oxygen composition space is exceedingly broad and result rigorous analysis of a wide range of compositions and their electronic structure has proved to be cumbersome, even for significantly large compute power ^{66,68}. However, in this work numerous metal oxides were identified to be stable structures. In particular the battery metals (Co, Ni and Mn) show stable compositions at MO₂ that aren't typically discussed in the context of batteries (neither layered nor spinel-like). This suggests that over prolonged periods both the delithiated layered structure and the delithiated Spinel structure may be subject to further decomposition while avoiding oxygen loss.

The impact that PBE, PBE+U and dispersion corrections have on structures and energetics of various layered materials was investigated. It was identified that unlike Na-ion the O3-type structure dominates across all ranges of lithiation (with the exception of x=0 in which O1-type is stable). PBE incorrectly predicts both lattice parameters and electronic structures and as such is a poor choice for modelling these materials. In agreement of prior work, the formation energy of half-lithiated structures is negative with the high-symmetry P2/m structure lying on the convex hull, similar Lithium arrangements showed negative formation energies but breaking the symmetry across the c-axis yield an energy penalty. This structure forms a good model system for the half-lithiated materials. Interestingly, this low energy P2/m structure still lies far above the the Spinel structure $\text{Li}_{\text{Td}}M_2O_4$ in energy.

With much of the work in later chapters investigating half and zero-lithiated layered structures, the PBE+U+D3 functional will be required to accurately capture the crystal structures of these materials. With the scope of the work being so large, the selected choice of investigated functionals was such to minimize computational cost, further investigation into the crystal structures of these materials would aim to elucidate the nature of these dispersion interactions. There is lack of prior work identifying the

3.4. Summary 75

validity of the Hubbard U, the choice of Hubbard U and the whether these choices are still valid upon introducing dispersion corrections. While briefly investigated by Aykol and Kim (for Co systems) it's found that much of difficulty regarding PBE is centered on Mn. In particular the differing magnetic configurations between U=0 and U=3.9 for O'3-type LiMnO₂ implies that values between these two may be subject to difficulties in predicting magnetic ground-states which in turn may suppress the Jahn Teller effect. With this Jahn Teller effect (and the resulting degradation routes) plaguing the material as a potential cathode candidate, ^{161,215,216} modelling work intent on investigating JT-suppression or the electronics of similar structures needs to take care to ensure the U-values used are appropriate.

Chapter 4

Ion migration in bulk cathode materials

Some of the findings within this Chapter have been presented online:

Bud Macaulay, & Denis Kramer. (2024). The Impact of Lattice Stress on the Layered to Spinel Transformation of Li-Ion Battery Cathode Chemistries. Journal of The Electrochemical Society, 171(3), 030509.

https://doi.org/10.1149/1945-7111/AD2D17²¹⁷

During cycling, the class of cathode materials discovered by Goodenough et al 14,161 can be described to operate between two extreme states of lithiation (Li₀MO₂ and Li₁MO₂), as seen by Figure 4.1. In reality, modern battery management systems inhibit complete delithiation of either electrode as a safety feature, with typical operating ranges of x=0.15 to x=0.85 in Li_xMO₂ 218,219 .

Prior work (see Chapter 3) has identified that this Goodenough structure is thermodynamically meta-stable to the Spinel structure ($\text{Li}_{1/2}\text{MO}_2$) at (and around) half lithiation. This process has been observed to occur rapidly 31,184,220 for layered LiMnO₂ with modelling data discovering this is due to a low lying 'dumbbell' structure, a key intermediate featuring T_d Mn and T_d across a metal vacancy 2,4 . Since

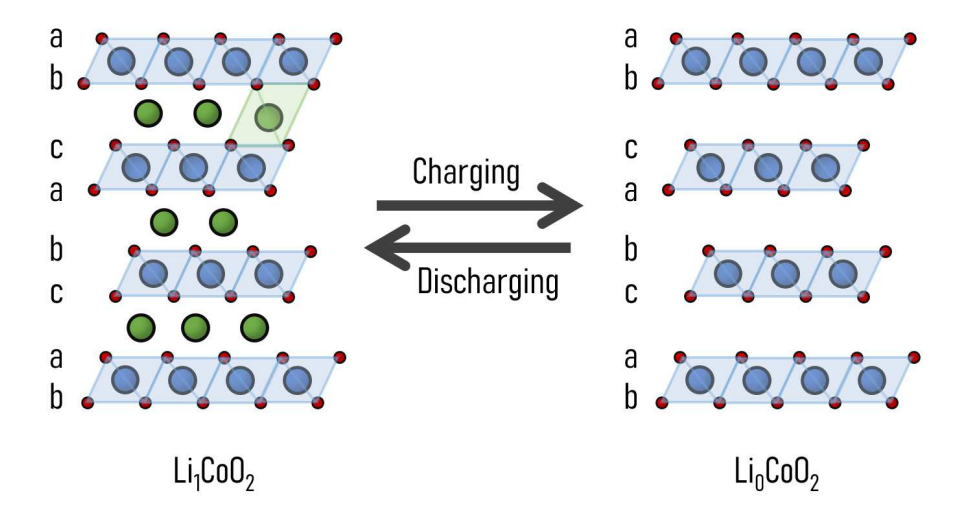


FIGURE 4.1: The Goodenough structure can be thought to operate between two extreme states of lithiation.

this class of materials cycles between states of high and low lithiation during normal use, they spend prolonged periods at and around half lithiation and thus this stable Spinel structure is formed. Consequently, much research has investigated the potential mechanism, energetics and factors that influence this process^{3,7,221–224}. This chapter aims to investigate the nature of this dumbbell intermediate, the factors that influence it's stability and potential routes of inhibiting layered to spinel deformation in bulk cathode materials.

4.1 Model structure of layered cathode materials

While $R\overline{3}m$ O2, P2 and P3-type layered structures were shown to be thermodynamically competitive, the O3-type (Goodenough) structure has been determined to be the ground-state for Co, Mn and Ni at high lithiation, with the Mn and Ni systems featuring Jahn Teller distortion and belong to a lower symmetry space-group (C2/m). These stable compositions, structures and their energetics across the Li_xMO₂ series was discussed in detail in Section 3.

To ease the comparison between similar structures and compare results with prior literature, its often convenient to discuss the lattice parameters for the $R\overline{3}m$ system after conversion to their C2/m space-group equivalents, this has been done throughout the body of this chapter. This is achieved via Equations 4.1 and 4.2.

drawn conclusions regarding defect energies.

$$C_{R\bar{3}m} = 3C_{C2/m}\sin\beta\tag{4.1}$$

$$A_{R\overline{3}m} = B_{C2/m} \tag{4.2}$$

PBE+U/PBE+U+D3 functional within this Cartesian basis can be found in Table 4.1 and Table 4.2 respectively. It's noted that there is a large disparity between functionals in calculating the c-axis size at the zero-lithiation end-member. Since the properties of these materials have been shown to be sensitive to lattice parameter ¹⁵⁹ these incorrect

lattice parameters (as seen with the PBE+U functional) may contribute to poorly

The calculated lattice parameters for the O3-type structures using a

LiCoO₂ CoO_2 LiNiO₂ NiO₂ LiMnO₂ MnO_2 A/Å 4.902 4.900 4.909 4.830 5.088 5.059 B/Å 2.831 2.839 2.941 2.788 3.092 2.921

C/Å 4.983 5.309 4.996 5.367 5.099 5.428 beta / degrees 109.14 109.15 107.66 107.92 106.3 108.53

TABLE 4.1: Calculated lattice parameters in the C2/m basis using a PBE+U functional.

	LiCoO ₂	CoO_2	LiNiO ₂	NiO_2	LiMnO ₂	MnO_2
A / Å	4.893	4.899	4.904	4.826	5.090	5.06
B / Å	2.825	2.825	2.926	2.785	3.084	2.923
C/Å	4.834	4.642	4.836	4.643	4.970	4.692
beta / degrees	109.71	110.7	108.5	110.7	107.58	111.14

TABLE 4.2: Calculated lattice parameters in the C2/m basis using a PBE+U+D3 functional.

At half lithiation, formation of the $Fd\overline{3}m \text{ Li}_{1/2}MO_2$ Spinel structure from the P2/m structure requires numerous ionic migrations (see Figure 4.2). Li migrates from their half occupied O_h sites to the 8a sites and one quarter of the metal ions migrate into the O_h site within the Li layer. Due to the numerous migratory steps in conjunction with a variable degree of lithiation, numerous proposed mechanistic steps are suggested in the literature. General consensus, however, is that migration is inhibited at and near the two end-member concentrations (Li_xMO_2 where x = 1 and 0) as when x is near 1, all O_h sites within the lithium layer are occupied and there is no space for the metal to migrate into. Constrastingly, when x is near 0, the metal ions are in the +4 oxidation

state which has been shown to be resistant to metal migration through the use of crystal field theory by Ceder and Reed⁴.

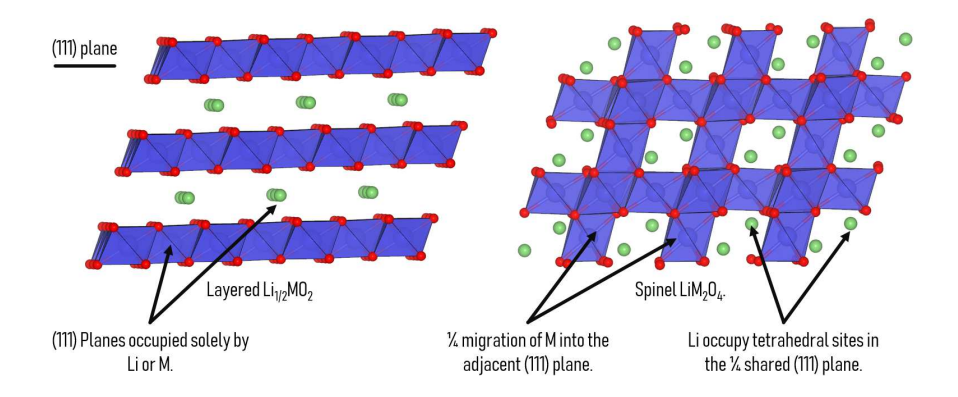


FIGURE 4.2: Migration from the P2/m structure to the Spinel structure requires numerous steps. *Adapted from Ceder and Reed*.²

4.2 Transition state analysis of the end-member Li_0MO_2

The zero lithiation end-member has been quoted to be resistant to layered to spinel degradation by Ceder and Reed,² with transition state values in excess of 2 eV for Co, Ni and Mn. However, the functional used in that body of work was a pure-PBE functional, which has been demonstrated to predict inaccurate lattice constants and (in the case of Mn) poorly models the electronic structure (See Chapter 3). Figure 4.3 demonstrates the two pathways suggest by Ceder and Reed for metal migration into an O_h site in the Li layer. The first is the 'linear path' (A \rightarrow F) in which the metal traverses the shortest possible distance from the O_h site in the Metal layer directly to the O_h site in Li layer via their shared polyhedral edge. Alternatively, they proposed the 'open' path (A \rightarrow E \rightarrow F) in which the metal traverses via polyhedral faces through a shared vacant tetrahedron. While this pathway is longer (atleast 1.15x) it maximises the distance from the repulsive O^{2-} ions.

4.2.1 Generation and structure of initial and final states

Using the monoclinic equivalents of the O3-type delithiated crystal structures found in Section 3 and referenced in Table 4.1, $3 \times 3 \times 2$ super-cells were generated and fully

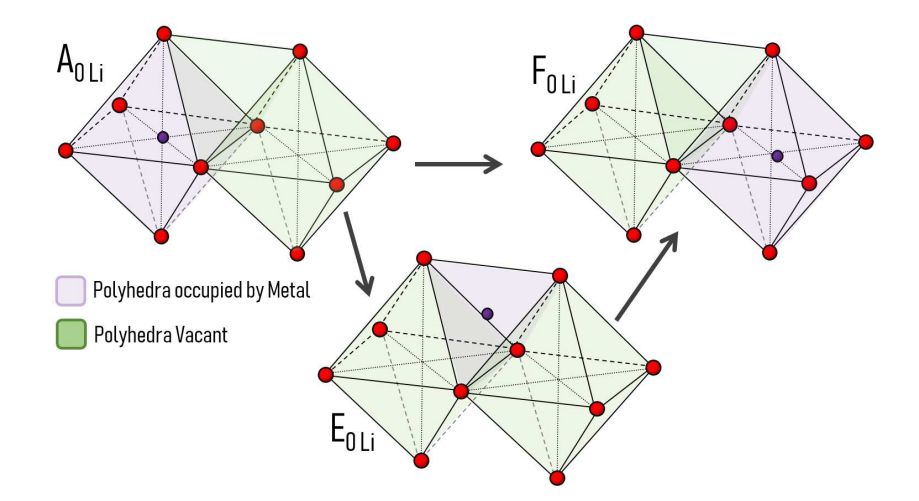


FIGURE 4.3: Pathways for O_h to O_h migration. The shorter pathway (A \rightarrow F) results in close M-O proximity and high coulombic repulsion. The longer pathway (A \rightarrow E \rightarrow F) minimises this repulsion by passing through a T_d intermediate. Adapted from Ceder and Reed. ²

relaxed (forces \leq 2 meV/atom) using a 550 eV plane-wave cutoff energy and a $1 \times 2 \times 2$ k-grid for both the PBE+U and the PBE+U+D3 functional. This size supercell has been shown to be sufficient in eliminating defect-defect interactions³. While these materials have been shown to adopt complex antiferromagnetic orderings, for this body of work they were initialized to be ferromagnetic, as the relative energies of AFM vs FM configurations is significantly small ^{157,225}.

As seen in Figure 4.4, both the final state F and the tetrahedral state E are characterised by migrating a metal atom out of the MO_2 into the center of a neighbouring polyhedra site in the Li layer. An ionic geometry optimization was performed on these states with lattice parameters fixed (at those found for the undefected state A) such to model an isolated defect within a large crystal. Additionally, since PBE+U has been shown to incorrectly calculate the lattice parameter of this end-member, corrected lattice parameters were used and defected structures calculated in a PBE+U functional (labelled PBE+U-fixed) in a bid to identify whether defect energies are a result of the lattice parameter or the functional itself.

Relaxation of structure E and F results in minimal disruption to the MO_2 sheets, with all metal ions (other than the migratory ion) deviating less than 0.03 Å from their initial positions for all three metal systems. For Structure E, the metal occupying a T_d

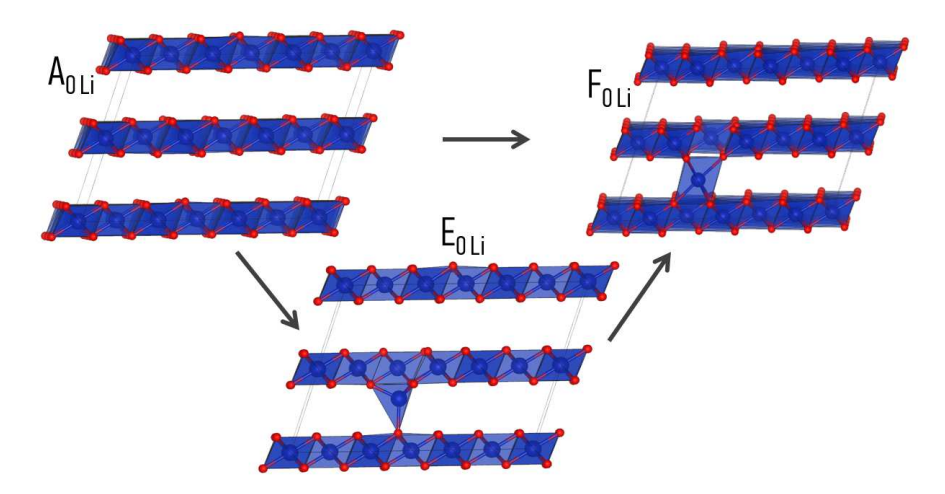


FIGURE 4.4: Potential pathways for metal migration at zero-Lithiation. The metal migrates through the shared polyhedral edge in the "restricted pathway" (A \rightarrow E). Alternatively, the metal migrates through a shared tetrahedron via polyhedral faces in the "open pathway (A \rightarrow E). Adapted from Ceder and Reed. ⁴

geometry results in the bound oxygen in the adjacent MO_2 sheet undergoing a small displacement (less than 0.15 Å) such to reduce the $M_{Td}-O$ bond length across the plane. This is exacerbated when using the PBE+U functional with it's increased layer spacing. Figure 4.5 shows that large lithium layer spacing results in a significant $M_{Td}-O$ bond-length across the Li layer despite increased oxygen migration. This is further observed in structure F, in which the enlarged Li layer space results in asymmetry of the migratory M and a pseudo-octahedral geometry. By utilising corrected lattice parameters (PBE+U-fixed) the layer spacing is closer to that of PBE+U+D3 and as such the resulting oxygen distortion is reduced.

4.2.1.1 Electronic structure of states A, E and F

Transition metals are noted for the variety of oxidation states they can possess compared to much of the rest of the periodic table. This is the result of incompletely filled d-orbitals, allowing a variety of coordinating ligands and oxidation states. Coordinating a metal ion raises the barycenter of the 3d orbitals (as the negatively charged ligands repel the orbitals). For an octahedral coordination the typical five-fold degenerate d orbitals are split via into two distinct groups, the triply-degenerate t_{2g} and the doubly-degenerate e_g orbitals. (see Figure 4.6). The energy between these two sets of orbitals is called the ligand field splitting (Δ). Since the total energy of these

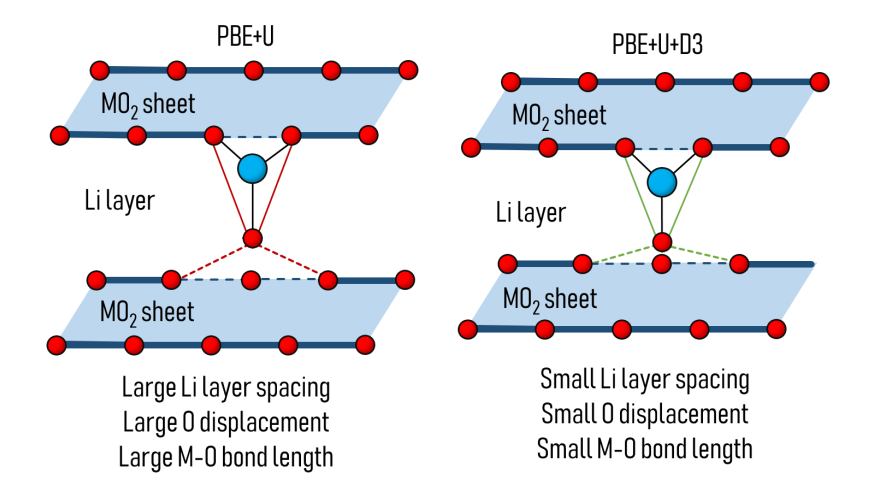


FIGURE 4.5: Structure E results in moderate displacement of the metal-bound oxygen across the Li layer. This displacement is increased in the large layer spacing structure predicted by PBE+U. Despite this increased displacement the $M_{Td}-O$ bond is longer than that seen in the PBE+U+D3 structure.

orbitals is preserved, the t_{2g} orbitals are lowered by $\frac{2}{5}\Delta_o$ while the e_g orbitals are raised by $\frac{3}{5}\Delta_o$. For tetrahedral coordination the reverse degeneracy is observed and via crystal field theory the magnitude of $\Delta_t = \frac{4}{9}\Delta_o$.

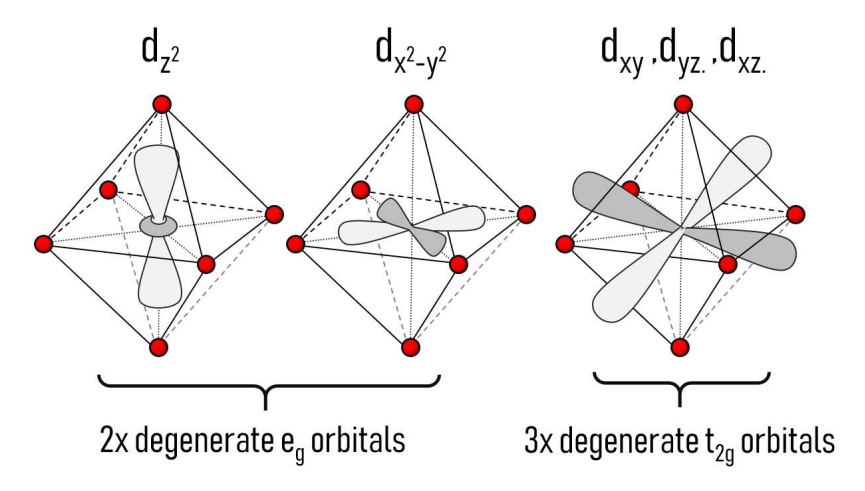


FIGURE 4.6: In an octahedral coordination, the d orbitals (quantum number $\ell = 2$) are split such that the orbitals directed at the ligands (e_g) are higher in energy than the orbitals directed away (t_{2g}).

Occupation of the electronic orbitals typically obey Aufbau's principle ^{225,226} in which the lowest energy orbitals are occupied first. However pairing electrons result in electron-electron repulsion and the rise of Hund's rules. Interesting, for many 3d transition metals the magnitude of this electron-electron repulsion term is similar scale to the ligand field splitting energy. As such it's common to observe both high-spin (in which Hund's rules are obeyed) and low-spin (in which Hund's rules are not)

transition metal complexes. A complex will be low-spin when $\Delta_o > \Delta_s$ (where Δ_s is the energy penalty for pairing an electron).

For an octahedrally coordinated metal in the delithiated structure the oxidation state is +4. This yields 5, 6 and 3 d-electrons available to populate the d-orbitals for Co, Ni and Mn respectively. Mn⁴⁺ (with three d electrons) only has one valid occupation of the d orbitals (t_{2g}^3). Constrastingly for both Ni and Co two possible configurations are valid. By integrating the spin-density over atomic sites using the methodology outlined by Bader ¹⁴⁸ these two metals were calculated to be in their low-spin configurations (t_{2g}^5 and t_{2g}^6 for Co and Ni respectively). The population of the d orbitals in these configurations can be seen in Figure 4.7 and Table 4.3 shows the net spin and associated crystal field stabilisation. Co and Ni being low-spin indicates that $\Delta_o > \Delta_s$ for these metals. While uneven occupation of the t_{2g} orbitals does would indicate that the CoO₂ structure would be Jahn Teller active this distortion is minimal (< 1%) as is typical for uneven occupation of the t_{2g} orbitals. This results in none of the end-member ground state structures showing a Jahn Teller effect.

	Configuration	Net spin	Crystal Field Stabilization Energy
Co ⁴⁺ LS	t_{2g}^{5}	1	$2\Delta_s - rac{10}{5}\Delta_o$
Co ⁴⁺ HS	$t_{2g}{}^3e_g^2\\$	5	0
Ni ⁴⁺ LS	t_{2g}^6	0	$3\Delta_s - \frac{12}{5}\Delta_o$
Ni ⁴⁺ HS	$t_{2g}^4 e_g^2$	4	$\Delta_s - rac{2}{5}\Delta_o$
Mn ⁴⁺ LS/HS	t_{2g}^{3}	3	$-rac{6}{5}\Delta_o$

Table 4.3: Possible d-electron configurations and resulting crystal field splitting for M^{4+} ions in an octahedral coordination environment.

Figure 4.8 shows the occupation of the d orbitals for the migrating ion across the different states. Migration of a metal ion into the T_d site (state E) can be modelled as a simple tetrahedral defect reaction, $M_{\text{oct}}^{4+}(M \text{ layer}) \to M_{\text{tet}}^{4+}(\text{Li layer})$. In this state the crystal field splitting is for a T_d geometry, where there lies two low-energy e orbitals and three high energy t_2 orbitals separated by Δ_t . Where Δ_t is approximately $\frac{4}{9}$ the value of Δ_o for the same species. This reduction in splitting of the d orbitals yields Δ_s Δ_t resulting in all tetrahedral complexes being high spin. Using the same methodology outlined in Appendix A investigation of spin-density of the metal sites

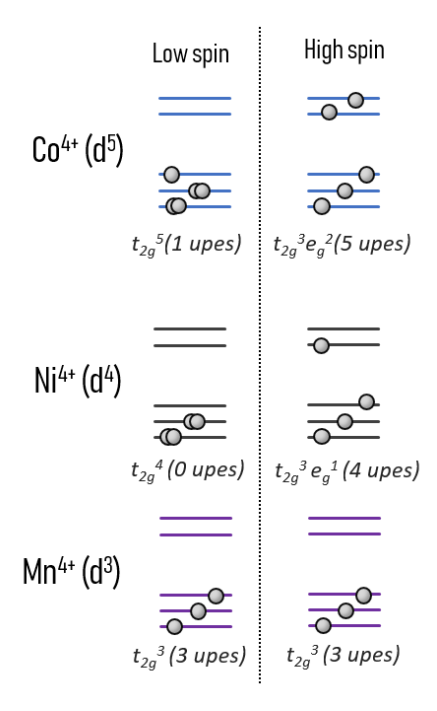


FIGURE 4.7: Occupation of the d-orbitals for M^{4+} (M = Co, Ni and Mn) can be either be low-spin or high-spin and is the result of the relative sizes of Δ_o (the d orbital splitting) and Δ_s (the spin-pairing energy).

for state E indicate that all non-migrating sites preserve their spin. Interestingly, however, the spin-density around the T_d site for all three metal systems suggests a high spin occupation of the d orbitals, with much of the electron density located along the M-O bonds. This suggests a spin-transition (from low spin to high spin) for both Ni and Co during the migration process. Surprisingly, this same high spin occupation is preserved as the ion proceeds back into the octahedral site within the Li layer: M_{tet}^{4+} (Li layer) $\rightarrow M_{\text{oct}}^{4+}$ (M layer). This gives an indication to the magnitude of Δ_s in which the increased layer spacing results in a smaller Δ_o and the energetic penalty for electron pairing being outweighed.

This resulting phenomenon is conveniently explained by a simplified molecular orbital diagram for a metal and its ligands (see Figure 4.9). For an octahedral complex, six metal orbitals combine with six ligand orbitals to form six σ bonds and six σ^* anti-bonds. The metal e_g orbitals contribute to the e_g bonding and e_g^* anti-bonding orbitals. Whereas the metal t_{2g} orbitals contribute to the low-lying π (t_{2g}) orbitals and the t_{2g}^* . It's common practice to presume the low-lying bonding orbitals are occupied and refer to the orbitals near the fermi-level as e_g and t_{2g} as seen prior. An increased

Free M ⁴⁺ ion	Octahedral M ⁴⁺ Ion (A)	Tetrahedral M ⁴⁺ Ion In Li layer (E)	Octahedral M ⁴⁺ Ion In Li layer (E)
Co ⁴⁺ (d ⁵)	$\begin{array}{c} \bullet \\ \bullet \\ \bullet \\ \bullet \\ t_{2g}^{5} \end{array}$	$ \begin{array}{ccc} \bullet & & \\ \bullet & & \\ e^2t_2^3 & & \\ \end{array} $	$ \begin{array}{cccc} & & & & & \\ & & & & \\ & & & & \\ & & & &$
Ni ⁴⁺ (d ⁶)		• • • • • • • • • • • • • • • • • • •	$ \begin{array}{c} $
Mn ⁴⁺ (d ³)	$\begin{array}{c} \longrightarrow \\ \longrightarrow \\ \longrightarrow \\ t_{2g}^{3} \end{array}$	• — — — — — — — — — — — — — — — — — — —	$ \begin{array}{c} $

FIGURE 4.8: Calculated d orbital occupation of a migrating M^{4+} ion (M = Co, Ni and Mn) at stable intermediates A, E and F.

M-O bond distance (within typical bond-ranges) results in a reduced orbital overlap and all orbitals (both bonding and anti-bonding) become a closer representative of their free-ion equivalents. Of-course this must be true as the extreme case in which the M-O bond distance is exceedingly large, the ions become free with no orbital overlap or d-band splitting.

Quantitatively, the energy difference between states A and E can be estimated from ligand field theory. Migrating an octahedral M ion into a tetrahedral site results in a change of the d-orbital occupancy. For Co⁴⁺ this occupancy change is: $t_{2g}^5 \to e^2 t_2^3$ and therefore results in an energy change of $2\Delta_o - 2\Delta_s$. Ni⁴⁺ has an occupancy change of $t_{2g}^6 \to e^3 t_2^3$ and an associated energy change of $\frac{12}{5}\Delta_o - \frac{3}{5}\Delta_t - 2\Delta_s$. Finally Mn⁴⁺ an occupancy change of $t_{2g}^3 \to e^2 t_2^1$ with an associated energy change of $\frac{6}{5}\Delta_o - \frac{4}{5}\Delta_t$. Similarly, using the same arguments. It can be shown that $\Delta_O(Li\ layer) \le \Delta_s \le \Delta_O(M\ layer)$ for both Co⁴⁺ and Ni⁴⁺. Due to the extended lattice parameter predicted by the PBE+U method, this reduction of Δ_o would likely be exacerbated.

The exact Li-layer spacing in which this spin-transition is maintained for a octahedral complex in the Li layer could be measured by iteratively decreasing the Li layer

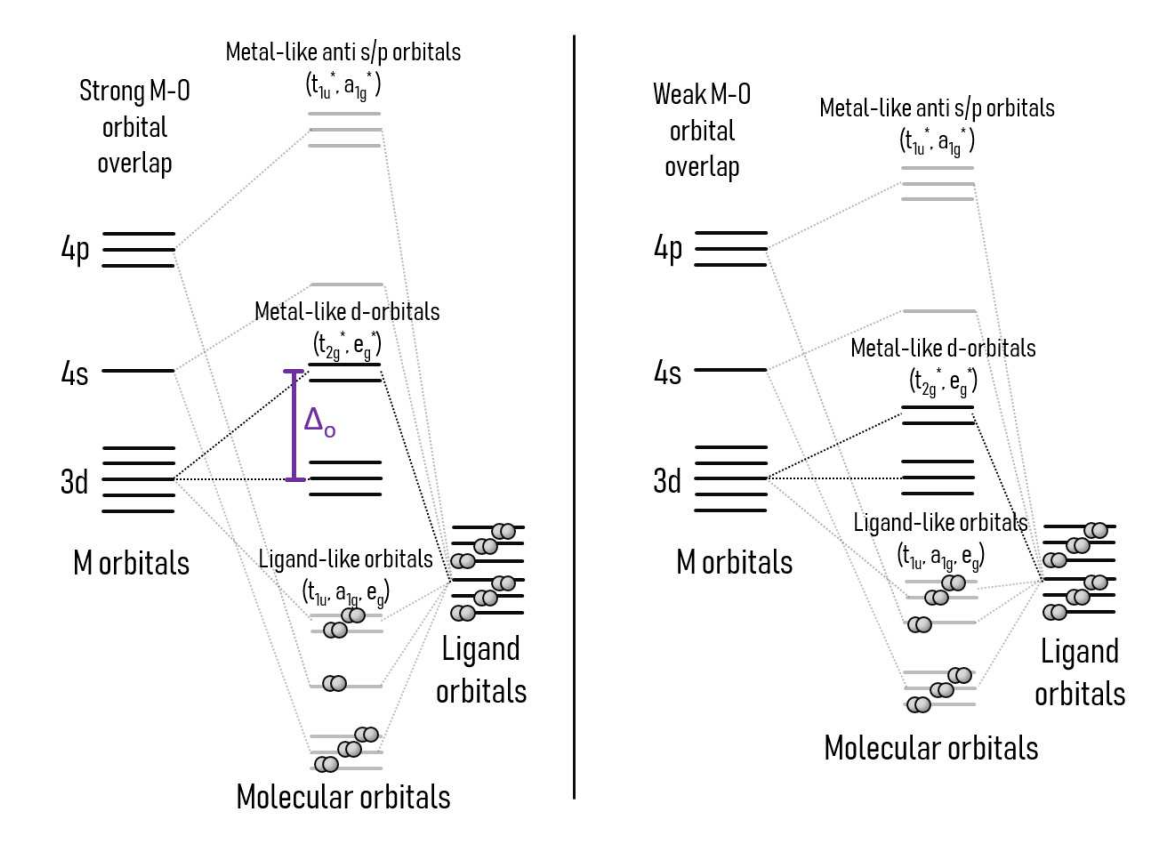


Figure 4.9: Qualitative molecular orbital diagram for a ML_6 octahedra. This diagram only illustrates σ bonding interactions. Typically t_{2g}^* and e_g^* have their superscript dropped when discussing transition metals. Left) ML_6 with strong orbital overlap. Right) ML_6 with poor orbital overlap.

spacing, however due to the relative energetic barrier for this degradation route (discussed in Section 4.2.2) this was not investigated.

4.2.2 Calculated minimum energy pathways for metal migration in Li₀MO₂

The calculated formation energies for the final Structure F was found to be substantially higher than the undefected Structure A for all three metals. These values are similar to those calculated by Reed and Ceder⁴. Their methodology differs in someways however, they opted to use a smaller unit-cell (6x f.u.) which is likely to feature some defect-defect interactions. Additionally, the functional of choice was a pure-PBE functional (as was common place at the time), which likely poorly predicts the lattice parameter.

It's found that the final structure (F) was calculated to be significantly higher in energy than the undefected structure for all metals (>2.5 eV) irrespective of functional choice.

The tetrahedral intermediate (E) is similarly large (>2 eV for Ni and Mn and >1.5 eV for Co). By "fixing" the lattice parameters of these structures the error between functionals is lost. This suggests that while dispersion corrections don't directly impact the formation energy of defects the calculated lattice parameters are important in accurately modelling such processes. These results are tabulated in Table 4.4 and indicate that both state E and F are unlikely to be long-lived intermediates in formation of the M_2O_4 spinel framework.

		CoO2	NiO2	MnO2
	DFT+U	1.98	2.73	2.72
E energy / eV	DFT+U-fixed	1.87	2.81	2.70
.	DFT+U+D3	1.82	2.83	2.63
F energy / eV	DFT+U	3.01	4.31	3.85
	DFT+U-fixed	2.95	3.79	3.69
	DFT+U+D3	2.84	3.85	3.75

TABLE 4.4: Defect energies at zero lithiation. state E is a Tetrahedral M defect in the Li layer. state F is a Octahedral M defect in the Li layer.

To calculate the minimum energy pathway, a linear interpolation of five images was taken between states A, E, and F with images spaced equidistant. For the open pathway (A \rightarrow E \rightarrow F), the initialised bands have midpoint images which feature the migrating metal between the shared polyhedral (O_h/T_d) face and has a trigonal planar M-O geometry. Whereas the shorter pathway (A \rightarrow F), the metal is edge-bound with a linear M-O geometry. The five image nudged elastic band method was performed between states (A \rightarrow E and E \rightarrow F) using force-based optimisers devised by Henkelmann et al 148,149 , with a force convergence criteria of > 0.085 eV/Å. These parameters have been demonstrated to be sufficient at locating transition states in similar materials ^{30,227}. Due to its nature, initial attempts at applying the nudged elastic band method onto the restricted pathway (A \rightarrow F) resulted in the central image instead migrating to the neighbouring tetrahedral site and thus being representative of the open pathway (A \rightarrow E \rightarrow F). Ceder and Reed, instead used an alternate restricted relaxation method, by redefining the crystal such that the edge-bound metal is located at the inversion centre of the cell, thus holding the transition state at an unstable equilibrium in 'a coin on its edge' fashion. Instead, an alternate approach was taken here. The migrating ion was fixed between the shared polyhedral edge and

neighbouring ions were free to relax. Using a low tolerance force convergence (> 0.35 eV/Å) large ion displacement was inhibited qualitatively reasonable results obtained.

Convergence was achieved in under 40 ionic steps for each image within the nudged elastic band. A spline curve was fitted between the intermediates with the calculated pathway being normalised to the energy of the undefected Structure A (see Figure 4.10). Similarly to Ceder and Reed, both the short (face-bound) and long (edge-bound) pathways feature a high energetic barrier, with a cumulative activation barrier > 3 eV for all 3 metals. In the case of the open path, there lies a "relatively stable" intermediate in which the metal occupies the T_d in the Li layer. However this defective structure still lies at-least 2 eV for all metals and as such is an order of magnitude higher than typical Li migration. The impact that functional plays on this pathway is minimal at best with transition state energies varying by less than 5%. For the pathway in which lattice parameters are "fixed" by using those calculated by PBE+U+D3 results in the results in slight changes in the MEP, qualitatively this results largely in the pathway shifting closer to that calculated by the PBE+U+D3 method and as such is an "intermediate" of the two methods.

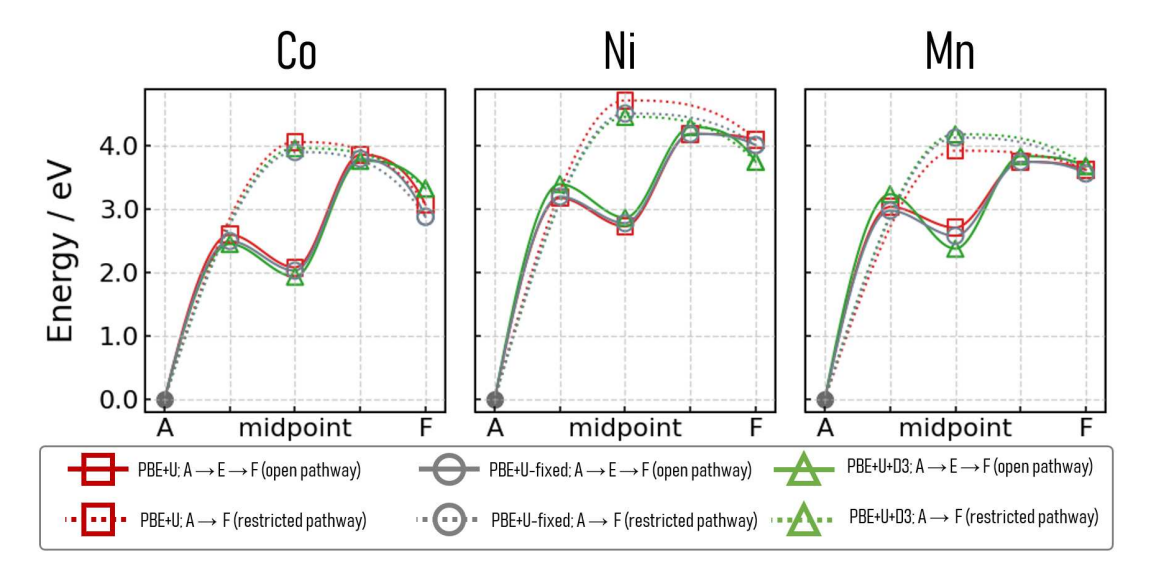


FIGURE 4.10: Calculated minimum energy pathways under various functionals as a metal migrates from an O_h site in the metal layer (State A) to an O_h site in the Li layer (State F). The open pathway features a relatively low lying intermediate as the metal occupies a T_d site in the Li layer (State E).

Overall similarly to Reed and Ceder, M⁴⁺ seems to be largely impervious to metal migration in these layered structures. The restricted pathway while shorter results in

extensive Coulombic repulsion and as such is infeasible as a valid migration route. The occupation of the tetrahedral site (state E) while more likely still suffers a large associated energy penalty for both Co, Mn and Ni which is due to the differing occupation of the d orbitals according to CFSE. Since both PBE+U and PBE+U+D3 largely predict the same electronic structure the resulting minimum energy pathways for this degradation route are largely un-impacted by functional choice with most of the differences between the functional able to be attributed to a varied lattice parameter.

Additionally, an alternate (yet similar) pathway to O_h defects exists. A layer shear (either before or after T_d occupation) of a MO₂ sheet would result in T_d sites becoming O_h and vice versa. Since the energy barriers between O2 and O3 stacking sequences have been demonstrated to be small in Section 3, further investigation detailing the energetics of this layer shear while defects are present would elucidate higher order phase transformation from point defects.

4.3 Transition state analysis at the dilute limit of lithiation

With prior work investigating the 'dumbbell structure' and its necessity to facilitate layered-to-spinel degradation, there is little investigation into this dumbbell formation at the dilute limit, that is as Li concentration reduces to near-zero. Of-course the end-member structure seen in Section 4.2 is incapable of forming a Li-M dumbbell as the Li concentration is zero. Instead a similar model structure denoted A_{1Li} in which a singular Li is placed in an O_h site within the Li layer (see Figure 4.11: A_{1Li}) is employed. Formation of a antisite has been discussed at half lithiation prior, albeit with conflicting pathways. Ceder and Reed⁴ investigated Metal migration into a neighbouring tetrahedral site in the Li layer followed by Li migration. Constrastingly, Seymour et al³ proposed dumbbell formation is initiated via migration of the Li ion followed by the metal (i.e the reverse pathway). Due to the facile nature of Li mobility as well as the relative thermodynamics of T_d Li vs. O_h Li, both pathways will be contributing to the total path regardless of the relative kinetics of each path. It's an

expectation that in reality the pathway is likely to be concerted in nature. While the two publications disagree on the order of steps in the pathways, both publications agree that metal occupation of a T_d site in the Li layers incurs a substantial energetic penalty if any of its faces are shared with a cation. Which of-course for this near end-member is a non-factor as their are no other neighbouring Lithium in the Li layer.

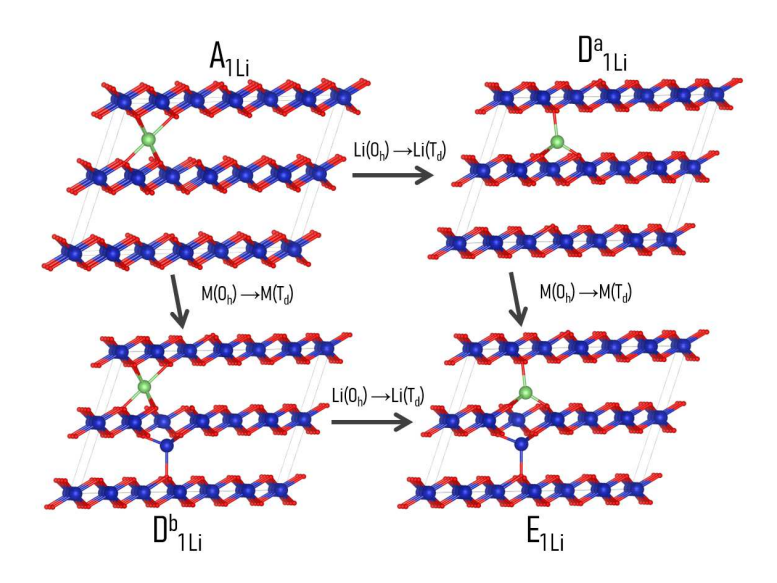


FIGURE 4.11: Suggest pathways for dumbbell formation at the dilute limit. Pathway $A \to D^a \to E^3$ is Li migration followed by M migration. While Pathway $A \to D^b \to E^4$ is the reverse pathway.

4.3.1 Structure of intermediates at the dilute limit

The crystals structures used for Section 4.2 were generated with a Li ion placed at the center of the O_h and T_d site in the Li layer (A_{1Li} and D^a_{1Li} in Figure 4.11 respectively). Similarly to Ceder and Reed⁴ the intermediates featuring T_d metal (D^b_{1Li} and E_{1Li}) was initialised by placing the metal ion at the T_d center within the Li layer. This dumbbell structure is characterised by a cooperative interaction of these T_d cations across a vacancy.

These structures were geometry optimized with the unit cell fixed at their delithiated lattice parameters to model the dilute limit of lithiation. Introduction of Li into the Li layer results in minimal ionic distortion (> 0.050 Å) of neighbouring ions and the planar MO₂ sheets remain intact. Both the PBE+U and PBE+U+D3 functionals used for the zero-Li end-members were employed with a plane wave cut-off of 550 eV.

For state A_{1Li} , the structure is initialised such that the Li ion is located at the center of a O_h site in the Li layer. This LiO₆ shares corner connectivity with six metals (where M-O-Li-O-M $\approx 180^\circ$). However, due to the extended Li layer, the LiO₆ octahedra is distorted to span this large layer spacing. Figure 4.12 shows that this distortion reduces the local symmetry about this site from the O_h point-group O_h to a D_{3d} point-group O_h as the angle between Li-O bonds spanning the Lithium layer deviate from 90° .

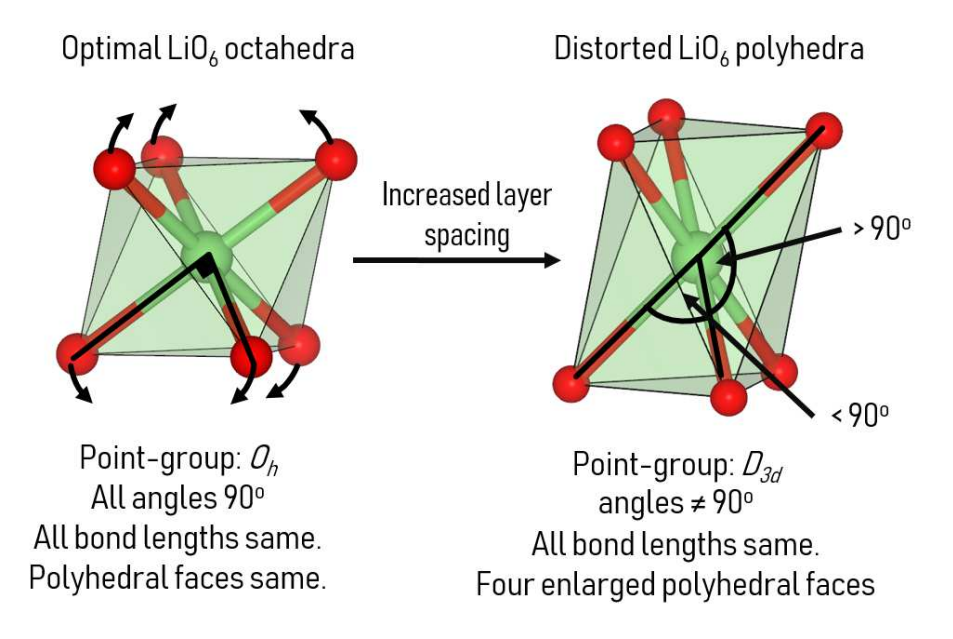


FIGURE 4.12: Expected distortion of a octahedron that spans an enlarged Li layer.

Figure 4.13i, shows the initialised geometry for state A_{1Li} ($Li_1Co_{36}O_{72}$ shown as example), in which the Li ion lies at the center of the distorted octahedra. If the charge from the Li ion was distributed evenly throughout the structure it would impart an change in oxidation state for each metal ion of $-\frac{1}{36}$ per f.u. Perhaps more expected would be for this charge would be localised in a around the defect. In this case, localisation would be around the Li site, since this structure (A_{1Li}) has an inversion center at the center of this site, the effected ions would be expected to incur this oxidation change evenly around this inversion center (with the charge being distributed symmetrically through the Li-O-M-O connectivity of the structure). However as seen in Figure 4.13ii, upon relaxing the structure, the symmetry is broken with the Li ion preferentially relaxing toward the LiO₆ polyhedral edge, shortening a two Li-O bonds and the Lithium lying closer to a lone metal. While not a large

deformation (<0.2 Å) this migration impacts the oxidation state of the nearby metal site with the near metal ion being M^{3+} . In the case of the Cobalt system, this is evidence by the metal ion becoming spin neutral as the valence changes from Co4+ to Co3+ filling the low-lying t_{2g} orbitals (see Figure 4.13iii). This same redox activity has been observed for both Nickel and Manganese in this low concentration model, with the near metal ion being M^{3+} .

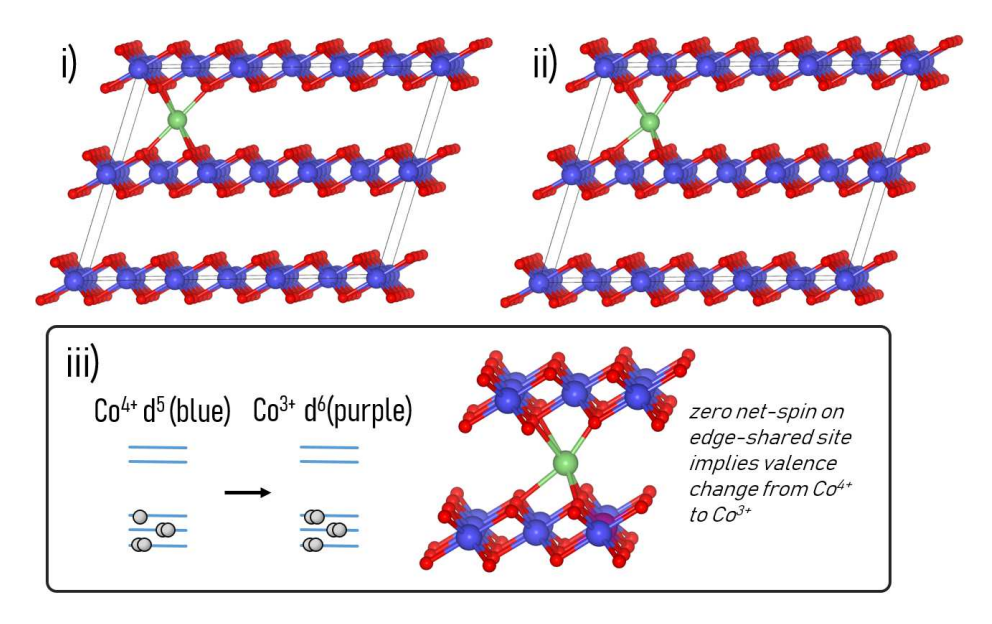


FIGURE 4.13: i) Initialised structure for a near-zero Li metal oxide, the Li is placed in the center of the pseudo-octahedral site. ii) Relaxed geometry for a near-zero lithiated metal oxide. The Li ion has migrated towards the octahedral face. iii) Resulting spin density of the close (edge-shared) metal site at initialisation and relaxation of the structure.

Similarly to state A_{1Li} the large layer spacing results in distorted occupation of the T_d site for state D_{1Li}^a . This distorted tetrahedral site has point-group symmetry of C_{3v} and the central site can rest somewhere between two extremes. In this enlarged spacing the Li ion can relax either toward the triangular face with a corresponding reduction in three Li-O bond lengths (Figure 4.14i) or the Li ion relax away from the triangular face with elongation of these three Li-O bond lengths (Figure 4.14ii).

For all three metals the calculated Li-O bond lengths indicate that the Li site preferentially relaxes downward to the shared metal face (Figure 4.14i). As seen in Table 4.5 the extent of this relaxation onto the shared face would initially appear functional dependent. However only the long Li-O bond changes significantly. While the pure-PBE functionals enlarged layer spacing results in the long Li-O bond

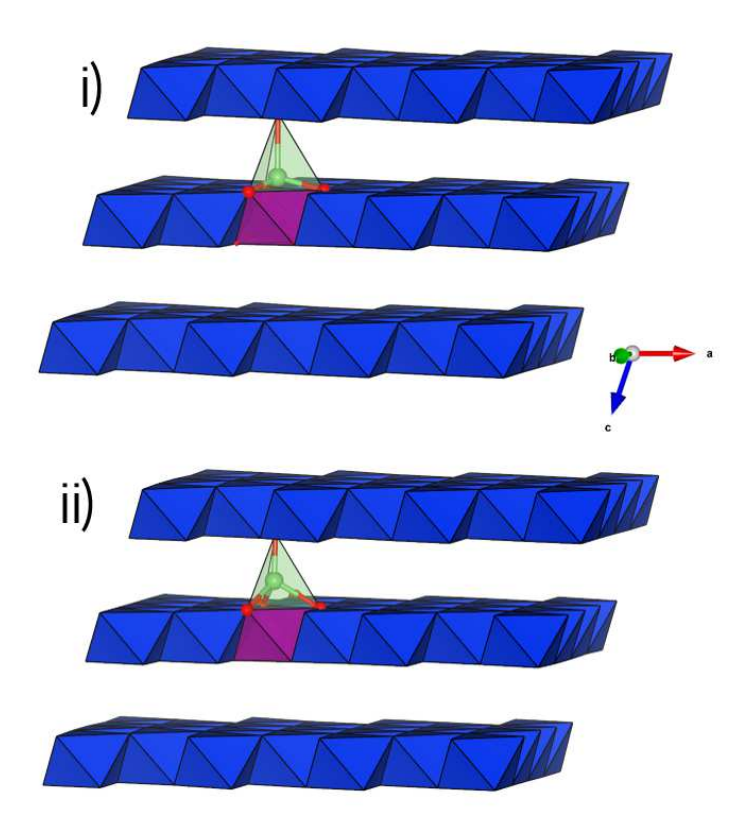


FIGURE 4.14: The Li ion in State D^a_{1Li} can lie between one of the two extreme states, i) the Li ion relaxes toward the MO_2 sheet. ii) the Li ion relaxes away from the MO_2 sheet.

spanning the layer being severely elongated (+15%), the length of the three shortened Li-O bonds however are similar between functional. This indicates there is no effective Li-O bond across the layer spacing, with the Li being effectively 3-coordinate. This relaxation into MO_2 layer results in a small displacement of the face-shared metal results. This indicates that the nature of dumbbell formation at the dilute limit is concerted to some degree and that T_d Li may facilitate metal migration. Similarly to the O_h state (A_{1Li}), this tetrahedral Li imparts a valence change on the shared metal face.

As indicated by the Figure 4.5 integrating the spin density around this displaced metal site indicates a valance change from the typical 4+ that is seen on all other metals to 3+.

Relaxation of the intermediate structure from the pathway suggested by Reed and Ceder⁴ (D_{1Li}^b) showed further migration from the O_h center to the shared-face for all three metals regardless of functional choice. While not discussed by Ceder and Reed their methodology used symmetry constraints (and a differing concentration of Li)

System	Li layer spacing / Ang	Li-O bond lengths (state D) / Ang	Metal displacement (state D) / Ang
Cobalt (PBE+U)	2.96	$3 \times 1.85 \ 1 \times 2.06$	0.24
Cobalt (PBE+U+D3)	2.61	$3 \times 1.821 \times 1.88$	0.28
Nickel (PBE+U)	3.05	$3 \times 1.87, 1 \times 2.25$	0.26
Nickel (PBE+U+D3)	2.58	$3 \times 1.84, 1 \times 1.91$	0.30
Manganese (PBE+U)	2.98	$3 \times 1.96, 1 \times 2.23$	0.43
Manganese (PBE+U+D3)	2.68	$3 \times 1.98, 1 \times 2.04$	0.50

TABLE 4.5: Calculated Li-O bonds near the dilute limit for the tetrahedral Li system (D_{11i}^a) .

effectively freezing Li ions and as such it's unlikely they would've have discovered this effect. This migration is toward the T_d site opposing the Metal and as such these structures actually lie somewhere between state D_{Li}^b and state E_{1Li} . As a result the calculated intermediate energy (and corresponding MEP) is concerted in nature.

It would be possible to restrict the mobility of the Li ion as to remain within the center of the psuedo-octahedral site. This would yield insight into the impact of edge-shared Li-M polyhedra on the energetics of T_d metal defects. However, due to the high mobility of Li ions this was dismissed as it would not be representative of the cathode material in reality.

4.3.2 Electronic structure and calculated minimum energy pathway at the dilute limit of delithiation

The relative defect energies were calculated with respect to the O_h single Li structures (A_{1Li}) . The defect energies of the T_d Li states (D^a) is small (near zero for Co and Ni and < 0.25 eV for Mn) and aligns with literature values seen for similar structures 3,37 . In particular Kang et al 37 demonstrated that at 'equilibrium layer spacings' tetrahedral Li is stressed and at an enhanced layer spacing (i.e those seen here) this stress is relieved, with the site energy reducing to zero as the Li become a surface-bound free ion. Such process is not observed for the Mn system and further elongation may be needed to see this effect.

For all three metals systems, it was found that T_d metal defects (states D_{1Li}^b and E_{1Li}) are destabilised with respect to state A_{1Li} irrespective of functional choice within the

parent delithiated lattice. Interestingly, in comparison to the zero-Li systems investigated prior, this degree of destabilisation is significantly reduced. In particular a T_d metal defect in the Mn systems is reduced from ≈ 2.7 eV to 0.7 eV with the inclusion of a cooperative Li dumbbell. Typically, degradation of Mn cathodes has been attributed to the low-energy of Mn $O_h \rightarrow T_d$ 'hops', however typically this is the result of a charge disproportionalition reaction ($2Mn^{3+} \rightarrow Mn^{2+} + Mn^{4+}$) that is facilitated at half lithiation 3,4 . This process requires two nearby Mn^{3+} ions and as such should be increasingly rare at low Lithium concentrations. This model system used here however, features only a singular Mn^{3+} per unit cell and as such no charge disproportionation is possible.

Similarly, the T_d M defects without a cooperative dumbbell (state D_{1Li}^b) present a reduction of destabilisation (albeit to a lesser extent). This indicates that even edge shared Li/M polyhedra impact the nature of metal migration and that the cooperative dumbbell may not be a necessary feature in cathode degradation. Table 4.6 summarises these defect energy normalised to state A.

System	Δ Energy (state D^a) / eV	Δ Energy (state D^b) / eV	Δ Energy (state E) / eV
Cobalt (PBE+U)	0.03	1.64	1.22
Cobalt (PBE+U+D3)	0.14	1.50	1.05
Nickel (PBE+U)	0.07	1.76	1.41
Nickel (PBE+U+D3)	0.08	1.56	1.301
Manganese (PBE+U)	0.22	0.94	0.68
Manganese (PBE+U+D3)	0.12	1.22	0.76

TABLE 4.6: Calculated energies (normalised to state A) for defects at the near-delithiated end-member.

While, no such disproportionaiton reaction can occur the close proximity of a lone Li ion to a metal site results in a formal valence change of the migratory Metal ion from 4+ to 3+. This is observed for both the Li-M face shared structure (state D^a_{1Li}) and the undefected structure (state A_{1Li}). The change in d-states can be mapped for this structure as the dumbbell is formed. Figure 4.15 shows the change in d-states across the two discussed pathways for a Co ion near zero-lithiation. With no Li present, the system is charge neutral and therefore the metal ions lie in a +4 oxidation state. Relaxation of Li-ion into a Octahedral site in Li layer results in a symmetric breaking

of the structure as the metal migrates toward the polyhedral edge. This induces a valence change on the near edge-shared metal (from +4 to +3). Ceder and Reed⁴ discuss the prevalence and energetics of a Li-Mn²⁺ dumbbell, however the work here suggests that a slow process exists in which an unstable yet feasible Li-Mn³⁺ dumbbell forms which is free to degrade further into spinel.

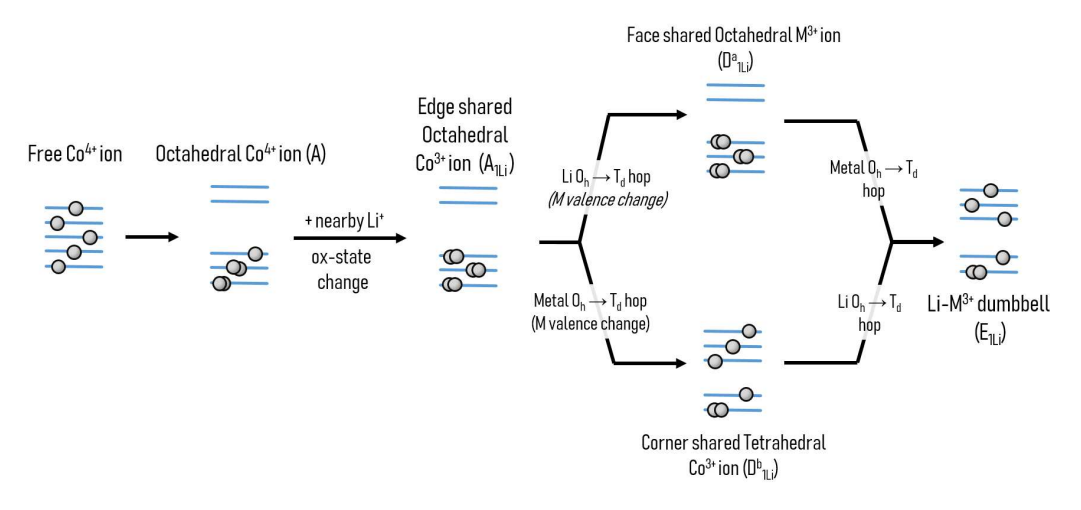


FIGURE 4.15: The change in d occupation for a Co ion in various states. The change in chemical environment/geometry can often have an associated spin moment change.

When modelling this metal migration as simple tetrahedral defect reaction M_{oct}^{3+} (M layer) $\to M_{\text{tet}}^{4+}$ (Li layer), Pauling's first rule would predict lower tetrahedral defect energies in fully delithiated systems opposed to these near-zero systems since +4 cations have smaller radii than the +3 cations. However, It appears that for these layered metal systems ionic size effects do not play a significant role in the preference for O_h or T_d occupancy. Instead, valence and electronic structure are more decisive factors in the site preference of metals in layered structures within a cubic-close packed oxide framework. 229

Similar to the zero-Li systems the energy penalty for the T_d defect in both pathways can be estimated from crystal field theory. However with the caveat that the spin density predicts that the close proximity of an Li ion results in a valence change of the migrating metal from M^{4+} to M^{3+} . This results in an additional electron occupying the d-orbitals. For Co^{3+} the tetrahedral defect reaction has a change in crystal field splittings as $t_{2g}^6 \rightarrow e^3 t_2^3$ and therefore results in a penalty of $\frac{12}{5} \Delta_o - \frac{3}{5} \Delta_t - 2\Delta_s$. Ni³⁺ has a filled t_{2g} orbital and a singular electron in the destabilising e_g and therefore the

tetrahedral defect reaction is: $t_{2g}^6 e_g^1 \to e^4 t_2^3$ with a penalty of $\frac{9}{5}\Delta_o - \frac{6}{5}\Delta_t - \Delta_s$. Finally, O_h Mn³⁺ has four high spin electrons occupying the d orbital and therefore the the tetrahedral defect reaction is: $t_{2g}^3 e_g^1 \to e^2 t_2^2$ and a penalty of $\frac{3}{5}\Delta_o - \frac{2}{5}\Delta_t$. All metals show a spin change between O_h and T_d metal structures that align with those predicted via crystal field theory implying that modelling the process as a defect reaction is valid as first order approximation.

The chemical system has changed (both formula unit and valence) between the zero Li and near-zero Li models, and as such Δ_o would change. Therefore direct comparison of energy penalties is not possible. However using $\Delta_t = \frac{4}{9} \Delta_o$ and assuming an insignificant change in Δ_o between systems, the energy penalty for T_d defect in Low-Li concentration Mn cathodes is reduced upon a valence change induced by a nearby Li (from $\frac{38}{45}\Delta_o$ to $\frac{19}{45}\Delta_o$).

Calculation of the minimum energy pathway across these relatively stable intermediates was achieved via the nudged elastic band method. Similarly to the methodology for the zero-Li systems, the 5 image nudged elastic band method was performed between these stable structures using force based optimisers and a force convergence criteria of $< 0.085 \, \text{eV/Ang}$. The resulting pathway models two distinct $O_h \to T_d$ "hops" and as such the midpoint images feature face-bound cations (with trigonal planar geometry). The method has been shown to be poor for concerted processes, often migrating individual ions sequentially, since both the hops were demonstrated to somewhat concerted this caveat in taken into consideration. Convergence was achieved in under 40 ionic steps for each band. A spline curve was fitted between the intermediates with the calculated pathways being normalised to the undefected Structure A_{1Li} .

Figure 4.16 shows the the minimum energy path for dumbbell formation using the mechanistic steps described by Seymour et al³. Both the PBE+U and PBE+U+D3 methods qualitatively align with normalised defect energies lying < 0.2 eV between the functionals. Li migration (A \rightarrow D^a) is low energy with transition state being found on the midpoint image, where the Lithium ion lies in the shared O_h/T_d face and has trigonal planar coordination to oxygen. Similarly to Kang et al³⁷ this transition state

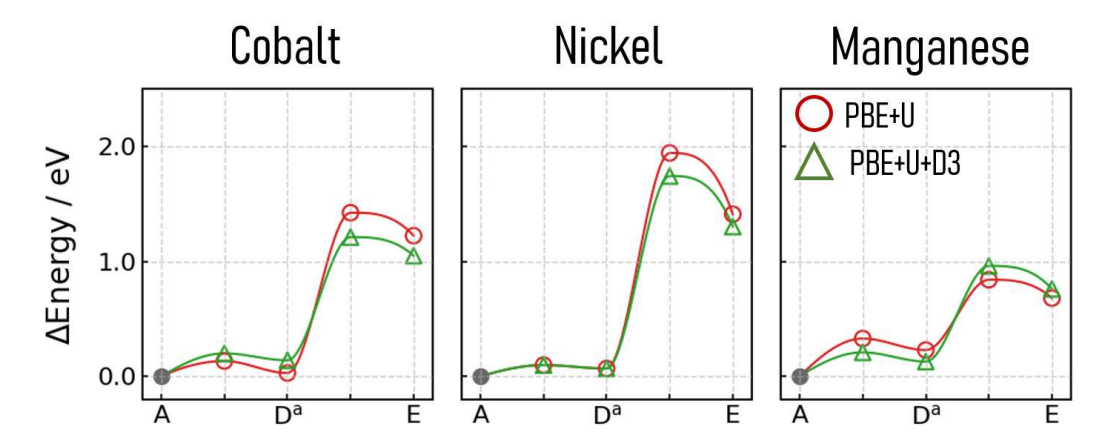


FIGURE 4.16: Calculated minimum energy pathway from the undefected structure structure (A) through intermediate D^a to the dumbbell structure formation at the dilute limit of lithiation for Co, Ni and Mn systems. This pathway is characterized by a $O_h \rightarrow T_d$ Li migration followed by a $O_h \rightarrow T_d$ Metal migration.

has a energy penalty similar to a T_d defect. Since these materials intend to be highly mobile in Lithium these results are as expected. Interestingly, even just a small concentration of Li may act as a nucleation site for degradation as the transition state energy for metal migration is significantly reduced (in comparison to similar structures in the prior section). However, these values are still significantly large for both the Cobalt and Nickel systems. This in conjunction with a destabilised final state implies that the dumbbell structure is short lived and further degradation to spinel will be slow.

The transition state energy for the Mn dumbbell for these near-zero lithiated systems is similar to the activation barrier for Li migration (< 1 eV). This suggests that dumbbell can form in pure Mn cathodes regardless of state of lithiation. While the Li-Mn²⁺ ion has been demonstrated by Ceder and Reed to be significant in forming the Mn dumbbell (with a negative formation energy)². The low lying formation energy and feasible activation barrier implies that this alternative dumbbell will form at low Li concentrations in which further degradation to the stable Spinel structure is facilitated.

The pathway suggested by Ceder and Reed shows little dependence on functional choice. This suggests that both Li and Metal migration is not dependent on van der Waals interactions. A larger transition state energy for metal migration ($A \to D^b$) is observed in comparison to the alternate pathway. The transition states (i.e face bound

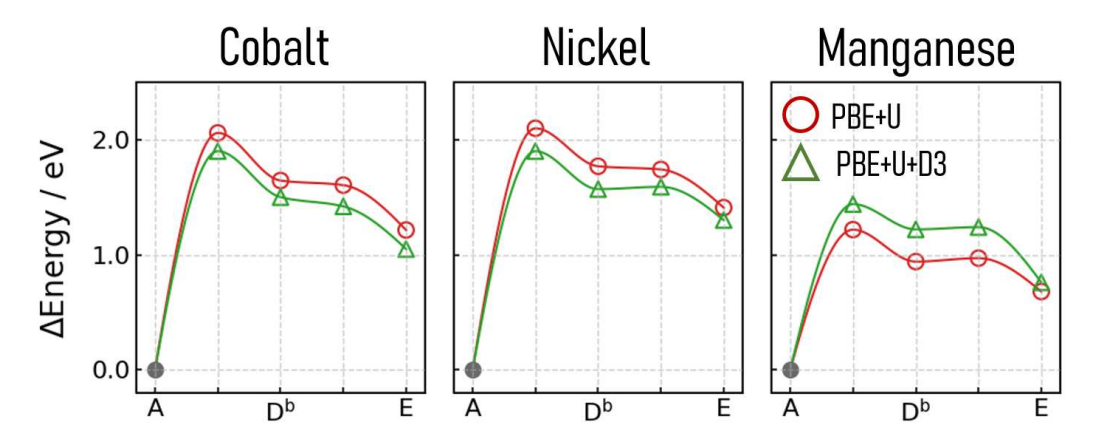


FIGURE 4.17: Calculated minimum energy pathway from the undefected structure structure (A) through intermediate D^b to dumbbell formation at the dilute limit of lithiation for Co, Ni and Mn systems. This pathway is characterized by a $O_h \to T_d$ metal migration followed by a $O_h \to T_d$ Li migration.

metals) lie at > 1.5 eV for Co and Ni and > 1 eV for Mn. A similar trend is observed for the Mn system in this pathway, in which T_d Mn³⁺ is still destabilised but at a much decreased energetic barrier compared to the zero-Li systems studied prior. Interestingly the second half of this pathway is spontaneous with zero transition state energy. This implies that a isolated Tetrahedral metal defect effectively drags nearby Li into the opposing tetrahedron locking them into this configuration as a means of stabilisation. While interesting, the rapid dynamic 'hopping' of Li ions means first part of the Seymour pathway is always active and the pathway by Ceder and this effect is unlikely to be critical.

In summary the presence of a neighbouring Li ion impacts the feasibility of both metal migration and dumbbell formation significantly even at low Li concentrations when M^{3+} isolated. This uncovers a new route in cathode degradation at a Li concentration previously considered resistant. At exceedingly low Li concentrations the ions preferentially relax away from the center of the O_h sites to form a cooperative Li- M^{3+} interaction with a metal with a shared polyhedral edge. The barrier for Li migration to a tetrahedral site is small and as such can feasible migrate into the the tetrahedron of which the $M^{3+}O_6$ polyhedron shares a face. In both the edge-shared and face-shared states metal migration and dumbbell formation is significantly reduced. This is exacerbated for the Mn system in which Mn^{3+} has a low crystal field penalty for an O_h $\rightarrow T_d$ defect reaction. This suggest that layered LiMnO2 cathodes are susceptible this

degradation route (albeit slower) even at Li concentrations previously described at resistant.

4.4 Transition state analysis at half lithiation

At half lithiation layered to spinel (LiM₂O₄) degradation through a dumbbell intermediate has been investigated in detail prior. In particular the work by Ceder and Reed^{2,4} investigates the role that electronic structure imparts on the degradation of meta-stable structures. Similarly to Section 3 it's suggested that layered cathode materials with formula unit Li_xMO₂ are meta-stable to a transformation to spinel for all 3d metal at a range of lithiations, in particular half lithiation. However, degradation is slow unless a low energy dumbbell structure is obtained, which is only observed for the Mn system. This dumbbell has been described as low energy due to a beneficial charge disproportionation reaction for Mn³⁺. More recently, Seymour et al³ used a Hybrid Eigenvector-Following method to investigate this Mn system in detail. It's concluded that the nature of this stable Li-Mn dumbbell is sensitive to the choice of modelling techniques, in particular defect-defect distance (in which a $3 \times 3 \times 2$ unit cell proved sufficient to ensure no interactions) and choice of Hubbard U in which a larger Hubbard U value destabilised the intermediate. In a follow up paper⁷ attempts to inhibit this dumbbell structure through trivalent dopant effects (Al³⁺, Cr³⁺ etc) showed moderate success.

While utilising different methods and principle structures both publications agree that tetrahedral metal defects are inhibited if the T_d site shares a face with any cation. This results in metal migration being a statistical non-factor at high degrees of lithiation where the likely-hood of trivacant tetrahedral sites becomes exceedingly rare or require numerous Li $O_h \to T_d \to O_h$ 'hops' to form. Figure 4.18 demonstrates how a particular arrangement of Li impacts the potential available sites for degradation, viewing the structure down the c axis shows hexagonal arrangement of O_h and T_d sites in the Li layer, if any of the three neighbouring O_h sites is occupied the T_d defect

reaction in unfeasible at this site. Of-course this has the caveat that these materials are dynamic in their Li arrangement and concentration especially during cycling.

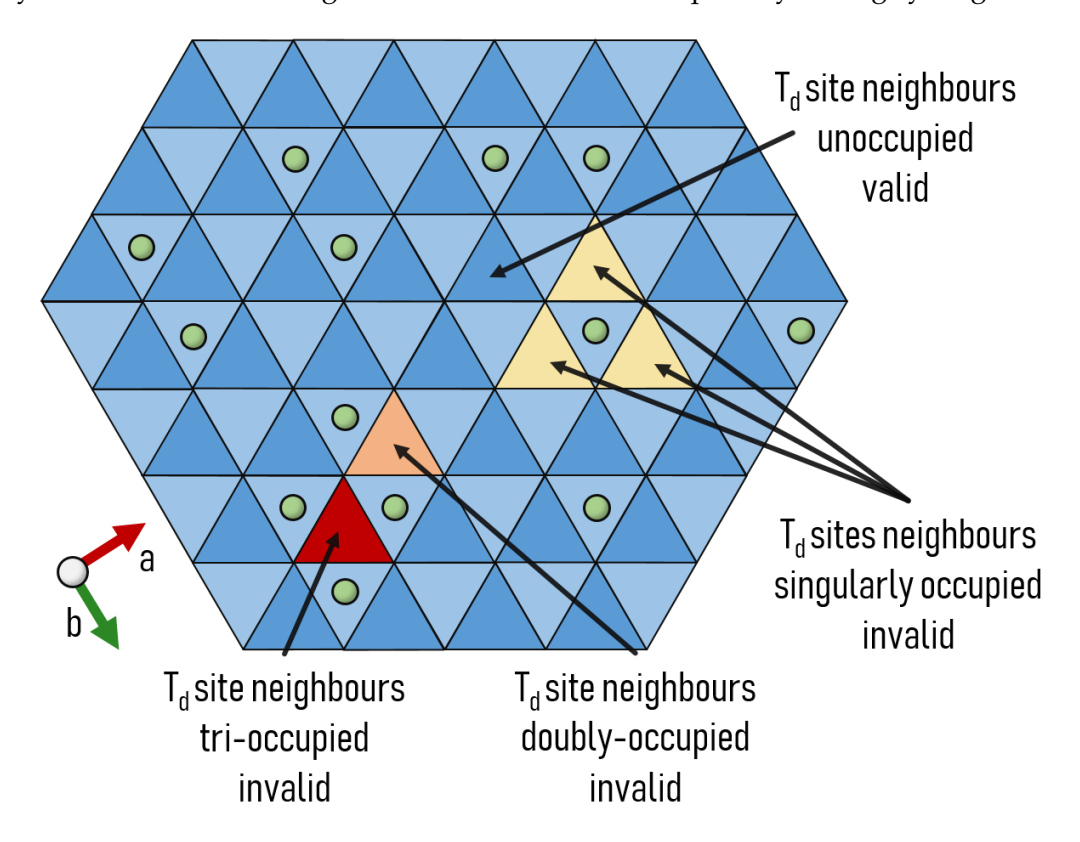


FIGURE 4.18: Metal Oxide cathode as as seen looking down the c-axis. $O_h \to T_d$ metal migration into the Li layer is only possible when the T_d site has no O_h neighbours (i.e all faces unshared).

4.4.1 Structures of intermediates across pathway

Considering all possible ${\rm Li^+/V_{Li}}$ orderings at half lithiation, in principle yields an infinite number of potential structures. Prior work ¹⁸⁸ (Section 3), however, has identified the high symmetry structure belonging to the P2/m space group to be low energy for ${\rm Li_{1/2}MnO_2}$, the structure has alternating ${\rm Li^+/V_{Li}}$ chains across the b-axis and features a charge ordering of ${\rm M^{3+}}$ and ${\rm M^{4+}}$ aligned with the ${\rm Li^+/V_{Li}}$ ordering as seen in Figure 4.19.

In Figure 4.19 the crystal structure shown is $\mathrm{Li}_{1/2}\mathrm{MnO}_2$ which features a strongly Jahn Teller distorted Mn^{3+} species and as such the crystal structure is heavily Jahn Teller distorted resulting in a large disparity between vacancy site size and Li site size. Constrastingly the Co and Ni are largely undisturbed by Jahn Teller distortions. The

 MO_6 polyhedra for both the Cobalt and Nickel systems are relatively undisturbed from regular octahedrons at half lithiation, with the M-O bond lengths varying by 2% and 9% for Cobalt and Nickel polyhedra, respectively. Due to the large Jahn Teller effect of LiMnO₂, however, the distortion away from a regular octahedron in the Manganese systems is much more pronounced with M-O bond lengths varying by 15% (1.97 - 2.28 Å). This Jahn Teller effect has been shown to result in an asymmetric planar lithium migration, where migrating along the b-axis has a large energetic barrier⁷.

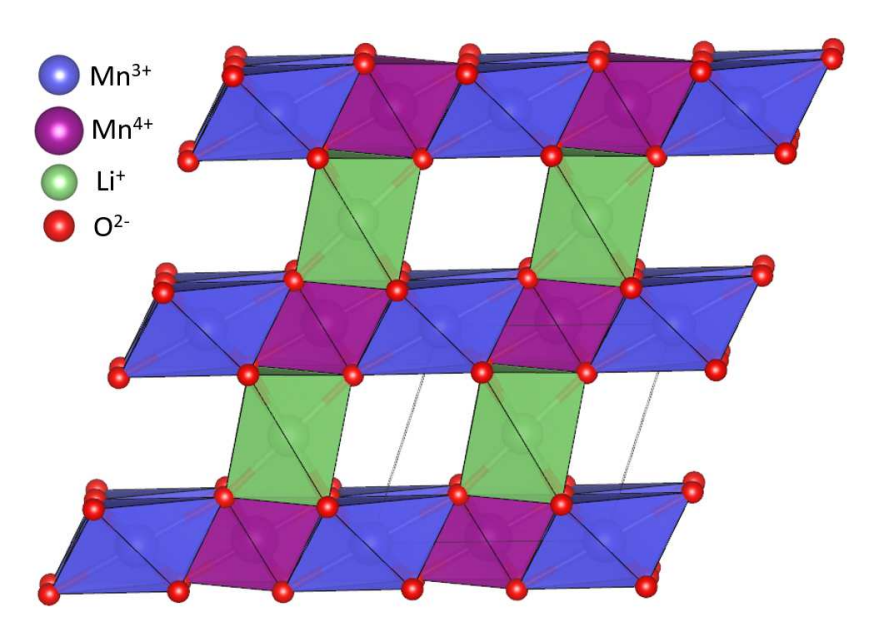


FIGURE 4.19: The P2/m structure of $\text{Li}_{1/2}\text{MO}_2$ has been previously identified as low energy, Li^+ and V_{Li} alternate across the a-axis of the structure, resulting in vacancy channels across the b-axis. With a charge ordering of Mn^{4+} and Mn^{3+} ions running parallel to these channels.

While PBE+U and PBE+U+D3 have predicted differing lattice parameters, they largely align with the experimental results at half lithiation. The calculated lattice parameters converted of these structures using the PBE+U functional can be found in Table 4.7.

	$Li_{0.5}CoO_2$	$Li_{0.5}MnO_2$	$\text{Li}_{0.5}\text{NiO}_2$
A / Å	4.812	5.315	4.948
B / Å	2.845	2.901	2.786
C / Å	5.075	5.182	5.123
β / degrees	106.58	108.44	108.20

TABLE 4.7: Relaxed lattice parameters of $\text{Li}_{\frac{1}{2}}\text{MO}_2$ within the P2/m framework.

Dumbbell formation has been shown to have a lower activation barrier when the Lithium migrates first for near-zero Li systems. While, Reed and Ceder² proposed metal migration as the first step, Li migration is labile and thus likely to be the predominant first step. As a result, the pathway suggested by Seymour was chosen to be investigated. Their methodology utilises five distinct structures (see Figure 4.20) starting from the known low-energy P2/m structure. Steps $A \to B \to C$ is a $(O_h \to T_d)$ → O_h) Li rearrangement from the highly ordered Li⁺/V_{Li} structure to the low symmetry structure of a lone lithium in an octahedral site (C) in the vacancy chain. This step is necessary step to leave a trivacant tetrahedral site for future metal migration. Structures A and C are differing configurations within the Li_{1/2oct}MO₂ fixed to the same parent lattice (found by relaxing structure A). Steps $C \to D \to E$ features a lithium migration to the dumbbell site $(O_h \rightarrow T_d)$ across the metal plane from said trivacant site followed by a metal migration step $(O_h \rightarrow T_d)$ within the lithium layer. This process has been demonstrated to be somewhat concerted at zero-Li, with occupation of the T_d site resulting in a small displacement of the face-shared metal ion.

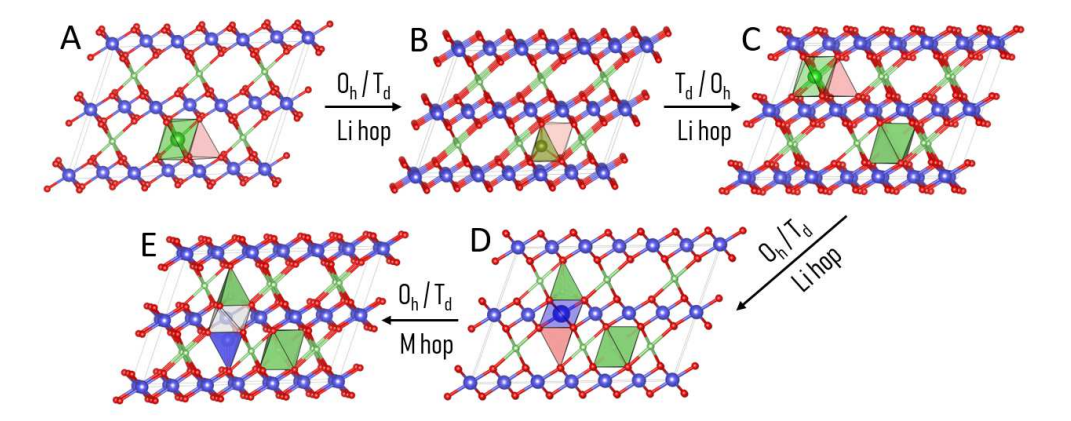


FIGURE 4.20: The principle pathway for dumbbell formation, is a multi-step process featuring many O_h - T_d 'hops'. Starting from the P2/m a lithium migration is required to free the dumbbell site of neighbouring lithium. Migrating ions are indicated via shaded polyhedra. Adapted from Seymour et al.³

Seymour et al 3 also discuss an additional intermediate between steps D and E which is characterised by the metal ion entering a pseudo square-pyramidal structure this intermediate lies < 20 meV below the transition state and as such would be short lived and unlikely to be found via the nudged elastic band method. All structures are

were initialised with ions placed at the center of their polyhedral sites. These sites are moderately distorted at half lithiation due to charge ordering effect.

Lattice parameters are modelled well between functional (PBE+U vs PBE+U+D3) and dispersion interactions has not been shown to be necessary in predicting the energetics or structure of any particular T_d defect. As a result the spin-polarized PBE+U functional was used to reduce computational cost, with a plane wave cutoff of 600 eV. This choice of plane wave cutoff is to align with those seen in the literature^{3,7}. A 3 × 3 × 2 supercell of the relaxed P2/m structure seen in Figure 4.19 was used for the defected structures and has been previously shown to be sufficiently large³ to expect near zero defect-defect interactions. Unit-cells were fixed across between intermediates at the lattice parameters of the undefected structure. A 2 × 2 × 1 K-point grid has been shown to sufficiently model the electronic properties of similar systems this size³.

State A, B and C are steps along a divacancy mechanism and thus related by Li T_d/O_h hops. Similarly to the near-zero Li case and work by Seymour et al, migration of a Li ion into the T_d site within the vacancy chain (state B) results in a strong repulsion which is compensated by a moderate displacement of the face-shared Metal ion downward 3,37 . Due to the occupied neighbouring octahedrons this metal site is inhibited from further migration into a Li-M dumbbell, requiring further Li migration. Tetrahedral Li is a common feature during Li migration (both charge and discharge) and as such these state are prevalent throughout cathode material. The imparted displacement of metal ions within the MO2 sheet indicates an associated structural sensitivity during cycling. Interestingly the scale of this displacement is largest for the Mn systems and further migration to the O_h site within the vacancy chain (state C) relieves much of this displacement. This effect is shown in Figure 4.21 and summarised metal displacements can be found in Table 4.8.

	Cobalt	Nickel	Manganese
M displacement (B)/ Å	0.13	0.26	0.42
M displacement (C) / Å	0.03	0.07	0.19

TABLE 4.8: Displacement of face-shared metal ion for state B and state C.

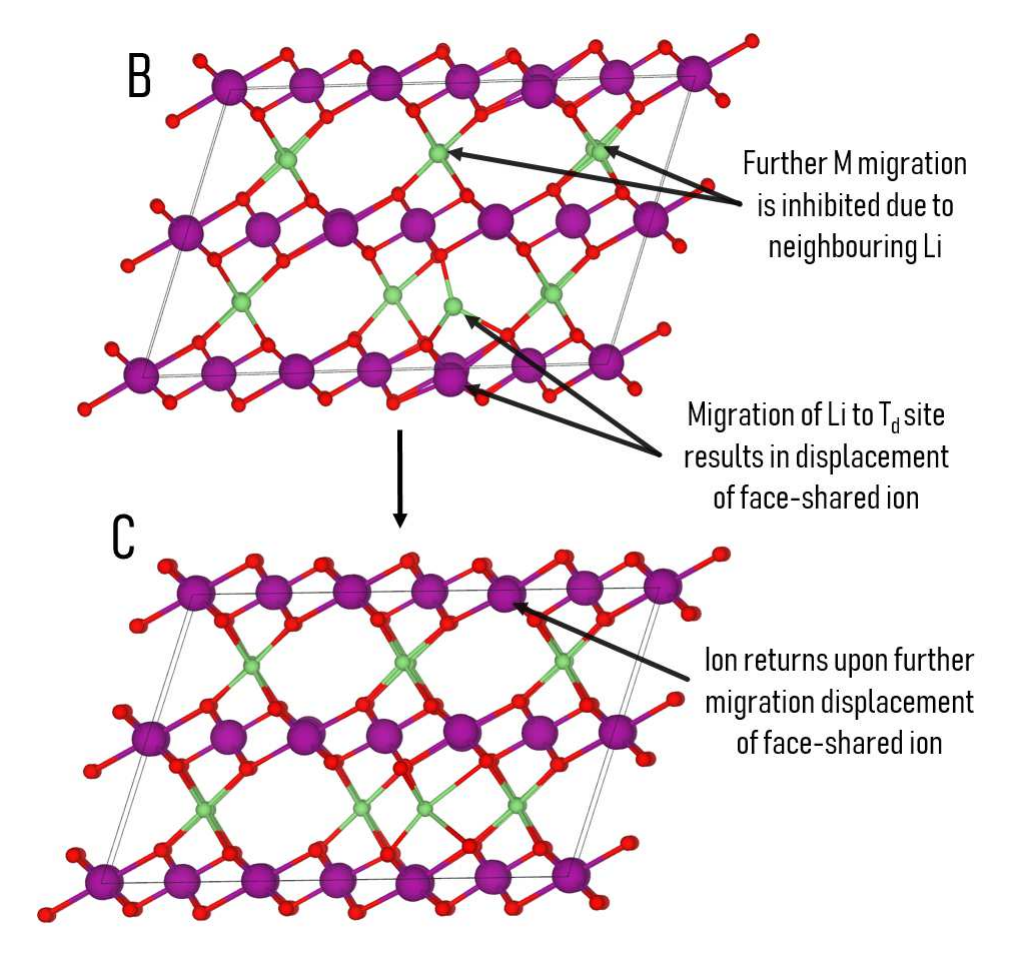


FIGURE 4.21: States B and C are related by an $T_d \to O_h$ Li migration. The T_d Li in state B induces a significant displacement of the metal site in the layer below. This is displacement is alleviated upon Li migration to the O_h site (C).

Both state B and C are destabilised with respect to the high symmetry structure A, this is expected since this structure was determined to be low lying in Section 3. Both these states are low-lying with defect energies < 0.25 eV for all three metals, this falls in the range of typically quoted Li migration energies for Li and indicates that this Li migration behaves as expected for this system³⁷. The fixing of the unit cell results in the vacancy plane remaining elongated and the bond lengths of the migratory Li in state C being elongated. Interestingly, similarly to the near-zero Li case, this ion breaks the local symmetry for all three metal systems, preferentially relaxing toward the polyhedral face of between the initial O_h site in state A and the optimal site in state C. This is likely to compensate the newly formed vacancy in the Li chain. More importantly, the Mn system maintains it's charge ordering of Mn³⁺ and Mn⁴⁺ ions in chains along the b-axis is maintained throughout this Li transformation. This results in a breaking of the 180° Li-O-M³⁺-O-Li network (briefly discussed in Section 3) and a

reduction in the stabilizing hybridization. These two effects result in state *C* lying significantly destabilised for the Mn system in comparison to the other two metals. These defect energies can be found in Table 4.9.

	Cobalt	Nickel	Manganese
Defect energy (B)/ eV	0.17	0.15	0.22
Defect energy (C) / eV	0.09	0.06	0.20

TABLE 4.9: Defect energies for Li migration steps B (T_d) and C (O_h).

Similarly to state B, state D is characterised as a Li O_h to T_d migration from the defective state C) and as such is destabilised similarly. As summarised in Table 4.10 the defect energy of this site is equivalent to the calculated cost of a T_d defect (state B) and an O_h defect (state C) suggesting there is no evidence of an defect-defect interaction (either positive or negative) between the two defects ($Li_{tet,vacchain}$ and $Li_{oct,vacchain}$) within this structure. Geometry optimization of state D results in a similar displacement of the face-shared metal ion to that seen in state B, with the metal migrating away from the face-shared ion toward the dumbbell site. However, with the first half of the pathway ($A \rightarrow B \rightarrow C$) freeing the tetrahedral site, this metal migration is increased. Values of this displacement can be found in Table 4.10.

	Cobalt	Nickel	Manganese
M displacement (D) / Å	0.16	0.09	0.45
Expected Defect energy $(B + C)/eV$	0.26	0.21	0.42
Calculated Defect energy (D) / eV	0.24	0.20	0.44

TABLE 4.10: Displacement of face shared metal ion and Expected/Calculated defected energies of state D.

While Li environment was shown to impart localised redox activity at the near-delithiated case, the parallel charge ordering of the principle structure A was maintained throughout all Li migration steps (A through D). This is evidenced by spin moments on all metal ions remaining consistent for all ions throughout these steps with the integrated Spin density and the corresponding d-orbital occupations shown in Figure 4.22. This suggest that the redox activity of these materials are less sensitive to local Li environment at half lithiation.

For all three metals, geometry optimization of the dumbbell structure (E) was achieved in under 40 ionic steps. Similarly to the near-zero Li systems, this dumbbell

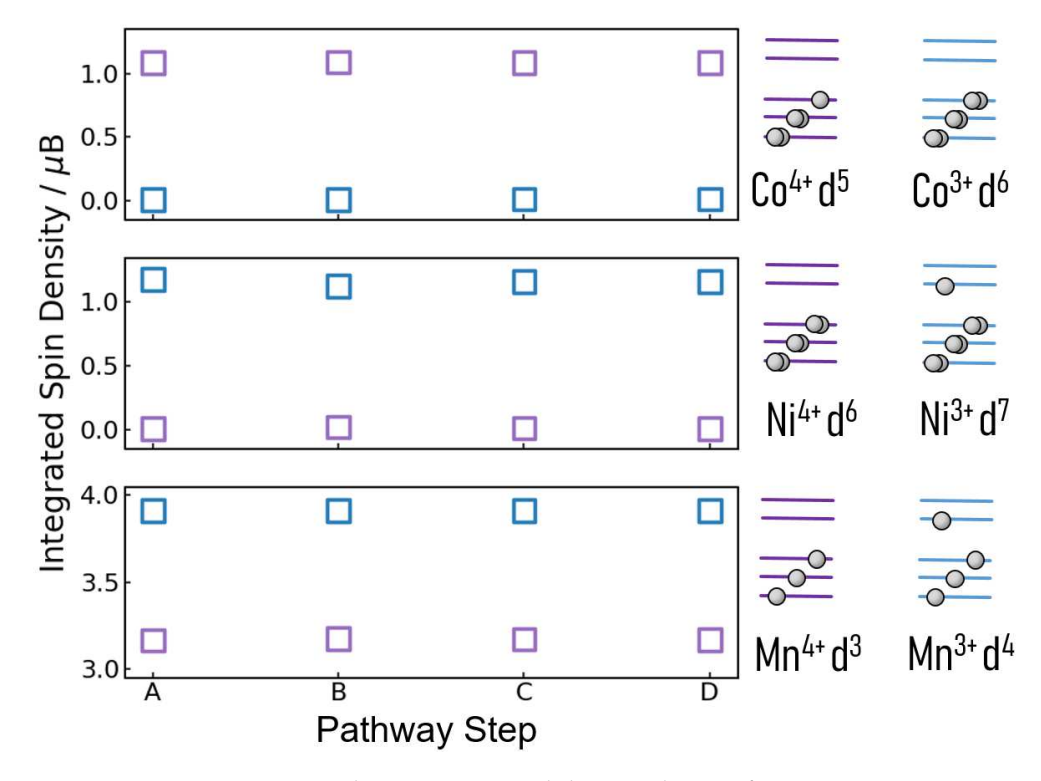


FIGURE 4.22: Integrated net spin around the metals sites for Li migration steps across the pathway (A through D). The retention of on-site spin density suggests the charge ordering is maintained despite Li rearrangement.

site is characterised by a cooperative T_d metal site and T_d Li site spanning across a vacancy in the MO₂ sheet. It's found that state E is destabilised in comparison to state A for both Co and Ni systems (0.41 eV and 0.65 eV respectively), while this state is low lying for the Mn systems (0.05 eV). This result is in disagreement to Ceder and Reed, with their publication finding the Mn dumbbell to be stable⁴. However, the extent of this stabilisation has recently been shown to be dependent on the choice of Hubbard U value³ (for which Ceder and Reed used 0).

In the publication by Ceder and Reed, they qualitatively determine the CFSE for a plethora of 3d transition metals in a similar composition as state E. Their discussion is largely focused on qualitatively estimating the associated change in CFSE upon forming this state E. However, only one potential d-orbital occupation is suggested. It's claimed that this dumbbell structure features a charge disproportionation of nearby metal site and a change in the d-occupancy accordingly. However, in principle the ground state electronic structure of state E could feature no such process (i.e. a simple T_d defect reaction).

Of-course many factors other than crystal field stabilisation will influence the stability of T_d defects, some of which are discussed by John Reed, however it shown to produce qualitatively reasonable results⁶. Using crystal field theory, the ground-state electronic structure for state E will be the d-occupation which results in the smallest change in CFSE of the following two potential processes. The first in which the nearby ion participates and therefore:

$$2 O_h M^{3+} \rightarrow O_h M^{4+} + T_d M^{2+}$$
 (4.3)

Or the alternative, in which the neighbouring ion does not participate and therefore:

$$2 O_h M^{3+} \rightarrow O_h M^{3+} + T_d M^{3+}$$
 (4.4)

Figure 4.23 shows the d-orbital occupancies of a low-spin Co system in the dumbbell configuration alongside the resulting change in CFSE of these two possible electronic states. Qualitatively, it's found that the dumbbell structure incurs a large destabilisation effect regardless of the electronic configuration and both configurations being predicted to have similar impact on the total energy $(\frac{34}{15}\Delta_0 - 2\Delta_s \text{ vs } \frac{32}{15}\Delta_0 - 2\Delta_s)$. Interestingly this destabilisation is heavily dependent on the electron pairing energy Δ_s , which while being unknown has bounds. Since an octahedral Co^{3+} ion has been demonstrated to be low-spin the upper bound for Δ_s is equal to Δ_o . Additionally, while Δ_s could be as low as 0, in practice all tetrahedral 3d metal complexes are high spin and thus Δ_s is greater than $\frac{4}{9}\Delta_o$ (using $\Delta_t \approx \frac{4}{9}\Delta_o$). Using cited literature values of Δ_o for low-spin Co^{3+} as between 2.1 to 4.2 eV and the bounds for Δ_s , the energy change for both d-occupations can be calculated. If Δ_s is set equal to Δ_o the energy change drops to $\frac{4}{15}\Delta_o$ and $\frac{2}{15}\Delta_o$ for the participating and spectating configuration respectively. This change in CFSE corresponds to an energy change between 0.28 eV and 1.2 eV and will have similar energy cost as the near-zero Li system.

Similarly, the d-occupancies for a low-spin Ni³⁺ system in the dumbbell configuration can be seen in found Figure 4.24. It's demonstrated that the change in CFSE is once again positive for both electronic configurations. Interestingly, the disproportionation

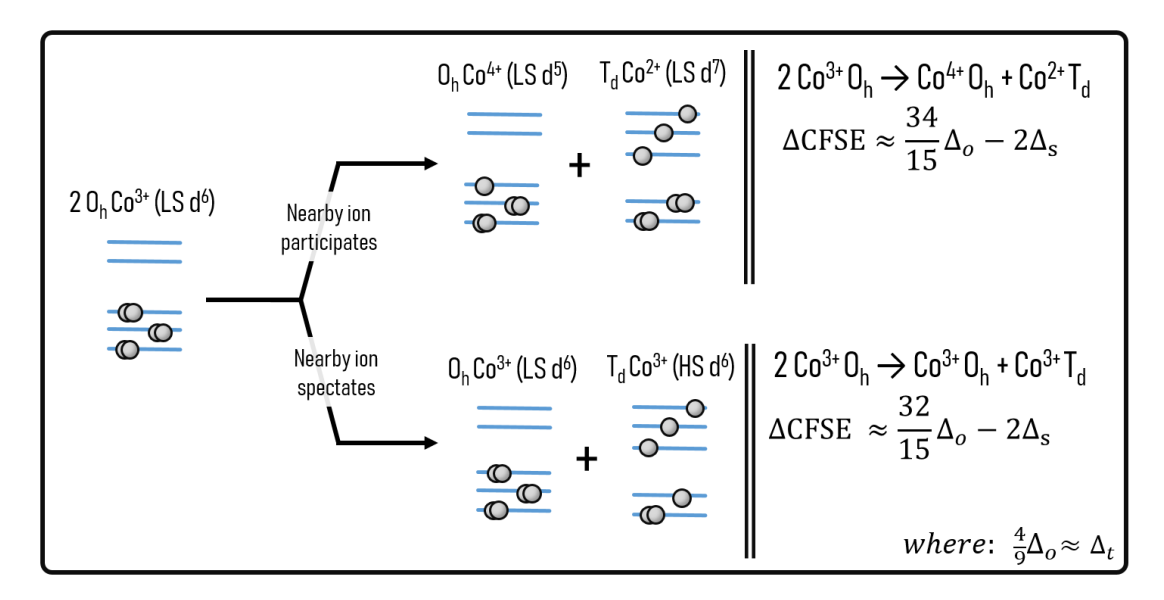


FIGURE 4.23: Possible changes in d occupation for Co during the metal migrating to the T_d in dumbbell structure step D \rightarrow E. For the spectating pathway there is no redox activity, while the participating pathway involves a charge disproportionation reaction.

configuration results in the same net-spin and as such is independent on the spin-pairing energy. Constrastingly, the spectating configuration does depend on this energy. It's found that these two configurations yield a similar change in CFSE ($\frac{38}{45}\Delta_o$ vs $\frac{37}{45}\Delta_o$ for participating and spectating configuration respectively) when Δ_s is equal to $\frac{4}{9}\Delta_o$ which is a loose lower bound. This suggests that energy penalty for dumbbell formation is expected to be qualitatively similar both at near-zero Lithiation (where charge disproportionation cannot occur) and at half-Lithiation.

However, this same conclusion cannot be drawn for the Mn system. When considering charge disproportionation the change in CFSE for the Mn system changes drastically. Figure 4.25, shows that the energy penalty for dumbbell formation is predicted to be zero (near-zero when considering Jahn Teller distortion of d-orbitals) when a neighbouring ion participates via a charge disproportionation. This barrier is significantly reduced in comparison to the spectating ion configuration ($\frac{4}{9}\Delta_0$). This suggests that the conclusions drawn by Ceder and Reed hold and that dumbbell formation at half lithiation is facilitated by charge disproportionation. While other factors outside of crystal-field theory influence the likely-hood of charge disproportionation, Reed also states that cationic arrangement and electron-electron repulsion effects aid this process. ²³⁰

FIGURE 4.24: Possible changes in d occupation for Ni during the metal migrating to the T_d in dumbbell structure step D \rightarrow E. For the spectating pathway there is no redox activity, while the participating pathway involves a charge disproportionation reaction.

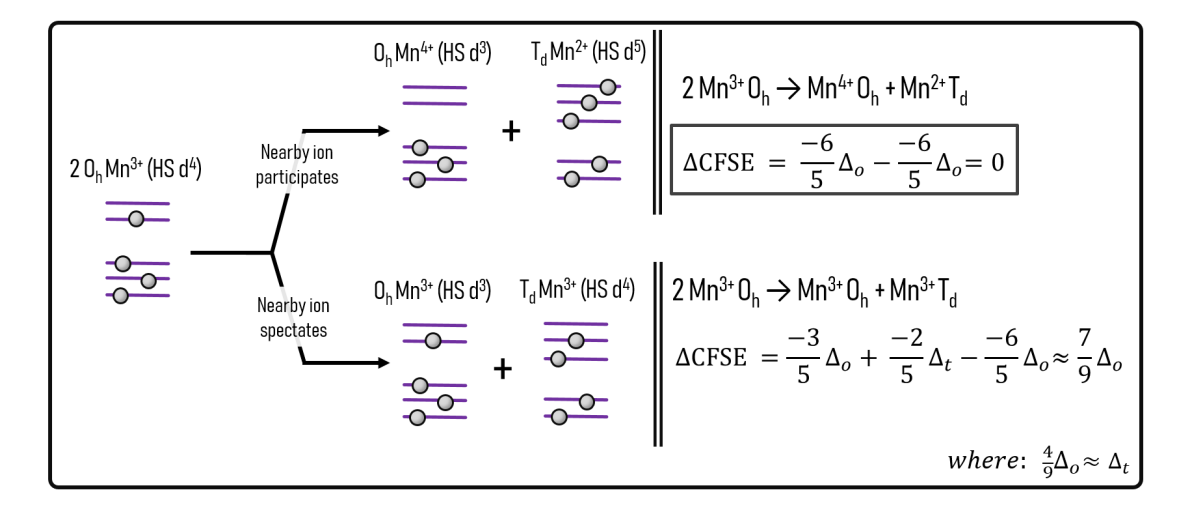


FIGURE 4.25: Possible changes in d occupation for Mn during the metal migrating to the T_d in dumbbell structure step D \rightarrow E. For the spectating pathway there is no redox activity, while the participating pathway involves a charge disproportionation reaction.

Step D \rightarrow E, is a $O_h \rightarrow T_d$ metal migration. This step has been discussed in detail for zero and near-zero Li prior but the possibility for an alternate electronic configuration yields differing results. The migrating metal was placed in the centre of a T_d in the Li layer (opposing the T_d in the layer above). Relaxation of this State (E) reveals that dumbbell formation incurs an energy penalty with state E lying at +0.48eV and 0.69eV above state A for Ni and Co respectively. These energy penalties are similar to those found observed for the near-zero Li system indicating that there is little qualitative

difference between Li - M dumbbells formed at near-zero and half lithiation. For the Mn system, however, there is a large reduction in the total energy between states D and state E, with state E lying thermodynamically near the undefected state A (0.045 eV). This indicates that T_d Mn may rapidly form as a Li-Mn dumbbell as a route to alleviate the incurred stress of T_d Li, where this state is free to degrade further toward the Spinel structure. These defect energy for the dumbbell is in is in agreement with prior literature.

It is noted that the spin density around the metal sites significantly changes between state D and E for all three metals, indicating a redox process occurs during the transformation. The nature of this process is discussed in Section 4.4.2.

4.4.2 Calculated minimum energy pathway under equilibrium conditions

While, a low energy Li-Mn dumbbell suggests thermodynamic feasibility of this particular route of degradation, only mapping the minimum energy pathway will yield insights into the rate and energy barriers for such process. As seen prior, calculation of the minimum energy pathway was achieved via the nudged elastic band method. Five images were constructed between stable intermediates across the full pathway (A-B-C-D-E) using a linear interpolation for a total of 25 images (5 of which fixed at A, B, C, D and E). The nudged elastic band method was performed with a convergence criteria of < 0.085 eV/Ang. Since all steps across the pathway are characterized by a T_d to O_h "hops" the resulting midpoint images feature face-bound cations. The calculated minimum energy pathway was normalised to the undefected structure and a spline curve was fitted between images.

The activation energies for Li migration steps are small for both Co and Ni having a thermodynamic barrier close to the defect energy of a T_d Li (< 0.25 eV transition states). These barriers remain consistent for all Li steps across the pathway ($A \rightarrow B$, $B \rightarrow C$ and $C \rightarrow D$) suggesting that Li mobility is largely localised and uninfluenced by Li/V_{Li} ordering. A similar result is observed for the Mn system albeit with increased energy barriers (by approx 20%) and is consistent with the values seen in prior

publications.^{3,7} The energy barriers are similar to those found for the near-zero Li case, suggesting that the binding of Li within the Li sheets is small and unimpacted by metal oxidation state changes or degree of Lithiation.

The transition state energy for the metal migration step lies 1 eV above state D for both Co and Ni. This drastically contrasts the transition states seen for Li migration and these differences suggest that typical operating conditions that drive Li mobility in these materials will not increase the rate of dumbbell formation by an appreciable amount. However, the transition state (D \rightarrow E) for the Mn system lies less than 0.2 eV above state D, this is similar to the energy barrier for Li migration. This in conjunction with a low lying dumbbell (state E) suggests that thus the driving forces that drive the Li intercalation process will cause dumbbell formation which is free to further proceed to the defective spinel framework. The complete minimum energy pathway for the three metals is found in Figure 4.26.

If the O_h to T_d defect reaction results in the number of unpaired d electrons changing integration of the spin density around the migrating site will elucidate the nature of the process occuring. However, due to partial occupancies, orbital contributions and the change in relative orbital overlaps between T_d and O_h metals 231 , some change in spin density around the metal site is expected even when the number of unpaired electrons is kept constant. Therefore, the magnetic moment of the migrating site isn't sufficient in discerning the exact nature of this metal migration. Importantly, however, the charge disproportionation reaction results in oxidation of a neighbouring site from 3+ to 4+ in addition to reduction of the migrating site.,Evidence of redox activity can be obtained by integrating the spin density over all metal sites, where oxidation of a neighboring site implies a disproportion reaction and serves as evidence of reduction of the migrating metal.

Determination of the netspin around each site was achieved using the same methodology outlined in Appendix A. The net spin around each metal site for each image across step $D \to E$ can be found in Figure 4.27iii. As expected, for state D, the spin states of each metal site falls into one of two groups, the first corresponds to a M^{3+} ion while the other a M^{4+} ion. The migrating ion and the other metals occupying

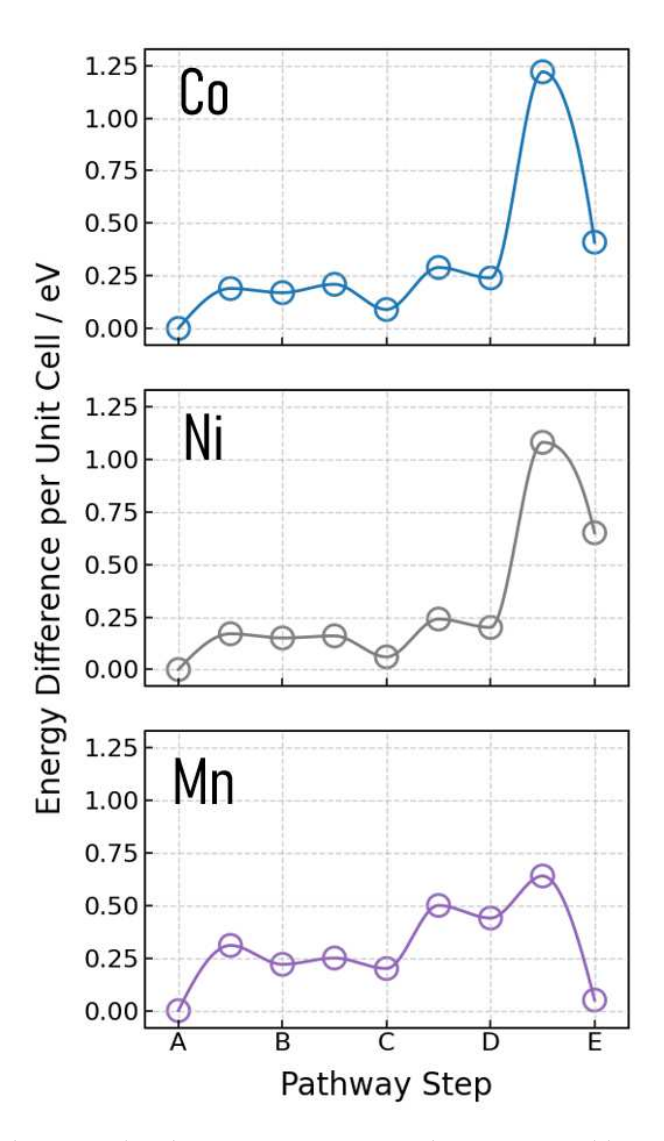


FIGURE 4.26: The normalised minimum energy pathways at equilibrium for dumbbell formation for Co, Ni and Mn. States A through D are Li rearrangements of one another and thus have low energy transition states. State E is the Li-M dumbbell.

the vacancy chain are formally in the +3 oxidation state. While, those in the Li chain are in the +4 oxidation state. As expected, the spin density around the migrating site changes during migration.

For both Co and Mn, a neighbouring metal ion in the vacancy chain also shows a significant spin moment change during migration. This spin moment change is such to suggest this ion has been oxidised from M^{3+} to M^{4+} , with the final magnetic moment being similar to the Li chain M^{4+} ions. This suggests that both participating pathway is lower in energy for Co and Mn and the resulting dumbbell is stabilised by a charge disproportionation reaction resulting in a Li $-M^{2+}$ dumbbell. This result is

as predicted for the Mn system with a large reduction in the energy penalty calculated via crystal field theory (Figure 4.25). However, crystal field theory suggests that while similar in energy penalty, the spectating pathway should be preferred for Co. This highlights some of the issues with crystal field theory as a predictive tool. Although Δ_0 and Δ_s have been assumed to remain constant for a given metal as to allow comparison across the T_d M formation, this is incorrect. Oxidation state, local coordination and bond lengths can vary the crystal field splitting significantly.

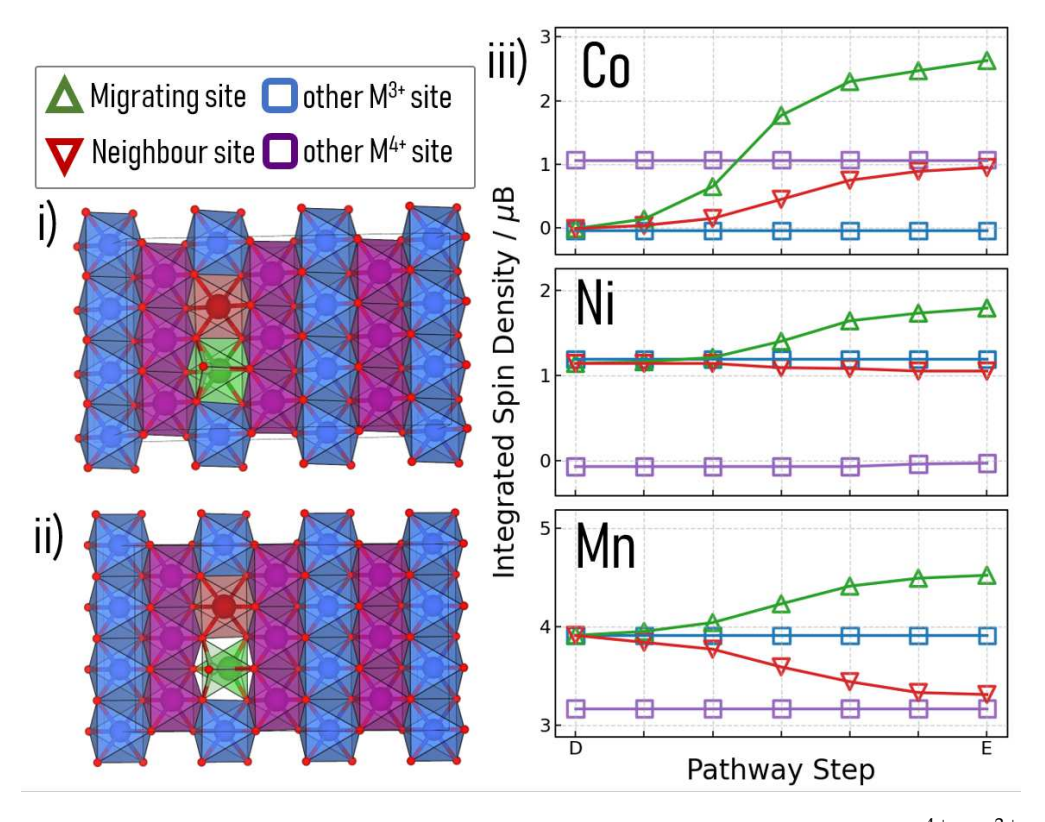


FIGURE 4.27: i/ii) State D and E as viewed down the c axis. State D shows a M^{4+}/M^{3+} charge ordering with the migrating ion lying within the vacancy chain. Li is removed for clarity, colors match those seen in iii. iii) Integrated spin densities of metal sites across the $O_h \rightarrow T_d$ metal migration step.

The result that the Co and Mn systems undergo a charge disproportionation reaction has been studied at detail prior $^{2-4,7}$, however there is little investigation regarding Ni systems in the literature. Interestingly, the principle pathway for the Ni system was predicted to be dependent on the relative scale of Δ_s vs Δ_o . It's found that the magnetic moment of a neighbouring metal does change during dumbbell formation. However, this change is small (from 1.14 μ_B to 1.05 μ_B) suggesting a small polarisation and that the neighbouring metal is not oxidised. This suggests that the spectating

pathway is the minimum energy path for Li-Ni dumbbells at half lithiation and that Ni^{2+} is an immobile species.

4.4.3 Lattice strain and its impact on ion migration

Despite it's large theoretical capacity and low-toxicity, this charge disproportionation reaction has long plagued pure Mn as an unsuitable cathode material, often instead it's found as a small composition % of mixed metal materials, most commonly NMC (Nickel-Manganese-Cobalt). In this alloy material, layered to spinel degradation has been shown to reduced, with degradation occurring near the surface.

At a given state of charge, a pure Mn cathode has formula unit Li_xMnO_2 and thus the Mn species is between a +3 and +4 oxidation state. While the +4 oxidation has been demonstrated to be resistant to degradation, the +3 oxidation state is labile. High nickel NMC eliminates Mn^{3+} from forming altogether, irrespective of state of charge. The high electronegativity of Ni results in preferential reduction of the Nickel species, with the structure often cited as $LiNi^{2+}Co^{3+}Mn^{4+}O_2$ within the literature. ^{223,232,233} This material isn't without it's problems, in particular Li^+/Ni^{2+} particle exchange often results in the loss of cathode material into the electrolyte ^{63,234}.

High composition Mn cathodes have not been complete abandoned however, more recently attempts at inhibiting layered to spinel degradation through trivalent dopants has shown some promise. 235,236 However, modelling work has indicated that these dopants have some issues 7 . Firstly, large dopant species increase the barrier to Li migration which may impact battery performance. Secondly, while small dopants increase the barrier to T_d Mn migration they themselves are liable to the same process. Finally the energy barrier to Mn migration is only impacted when neighbouring a dopant, which will require high dopant concentrations.

Instead, an alternative approach is suggest here. Rather than inhibiting the mobile $\mathrm{Mn^{2+}}$ by reducing the feasibility for $\mathrm{Mn^{3+}}$ to charge disproportionate, a structural approach is taken. With the unit-cells of these materials has been discussed to flex significantly with state of charge, with volume changes quoted to be upward of 15%

between high and low degrees of lithiation.²³⁷ Interestingly, the relative rigidity of the M-O bonds results in much of this volume variation being derived from the c-aligned Li-O bonds.

It has been demonstrated that at low rates of charge or discharge, the crystal stresses remain small, as Li diffusion is slow and the lattice parameter changes corresponding to the state of charge. However, at exceedingly fast charge or discharge, these materials have been demonstrated to delithiate non-uniformly, with the rapid delithiation of near-surface layers 206,238 . This results in localised lattice strain as the local lattice parameter of a Li_xMO_2 sub-crystal is enforced by crystallite lithiation despite the degree of lithiation differing (see Figure 4.28). Given time to rest the materials proceed to an equilibrium state, with lithium diffusing so that the state of charge of any sub-crystal matches the crystallite lithiation.

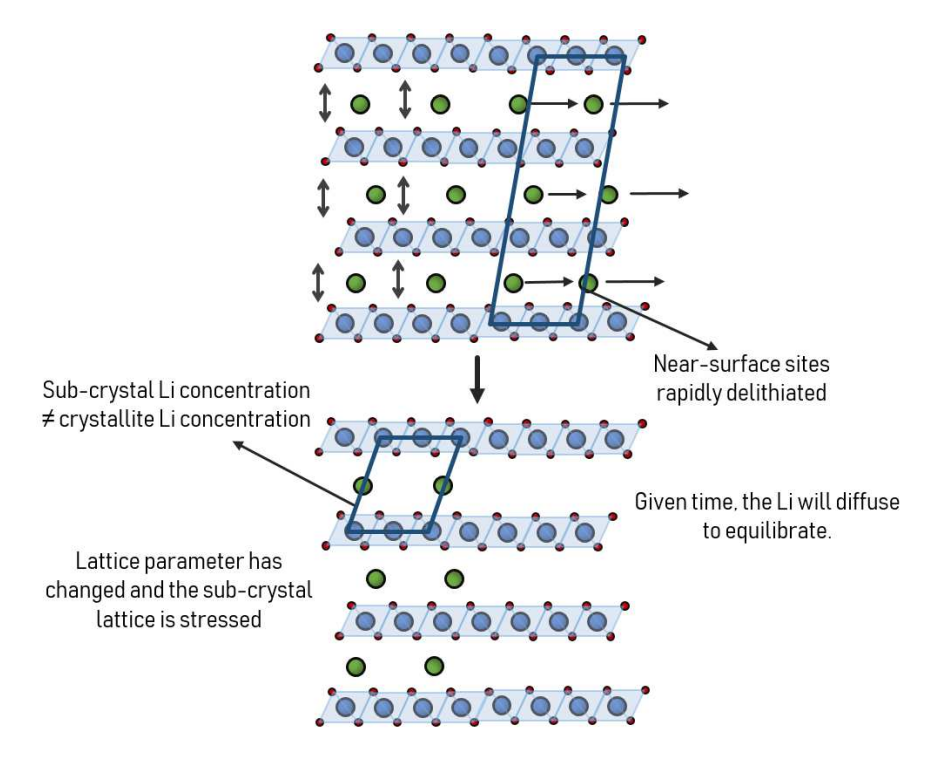


FIGURE 4.28: At high rates of delithiation, surface state delithiate rapidly, resulting in a mismatch of local and global lithiation and induced lattice strain.

Discerning the likelihood and scale of these high C-rate stresses is a difficult task, instead this section aims to investigate the impact on degradation that lattice stress may impart in general. This may serve as an outlook for inhibiting layered to spinel degradation as an outlook for increasing battery lifespan. It's known that cycling of

lithium causes lattice strain sufficient to cause particle cracking ²⁰⁷ and large lattice spacing variability ^{239–241} and Li migration energies are dependent on local lattice parameter, therefore it stands to reason that metal migration can be effected similarly. Introduction of cathode stresses that manipulating the c-axis of these materials (either chemically through dopants or physically through an external force) may yield spinel resistant cathodes.

4.4.3.1 Strain-sensitivity of lattice parameters

While there is very little research regarding ${\rm Li/V_{Li}}$ configurations as a function of external lattice stress, it's expected that the low energy ${\rm Li_{1/2}MO_2}$ P2/m structure that was identified under equilibrium conditions will remain a valid low-energy model configuration for strain cathodes at half lithiation. Using the same methodology as prior, the relaxed lattice dimensions were calculated with DFT+U using the Perdew-Burke-Enzernhof (PBE) spin polarized generalized gradient approximation functional, yielding an energy convergence to within two meV/atom. A varied isotropic force was applied to the structures to investigate the response of key lattice parameters under stress by adding a penalty to the diagonals of the stress tensor.

Figure 4.29 demonstrates the impact that external stress imparts on the Li layer spacing for the lattices of these crystals. Other key lattice parameters are found in Figure 4.30. It should be noted that c-axis lengths are converted to the $R\overline{3}m$ equivalents because within the monoclinic cell the c-axis does not run perpendicular to the MO_2 sheets and thus the results appear disingenuous, this issue does not arise for the calculation of the layer-spacing because these are be definition the distance between adjacent oxygen planes and thus perpendicular to the MO_2 sheets. A wide range of stresses (from -4 GPa to +4 Gpa) were applied to the equilibrium lattices to investigate the crystal deformation. Only moderate energy costs are seen across the range of investigated stresses, (< 100 meV/f.u.) under isotropic stress and thus these stressed lattices model realistic crystal deformations 242,243 that may act as nucleation sites for spinel formation. This application of a compressive of tensile force results in a near linear change in volume of the structures as expected. Additionally, in agreement

with Kang and Ceder³⁷, the c-axis, and in particular the lithium layer spacing is highly susceptible to stress and accounts for the majority of the volume change. Constrastingly, the change in the metal layer spacing is near-zero highlighting the rigidity of the Metal-Oxygen bond. It's found that the change in Li layer spacing (between -4 GPa and +4 GPa) aligns with the change in Li layer spacing observed experimentally as these materials cycle from high to low degrees of lithiation. This suggests that these stresses can be expected in non-uniform delithiation.

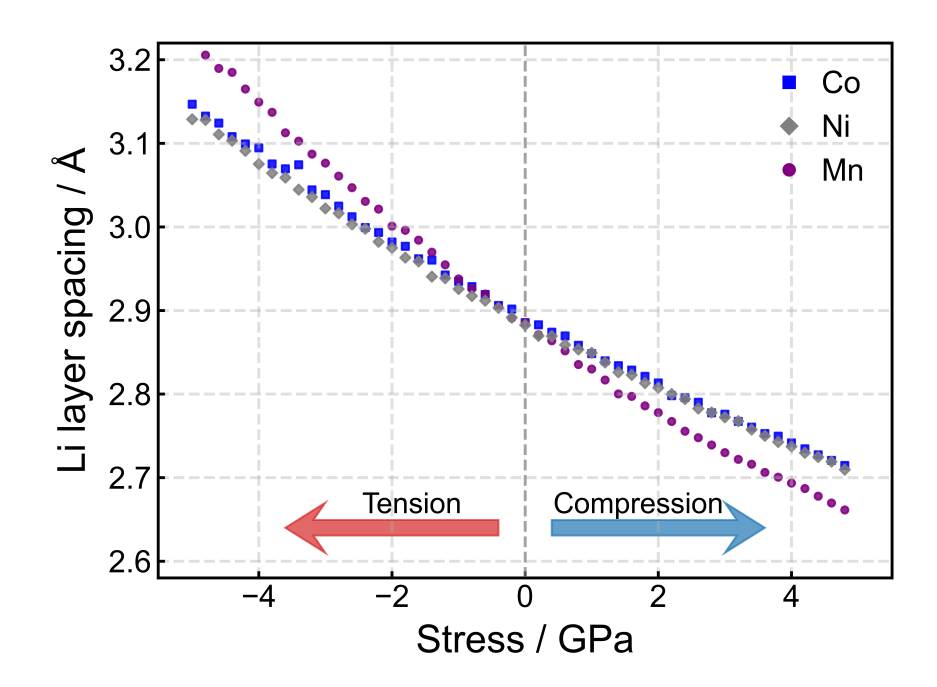


FIGURE 4.29: The response of Li layer spacing (Oxygen-Oxygen *dspacing* as calculated in Song et al²⁴⁴) under varying isotropic stress for half lithiated Co, Ni and Mn oxides.

Interestingly, the Mn system is particularly susceptible to stress, with a steeper gradient found for the both the Li layer spacing and volume. Closer investigation of this system reveals that while the M-O bonds are rigid in these systems (in comparison to Li-O), the Jahn Teller extended bonds in the Mn system are sensitive to external stress. Figure 4.31 demonstrates the change in both M-O bond lengths and Li-O bond lengths as a function of applied stress. It's found that while the non-elongated Mn-O bonds share a similar response to stress as the Co-O bonds, the elongated bonds vary significantly.

This, is the result of a peculiar trend in the periodic table, in which Mn described to lies at the bottom of the "double-hump" observed for the transition metals. Prior

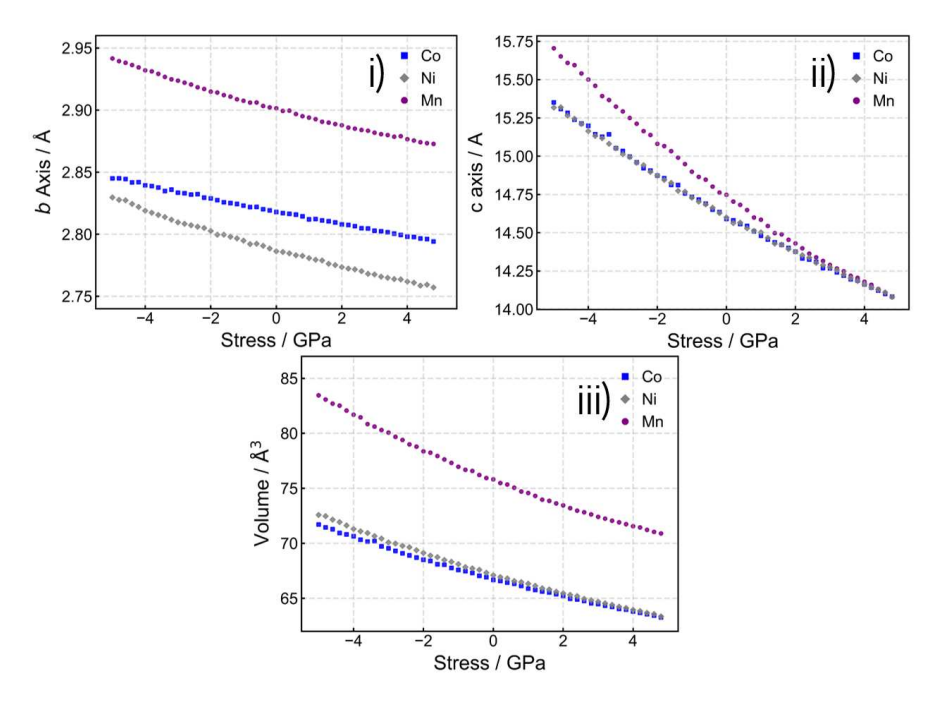


FIGURE 4.30: The response of other key lattice parameters under varying isotropic stress for half lithiated Co, Ni and Mn oxides.

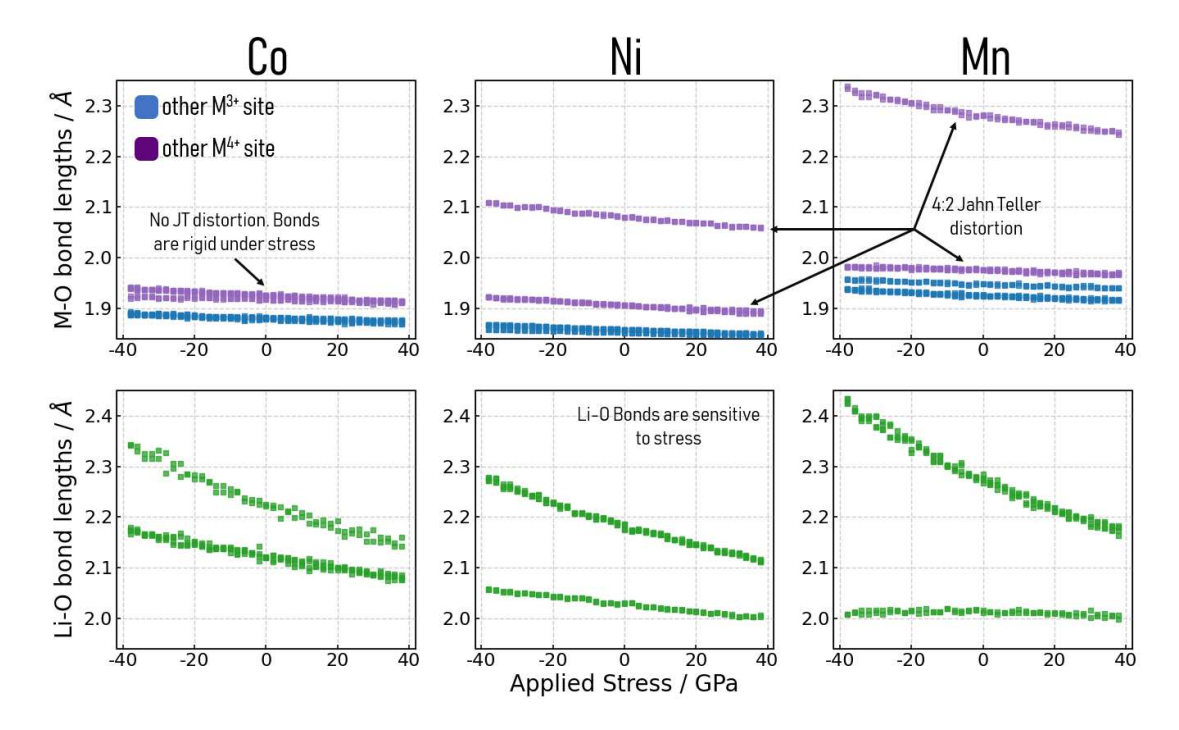


FIGURE 4.31: top) The response of M-O bond lengths as a function of applied stress, both Ni and Mn show a 4:2 split in the M^{4+} -O bonds indicating Jahn Teller distortion (which are more susceptible to stress). bottom) The response of Li-O bond lengths as a function of applied stress, the elongated Li layer results in LiO₆ polyhedra being distorted (and thus having different bond lengths.)

literature has discussed the relative strengths of the 'M-O bond' ²⁴⁵. It's shown for Mn-O, the bond-dissociation energy is peculiarly low, due to a lack of covalent

bonding (in comparison to the rest of the d-block).

4.4.3.2 Strain and its effect on key intermediates across the primary degradation pathway

With the assumption that lattice strain doesn't open new avenues to spinel formation, investigating the same intermediates analysed at equilibrium but with strained lattice parameters derived from external stress will yields insight into the feasibility of spinel formation under local lattice strain. This may yield avenues to further understand how spinel degradation occurs and potential insight into mitigating such processes. The pathway for dumbbell formation is reiterated in Figure 4.32.

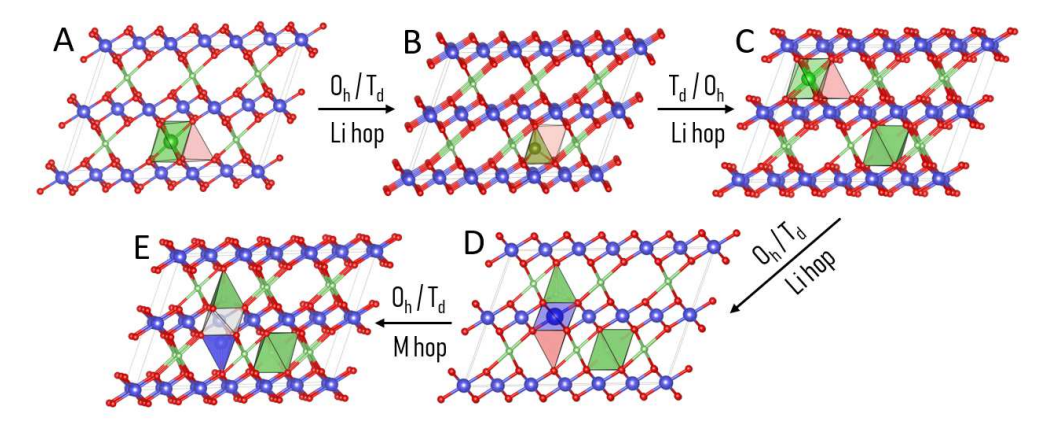


FIGURE 4.32: The principle pathway for dumbbell formation at equilibrium³ was investigated at strained lattice parameters. *Figure Repeated for clarity*.

The energy differences for these intermediates within a strained lattice (normalised to the equilibrium lattice) can be found in Figure 4.33. It's found that the energy of all states (A through E) respond harmonically with respect to strain. This suggests that the total energies are responding to the incorporated strain and no secondary process is occurring. Interestingly, it's observed that the structures with tetrahedral lithium (state B and state D) have minima at non-zero isotropic strain, indicating that tetrahedral lithium is under local compressive stress at equilibrium lattice parameters. The minima for these energy curves are calculated to be at 1.4, 0.6 and 0.2 GPa of tensile strain for Co, Ni and Mn, respectively. Similar work by Kang and Ceder³⁷ concluded that for Cobalt systems moderate expansion of the c-axis lattice parameter may facilitate T_d Li formation and thus improve battery performance. This result is

corroborated here, with these energy curves suggesting that all three metals will benefit from a slighty expanded lattice parameter. At exceedingly large levels of expansion, the Li layer spacing increases such that the Li acts more like a free ion (similar to the near-zero Li case investigated earlier). This is evidence by the energy differences between T_d and O_h Li reducing to zero for Co and Ni at > 35 GPa tensile strain, the Mn system retains a small energy barrier that will likely reduce at further Li layer expansion.

The cooperative 180° Li-O-M-O-Li connectivity is broken when a Li ion occupies the octahedral site in the vacancy chain (state C), this results in a small destabilisation at equilibrium lattice parameters. For both Co and Mn, this destabilisation is alleviated when the lattice is under a sufficient enough tension indicating that high Li layer spacings result in the loss of layer to layer connectivity. Interestingly, the reverse relationship is observed for the Ni system with compressive strain aiding to stabilise state C relative to A. Investigation of the electronic structure indicated no clear disparity between both the expanded and compressed systems, with the Jahn Teller ordering and spin states remaining consistent between the structures. Further investigation would be required to conclusively state a reasoning for this effect. reasoning as to why Ni does not obey this trend

State E features the important Li-M dumbbell structure and as such its stability is of high importance. While the equilibrium energies of these defects lie at 0.41, 0.65 and 0.05 eV for Co, Ni and Mn respectively this changes drastically at varied strain. For both Co and Ni state E remains destabilised regardless of the applied strain. Under high tensile strain (4 GPa), the Li-M dumbbell lies at 0.50 eV and 0.75 eV above state A for Co and Ni dumbbells respectively. Similarly, under high compressive strain (4 GPa) the dumbbell lies at 0.37 eV and 0.53 eV above state A for Co and Ni respectively. These values remain large even under high degree of lattice deformation and as such the it's unexpected that localised lattice strain will facilitate Li-Co or Li-Ni dumbbell formation.

Interestingly, the Li-Mn dumbbell state varies drastically with respect to applied stress. When under large compressive strain (4 GPa), state E is stabilised relative to

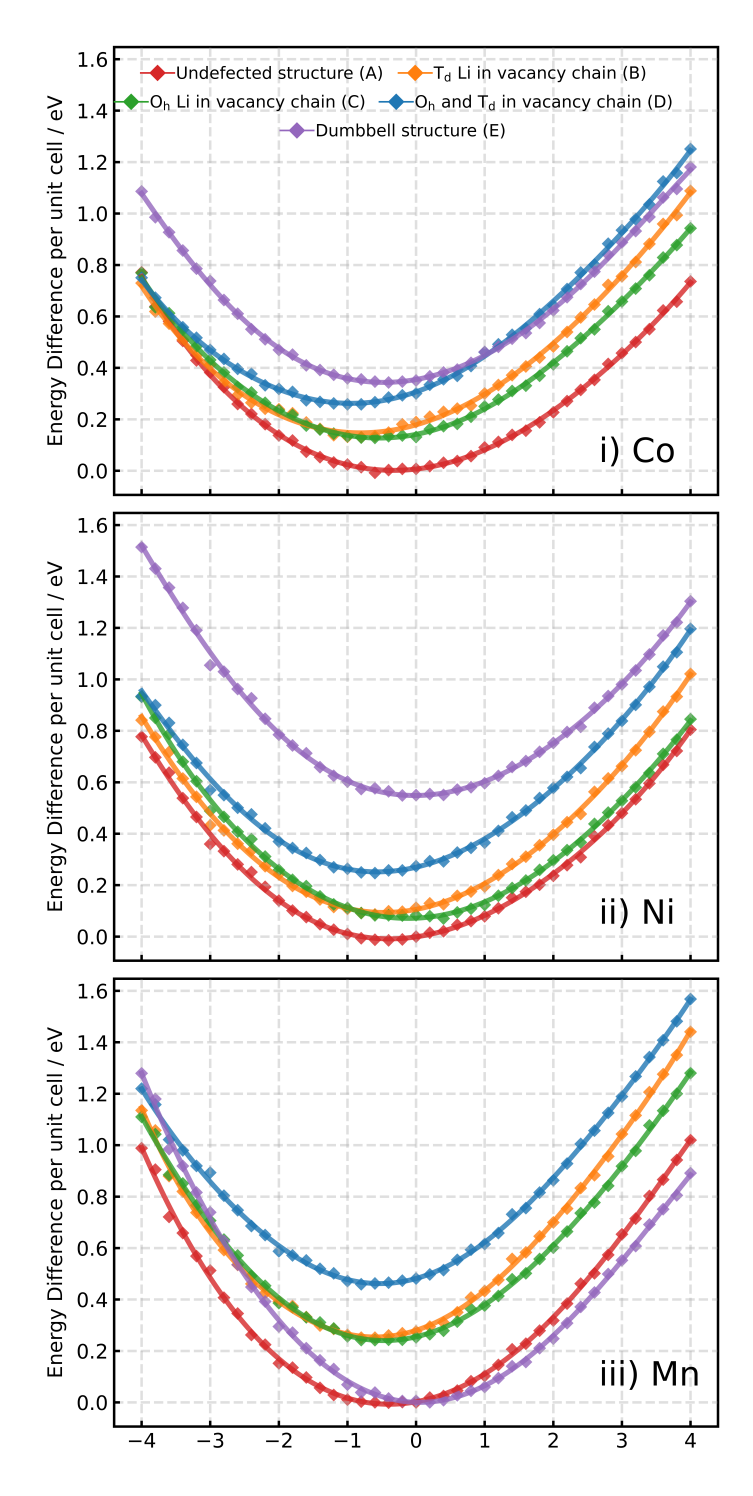


FIGURE 4.33: Harmonic relationship of key steps in the layered to spinel transformation for (i) $\text{Li}_{0.5}\text{CoO}_2$, (ii) $\text{Li}_{0.5}\text{NiO}_2$ Ni and (iii) $\text{Li}_{0.5}\text{MnO}_2$.

state A (-0.13 eV), indicating that this state is likely to be long-lived and able to proceed further to the Spinel structure. As a cathode material, Mn may degrade rapidly if the c-axis lattice parameter is decreased. With the trend to incorporate Mn into Nickel/Cobalt materials, which typically have a smaller c-axis lattice parameter,

 T_d migration may be exacerbated. As a result cathodes with small c-axis lengths require a composition that inhibits the generation of Mn³⁺ to reduce degradation rates. In contrast, the application of a large tensile strain (4 GPa), significantly destabilises the Li-Mn dumbbell with configuration E lying 0.3 eV higher than configuration A. This indicates the Li-Mn dumbbell will be short lived if the local lattice parameter is expanded.

Analysis of the electronic structures of the Mn system at high compression and tension showed that the charge ordering and Jahn Teller effect remains consistent. This suggests that the nature of this change in stability is not an electronic effect. Further analysis is required to discern the nature of this stability.

4.4.3.3 Strain and its effect on the transition states for dumbbell formation

While calculations on the intermediates yields insight into the stability of these structures, the energy barriers for each subsequent step will dictate the feasibility of this degradation route. Barriers for Li migration are typically small and metal mobility has been shown to be complex and oxidation state dependent^{2,3}. Calculating the minimum energy pathway as a function of lattice strain would yield insight into whether the transition states vary and thus the relative rates of Li migration and more importantly, dumbbell formation.

Applying the same methodology seen at equilibrium states, directly to the 120 different parent lattices calculated would be a computationally mammoth task. While calculation of the intermediates only requires five geometry optimizations per metal per lattice, calculating the minimum energy pathway requires individual numerous images between these intermediates to form the band. With the typical nudged elastic band calculation taking upwards of five times as long (per image) as a single image geometry optimization applying this procedure to the 600 intermediates would be cumbersome.

The change in lattice parameter varies smoothly with respect to applied stress.

Therefore the minimum energy pathway calculated within a strained lattice will be

expected to vary smoothly as a function of stress. As a result, linearly interpolating between intermediates for each parent lattice and minimizing the resulting band (i.e the parallel approach) is highly inefficient (Figure 4.34i). Instead, a serialised approach is taken, in which the ionic coordinates the calculated minimum energy pathway is ported onto an adjacent lattice, as seen in Figure 4.34ii.

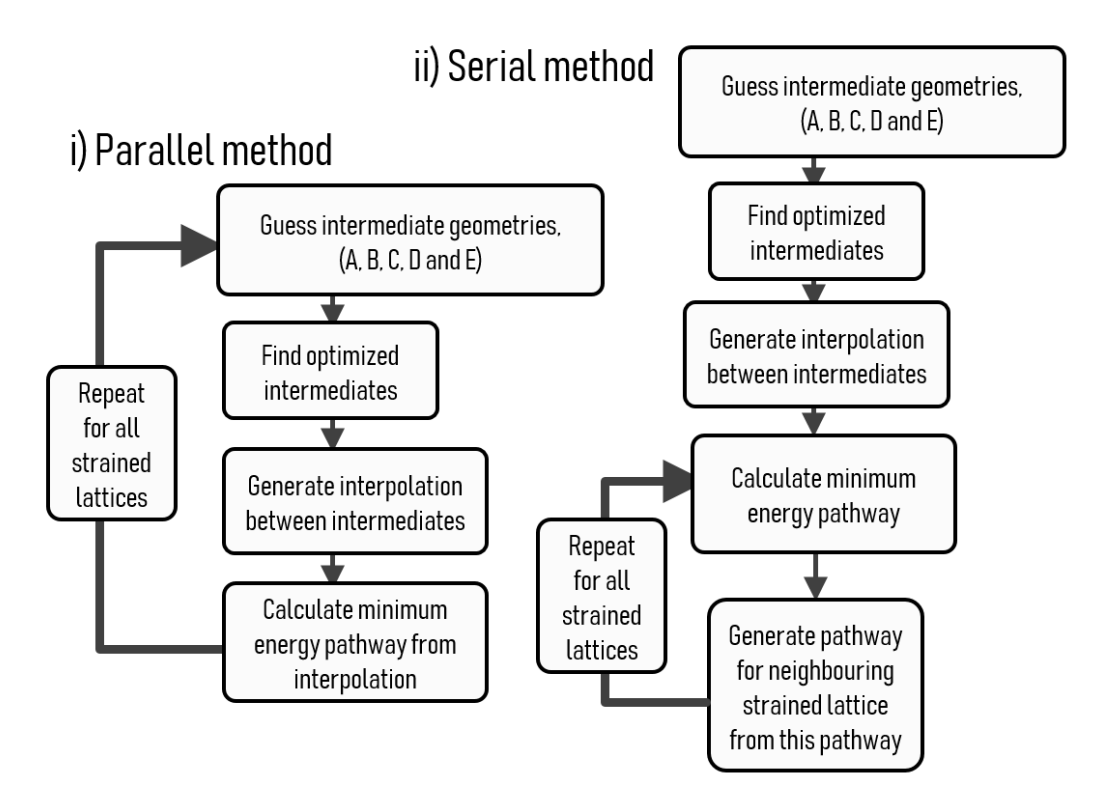


FIGURE 4.34: Scheme for calculating the minimum energy pathway with respect to strain state. i) Is the parallel approach, generating the linear interpolation for each individual strain state and calculating the MEP from it. ii) Using the known minimum energy pathway for a given strain, the minimum energy pathway can be assumed to be close and a full linear interpolation is not required. This is valid because the lattices vary smoothly between strain states. This results in significant reduction in computation time.

This approach has some benefits and some drawbacks. Firstly, since the results of one calculation feed directly into another 'daisy chain'-like, submission of results is serial, having to wait for one set of results before calculating the next despite them being independent. Fortunately, since the initialised band is close to the minimum energy pathway, this approach reduces the number of ionic steps across each band from roughly 40 to less than 10 thus the lost time due to waiting to submit calculations is accounted for through the reduction of compute time. Finally, since the results are serial, miscalculating or finding an alternate energy pathway at one step will be

carried forth through all the future calculations. The resulting minimum energy pathways can be found in Figure 4.35, where it's seen all MEP's vary smoothly with respect to strain. A spline was fitted to the pathways and a color-map indicates the strain state.

As shown in Figure 4.35i, the relationship between stain and the minimum energy pathway is linear for the Co system, with tension reducing the energy barriers for all Li (A through D) and Co migration steps (D to E). The transition state energy for Li migration increases (from 0.19 eV to 0.33 eV) going from an equilibrium lattice to a high compressed lattice (4 Gpa). Constrastingly, application of a large tension, results in a reduction of this Li migration transition state, lying near zero. Importantly, these transition state energies remain significantly lower than the transition state for Metal migration, which lies between 1.04 and 1.38 eV above state A for tension and compression respectively, indicating that even at strain states far away from equilibrium the relative rate of Co migration is orders of magnitude lower than Li migration.

A similar result is observed for the Nickel system (Figure 4.35ii), where the energy barrier for Li migration is reduced with tension. Interestingly, the vacancy occupied Li structure (C) has a inverse relationship with respect to strain, with this low-symmetry structure lying near-zero with respect to state A. Interestingly, the transition state energy for a Li migration out of this site is maximised while under tension. This indicates that Ni cathodes under tension will preferentially arrange the Li/V_{Li} to be low-symmetry, which are long-lived provided this tension is held. This potentially opens an avenue to control the Li arrangement through the use of stress. However, the relatively low energy barriers (less than 0.25 eV above state A) likely inhibit the feasibility of such process. Once again, the activation barrier for metal mobility remains high irrespective of crystal strain lying 1.10 eV under high tension and 1.30 eV under high compression (relative to state A).

Constrastingly, the Mn system shows a differing relationship (see Figure 4.35iii). Tensile strain eases Li migration (with transition state energies reducing to 0.15 eV) and compressive strain inhibits it (0.5 eV transition state). However, the opposite effect

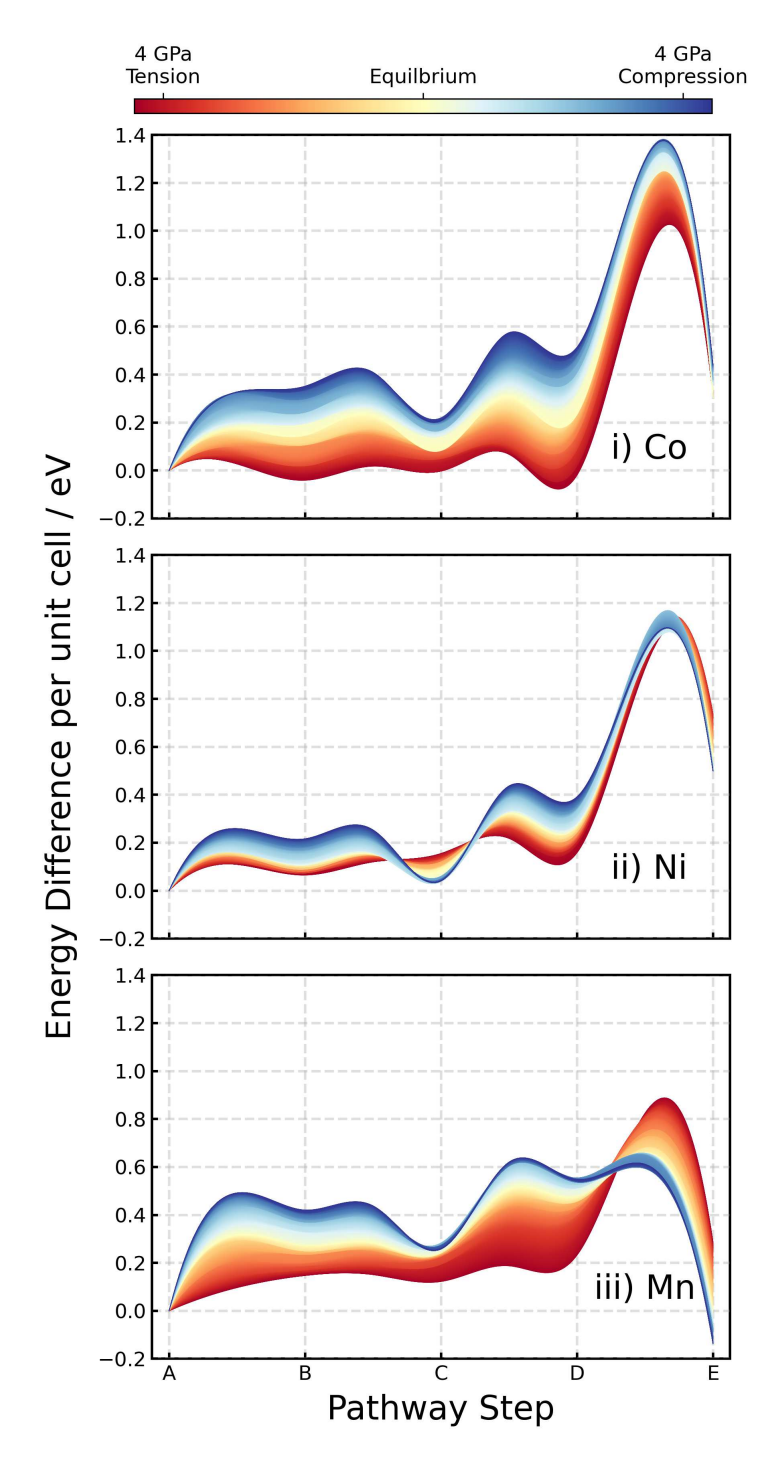


FIGURE 4.35: Calculated MEP's under varying compression/tension, normalized to state A at it's given stress. Pathway steps correspond to those seen in Figure 4.32, in which the dumbbell structure E is noted to be a precursor in spinel formation.

is seen for Mn migration, with tensile strains increasing the transition state energy 0.9 eV above state A and compressive strain reducing this transition state to 0.59 eV. Worryingly, state under this compression state E is stabilised relative to A and the

transition state lies just 70 meV above the preliminary state D indicating that inducing lattice strain while there lies a high proportion of T_d Li will rapidly facilitate dumbbell formation which is stabilised and thus likely to proceed to the stable Spinel structure.

The lower activation barrier for Li migration indicates increased performance, therefore it would be beneficial to hold these materials under tensile strain. This is of paramount importance for Mn cathodes as tension not only improves Li mobility but inhibits the dumbbell structure (state E). Tensile strain during cycling increases the likelihood of T_d Li (state D). If this is followed by compressive strain, these would readily progress to the dumbbell structure (state E). Therefore, charge/discharge dynamics, which feature rapidly changing stresses (i.e alternating between large tension and compression) should be avoided.

The stability of the dumbbell structure in conjunction with a low-lying activation barrier has long yielded pure Mn oxides cathodes to be an unviable choice as a cathode material. While current methods for mitigating Mn diffusion involve avoiding the formation of Mn³⁺ altogether, ²⁴⁶ it is found that Mn diffusion can be reduced structurally. Synthesis routes that increase the c-axis length offer increased Li diffusivity and a hindered route for Mn diffusion aiding both battery performance and lifespan. Large dopant metals that offer layered structural changes, in particular expansion of the lithium migration plane, are an alternate path to explore in reducing spinel formation during cycling. This is evidenced by the resistance of Na-Ion cathodes to this particular degradation route.

Finally, these findings may be generalized to NMC materials if possible charge ordering ²⁴⁷ and non-uniform distribution of valance states ^{248,249} are given due consideration. However, the metal occupancy issue has long plagued atomistic modelling of this class of materials, in particular in regards to isolated defect interactions. ²³⁴.

4.5 Summary of factors influencing layered to spinel transformation.

While a multitude of pathways to form spinel exist, the mechanism governing a preliminary dumbbell structure has been discussed at detail both at low and half lithiation. This section aims to be a summary of the key conclusions from this Chapter, drawing together the results from prior publications in comparison to those seen here.

Functional choice has been a debated topic for this class of materials within the past 20 years and parametrization of Hubbard U values still raises some concerns. While Seymour et al³ demonstrated that the choice of Hubbard U value impacts defect energies and the minimum energy pathway, it was concluded here that, provided the lattice parameters align with those seen in the literature, the use of dispersion corrections within the functional of choice doesn't significantly impact the defect energies nor the minimum energy pathways. However, careful consideration must be taken to ensure that the Li layer spacing is reasonable at near-zero lithiation which U value and choice of dispersion correction may impact.

Two systems were investigated to model the delithiated state. Ceder and Reed 4,6 modelled a system at a complete state of delithiation (with f.u. MO_2) and showed that such systems are exceedingly unlikely to degrade to spinel (due to the M^{4+} ion being resistant to T_d coordination). This results is qualitatively agreed upon here, both the T_d and O_h coordination of metal within the Li layer results in a drastic destabilisation of the structures. However, this work investigated an additional system, a system that is dilutely lithiated (1 Li per f.u.). This system investigates dumbbell formation in system where the metal sites have a different electronic structure to those investigated before. The lone Li results in reduction of a nearby metal ion to 3+ state. The 3+ ion has increased mobility due to a improved change in crystal-field stabilisation. However, transition states remain exceedingly high in energy.

At half lithiation, Li configuration is important, as the lack of trivacant sites yields an inability for metal migration. Within the literature, it's common to start from the P2/m structure³ as this structure is considered the "ground-state" ${\rm Li^+/V_{Li}}$ configuration.

Ceder and Reed, used a differing system and a pure-PBE functional, however their results qualitatively align with those seen here (for Co and Ni), with much of the difference likely due to their use of U=0 for both systems (i.e. on-site interaction). While the results here are in agreement with Seymour et al³, they demonstrated a Hubbard-U sensitivity for T_d Mn and as such improved ab initio methods for determining Hubbard U⁶⁵ value will likely further improve these models. Additionally, in a follow-up publication Seymour et al⁷ attempted to investigate methods to mitigate the Mn dumbbell through trivalent metals (M³⁺) and showed some success. However, similar improvements are observed here through the use of lattice strain, in which the dumbbell changes from being stable (in comparison to the P2/m structure) to significantly destabilised (+300 meV)

Using prior literature values and transition state theory, the rates of these processes can be estimated. Of course, the investigated pathway at half lithiation involves numerous "Li hops" and as such the transition state energy for $O_h \to T_d$ metal migration is dependent on lithium configuration.

Transition state theory states that for a given pathway, the rate (k) of said pathway is proportional to the exponent of the activation energy:

$$P \xrightarrow{k} Q \tag{4.5}$$

where:

$$k \propto \exp\left\{-\frac{E^{\ddagger}}{RT}\right\} \tag{4.6}$$

Where E^{\ddagger} is the transition state energy for step P \rightarrow Q. For a two step process the overall rate is the product of both steps:

$$P \xrightarrow{k_1} Q \xrightarrow{k_2} R \tag{4.7}$$

$$k_{1,2} \propto k_1 \cdot k_2 \tag{4.8}$$

Which using the Arrhenius equation:

$$k_{1,2} = A \exp\left\{-\frac{E_1^{\ddagger}}{RT}\right\} \cdot \exp\left\{-\frac{E_2^{\ddagger}}{RT}\right\} \tag{4.9}$$

$$k_{1,2} = A \exp\left\{-\frac{(E_1^{\ddagger} + E_2^{\ddagger})}{RT}\right\}$$
 (4.10)

With E_1^{\ddagger} as the transition energy for step 1 and E_2^{\ddagger} as the transition state energy for step 2. Which yields the results that for a multi-step process, the rate is proportional to exponential of the peak energy seen on the minimum energy pathway.

Rates of Li migration have been discussed in detail in numerous publications ^{5,37,250} where it's generally accepted the energy barrier for Li diffusion is around 0.2 eV. Figure 4.36 summarises the dumbbell transition state energy (relative to the undefected structure A) for equilibrium lattices seen throughout this Chapter and in the literature.

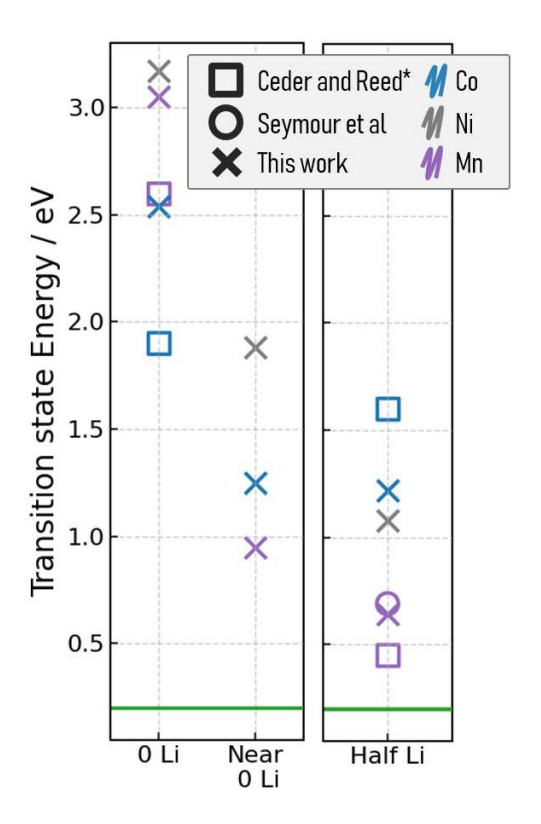


FIGURE 4.36: Transition state barriers for $O_h \to T_d$ metal migration under equilibrium lattice parameters. The green line represents a typical migration barrier for Li diffusion⁵. *Ceder and Reed's^{4,6} work differs from the work here and by Seymour et al³, in that no on-site interaction was include (i.e U = 0 in the Hubbard model)

Due to the nature of the Arrhenius equation, even small increases in the activation can greatly inhibit a process from occurring at room temperature. Processes > 1 eV will have no appreciable rate, being $> 1 \times 10^9$ times slower than Li diffusion. However, with energy barriers < 0.7 eV (including the Li rearrangement steps) for Mn migration at half Li, it's generally concluded (both here and in the literature) that Mn migration will have a appreciable rate and the dumbbell pathway is the predominant route for bulk spinel formation.

A comparison into the routes of inhibiting this dumbbell, via trivalent substitution (as modelled by Seymour et al 7) and via strain lattices is summarised in Figure 4.37. Seymour et al 7 use a hybrid eigenvector following method to find the transition state (which results in an MEP that differs from that found here). Additionally they normalised their transition states results relative to the Li rearranged state (D), however direct comparison is still possible as the trivalent substitution does not effect the dynamics of Li migration. From Figure 4.37i, its clear to see that the results align between works, with their undoped system aligning with the unstrained work seen here. Importantly, they suggested an Al dopant would inhibit the layered to spinel transformation by raising the activation barrier by 0.113 eV. At room temperature this corresponds to a rate reduction of a factor of 80 (compared to the undoped material). In comparison application of a large tensile strain (4 GPa)increased the activation barrier by 0.26 eV, which corresponds to a relative rate reduction of a factor of 2.3×10 5 . Additionally, this dumbbell is unfavoured lying significantly above the undefected structure A (see Figure 4.37ii).

Further work would investigate the nature of NMC materials and whether the high nickel composition imparts localized lattice strain onto $\mathrm{Li_xMnO_2}$ sub-crystals, the reduced lattice parameter from these systems could act as nucleation sites for spinel formation. Additionally, there is little experimental work regarding expansion of the c-lattice parameter through synthetic methods. These synthesis routes could eliminate spinel formation and revitalise pure-Mn cathodes. Investigation into the dynamics of Na-Ion cathodes could yield insight into the extent that lattice expansion inhibits structural breakdown of these spinel-resistant materials.

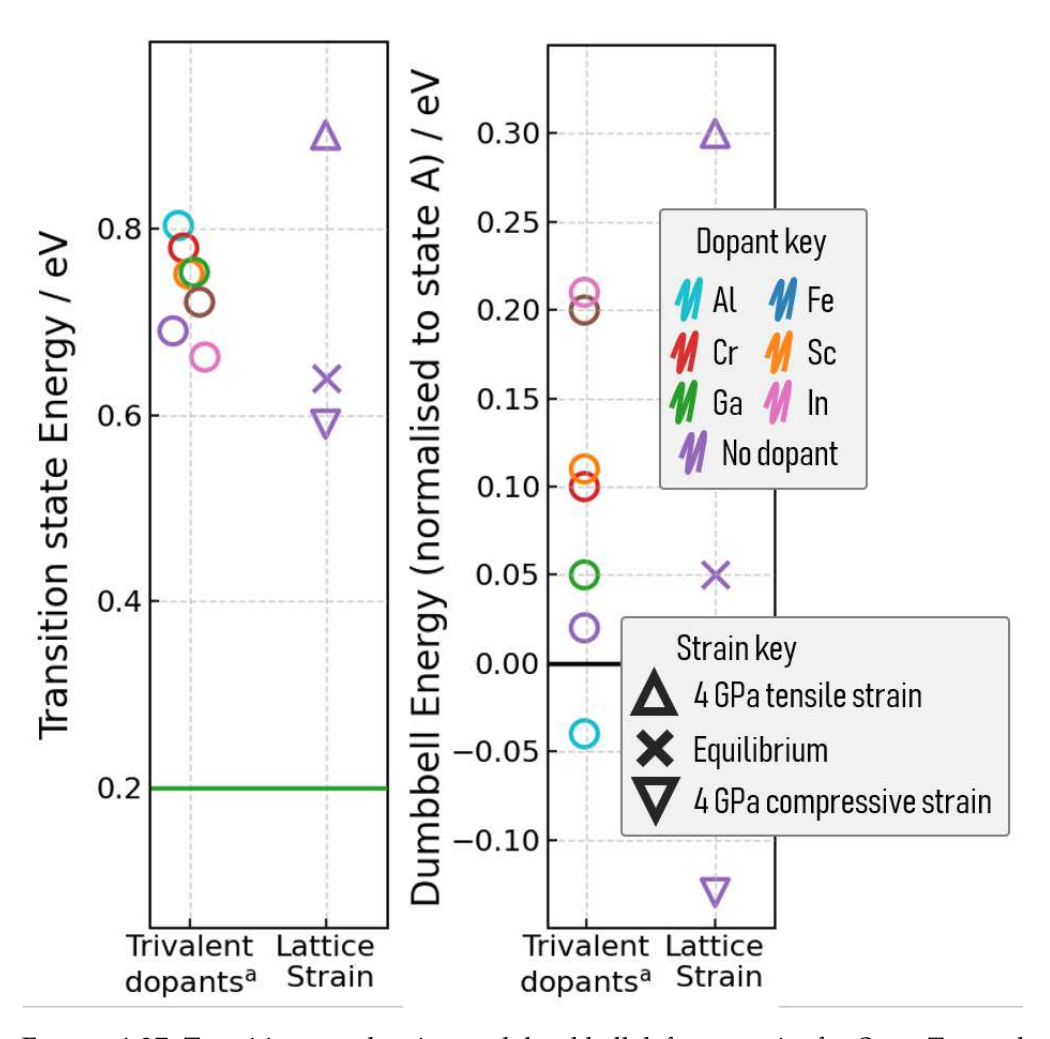


FIGURE 4.37: Transition state barriers and dumbbell defect energies for $O_h \to T_d$ metal migration seen in the literature and in this work. Seymour et al⁷ investigated dopant effects.

Chapter 5

Ion migration in surface cathode materials

While bulk cathode material have been shown to degrade slowly to Spinel, the surface layers of these materials rapidly degrade with a phase transformation noted to occur at the surface. Research by Lin et al ⁶³ provided experimental details and confirmation of degradation of a wide variety of battery materials (LCO, NMC, MNO, NCO). Often experimentally, STM, XRD, EELs and other analytical important tools to readily map the surface of these complex materials both at synthesis and end of line in a bid to understand the degradation that occurs, both within the bulk and on the surfaces.

However, when taking in situ measurements on surfaces, it is often difficult to get the resolution required to identify migration pathways or potential routes of inhibiting such pathways. It is known, that these layered structures initially undergo rapid transformation of their surfaces layers (< 5nm) during the first few cycles as some cathode material is sacrificially lost in forming the surface-reconstruction layer. The work by Lin et al 63 identified that this transformation proceeds through the Spinel structure and eventually to rock-salt.

In the context of mixed metal cathodes (NMC for example), this process has been shown to preferentially migrate particular metal species with enhanced activity observed for both Mn and Co at the surfaces. With the layered bulk valences being

 Ni^{2+} , Mn^{4+} and Co^{4+} whereas this rock-salt surface is Ni^{2+} , Mn^{2+} and Co^{2+} . Interestingly, these surface spectroscopic methods show the rock-salt structure is the primary surface material, however, a few bridging layers of Spinel are found between the rock-salt and layered boundaries. This process occurs both during battery operation, where large oxidizing over-potentials (up to 4.5 V) results in oxygen dissolution and loss of battery material 251,252 and at rest, where thermodynamics drives reactions between electrolyte and cathode material. 253

Some attempts are found in the literature through protective coatings ^{254,255} with moderate success at inhibiting battery breakdown. However, these surfaces coatings replace active battery material and as result reduce the energy densities.

Surface-bound spectroscopic techniques have determined that Co and Mn²⁵⁶ are preferentially found at the surface in NMC even in un-cycled materials. With limited modelling data regarding the transition states of near-surface degradation routes and in situ methods unable to reach atomistic resolutions, this suggest that both Co and Mn have increased sensitivity but also a thermodynamic tendency to segregate toward the surface.

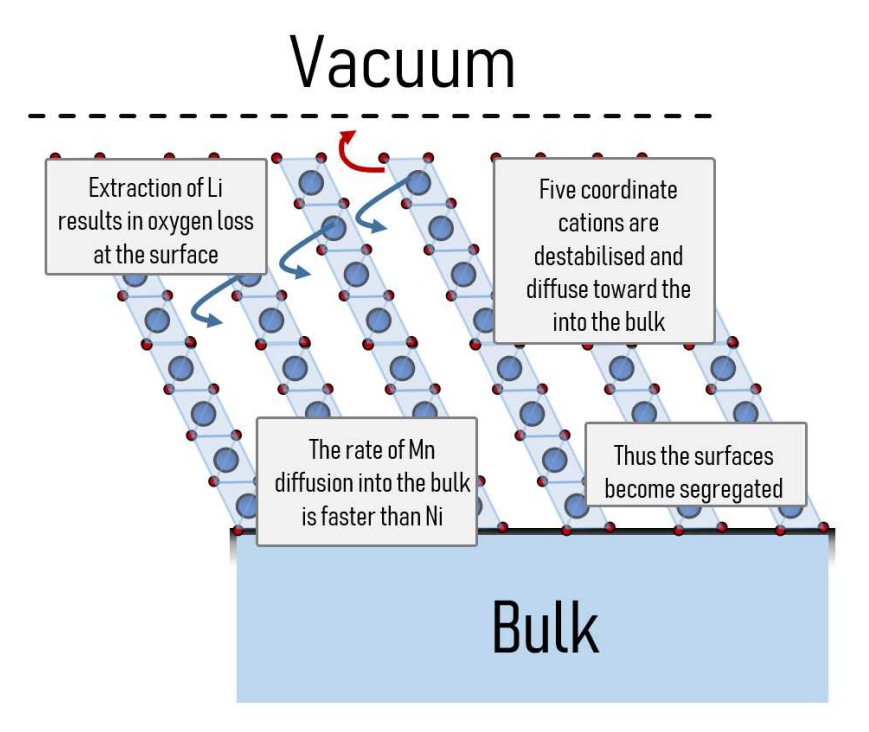


FIGURE 5.1: Proposed mechanism for metal segregation at the surfaces of cathode crystallites. *Adapted from Boulineau et al.* ⁴⁶*Repeated for clarity**

Figure 5.1 suggests a mechanism for surface segregation as seen by Boulineau et al. ⁴⁶ It's suggested that five-coordinate Manganese located at the surfaces of NMC uses vacancies within the Li layer to migrate away from the surface and return to an O_h coordination. This migration route is equivalent to layered to Spinel degradation but results in the segregation of Ni at the surfaces of these materials. Since the pathway is a $O_h \rightarrow T_d$ it stands to reason that the dumbbell structure may be a key intermediate at these surfaces.

Key surfaces have been identified for metal oxides, this Chapter aims to investigate both the thermodynamics and energy barriers of these surfaces in the context of metal segregation and layered to Spinel degradation.

5.0.1 Identification of low energy surfaces for layered cathodes

The traditional synthetic route for LiCoO₂ proposed by Reimers et al²⁰⁰ temperatures upward of 900°C. Alternative low temperature syntheses exist (chemical lithiation²⁵⁷, sol-gel processes²⁵⁸ and laser ablation²⁵⁹) with differing synthesis routes resulting in different layer stacking. Most methodologies, however, apply a long heat-treatment at the end of synthesis to form an electrochemically favourable product.

This heat treatment step anneals the material, recrystallizing the material under a lower temperature gradient to reduce lattice strain. 260 . Since the crystallites in NMC are small (> 20 μ m) and delithiation into the electrolyte occurs at the surface, surface processes are an important feature of these materials.

Modelling work by Kramer and Ceder 47 investigated the factors influencing the morphology of the O3-type LiCoO₂ system where it has been found that annealing these materials in an oxidizing environment yields flat hexagonal crystallites, whereas a reducing environment yields cubic crystallites. Delithiation through the [0, 0, 0, 1] surface is impossible as it would require require lithium to migrate perpendicular to the Li plane (i.e through the M-O polyhedra). It's also concluded that synthesis routes that inhibit the [0, 0, 0, 1] surface area of crystallites will have enhanced battery

performance. Both this paper and more recently 52 has identified low-energy surfaces that constitute the majority of crystallite surfaces (> 95%)

5.0.1.1 Tasker type surface cleavage

Practical surface cleavage often involves adsorption of atmosphere (commonly carbon monoxide, oxygen or hydroxide adsorption) and surface reconstruction to result in charge neutral/non-polar crystallites. However trying to model such systems yields a few caveats that have to be pondered.

- When cleaving the bulk, what bonds are cleaved?
- Upon surface cleavage is the freshly exposed surface terminated by some species (O, H, OH, CO, etc)?
- Is the resulting slab stiochiometric such that the f.u is the same as the bulk species?
- Does the resulting slab have a mirror plane parallel to the surface?
- There lies in principle an infinite number of valid cleavages. Which of these are likely in practice?

Cleavage of a bulk material results in surfaces that may be asymmetric and/or non-stiochiometric depending on the initial cell and the Miller plane of which the bulk was cleaved across. Figure 5.2 show three different unit-cells, these results in different types of slabs upon cleaving along the (001) plane. The surface terminology defined by Tasker²⁶¹ indicates there are three distinct types of surfaces. The first (Tasker Type 1) is formed when the number of anions and cations are equivalent in each repeat unit (layer) of the formed slab. This results in a zero net charge and zero inter slab polarity. The second (Tasker Type 2) occurs when the number of anions and cations are non-equivalent per slab, but this is counterbalanced by the next repeat unit such that the full slab is uncharged. Finally, the third (Tasker Type 3) has no line of cleavage that results in a surface that is both stoichiometric and charge-balanced.

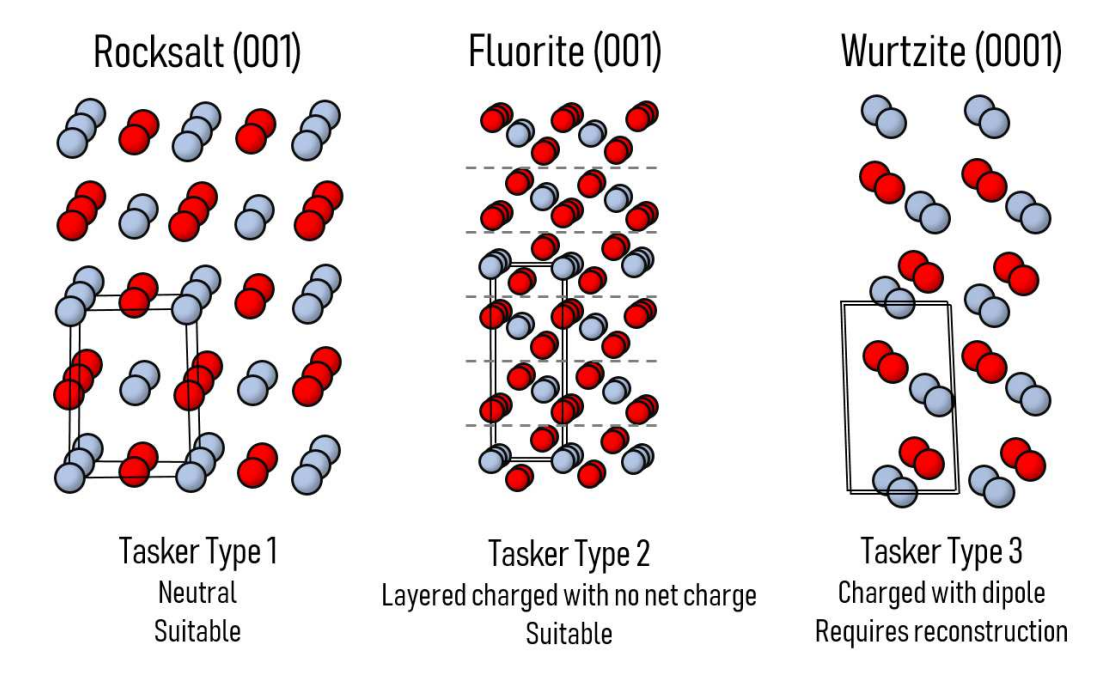


FIGURE 5.2: The three Tasker Type surfaces. Taker Type 1 surfaces are non-polar and uncharged, Tasker Type 2 surfaces have no net charge however individual layers are charged, Tasker Type 3 surface have a net charge perpendicular to the slab and would yield an infinite surface energy, as a result requires reconstruction to model. Image Adapted from Hinuma et al.⁸

Fortunately, methods of converting from a polar to non-polar surface have been derived and largely operate by moving numerous sites from one side of the slab to the other. Cleavage of surfaces in the context of modelling has been explored in detail by Sun and Ceder and much of these issues are handled within the PyMatGen surface-slab module. This module addresses much of the issues regarding non-convergences documented by Da Silva et al, the ensuring that both the bulk and surface systems are derived from the same transformed unit cell ensuring energies converge rapidly with respect to slab thickness and k-point density.

Simulation of surfaces is usually done by modelling a 'slab' of material. This slab is equivalent to the bulk material, however, with a large vacuum at the desired plane of cleavage (to stop interaction across the periodic boundary) effectively slicing across this plane. This slab has to be small enough to allow simulation within feasible time-limits while large enough that it does not collapse and models real world surfaces (see Figure 5.3). Due to the nature of K-points within VASP, it's often convenient to orientate the slab so that the surface is perpendicular to one of the lattice vectors of its simulation cell as such all slabs in this work have been realigned such

that the surfaces are perpendicular to the c-axis. This allows some of the computational cost of adding a large vacuum to the cell to be recuperated by only required a singular K-point in the direction of this vacuum.

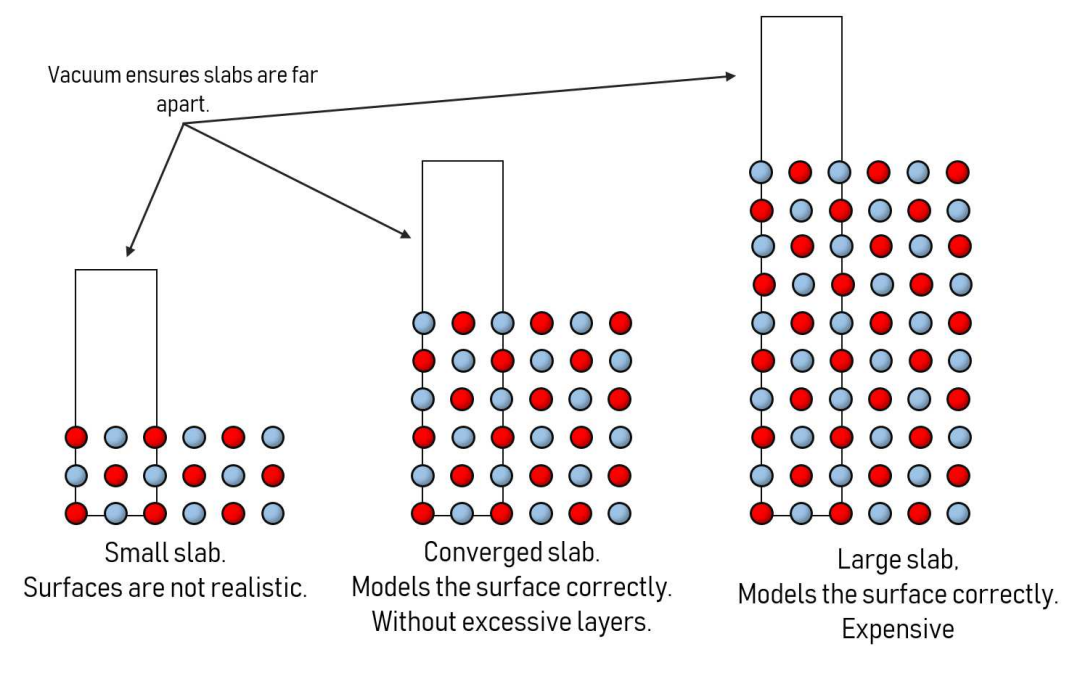


FIGURE 5.3: Slab models of surfaces need to be large enough to not collapse but small enough to be computationally feasible.

Of course, it's been demonstrated that lattice strain results in significant stretching of the Li-O bonding modes while the M-O bonds remain consistent, this implies the Li-O bond is weak. As a result all cleaved slabs break Li-O bonds when applicable (trying to keep the MO₂ framework when possible). This practice has been seen across modelling of these metal oxides previously.⁴⁷

5.0.1.2 Convergence of energy cut-off vacuum size and slab size

To avoid modelling systems that poorly describe the surface, either through slab interaction or insufficient slab size a series of convergence tests was performed on a model surface (1014) described to be 'low-energy'. Additionally, the K-GRID and Energy cut-off convergences are re-performed for this model surface, as higher energy plane waves are often required to describe the electronic structure of surface states.

Energy-cutoff convergences (see Figure 5.4) show that plane wave kinetic energy cut-offs of 900 eV and k-grids corresponding to a K-SPACING $> 0.35 \ {\rm \AA}^{-1}$ are required

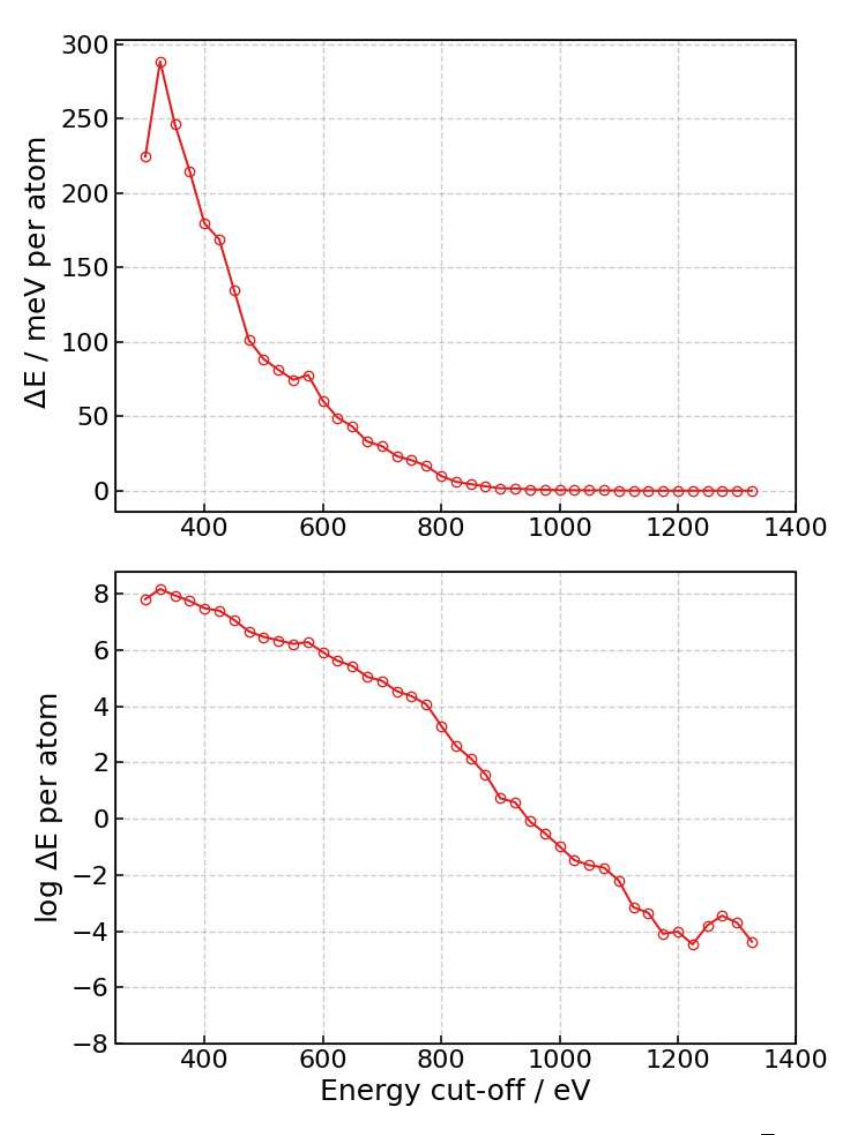


FIGURE 5.4: Convergence of plane wave energy cut-off of a $[1, 0, \overline{1}, 4]$ slab.

for total energy convergence of > 2 meV/atom. It's noted that total energy of a slab is related to the number of repeat units (layers) within the slab and therefore measurement of convergence of the total energy isn't directly possible. Instead, convergence of the surface energy is often cited in the literature.

Fiorentini and Methfessel 265 investigated numerous ways of calculating the surface energy from slab calculations). Typically, the surface energy γ is evaluated from a sufficiently large slab calculation and a separate bulk energy calculation:

$$\gamma = \lim_{N \to \infty} \frac{E^N(slab) - N \cdot E(bulk)}{2A}$$
 (5.1)

This surface energy is used to find convergence with respect to both slab thickness and vacuum size (see Figure 5.5). Slab thickness convergence is achieved at nine repeat units. Similarly, convergence of the vacuum size is found at 5 Å. While not seen here, too small a vacuum may result in 'charge sloshing', in which the electron density is passed from the surface of one slab to adjacent slab across the periodic boundary and electronic convergence is slowed, ²⁶⁶ since increasing the simulation cell only has moderate costs on the compute time a larger vacuum size is used. For all surfaces a minimum of 9 repeat units and a 11 Å vacuum is used.

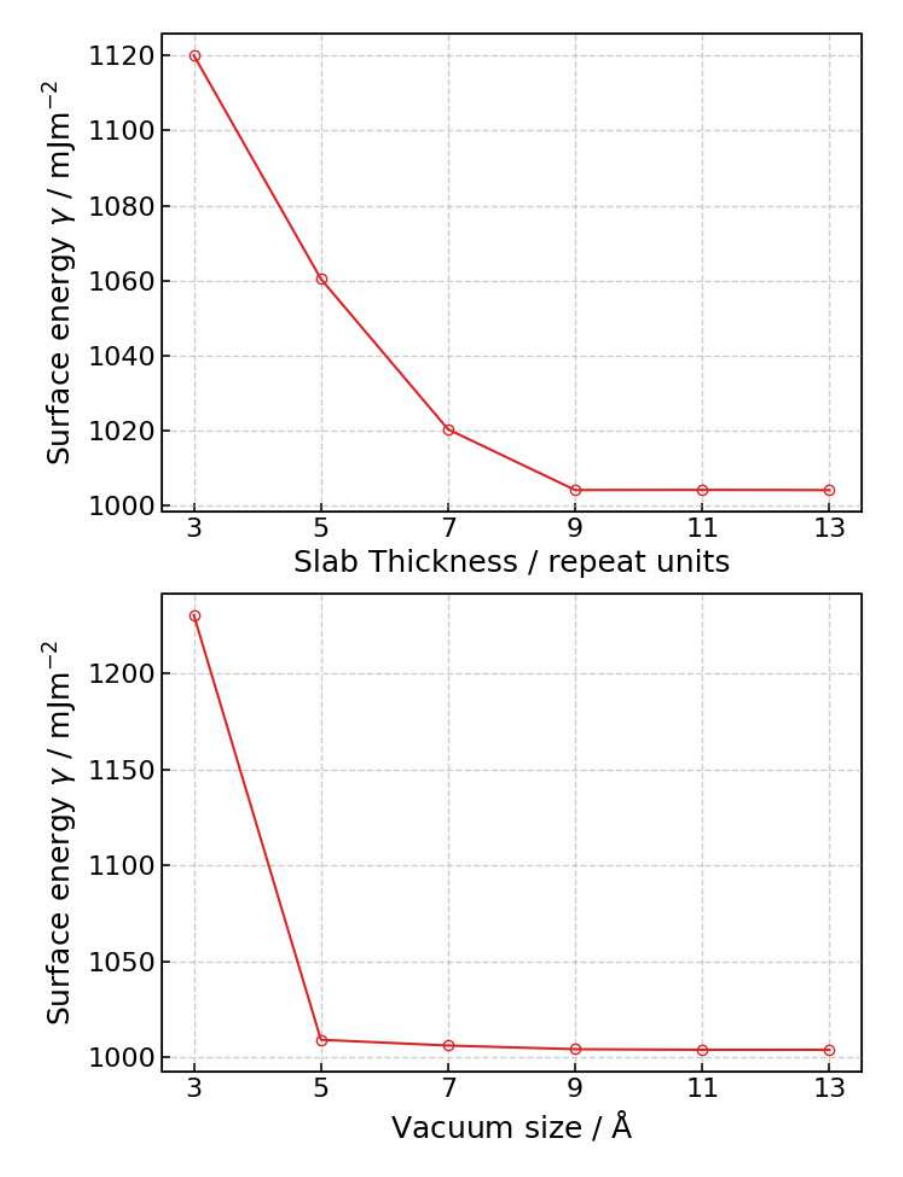


FIGURE 5.5: Convergence of necessary slab parameters. **top**) Surface energy convergence of slab size per number of mono-layers. **bottom**) Surface energy convergence of size of vacuum in simulation cell in Å.

5.0.1.3 Generation of surface slabs

The different O3-type metal oxides (LiCoO₂, LiNiO₂, LiMnO₂) belong to different parent lattices as the Jahn Teller effect lowers the space-group symmetry of the Mn (and to a much lesser extent Ni) system to the monoclinic structure (space-group C2/m). Similarly to the bulk systems this may yield confusion when talking about the surfaces of different systems, as similar surfaces (cleavage of the same bonds) are derived from different Miller planes. The Kramer methodology used the hexagonal notation to describe their surfaces and to avoid confusion with their work, the C2/m lattices for both Ni and Mn systems have been converted to their $R\overline{3}m$ O'3-type equivalents such that the all surfaces align with those seen by Kramer and Ceder⁴⁷.

This lattice conversion is achieved by the matrix transformation:

$$L(R\overline{3}m) = \frac{1}{6} \begin{bmatrix} 3 & 3 & 0 \\ 3 & -3 & 0 \\ -1 & 1 & 1 \end{bmatrix} L(C2/m)$$
 (5.2)

This results in the following Miller plane conversions in Table 5.1.

Miller Plane (C2/m)	Miller Plane (R3m)
[1, 1, 1]	$[1, 0, \overline{1}, 4]$
[0, 0, 1]	[0, 0, 0, 1]
[-1, 1, 1]	$[0, 1, -\overline{1}, 2]$
[0, 1, 0]	$[1, 1, -\overline{2}, 0]$
[3, 3, -1]	$[1, 0, -\overline{1}, 0]$

TABLE 5.1: The Miller planes in the C2/m lattice and their equivalents when converted to the $R\bar{3}m$ lattice.

The selected choice of surfaces to investigate was limited to those outlined by Kramer and Ceder. These surfaces are noted for their low Miller index (4 max) and are resultant of minimal coordination loss of Co. This is because coordination loss of transition metals creates high energy surfaces. While, the high symmetry of the $R\overline{3}m$ lattice results in plenty of these surfaces being equivalent (i.e. the $[0,1,\overline{1},2]$ and $[1,\overline{1},0,2]$), with equivalency easy to find via index permutation and inversion, this is not true

in the transformed systems. The Jahn Teller effect breaking the a/b axis symmetry of the lattice results in slabs which are near-equivalent with the only difference being the alignment of the Jahn Teller bonds to the surface. The Jahn Teller effect is likely to have significant impact on the total energy of a system ^{267–269}, the alignment of Jahn Teller bonding to a surface has been shown to have similar impact on the surface energies of these systems ⁵², however there is little suggestion that surface directional Jahn Teller are practical as such this effect was not investigated.

Using the PyMatGen Slab module, all surfaces were generated to have a minimum repeat unit of 9 layers (around 20 Å) and 15 Åof vacuum. These slabs were aligned with their normal parallel to the c-axis and are centrosymmetric to minimize polarity between slabs. Excluding the electrostatic differences between Li and Co, the $[1, 0, \overline{1}, 4]$, $[1, 0, \overline{1}, 0]$ and the $[1, 1, \overline{2}, 0]$ are possible to cleave such that the resulting surfaces are non-polar and stiochiometric, thus being Tasker Type 1/2 and possessing a finite energy. However, this is not possible with the [0, 0, 0, 1] and $[0, 1, \overline{1}, 2]$ surfaces with stiochiometric cleavage resulting in slab polarity and are not suitable for DFT calculation. In the literature two methodologies of addressing this are seen. Firstly, non-stiochiometric cleavage and using chemical potentials to accurately calculate surface energies, Secondly, migration of half a mono-layer from one surface to the other yields a charge neutral slab (see Figure 5.6 as examples).

Both methods yield slabs with some drawbacks and approximation. Throughout this body of work the second methodology was employed, migrating a proportion of the species to the other side of the slab to obtain charge neutrality. It should be noted that in reality cathode surfaces are far from pristine with numerous different adsorbates and terminating groups. The slabs used here are approximate models aimed to investigate an 'idealised' surface. The surfaces investigated can be found in Figure 5.7.

The [0, 0, 0, 1] slab has been reconstructed by migrating $\frac{1}{2}$ of the Li ions to the other side of the slab. This results in a $\frac{1}{2}$ mono-layer surface of Li, zero surface Cobalt and charge neutrality. Similarly, the $[0, 1, \overline{1}, 2]$ has been reconstructed by migrating $\frac{1}{2}$ of the oxygen to the other side of the slab, this results in this surface having five coordinate surface Co. Cleavage across the $[1, 0, \overline{1}, 0]$ plane yields a slab that is non-polar with Co

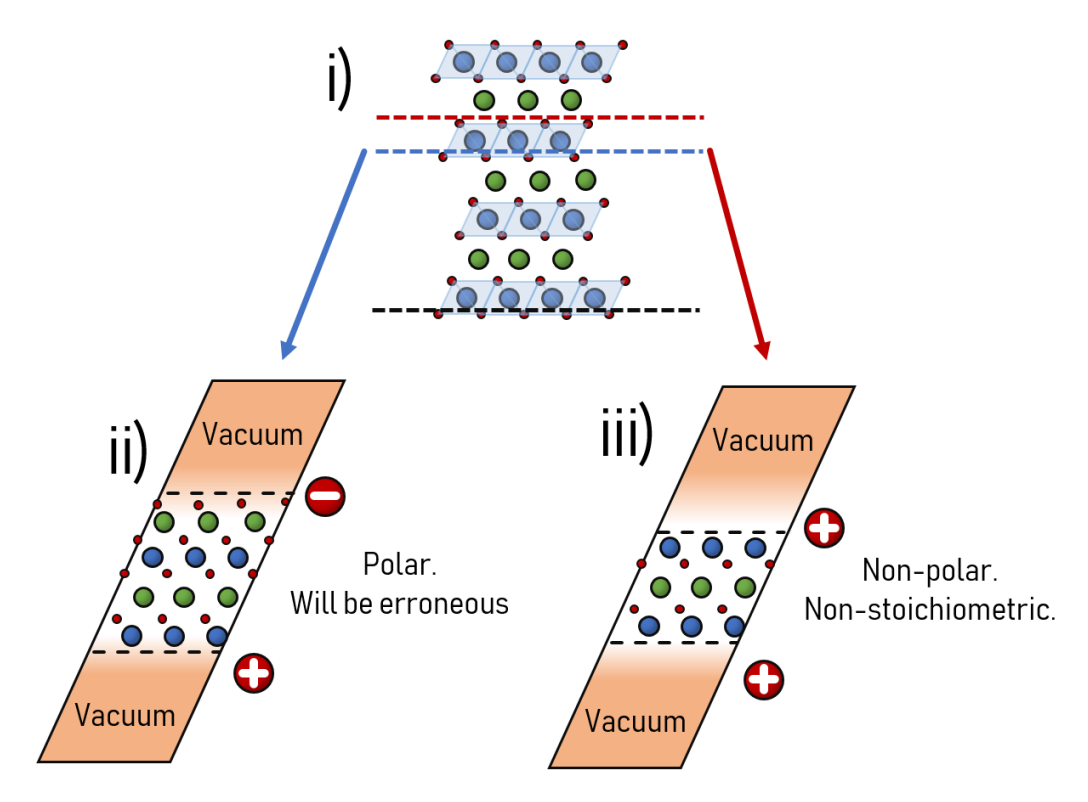


FIGURE 5.6: Cleavage of the [0, 0, 0, 1] surface is impossible without slabs being either polar (ii) or non-stiochiometric (iii).

that is three coordinate and five coordinate, cleavage of the $[1, 1, \overline{2}, 0]$ plane yields a surface that is non polar with four and six coordinate surface Co. Finally, the $[1, 0, \overline{1}, 4]$ slab is non-polar and has five and six coordinate surface Co.

These surfaces were investigated at end members of lithiation (Li_xMO_2 where x = 0 and 1) for Co, Ni and Mn systems.

5.0.1.4 Surface energies of layered metal oxides

Previous literature has discussed surface energies of a plethora of battery materials. $^{47-51,270,271}$. In particular Kramer and Ceder discuss the Wulff shape and electronic structure of the O3-type LiCoO₂ surfaces under various conditions. More recently, the electronic structures have been shown to be highly sensitive to the initialised magnetisation, with a previously undiscovered intermediate spin-state (between high and low) being shown to exist at these surface.

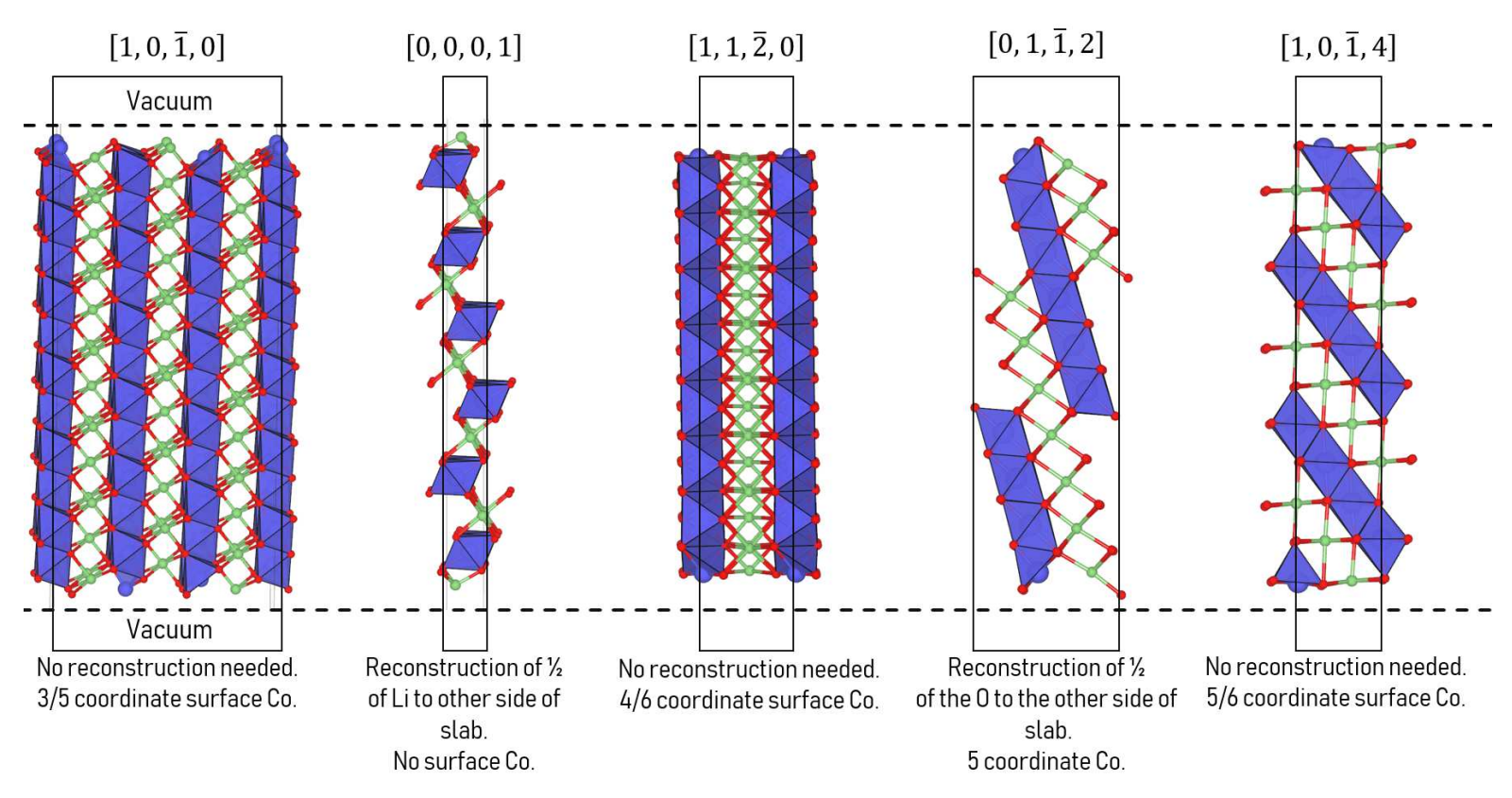


FIGURE 5.7: The generated surface slabs for LiMO₂. When applicable they have been reconstructed to be non-polar.

Surface energies for a few surfaces have been reported in the literature for all three metals, $^{47-52}$ as is common in cathode research, data for the Co system is ubiquitous while there are some gaps in the literature for the other metals. Despite this, the Co surfaces are still delivering new insight. The electronic structure for the $[1, 0, \overline{1}, 4]$ surface has been shown to be highly sensitive to the initialised magnetization, with an intermediate spin-state being shown to stabilise this surface. The summarised surface energies can be found in Table 5.2.

	LiCoO ₂		LiNiO ₂		LiMnO ₂	
	$\overline{\gamma}$	γ (ref.)	γ	γ (ref.)	γ	γ (ref.)
[0, 0, 0, 1]	1644	1250^a , 1490^d , 1040^e , 824^f	910	729 ^f	1041	868^{f}
$[1, 0, -\overline{1}, 0]$	3104	$2943^a \ 2321^f$	2130	1897 ^f	2317	2068^{f}
$[1, 1, -\overline{2}, 0]$	2388	2241^a , 1540^e , 1537^f	2011	1801^b , 1437^f	1791	1652^{f}
$[0, 1, -\overline{1}, 2]$	1328	2100^a , 1652^e , 2134^f	1365	1738^{f}	1581	1627^{f}
$[1, 0, \overline{1}, 4]$	818*	1048^a , 873^b , 1048^e , 1028^f	525	625^b , 446^f	493	262^{f}

TABLE 5.2: Calculated surface energies in mJ/ m^{-2} in comparison to those found in the literature. The [1, 0, $\bar{1}$, 4] surface is found to be low energy for all three metals. Lit. a: Kramer and Ceder⁴⁷, b: Vallverdu et al²⁷², c: Dahéron et al²⁷³, d: Hu et al²⁷¹, e: Hong et al²⁷⁴, f: Jiao et al⁵².

Some of the delithiated equivalents of the surfaces seen in Figure 5.7 were also investigated and their surface energies can be found in 5.3. From publication to publication that there is a large disparity seen regarding the scale of surface energies, with $\pm 50\%$ seen between publications. Additionally, few publications have investigated multiple surfaces for all three metal systems ⁵². Between, publications the one consistent trend is that the $[1, 0, \overline{1}, 4]$ surface is a low energy surface and this along with the [0, 0, 0, 1] surface contributes most of the surface area in these crystallites forming hexagonal platelets. ³⁴

	CoO ₂ γ	NiO ₂ γ	MnO ₂ γ
[0, 0, 0, 1]	910	881	1047
$[1, 0, -\overline{1}, 0]$	_		_
$[1, 1, -\overline{2}, 0]$	_		_
$[0, 1, -\overline{1}, 2]$	913	704	1104
$[1, 0, \overline{1}, 4]$	745	604	914

TABLE 5.3: Calculated surface energies in mJ m^{-2} for delithaited surface slabs. The [1, 0, $\overline{1}$, 4] surface remains low energy for these surfaces.

Since the majority of synthesis methods form cathode material at high lithiation, the surface energies for the delithiated end-members will not play a thermodynamic role

in crystallite shape at synthesis and thus are less relevant. The majority of the results seen for the lithiated member are in agreement with Jiao et al 52 . A large proportion of these crystallites are going to consist of the both the $[1, 0, \overline{1}, 4]$ and the [0, 0, 0, 1] surfaces. The [0, 0, 0, 1] surface inhibits Li migration upon formation and there is limited interest in investigating layered to Spinel transformation of this surface, instead inhibiting it's formation is a more relevant point of discussion. Kramer and Ceder discuss inhibiting [0, 0, 0, 1] formation at synthesis by using a reducing environment. Constrastingly, methods that inhibit breakdown of the key $[1, 0, \overline{1}, 4]$ surface could yield significant battery performance as Li diffusion occurs through this surface and this has a large crystallite coverage.

Relaxation of the $[1, 0, \overline{1}, 4]$ surface showed limited ionic migration for the Cobalt system, with ionic displacements of both metal and Li sites being < 0.10 Å. A small change in the of the surface bound oxygens was observed, this is likely compensating the dangling bond of the square pyramidal surface metal. This results in one oxygen migrating slightly toward the vacuum (0.11 Å) and the neighbouring oxygen migrating away (0.06 Å). This displacement is further pronounced in the zero-Li slab (CoO_2) with the surface oxygen migrating 0.38 Åtoward the vacuum, suggests that Li-O surface interactions inhibit this process. To further investigate, the dangling bonds of this Cobalt slab was terminated with an oxygen species and this small displacement was no longer seen. Since these surfaces are rarely pristine it's unclear whether this effect is a result of the model and if its likely to exist. The initialised (light colors) and relaxed (dark colors) surfaces are shown in Figure 5.8.

Constrastingly, relaxation of Ni and Mn slabs do show significant ionic migration. This is not in the c-axis but in the surface states. This effect is significant in the LiMnO₂ slab and is likely the result in the change in distortion Jahn Teller as the Jahn Teller extended M-O bond lengths become less distorted (from 20% extended to just 6%). With the lattice parameter of these surface states governed by the bulk crystallite it's likely that such states are unable to fully relax and thus are in a strain state. The initialised and relaxed of the LiMnO2 slab surface is shown in Figure 5.9.

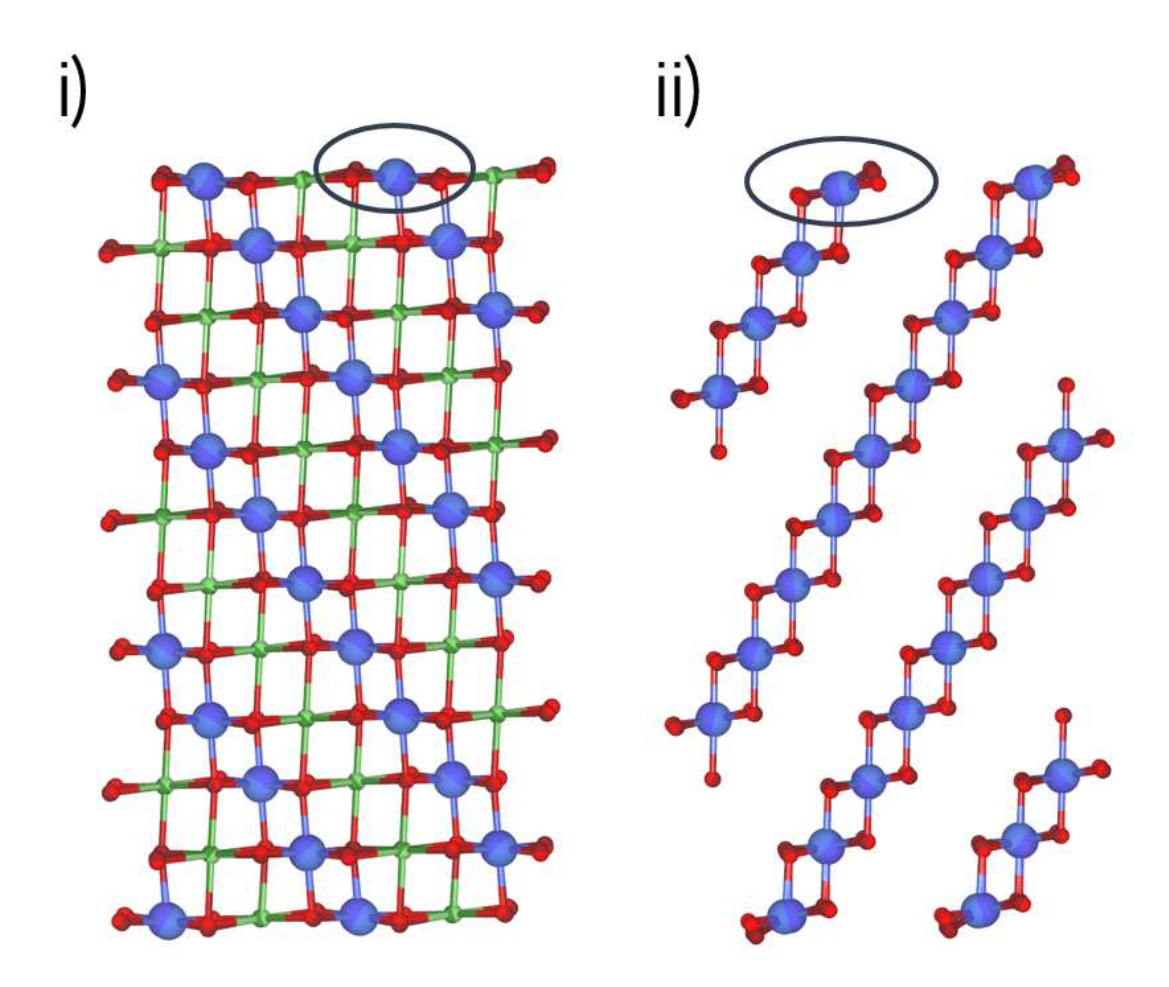


FIGURE 5.8: Relaxation of the $[1, 0, \overline{1}, 4]$ LiCoO₂ surface results in a small migration of the surface oxygen into the vacuum, this is further pronounced in the delithiated surface slab. Light colors represent the initial slab, darker colors the relaxed slab.

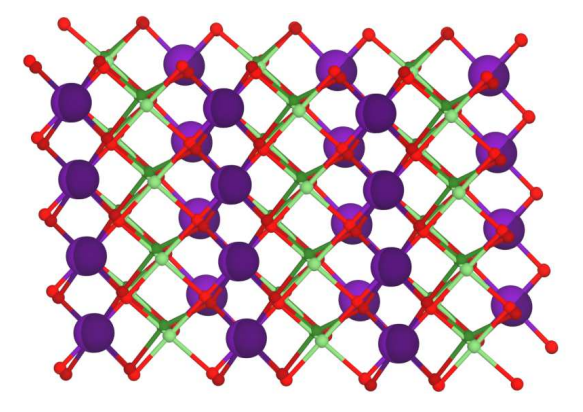


FIGURE 5.9: The surface geometry of a LiMnO₂ [1, 0, $\overline{1}$, 4] slab. Relaxation a reduction of the Jahn Teller distorted Mn-O bonds. Light colors represent the initial slab, darker colors the relaxed slab.

The final net spin of the LiCoO₂ [1, 0, $\overline{1}$, 4] slab is highly sensitive to the initialised magnetic spin. Setting the net spin of each Co site to zero (as is with the bulk) often results in the slab being spin zero and a corresponding surface energy of ≈ 1000

meV/m⁻2. However initialising the magnetic moment of the surface sites to be high-spin results in a surface energy of ≈ 900 meV/m⁻2.

Importantly, Hong et al 48 discuss in detail the presence of a stabilised "intermediate spin state" that results in a two-dimensional splitting of the d orbitals. This state is only found by initialising the surface spins to be between low and high spin, often requiring damping the mixing algorithm within VASP. This state is found to be the ground-state configuration for this surface yielding a surface energy of 745 meV/m^{-2} .

The presence of this spin state can be rationalised through crystal field theory. For [1, $0, \overline{1}, 4$] surface, a singular Co-O bond is cleaved and the surface metal polyhedra is CoO_5 in a square pyramidal geometry. The d orbitals of a metal in a square pyramidal coordination ML_5 are typically derived from O_h ML_6 that has dissociated a singular ligand. 60,230,275 . The possible d orbital occupation of the surface Co^{3+} state can be seen in Figure 5.10.

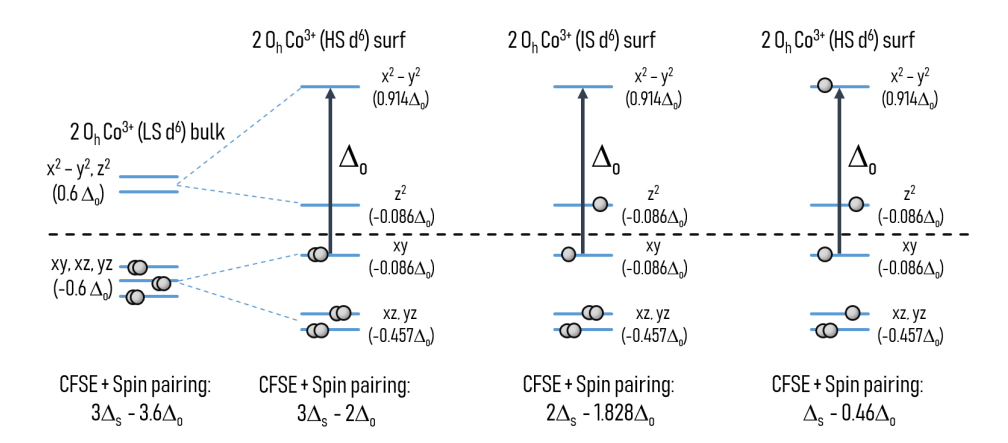


FIGURE 5.10: Crystal field splitting diagram for a Co^{3+} ion in an Octahedral and square pyramidal geometry. the destabilised z^2 orbital allowing an intermediate spin state.

For Co³⁺, this intermediate spin state unpairs an electron at the expense of only a small destabilisation of the crystal field and as a result, the intermediate spin state is favoured. It's likely that the degree of this stabilisation is dependant on the choice of Hubbard U and further investigation of these surface energies under this parameter is required.

5.1 Cation segregation energies in layered mixed metal oxides

Metal migration toward the surface (to form Spinel or to leech into the electrolyte) has been observed after cycling. ⁶³ While the exact pathway is likely dependant on composition, degree of lithiation, applied potential and the nature surface and question, investigating the is thermodynamics of segregation will identify the expected trends in NMC cathodes.

For instance, in Lithium rich Nickel-Manganese systems, the formation of Spinel at and near the surface has been identified to involve metal densification of which Mn has been demonstrated to migrate faster than Ni, yielding a Ni rich surface. 46,55. More recently, 54 DFT+U/HSE06 modelling suggests that there is no evidence of a driving force for Ni segregation in NMC under equilibrium. Instead, corroborating with the mechanism described by Boulineau et al 46 this process occurs via Li/Ni exchange, which is exacerbated under lattice strain.

Similarly to Garcia et al,⁵⁴ cation segregation energies are investigated, for the [1, 0, $\overline{1}$, 4] surface. However, a different approach is taken than their work. Suggesting a Co/Ni/Mn composition yields a disordered structure (of which there are in principle an infinite number of Co, Ni and Mn orderings). This is particularly problematic for slab generation as assigning these disordered sites naturally introduces segregation which is the exact thing attempting to be measured. Garcia et al ^{53,54} investigated the high symmetry stiochiometric case (Co = Ni = Mn = $\frac{1}{3}$) with the metal sites alternated between the metals in question. While entropically this configuration is the most likely there is evidence that these materials show little ordering with no superstructure ²⁷⁶ aswell as localised cation grouping. ^{277,278}

Instead, the configuration problem is avoided here by investigating the dilute binary compositions. That is the compositions $\operatorname{Li}_x M_1^\dagger M_{x-1}^* O_{2x}$ (where M^\dagger and M^* is Co, Mn and Ni). As seen in Equation 5.3 the thermodynamic driving force for a metal to be located at the surface of a slab is equivalent to the change in surface energy. By investigating slabs in which M^\dagger is located at the surface in comparison to slabs with

 M^{\dagger} in bulk the metal segregation energy can be calculated for a dilute metal M^{\dagger} within a parent LiM*O₂ slab (void of any interactions derived from ordering effects).

$$E(seg) = \Delta \gamma = \gamma(M^{\dagger} \text{at surface}) - \gamma(M^{\dagger} \text{in bulk})$$
 (5.3)

Clearly when $M^{\dagger} = M^*$ this segregation is zero as the two structures are equivalent.

To perform such a calculation however, the distance between M^{\dagger} sites must be sufficiently large to not interact across periodic boundary conditions and therefore the unit cell must be sufficiently large in the a and b axis. This in conjunction with the necessary large slab thicknesses results in these model slab being computationally demanding. A bulk calculation was avoided altogether by utilising the central layer within the slab as 'bulk'. The model $[1, 0, \overline{1}, 4]$ surface slabs for a Ni both within bulk and at the surface can be found in Figure 5.11. Similar slabs were prepared for Ni:Mn, Co:Ni, Mn:Ni, Mn:Co and Co:Mn such that the surface segregation is explored for all possible dilute configurations.

As seen in Figure 5.11i, the non-segregated slab is centrosymmetric on the Ni site (M^{\dagger}) , thus the small electrostatic differences between Ni and Co are cancelled and the slab remains symmetric and non-polar. For the surface segregated slab (Figure 5.11ii), the migration of a Ni to one of the surfaces would result in this symmetry breaking and the slab being polar, to combat this, centrosymmetry is abused once more, defects are placed at opposite sides of the slab thus ensuring no polarity. This would result in a loss of the stiochiometry (since now two metals are segregated per formula unit). As seen in Figure 5.11, to re-establish stiochiometry the non-segregated slab is half the size of the segregated slab $(2 \times 1 \times 1 \text{ supercell})$. More importantly, this methodology ensures symmetry across the unit-cell greatly reducing the computational cost of these calculations.

These $[1, 0, \overline{1}, 4]$ slabs were relaxed using a 800 eV energy-cutoff within the PBE+U methodology used throughout this work. This choice of cutoff is such to match that seen in the literature ⁴⁷. Similar ionic relaxation was observed to the parent metal systems, with all metal sites moving less than 0.10 Å. For the bulk Co materials,

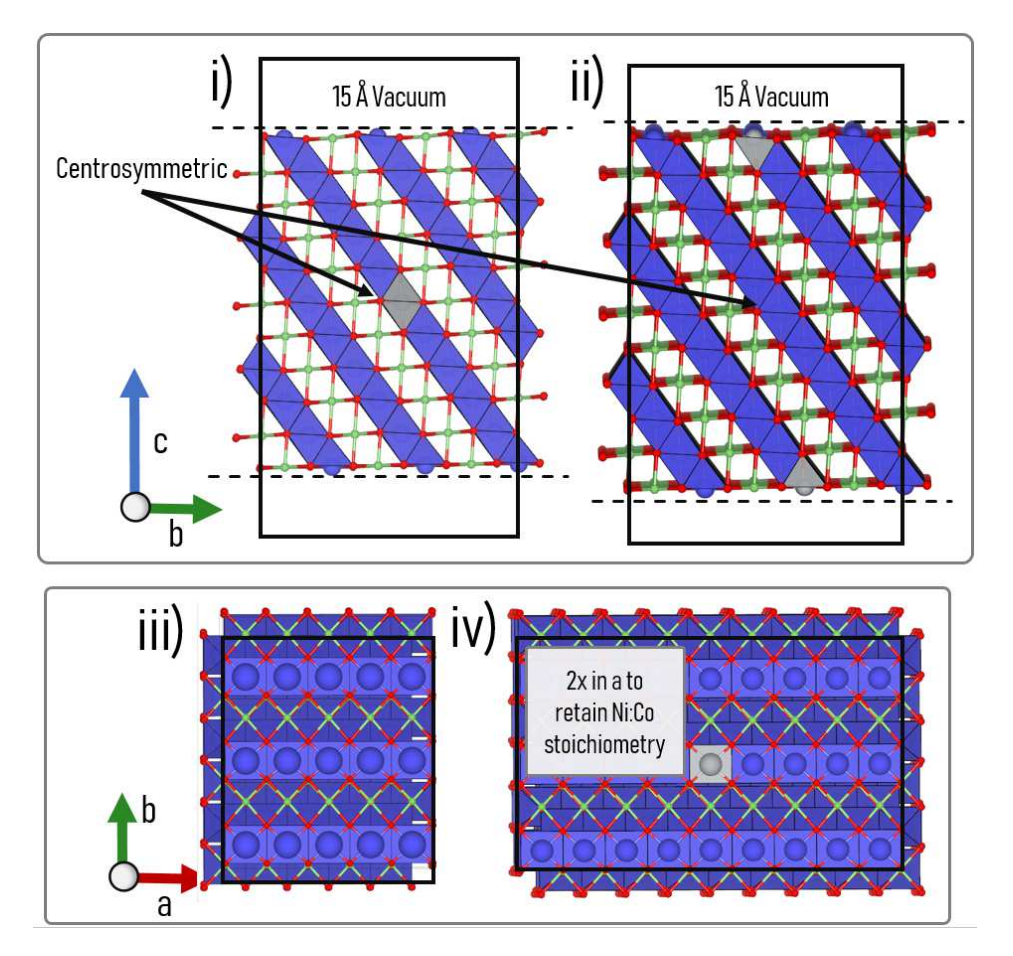


FIGURE 5.11: Slabs used for calculation of surface segregation energies. i/ii) The slabs as viewed down the a axis, M^{\dagger} is located in the bulk and at the surface respectively. iii/iv) The slab as viewed down the c axis, when M^{\dagger} is at the surface the unit-cell needs to be twice as big to maintain stiochiometry.

 $(\text{Li}_{102}\text{MnCo}_{101}\text{O}_{204} \text{ and } \text{Li}_{102}\text{MnCo}_{101}\text{O}_{204})$ the intermediate spin state that was found for surface Co is maintained, with similar sensitivity to the initialised magnetic moments as before. The low-spin state was also investigated and the segregation energies remained similar between systems.

It's found that both Ni and Mn dilute within a parent Cobalt lattice prefer to be located at the surface. Additionally, an isolated Co within a parent Ni or Mn lattice has a positive segregation energy and thus these surfaces are lower energy when they are mono-metallic (i.e. Co remains in the bulk). Both of these results suggest that in NMC surfaces that are low proportion Cobalt are likely to have increased stability.

Although the slab calculations for Ni vs Mn systems suggest that surface energies are lower when Ni is located at the surface (at both high and low concentration Mn), these

Parent lattice	Metal subs. (M†)	Preferred site	Energy difference (meV/M [†] atom)
LiNiO ₂	Mn	bulk	18.35
LiNiO ₂	Co	bulk	82.64
$LiMnO_2$	Ni	surface	-3.54
$LiMnO_2$	Co	bulk	112.2
LiCoO ₂	Ni	surface	-35.6
LiCoO ₂	Mn	surface	-34.50

TABLE 5.4: Segregation energies of LiM[†]M*O₂. Positive energies show a enthalpy to be located within the bulk while negative energies show enthalpy toward the surface.

energy differences are an order of magnitude smaller than the Cobalt cases (> 20 meV/atom) and unlikely to be significant. A summary of these segregation energies can be found in Table 5.4.

5.2 Ion migration for key metal surfaces

Boulineau et al⁴⁶ been demonstrated that there is some evidence that the surface composition of NMC will deviate from the bulk composition, with bulk material becoming Co rich and surfaces becoming Mn rich. This is troublesome since Mn has been shown to be liable to layered to Spinel degradation, which may be exacerbated by the harsh conditions near the surface.

However, investigating metal migration pathways for these surfaces is challenging. Unlike the bulk material, each metal site is non-equivalent (along the c-axis) and therefore defects and the minimum energy pathway in forming them are site specific. As a result this investigation is limited to only the $[1, 0, \overline{1}, 4]$ surface.

5.3 Transition state analysis of surfaces at and near the end-member ${\rm Li_0MO_2}$

The end-member structures are perhaps the simplest surfaces to model. The removal of all Li sites reduces the degrees of freedom from depth-specific Li/ V_{Li} orderings. While, it's been demonstrated that layered cathodes are resistant to layered to Spinel

degradation in the bulk, there is no atomistic studies investigating these surfaces. Using the exact same pathway discussed for the bulk materials (A \rightarrow E), the defect energy of a T_d metal can be calculated as a function of depth from the surface.

5.3.1 Generation of initial and final states

A 12 layer [1, 0, $\overline{1}$, 4] slab was generated with an inversion center situated between layers 6 and 7 to maintain a non polar slab two defects were placed per unit cell (for each face of the slab). A $4 \times 3 \times 1$ supercell was used to ensure no defect-defect interaction. The undefected structure (A₁₀₁₄) can be found in Figure 5.12i. Interestingly, defects may form by migration to T_d in the Li layer either toward or away from the surface (Figure 5.12ii). Only migrations toward the surface was considered to reduce computational load.

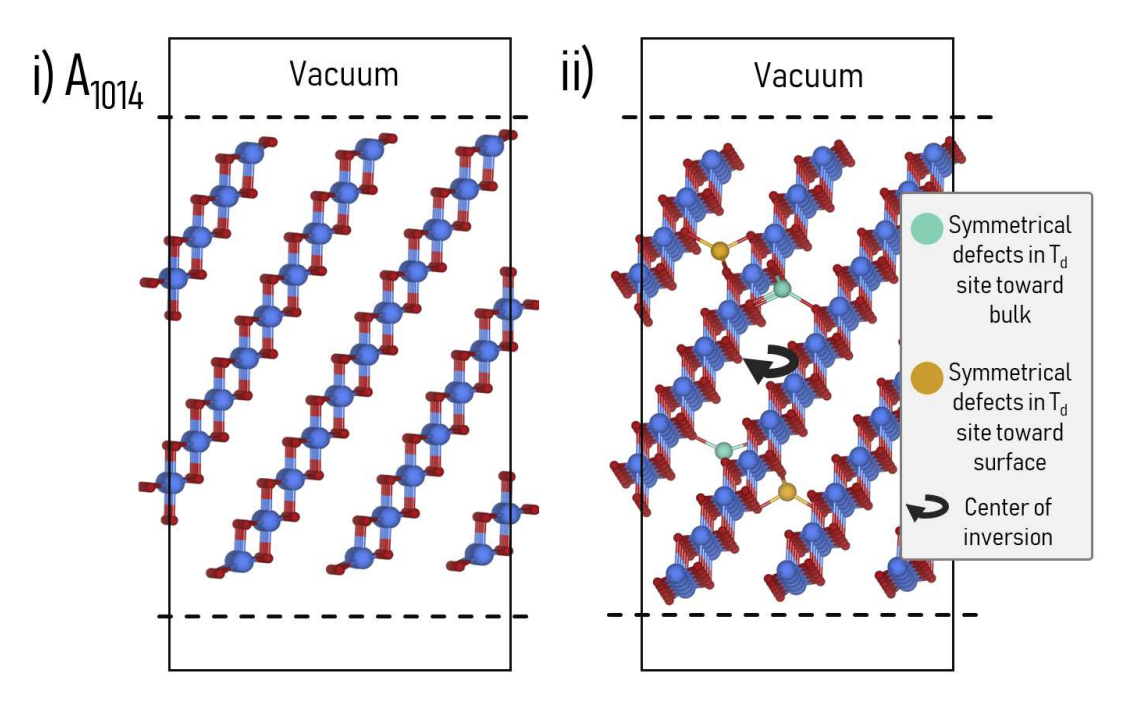


FIGURE 5.12: i) The undefected $[1, 0, \overline{1}, 4]$ slab of a zero-lithiated system. ii) symmetrical defects can either migrate toward (yellow) or away (green) from the surface.

Figure 5.13 shows that there There are numerous possible T_d defects states (E) (dependant on depth from surface). By measuring defect energies further and further into the bulk, the impact that surface states and the under-coordinate metal have on layered to Spinel transformation can be identified. Of course this surface effect only

penetrates so deep into the slab and thus at a certain layer depth N, the defect energy will be equivalent to the bulk defect energy. Using a slab of size 12 yields five possible $O_h \to T_d$ migrations to investigate.

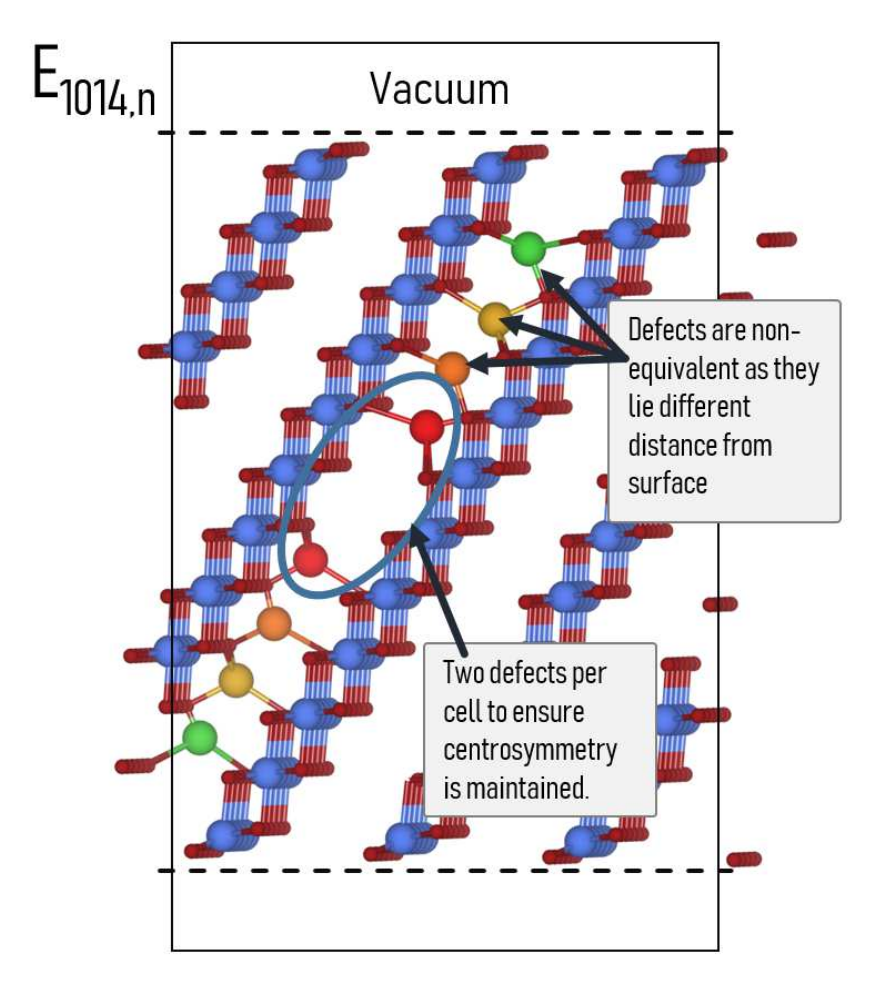


FIGURE 5.13: Unique T_d sites within the Li layer in which a metal can migrate into. Since each defect has a different distance from the surface they are non-equivalent.

5.3.2 Defect energies and minimum energy pathways at the surface of a zero Li crystallite.

Both the undefected slab and the defected slabs were geometry optimized using a 800 eV plane wave cut-off and the PBE+U functional seen for bulk calculations. Lattice parameters were fixed for all three metals at their bulk lattice parameter to model a crystallite surface. Similarly to the bulk delithiated systems, state E is higher in energy, with defects located far from the surface (i.e. orange and red in Figure 5.13) being representative of the bulk.

When the defect is located two or more monolayers away from the surface there is a near-zero disruption to the MO_2 sheets and the surface geometry for all three metals slabs. Upon relaxation, the surface oxygen deviates away from the slab toward the vacuum. However, the addition of a tetrahedral metal defect in the monolayer below $(E_{10\overline{1}4,1ml})$ reduces this effect pulling the oxygen back into the surface plane (see Figure 5.14).

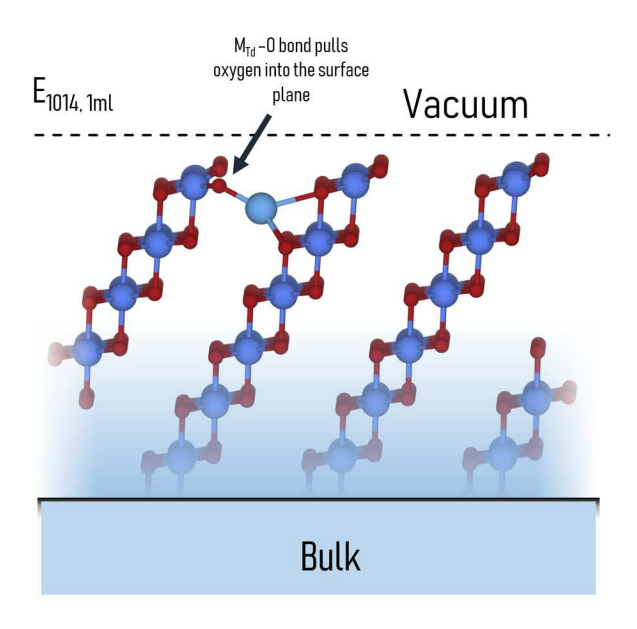


FIGURE 5.14: For the CoO_2 system a defect site close to the surface forms a bond with the surface oxygen and this oxygen is pulled back into the plane.

This T_d defect is notable in that it has a lower defect energy than that seen at the bulk (1.1 eV vs 2.0 eV for near-surface and bulk respectively). This suggests that the [1, 0, $\overline{1}$, 4] surface is stabilised when a metal site migrates into the Li layer just below the surface. The defect energies as a function of depth from the surface can be found in Figure 5.15. It's noted that the Mn system also shows significant stabilisation of the one monolayer deep defect however further investigation is required to discern the nature of this stabilisation.

Modelling transition states of these near surface defects using nudged elastic band theory is a next step to identifying the likelihood of dumbbell formation and thus Spinel degradation. However, investigating compositions away from the dilute limit of lithiation is problematic. The arrangement of Li/V_{Li} vacancies near the surface will likely play a significant role in surface energies and thus the pathway described for

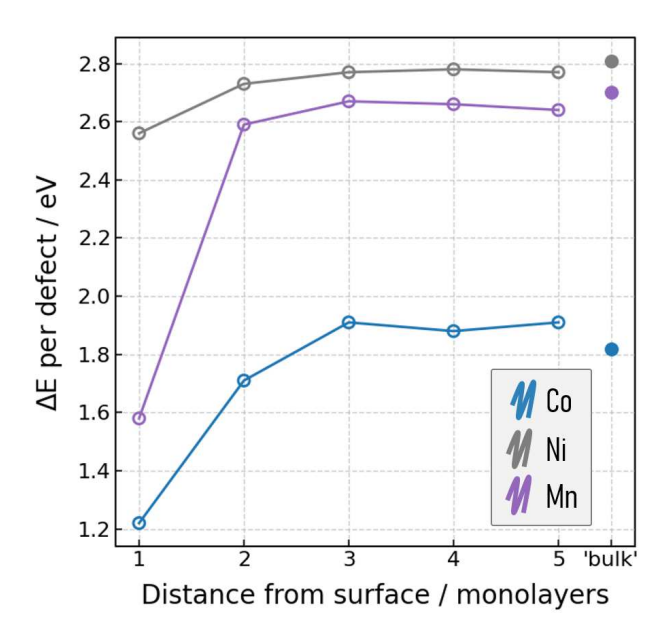


FIGURE 5.15: Tetrahedral defect energies as a function of depth for the delithiated [1, 0, $\overline{1}$, 4] surface slabs (MO₂ where M = Co, Ni and Mn). Filled circles indicate the bulk calculations.

the bulk systems is not applicable. While a specific $\mathrm{Li/V}_{Li}$ arrangement can be picked as a model system (i.e. one of high symmetry) there will be little confidence in conclusions drawn from those results without any investigation into the relative stability of this arrangement at the near the surfaces.

Additionally, while symmetry was utilised in these slabs as a means of keeping the slab non-polar this yields two migrating (albeit symmetric) ions migrating across the defect pathway. This has unforeseen consequences during the nudged elastic band calculation as the minimum energy pathway found discretizes the mobile ions into two distinct $O_h \rightarrow T_d$ hops. As a result, the model systems for defects seen here an inapplicable to transition state calculations.

5.4 Summary

NMC cathodes have displayed layered to Spinel transformation at and near the surface. ⁶³ Investigating mixed metal oxide surfaces yields a difficult configuration problem, where the relative ordering of Co/Ni/Mn determines the bulk unit cell and thus the polarity and surfaces of the Miller planes cleaved along. Since these

5.4. Summary 159

structures have been demonstrated to show no quantifiable ordering ²⁷⁶ an alternate approach of investigating the mono-metallic oxide surfaces and their equivalent binary oxides at the dilute limit. While this approach does not investigate the impact that relative metal ordering may or may not have at these surfaces it does describe a simple model to determine the thermodynamics of key cathode surfaces and the driving force to segregation.

Model surface slabs were investigated for $\text{Li}_x MO_2$ where M = Co, Ni or Mn and x = 0 or 1. Similarly to that found in the literature, 52 two key surfaces were found to have a low surface energy, the $[1, 0, \overline{1}, 4]$ and the [0, 0, 0, 1] surface. In particular the $[1, 0, \overline{1}, 4]$ surface is of high importance as the Li channels are directed toward the vacuum and thus channels will be in contact with electrolyte in a battery. Therefore investigating the driving forces to degradation at this surface are of high importance.

While metal segregation has been experimental observed, ⁴⁶ this has been attributed to a mechanism involving oxygen loss into the electrolyte. It's found here that when crystallite composition is maintained (i.e. no loss to electrolyte) the thermodynamics governing surface segregation (¿ 20 meV/ atom for binary Ni/Mn cathodes) are small suggesting that there is discernible change in surface energy when the concentration of metals at the surface deviate far from the bulk.

Tetrahedral defects were investigated for crystallites void of Li, this served as a simple model system where the configurational space is limited. Both the Co and Mn system displayed a significant stabilising surface interaction when the defect is bonded to a surface oxygen. The nature of this surface interaction is still an ongoing investigation, future work would like to investigate the extent of this interaction when the surface is terminated by a plethora of species.

It's identified that defects become representative of the bulk exceedingly close to the surface (three monolayers) indicating that future model systems need not investigate such a wide spread range of defect penetration depths. One area still left to explore is migration away from the surface, the mechanism by Boulineau et al ⁴⁶ specifically suggests metal ions using the Li plane to migrate away from the surface during

deoxygenation. Exploring the energy barriers to this process will yield insight into the validity of their mechanism.

Finally the dumbbell structure has been identified for bulk systems as an intermediate that facilitates Spinel formation. Investigating whether this dumbbell is found near the surface and the energy barriers to forming it will yield insight into methods that may inhibits surface degradation.

Chapter 6

Conclusions

In this research first principle calculation were used to investigate transition metal electrode materials. While phase stability has been discussed prior, there is a significant discrepancy within the literature regarding best modelling techniques, the parameters used and the crystal structures investigated for these metal oxide cathodes.

Using computational modelling stable compositions and their formation energies of binary metal oxides were investigated for the 3d transition metals metals. It was found that although layered structures are the predominant cathode structure, these structures with formula unit MO₂ are meta-stable. In particular Co, Mn and Ni all show that the delithiated Goodenough analog lies far above the convex hull. More importantly the stability of these structures at various degrees of lithiation and stacking sequences was investigated. Of the investigated stacking sequences (O3, O2 P2 and O1) the O3 type structure was found to be the thermodynamic ground state phase. However, it's been demonstrated that the choice of functional significantly impacts the trends observed for these materials with pure PBE functionals grossly mispredicting both lattice parameter and formation energies. This sensitivity to Hubbard U is a consistent and worrying trend observed in the literature, with formation energies varying by upward of 100 meV / f.u (with U = 0.0 and U = 3.3) and no clear determination of valid choice of U (with it often being seen as a user adjustable dial) identifying trends from literature source to literature source is an issue that is yet to be address by the scientific community at large.

At half lithiation it's found that a 180° Li-O-M-O-Li connectivity that runs through layer to layer results in the high symmetry P2/m structure being the low-lying and a good principle model structure for investigating processes at and around half lithiation. Additionally, at low degrees of lithiation, the interactions between MO_2 sheets are dominated by dispersion forces, with functionals void of dispersion corrections predicting significant lattice expansion in the delithiated state. A result that contradicts experimental results not observed.

Investigations into layered to spinel transformations were considered at zero, near-zero and half lithiation using the stable structures identified prior. Since the lattice parameter was shown to be significantly dependent on dispersion interactions at low lithiation, defect energies and minimum energy pathways were calculated in varied parent cells. It's found that the grossly mispredicted lattice parameter calculated in the PBE+U functional results in disagreement in defect energies. However, much of this disagreement is removed when using consistent lattice parameters between PBE+U and PBE+U+D3 indicating that this effect is solely from the lattice parameter and T_d defects do not require dispersion corrections to correctly model. The delithiated structures were demonstrated to be resistant to spinel transformation for Co, Ni and Mn system with defect energies in excess of 3.0 eV.

A novel pathway is suggested at the dilute limit of lithiation that avoid charge disproportionation, a lone Li ion within the Li layer has been shown to result in the reduction of a metal site in the MO_2 sheet. This valence change from M^{4+} to M^{3+} results in a significant change in the crystal field splitting energies for O_h and T_d metals and the energy barriers to forming a T_d metal defect in the Li layer decrease accordingly. While still involving large transition state barriers (greater than 0.8 eV) this pathway is exceedingly more feasible than the pathways discussed in the literature prior. This suggests that delithiated cathodes are only truly resistant to layered to spinel transformation when void of all Li and that any state greater than Li-zero may have an appreciable degradation rate.

The energy barriers for degradation of the half lithiated structure was also investigated, where its been argued through crystal field theory that the migrating

6.1. Future work 163

 $\rm Mn^{3+}$ species undergoes a charge disproportionation reaction with a neighbouring $\rm Mn^{3+}$ to form a stabilised Li- $\rm Mn^{2+}_{\it tet}$ dumbbell. This dumbbell has become a recurring thorn in the viability layered Mn cathodes. While doping strategies have investigated the stability of this dumbbell, here it's argued that the application of moderate tensile strain significantly destabilises this state and may be an avenue for hindering layered to spinel degradation and revitalising layered $\rm LiMnO_2$ as a cathode material.

Finally, a brief look is taken at the surfaces of these materials. Low energy surfaces have been identified and are constant across the three metals. In particular the $[1, 0, \overline{1}, 4]$ surface is of importance due to its low surface energy and the viability as a primary route of delithiation into the electrolyte. While there is little thermodynamic driving force for any particular metal to segregate toward this surface, it has been demonstrated that this can be stabilised by $O_h \rightarrow T_d$ metal migration toward this surface. This yields a insight into the energetics of near surface spinel formation.

6.1 Future work

There is significant variability in modern publications regarding choice of functional, in particular the values of Hubbard that correctly model cathodes. In particular, the framework for using the Hubbard U in binary or ternary metal oxides is unclear, these materials are known to occupy different oxidation states which is likely going to be sensitive to the scale of the on-site interactions. Development of a scheme or modelling framework that addresses these issues is likely to yield great benefit in unifying first principles modelling of these cathodes (and oxides in general). Bench-marking U values to hybrid functionals in the bulk of structures will likely further identify the pitfalls and shortcomings of DFT+U in general and elucidate strategies to avoid these.

The T_d defect energies of bulk mixed metal oxides was briefly considered investigating as both a means of identifying the viability of spinel formation in NMC and the impact of dopants. However this was avoided as addressing both the Li/V_{Li} orderings as well as $\text{M}^{\dagger}/\text{M}^{*}$ orderings was deemed challenging as the convex hulls for

the Li_xMO_2 system for the three metals indicates since they are likely coupled. Work identifying the extent of which metal arrangement and Li/V_{Li} arrangement are dependent on one another may yield a methodology for calculating transition state barriers for mixed metal oxides or even reveal that certain configurations are naturally resistant to this route of deformation.

Finally, the surface calculations have been briefly investigated here. Further investigation into the effect that termination of surface sites has on near-surface defects may yield a strategy to pre-coat these surface and inhibit spinel formation. Additionally, investigating metal $O_h \to T_d$ migration away from the surface will reveal insights into the mechanistic pathway for metal densification. Only the bare T_d metal defects have been investigated near the surface, these are large energy barriers within the bulk in contrast to the Li-M dumbbell formation. As a result work defining and identifying whether Li-M dumbbells are stabilised at the surface (both at near-zero and at half lithiation) is likely to yield a great insight into the rates of surface degradation.

References

- [1] M E Arroyo Y De Dompablo, A Van Der Ven, and G Ceder. First-principles calculations of lithium ordering and phase stability on Li x NiO 2. *Physical Review B*, 2002.
- [2] John Reed and Gerbrand Ceder. Role of electronic structure in the susceptibility of metastable transition-metal oxide structures to transformation. *Chemical Reviews*, 104(10):4513–4533, oct 2004. ISSN 00092665.
- [3] Ieuan D Seymour, Sudip Chakraborty, Derek S Middlemiss, David J Wales, and Clare P Grey. Mapping Structural Changes in Electrode Materials: Application of the Hybrid Eigenvector-Following Density Functional Theory (DFT) Method to Layered Li 0.5 MnO 2. *Chemistry of Materials*, 27(16):5550–5561, aug 2015. ISSN 0897-4756. URL https://pubs.acs.org/sharingguidelineshttps://pubs.acs.org/doi/10.1021/acs.chemmater.5b01674.
- [4] J. Reed, G. Ceder, and A. Van Der Ven. Layered-to-spinel phase transition in LixMnO2. *Electrochemical and Solid-State Letters*, 4(6), jun 2001. ISSN 10990062.
- [5] Anton Van Der Ven, Jishnu Bhattacharya, and Anna A. Belak. Understanding Li diffusion in Li-intercalation compounds. *Accounts of Chemical Research*, 46(5): 1216–1225, may 2013. ISSN 00014842. URL https://pubs.acs.org/doi/full/10.1021/ar200329r.
- [6] John Stuart Reed. *Ab-initio study of cathode materials for lithium batteries*. PhD thesis, M.I.T, 2003. URL https://dspace.mit.edu/handle/1721.1/29972.

[7] Ieuan D Seymour, David J Wales, and Clare P Grey. Preventing Structural Rearrangements on Battery Cycling: A First-Principles Investigation of the Effect of Dopants on the Migration Barriers in Layered Li 0.5 MnO 2. *The Journal of Physical Chemsitry C*, 2016. URL

[8] Yoyo Hinuma, Yu Kumagai, Fumiyasu Oba, and Isao Tanaka. Categorization of surface polarity from a crystallographic approach. *arXiv*, 2015.

https://pubs.acs.org/sharingguidelines.

[9] Anubhav Jain, Geoffroy Hautier, Shyue Ping Ong, Charles J. Moore, Christopher C. Fischer, Kristin A. Persson, and Gerbrand Ceder. Formation enthalpies by mixing GGA and GGA + U calculations. *Physical Review B - Condensed Matter and Materials Physics*, 84(4):045115, jul 2011. ISSN 10980121. . URL

https://journals.aps.org/prb/abstract/10.1103/PhysRevB.84.045115.

- [10] Luigi Galvani. *Aloysii Galvani De viribus electricitatis in motu musculari commentarius*. Ex Typographia Instituti Scientiarium, Bononiæ, 1791.
- [11] Alexander Volta and Joseph Banks. On the Electricity Excited by the Mere Contact of Conducting Substances of Different Kinds. In a Letter from Mr. Alexander Volta, F. R. S. Professor of Natural Philosophy in the University of Pavia, to the Rt. Hon. Sir Joseph Banks, Bart. K. B. P. R. S. *Philosophical Transactions of the Royal Society of London*, 90:403–431, 1800. URL https://about.jstor.org/terms.
- [12] Michael Faraday. V. Experimental researches in electricity. *Philosophical Transactions of the Royal Society of London*, 42(6):1286, dec 1832. ISSN 00027863. .
 URL
 - https://royalsocietypublishing.org/doi/abs/10.1098/rstl.1832.0006.
- [13] Aldo da Rosa. Storage of Energy. *Fundamentals of Renewable Energy Processes*, pages 821–862, jan 2013. .
- [14] John B. Goodenough. How we made the Li-ion rechargeable battery, mar 2018.
 ISSN 25201131. URL https://www.nature.com/articles/s41928-018-0048-6.

[15] K. Mizushima, P. C. Jones, P. J. Wiseman, and J. B. Goodenough. LixCoO2 (0;x;1): A new cathode material for batteries of high energy density. *Solid State Ionics*, 3-4(C):171–174, aug 1981. ISSN 0167-2738.

- [16] M Stanley Whittingham. Lithium Batteries and Cathode Materials. *Chemical Reviews*, 104(10):4271–4302, oct 2004. ISSN 0009-2665. . URL
 - https://pubs.acs.org/sharingguidelineshttps://pubs.acs.org/doi/10.1021/cr020731c.
- [17] Feixiang Wu and Gleb Yushin. Conversion cathodes for rechargeable lithium and lithium-ion batteries. *Energy and Environmental Science*, 10(2):435–459, feb 2017. ISSN 17545706. . URL https:

```
//pubs.rsc.org/en/content/articlehtml/2017/ee/c6ee02326fhttps:
//pubs.rsc.org/en/content/articlelanding/2017/ee/c6ee02326f.
```

- [18] M Stanley Whittingham and Fred R Gamble. THE LITHIUM INTERCALATES OF THE TRANSITION METAL DICHALCOGENIDES. *Mat. Res. Bull*, 0:0–363, 1975.
- [19] M. S. Whittingham. Electrical Energy Storage and Intercalation Chemistry. Science, 192(4244):1126–1127, jun 1976. ISSN 00368075. . URL https://www.science.org/doi/abs/10.1126/science.192.4244.1126.
- [20] Akira Yoshino. The Birth of the Lithium-Ion Battery. *Angewandte Chemie International Edition*, 51(24):5798-5800, jun 2012. ISSN 1521-3773. . URL https://onlinelibrary.wiley.com/doi/full/10.1002/anie.201105006https://onlinelibrary.wiley.com/doi/abs/10.1002/anie.201105006https://onlinelibrary.wiley.com/doi/10.1002/anie.201105006.
- [21] Renheng Wang, Weisheng Cui, Fulu Chu, and Feixiang Wu. Lithium metal anodes: Present and future. *Journal of Energy Chemistry*, 48:145–159, sep 2020. ISSN 2095-4956.
- [22] Xiaohui Shen, Zhanyuan Tian, Ruijuan Fan, Le Shao, Dapeng Zhang, Guolin Cao, Liang Kou, and Yangzhi Bai. Research progress on silicon/carbon composite anode materials for lithium-ion battery. *Journal of Energy Chemistry*,

```
27(4):1067-1090, jul 2017. ISSN 2095-495. . URL /doi/10.1016/j.jechem.2017.12.012.
```

- [23] Hui Cheng, Joseph G. Shapter, Yongying Li, and Guo Gao. Recent progress of advanced anode materials of lithium-ion batteries. *Journal of Energy Chemistry*, 57:451–468, jun 2021. ISSN 2095-4956.
- [24] Célestin Banza Lubaba Nkulu, Lidia Casas, Vincent Haufroid, Thierry De Putter, Nelly D. Saenen, Tony Kayembe-Kitenge, Paul Musa Obadia, Daniel Kyanika Wa Mukoma, Jean Marie Lunda Ilunga, Tim S. Nawrot, Oscar Luboya Numbi, Erik Smolders, and Benoit Nemery. Sustainability of artisanal mining of cobalt in DR Congo. *Nature Sustainability*, 1(9):495–504, sep 2018. ISSN 23989629.

 . URL https://www.nature.com/articles/s41893-018-0139-4.
- [25] Naoki Nitta, Feixiang Wu, Jung Tae Lee, and Gleb Yushin. Li-ion battery materials: Present and future, jun 2015. ISSN 18734103.
- [26] A. Kirubakaran, Shailendra Jain, and R. K. Nema. A review on fuel cell technologies and power electronic interface, dec 2009. ISSN 13640321.
- [27] Baha M. Al-Alawi and Thomas H. Bradley. Review of hybrid, plug-in hybrid, and electric vehicle market modeling Studies, may 2013. ISSN 13640321.
- [28] Quanlu Wang and Mark A. DeLuchi. Impacts of electric vehicles on primary energy consumption and petroleum displacement. *Energy*, 17(4):351–366, apr 1992. ISSN 03605442. . URL
 - https://linkinghub.elsevier.com/retrieve/pii/036054429290110L.
- [29] Zachary P. Cano, Dustin Banham, Siyu Ye, Andreas Hintennach, Jun Lu, Michael Fowler, and Zhongwei Chen. Batteries and fuel cells for emerging electric vehicle markets, apr 2018. ISSN 20587546. URL https://www.nature.com/articles/s41560-018-0108-1.
- [30] Oi Lun Li and Takahiro Ishizaki. Development, challenges, and prospects of carbon-based electrode for lithium-air batteries, pages 115–152. Elsevier, 1 2018. ISBN 9780128137949. . URL
 - https://linkinghub.elsevier.com/retrieve/pii/B9780128137949000041.

[31] Feng Lin, Isaac M. Markus, Dennis Nordlund, Tsu Chien Weng, Mark D. Asta, Huolin L. Xin, and Marca M. Doeff. Surface reconstruction and chemical evolution of stoichiometric layered cathode materials for lithium-ion batteries.

Nature communications, 5(1):3529, mar 2014. ISSN 20411723. . URL

www.nature.com/naturecommunications.

- [32] T. R. Ashwin, Yongmann M. Chung, and Jihong Wang. Capacity fade modelling of lithium-ion battery under cyclic loading conditions. *Journal of Power Sources*, 328:586–598, oct 2016. ISSN 03787753. .
- [33] Abbas Fotouhi, Daniel J. Auger, Karsten Propp, Stefano Longo, and Mark Wild.

 A review on electric vehicle battery modelling: From Lithium-ion toward

 Lithium-Sulphur, apr 2016. ISSN 18790690.
- [34] Kun Zhang, Biao Li, Yuxuan Zuo, Jin Song, Huaifang Shang, Fanghua Ning, and Dingguo Xia. Voltage Decay in Layered Li-Rich Mn-Based Cathode Materials. Electrochemical Energy Reviews 2019 2:4, 2(4):606–623, aug 2019. ISSN 2520-8136. .

 URL https://link.springer.com/article/10.1007/s41918-019-00049-z.
- [35] Ming Jiang, Dmitri L. Danilov, Rüdiger A. Eichel, and Peter H.L. Notten. A Review of Degradation Mechanisms and Recent Achievements for Ni-Rich Cathode-Based Li-Ion Batteries. *Advanced Energy Materials*, 11(48):2103005, dec 2021. ISSN 1614-6840. . URL https:

```
//onlinelibrary.wiley.com/doi/full/10.1002/aenm.202103005https:
//onlinelibrary.wiley.com/doi/abs/10.1002/aenm.202103005https:
//onlinelibrary.wiley.com/doi/10.1002/aenm.202103005.
```

- [36] Christoph R. Birkl, Matthew R. Roberts, Euan McTurk, Peter G. Bruce, and David A. Howey. Degradation diagnostics for lithium ion cells. *Journal of Power Sources*, 341:373–386, feb 2017. ISSN 0378-7753.
- [37] Kisuk Kang and Gerbrand Ceder. Factors that affect Li mobility in layered lithium transition metal oxides. *Physical Review B Condensed Matter and Materials Physics*, 74(9):094105, sep 2006. ISSN 10980121. . URL https://journals.aps.org/prb/abstract/10.1103/PhysRevB.74.094105.

[38] Kisuk Kang, Ying Shirley Meng, Julien Bréger, Clare P. Grey, and Gerbrand Ceder. Electrodes with high power and high capacity for rechargeable lithium batteries. *Science (New York, N.Y.)*, 311(5763):977–980, feb 2006. ISSN 1095-9203. . URL https://pubmed.ncbi.nlm.nih.gov/16484487/.

- [39] Chao Xu, Alice J. Merryweather, Shrinidhi S. Pandurangi, Zhengyan Lun, David S. Hall, Vikram S. Deshpande, Norman A. Fleck, Christoph Schnedermann, Akshay Rao, and Clare P. Grey. Operando visualization of kinetically induced lithium heterogeneities in single-particle layered Ni-rich cathodes. *Joule*, 6(11):2535–2546, nov 2022. ISSN 25424351.
- [40] Taolin Zhao, Na Zhou, Xiaoxiao Zhang, Qing Xue, Yuhua Wang, Minli Yang, Li Li, and Renjie Chen. Structure Evolution from Layered to Spinel during Synthetic Control and Cycling Process of Fe-Containing Li-Rich Cathode Materials for Lithium-Ion Batteries. ACS Omega, 2(9):5601–5610, sep 2017. ISSN 24701343. . URL
- [41] J. Vetter, P. Novák, M. R. Wagner, C. Veit, K. C. Möller, J. O. Besenhard, M. Winter, M. Wohlfahrt-Mehrens, C. Vogler, and A. Hammouche. Ageing mechanisms in lithium-ion batteries. *Journal of Power Sources*, 147:269–281, 9 2005. ISSN 0378-7753.

https://pubs.acs.org/doi/full/10.1021/acsomega.7b00689.

- [42] Felix Joho, Beat Rykart, Roman Imhof, Petr Novak, Michael E Spahr, and Alain Monnier. Key factors for the cycling stability of graphite intercalation electrodes for lithium-ion batteries. *Journal of Power Sources*, 81:1999–243, 1999. URL www.elsevier.comrlocaterjpowsour.
- [43] H J Santner, K.-C Möller, J Ivančo, M G Ramsey, F P Netzer, S Yamaguchi, J O Besenhard, and M Winter. Acrylic acid nitrile, a film-forming electrolyte component for lithium-ion batteries, which belongs to the family of additives containing vinyl groups. *JPS*, 2003.

[44] M C Smart, B V Ratnakumar, V S Ryan-Mowrey, S Surampudi, G K S Prakash, J Hu, and I Cheung. Improved performance of lithium-ion cells with the use of fluorinated carbonate-based electrolytes. *JPS*, 2003. .

- [45] D P Abraham, R D Twesten, M Balasubramanian, I Petrov, J Mcbreen, and K Amine. Surface changes on lini 0:8 co 0:2 o 2 particles during testing of high-power lithium-ion cells. *elsevier*, 2002. URL www.elsevier.com/locate/elecom.
- [46] Adrien Boulineau, Loïc Simonin, Jean François Colin, Carole Bourbon, and Sébastien Patoux. First evidence of manganese-nickel segregation and densification upon cycling in Li-rich layered oxides for lithium batteries. *Nano Letters*, 13(8):3857–3863, aug 2013. ISSN 15306984. URL https://pubs.acs.org/doi/full/10.1021/nl4019275.
- [47] Denis Kramer and Gerbrand Ceder. Tailoring the morphology of LiCoO2: A first principles study. *Chemistry of Materials*, 21(16):3799–3809, aug 2009. ISSN 08974756.
- [48] Liang Hong, Linhua Hu, John W. Freeland, Jordi Cabana, Serdar Ögüt, and Robert F. Klie. Electronic Structure of LiCoO 2 Surfaces and Effect of Al Substitution. *Journal of Physical Chemistry C*, 123(14):8851–8858, apr 2019. ISSN 19327455. URL https://pubs.acs.org/doi/full/10.1021/acs.jpcc.8b11661.
- [49] Eunseog Cho, Seung Woo Seo, and Kyoungmin Min. Theoretical Prediction of Surface Stability and Morphology of LiNiO2 Cathode for Li Ion Batteries. ACS Applied Materials and Interfaces, 9(38):33257–33266, sep 2017. ISSN 19448252. . URL https://pubs.acs.org/doi/full/10.1021/acsami.7b08563.
- [50] L. Wang, F. Zhou, Y. S. Meng, and G. Ceder. First-principles study of surface properties of LiFeP O4: Surface energy, structure, Wulff shape, and surface redox potential. *Physical Review B Condensed Matter and Materials Physics*, 76 (16):165435, oct 2007. ISSN 10980121. URL https://journals.aps.org/prb/abstract/10.1103/PhysRevB.76.165435.

[51] Marie-Alexandra Neouze and Ulrich Schubert. Review Surface Modification and Functionalization of Metal and Metal Oxide Nanoparticles by Organic Ligands. *Monatsh Chem*, 139:183–195, 2008.

- [52] Junyu Jiao, Genming Lai, Shihan Qin, Chi Fang, Xianqi Xu, Yao Jiang, Chuying Ouyang, and Jiaxin Zheng. Tuning of surface morphology in Li layered oxide cathode materials. *Acta Materialia*, 238:118229, oct 2022. ISSN 1359-6454.
- [53] Juan C. Garcia, Javier Bareño, Jianhua Yan, Guoying Chen, Andrew Hauser, Jason R. Croy, and Hakim Iddir. Surface Structure, Morphology, and Stability of Li(Ni1/3Mn1/3Co1/3)O2 Cathode Material. *The Journal of Physical Chemistry C*, 121(15):8290–8299, apr 2017. ISSN 1932-7447. . URL https://escholarship.org/uc/item/6rt3d5t1.
- [54] Juan C. Garcia, Javier Bareño, Guoying Chen, Jason R. Croy, and Hakim Iddir. Strain-driven surface reconstruction and cation segregation in layered Li(Ni 1-x-y Mn x Co y)O 2 (NMC) cathode materials. *Physical Chemistry Chemical Physics*, 22(42):24490–24497, nov 2020. ISSN 14639076. URL https://pubs.rsc.org/en/content/articlehtml/2020/cp/d0cp03942jhttps://pubs.rsc.org/en/content/articlelanding/2020/cp/d0cp03942j.
- [55] Pengfei Yan, Anmin Nie, Jianming Zheng, Yungang Zhou, Dongping Lu, Xiaofeng Zhang, Rui Xu, Ilias Belharouak, Xiaotao Zu, Jie Xiao, Khalil Amine, Jun Liu, Fei Gao, Reza Shahbazian-Yassar, Ji Guang Zhang, and Chong Min Wang. Evolution of lattice structure and chemical composition of the surface reconstruction layer in Li(1.2)Ni(0.2)Mn(0.6)O2 cathode material for lithium ion batteries. *Nano letters*, 15(1):514–522, jan 2015. ISSN 1530-6992. URL https://pubmed.ncbi.nlm.nih.gov/25485638/.
- [56] Meng Gu, Ilias Belharouak, Jianming Zheng, Huiming Wu, Jie Xiao, Arda Genc, Khalil Amine, Suntharampillai Thevuthasan, Donald R. Baer, Ji Guang Zhang, Nigel D. Browning, Jun Liu, and Chongmin Wang. Formation of the spinel phase in the layered composite cathode used in li-ion batteries. ACS nano, 7: 760–767, 1 2013. ISSN 1936-086X. URL

https://pubmed.ncbi.nlm.nih.gov/23237664/.

[57] W. I.F. David, M. M. Thackeray, P. G. Bruce, and J. B. Goodenough. Lithium insertion into beta-mno2 and the rutile-spinel transformation. *Materials Research Bulletin*, 19:99–106, 1 1984. ISSN 0025-5408.

- [58] H. Gabrisch, R. Yazami, and B. Fultz. A transmission electron microscopy study of cycled licoo2. *Journal of Power Sources*, 119-121:674–679, 6 2003. ISSN 0378-7753. .
- [59] Haifeng Wang, Young Il Jang, and Yet Ming Chiang. Origin of cycling stability in monoclinic- and orthorhombic-phase lithium manganese oxide cathodes. Electrochemical and Solid-State Letters, 2:490–493, 10 1999. ISSN 10990062. URL https://iopscience.iop.org/article/10.1149/1.1390880/meta.
- [60] Brian N. Figgis and Michael A. Hitchman. Ligand Field Theory and Its Applications (Special Topics in Inorganic Chemistry). Wiley-VCH, 1999. ISBN 0471317764. URL https://books.google.com/books/about/Ligand_Field_Theory_and_Its_ Applications.html?id=vGIvAQAAIAAJ.
- [61] Yu Xia, Jianming Zheng, Chongmin Wang, and Meng Gu. Designing principle for ni-rich cathode materials with high energy density for practical applications. *Nano Energy*, 49:434–452, 7 2018. ISSN 2211-2855.
- [62] Jiaxin Zheng, Yaokun Ye, Tongchao Liu, Yinguo Xiao, Chongmin Wang, Feng Wang, and Feng Pan. Ni/li disordering in layered transition metal oxide: Electrochemical impact, origin, and control. *Accounts of Chemical Research*, 52: 2201–2209, 6 2019. ISSN 0001-4842.
- [63] Feng Lin, Dennis Nordlund, Yuyi Li, Matthew K. Quan, Lei Cheng, Tsu Chien Weng, Yijin Liu, Huolin L. Xin, and Marca M. Doeff. Metal segregation in hierarchically structured cathode materials for high-energy lithium batteries.

 Nature Energy 2016 1:1, 1(1):1–8, jan 2016. ISSN 2058-7546. . URL https://www.nature.com/articles/nenergy20154.

[64] A. Van der Ven, M. Aydinol, G. Ceder, G. Kresse, and J. Hafner. First-principles investigation of phase stability. *Physical Review B - Condensed Matter and Materials Physics*, 58(6):2975–2987, 1998. ISSN 1550235X.

- [65] Matteo Cococcioni. 4 The LDA+U Approach: A Simple Hubbard Correction for Correlated Ground States. PhD thesis, University of Minnesota, 2012. URL http://www.cond-mat.de/events/correl12.
- [66] Shyue Ping Ong, Shreyas Cholia, Anubhav Jain, Miriam Brafman, Dan Gunter, Gerbrand Ceder, and Kristin A. Persson. The Materials Application Programming Interface (API): A simple, flexible and efficient API for materials data based on REpresentational State Transfer (REST) principles. *Computational Materials Science*, 97:209–215, feb 2015. ISSN 0927-0256.
- [67] F. Zhou, M. Cococcioni, C. A. Marianetti, D. Morgan, and G. Ceder.
 First-principles prediction of redox potentials in transition-metal compounds with LDA + U. *Physical Review B Condensed Matter and Materials Physics*, 70(23): 1–8, dec 2004. ISSN 1550235X. URL
 https://journals.aps.org/prb/abstract/10.1103/PhysRevB.70.235121.
- [68] Shyue Ping Ong, Lei Wang, Byoungwoo Kang, and Gerbrand Ceder. Li-Fe-P-O2 Phase Diagram from First Principles Calculations. *Chemistry of Materials*, 20(5): 1798–1807, mar 2008. ISSN 08974756. URL https://pubs.acs.org/doi/full/10.1021/cm702327g.
- [69] Anubhav Jain, Shyue Ping Ong, Geoffroy Hautier, Wei Chen, William Davidson Richards, Stephen Dacek, Shreyas Cholia, Dan Gunter, David Skinner, Gerbrand Ceder, and Kristin A. Persson. Commentary: The Materials Project: A materials genome approach to accelerating materials innovation. *APL Materials*, 1(1): 011002, jul 2013. ISSN 2166532X. . URL https://aip.scitation.org/doi/abs/10.1063/1.4812323.
- [70] Gabriel R. Schleder, Antonio C.M. Padilha, Carlos Mera Acosta, Marcio Costa, and Adalberto Fazzio. From DFT to machine learning: Recent approaches to

```
materials science - A review. JPhys Materials, 2(3):32001, jul 2019. ISSN 25157639.

URL https://doi.org/10.1088/2515-7639/ab084b.
```

- [71] Ryo Nagai, Ryosuke Akashi, and Osamu Sugino. Completing density functional theory by machine learning hidden messages from molecules. *npj Computational Materials*, 6(1):1–8, dec 2020. ISSN 20573960. . URL https://doi.org/10.1038/s41524-020-0310-0.
- [72] Frank Noé, Alexandre Tkatchenko, Klaus Robert Müller, and Cecilia Clementi. Machine learning for molecular simulation, apr 2020. ISSN 0066426X. URL https://doi.org/10.1146/annurev-physchem-042018-.
- [73] Evgenij Barsoukov and J. Ross Macdonald. *Impedance Spectroscopy: Theory, Experiment, and Applications*. Wiley and Sons, 2005. .
- [74] Ledyard R. Tucker and Charles Lewis. A reliability coefficient for maximum likelihood factor analysis. *Psychometrika*, 38(1), 1973. ISSN 00333123.
- [75] E. C. Aifantis. Internal length gradient (ILG) material mechanics across scales and disciplines. *Advances in Applied Mechanics*, 49, 2016. ISSN 00652156.
- [76] F. W. Tang, X. Y. Song, C. Hou, X. M. Liu, H. B. Wang, and Z. R. Nie. Modeling of Li diffusion in nanocrystalline Li-Si anode material. *Physical Chemistry Chemical Physics*, 20(10), 2018. ISSN 14639076.
- [77] Peter J. Bond, John Holyoake, Anthony Ivetac, Syma Khalid, and Mark S.P.
 Sansom. Coarse-grained molecular dynamics simulations of membrane proteins and peptides. *Journal of Structural Biology*, 157(3), 2007. ISSN 10478477.
- [78] Anubhav Jain, Yongwoo Shin, and Kristin A. Persson. Computational predictions of energy materials using density functional theory, 2016. ISSN 20588437.
- [79] Peter W. Shor. Algorithms for quantum computation: Discrete logarithms and factoring. In *Proceedings Annual IEEE Symposium on Foundations of Computer Science, FOCS,* 1994. .

[80] John A. Pople, Paul V. Schleyer, Warren J. Hehre, and Leo Radom. *AB INITIO molecular orbital theory*. Mcgraw-Hill book company, 1986. .

- [81] E. Schrödinger. An Undulatory Theory of the Mechanics of Atoms and Molecules. *Physical Review*, 28(6):1049, dec 1926. ISSN 0031899X. . URL https://journals.aps.org/pr/abstract/10.1103/PhysRev.28.1049.
- [82] P. A. M. Dirac and J. C. Polkinghorne. The Principles of Quantum Mechanics. Physics Today, 11(6):32-33, 1958. ISSN 0031-9228. URL https://books.google.com/books/about/The_Principles_of_Quantum_ Mechanics.html?id=XehUpGiM6FIC.
- [83] John Von Neumann, Robert T. (Robert Thomas) Beyer, and Herman H. (Herman Heine) Goldstine. Mathematical foundations of quantum mechanics. Princeton University Press, 1955. ISBN 0691028931. URL https://books.google.com/books/about/Mathematical_Foundations_of_ Quantum_Mech.html?id=JLyCo3R04qUC.
- [84] David J. Griffiths and Darrell F. Schroeter. Introduction to Quantum Mechanics. *Introduction to Quantum Mechanics*, aug 2018.
- [85] M. Born and R. Oppenheimer. Zur Quantentheorie der Molekeln. Annalen der Physik, 389(20):457-484, jan 1927. ISSN 15213889. URL https: //onlinelibrary.wiley.com/doi/full/10.1002/andp.19273892002https: //onlinelibrary.wiley.com/doi/abs/10.1002/andp.19273892002.
- [86] J. Franck and E. G. Dymond. Elementary processes of photochemical reactions. Transactions of the Faraday Society, 21(February):536–542, jan 1926. ISSN 0014-7672. URL https: //pubs.rsc.org/en/content/articlehtml/1926/tf/tf9262100536https: //pubs.rsc.org/en/content/articlelanding/1926/tf/tf9262100536.
- [87] D. R. Hartree. The Wave Mechanics of an Atom with a Non-Coulomb Central Field Part II Some Results and Discussion. *Mathematical Proceedings of the*

```
Cambridge Philosophical Society, 24(1):111-132, 1928. ISSN 14698064. . URL https://doi.org/10.1017/S0305004100011920.
```

- [88] V. Fock. N\u00e4herungsmethode zur L\u00f6sung des quantenmechanischen Mehrk\u00f6rperproblems. Zeitschrift f\u00fcr Physik, 61(1-2):126-148, jan 1930. ISSN 14346001. URL https://link.springer.com/article/10.1007/BF01340294.
- [89] J. C. Slater. The self consistent field and the structure of atoms. Physical Review, 32(3):339–348, sep 1928. ISSN 0031899X. . URL https://journals.aps.org/pr/abstract/10.1103/PhysRev.32.339.
- [90] J. C. Slater. The Theory of Complex Spectra. Physical Review, 34(10):1293, nov 1929. ISSN 0031899X. . URL https://journals.aps.org/pr/abstract/10.1103/PhysRev.34.1293.
- [91] E. K. U. (Eberhard K. U.) Gross, E. Runge, and O. Heinonen. *Many-particle theory*. A. Hilger, 1991. ISBN 9780750300728.
- [92] Robert G. Parr. Density Functional Theory of Atoms and Molecules. Horizons of Quantum Chemistry, pages 5–15, 1980. URL https://link.springer.com/chapter/10.1007/978-94-009-9027-2_2.
- [93] E. K.U. Gross, L. N. Oliveira, and W. Kohn. Rayleigh-Ritz variational principle for ensembles of fractionally occupied states. *Physical Review A*, 37(8):2805, apr 1988. ISSN 10502947. . URL https://journals.aps.org/pra/abstract/10.1103/PhysRevA.37.2805.
- [94] E. Wigner. On the interaction of electrons in metals. Physical Review, 46(11): 1002–1011, dec 1934. ISSN 0031899X. . URL https://journals.aps.org/pr/abstract/10.1103/PhysRev.46.1002.
- [95] P. Hohenberg and W. Kohn. Inhomogeneous electron gas. Physical Review, 136 (3B):B864, nov 1964. ISSN 0031899X. . URL https://journals.aps.org/pr/abstract/10.1103/PhysRev.136.B864.

[96] W. Kohn and L. J. Sham. Self-consistent equations including exchange and correlation effects. *Physical Review*, 140(4A):A1133, nov 1965. ISSN 0031899X.
URL https://journals.aps.org/pr/abstract/10.1103/PhysRev.140.A1133.

- [97] A. van de Walle and G. Ceder. Correcting overbinding in local-density-approximation calculations. *Physical Review B*, 59(23):14992, jun 1999. ISSN 1550235X. . URL https://journals.aps.org/prb/abstract/10.1103/PhysRevB.59.14992.
- [98] C. Stampfl and C. G. Van de Walle. Density-functional calculations for III-V nitrides using the local-density approximation and the generalized gradient approximation. *Physical Review B*, 59(8):5521, feb 1999. ISSN 1550235X. . URL https://journals.aps.org/prb/abstract/10.1103/PhysRevB.59.5521.
- [99] Kieron Burke, John P. Perdew, and Yue Wang. Derivation of a Generalized Gradient Approximation: The PW91 Density Functional. In *Electronic Density Functional Theory*, pages 81–111. Springer US, 1998. URL https://link.springer.com/chapter/10.1007/978-1-4899-0316-7_7.
- [100] John P Perdew, Kieron Burke, and Matthias Ernzerhof. Generalized Gradient Approximation Made Simple. *Phys. Rev. Letters*, 1996.
- [101] John P. Perdew and Wang Yue. Accurate and simple density functional for the electronic exchange energy: Generalized gradient approximation. *Physical Review B*, 33(12):8800, jun 1986. ISSN 01631829. URL https://journals.aps.org/prb/abstract/10.1103/PhysRevB.33.8800.
- [102] Takeshi Yanai, David P. Tew, and Nicholas C. Handy. A new hybrid exchange–correlation functional using the Coulomb-attenuating method (CAM-B3LYP). Chemical Physics Letters, 393(1-3):51–57, jul 2004. ISSN 0009-2614.
- [103] Peter Elliott and Kieron Burke. Non-empirical derivation of the parameter in the B88 exchange functional. *Canadian Journal of Chemistry*, 87(10):1485–1491, oct 2009. ISSN 00084042. . URL

https://cdnsciencepub.com/doi/10.1139/V09-095.

[104] Peter M.W. Gill. A new gradient-corrected exchange functional. Molecular Physics, 89(2):433-445, oct 1996. ISSN 13623028. URL https://www.tandfonline.com/doi/abs/10.1080/002689796173813.

- [105] Matthias Ernzerhof and Gustavo E. Scuseria. Assessment of the Perdew-Burke-Ernzerhof exchange-correlation functional. *The Journal of Chemical Physics*, 110(11):5029–5036, mar 1999. ISSN 0021-9606. URL /aip/jcp/article/110/11/5029/183578/
 Assessment-of-the-Perdew-Burke-Ernzerhof-exchange.
- [106] Jochen Autschbach and Monika Srebro. Delocalization error and "functional tuning" in Kohn-Sham calculations of molecular properties. *Accounts of Chemical Research*, 47(8):2592–2602, aug 2014. ISSN 15204898. . URL https://pubs.acs.org/doi/full/10.1021/ar500171t.
- [107] Heather J. Kulik. Perspective: Treating electron over-delocalization with the DFT+U method. *Journal of Chemical Physics*, 142(24):240901, jun 2015. ISSN 00219606. . URL /aip/jcp/article/142/24/240901/74204/
 Perspective-Treating-electron-over-delocalization.
- [108] S. S. Kancharla and S. Okamoto. Band insulator to Mott insulator transition in a bilayer Hubbard model. *Physical Review B - Condensed Matter and Materials Physics*, 75(19):193103, may 2007. ISSN 10980121. URL https://journals.aps.org/prb/abstract/10.1103/PhysRevB.75.193103.
- [109] Vladimir I. Anisimov, Jan Zaanen, and Ole K. Andersen. Band theory and Mott insulators: Hubbard ¡i¿U¡/i¿ instead of Stoner ¡i¿I¡/i¿. Physical Review B, 44(3): 943, jul 1991. ISSN 01631829. . URL https://journals.aps.org/prb/abstract/10.1103/PhysRevB.44.943.
- [110] A. I. Liechtenstein, V. I. Anisimov, and J. Zaanen. Density-functional theory and strong interactions: Orbital ordering in Mott-Hubbard insulators. *Physical Review B*, 52(8):R5467, aug 1995. ISSN 01631829. . URL https://journals.aps.org/prb/abstract/10.1103/PhysRevB.52.R5467.

[111] K Terakura ', A R Williams, T Oguchi, Minato Roppongi, Japan Ku, -Tokyo, and J Kubler. Transition-Metal Monoxides: Band or Mott Insulators. *Phys Rev Letters.*, 52, 1984.

- [112] V. I. Anisimov, M. A. Korotin, and E. Z. Kurmaev. Band-structure description of Mott insulators (NiO, MnO, FeO, CoO). Journal of Physics: Condensed Matter, 2 (17):3973, apr 1990. ISSN 0953-8984. URL https://iopscience.iop.org/article/10.1088/0953-8984/2/17/008https: //iopscience.iop.org/article/10.1088/0953-8984/2/17/008/meta.
- [113] Jorge E. Hirsch. Renormalization-group study of the Hubbard model. *Physical Review B*, 22(11):5259, dec 1980. ISSN 01631829. . URL https://journals.aps.org/prb/abstract/10.1103/PhysRevB.22.5259.
- [114] W. Nolting and W. Borgiel. Band magnetism in the Hubbard model. *Physical Review B*, 39(10):6962, apr 1989. ISSN 01631829. . URL https://journals.aps.org/prb/abstract/10.1103/PhysRevB.39.6962.
- [115] Elliott H. Lieb. Two theorems on the Hubbard model. Physical Review Letters, 62 (10):1201, mar 1989. ISSN 00319007. . URL https://journals.aps.org/prl/abstract/10.1103/PhysRevLett.62.1201.
- [116] Estefania German, Ricardo Faccio, and Alvaro W. Mombrú. Comparison of standard DFT and Hubbard-DFT methods in structural and electronic properties of TiO 2 polymorphs and H-titanate ultrathin sheets for DSSC application. *Applied Surface Science*, 428:118–123, jan 2018. ISSN 01694332.
- [117] M. Shishkin and H. Sato. DFT+ U in Dudarev's formulation with corrected interactions between the electrons with opposite spins: The form of Hamiltonian, calculation of forces, and bandgap adjustments. *Journal of Chemical Physics*, 151(2):24102, jul 2019. ISSN 00219606. URL /aip/jcp/article/151/2/ 024102/197878/DFT-U-in-Dudarev-s-formulation-with-corrected.
- [118] S. L. Dudarev, G. A. Botton, S. Y. Savrasov, C. J. Humphreys, and A. P. Sutton. Electron-energy-loss spectra and the structural stability of nickel oxide: An

```
LSDA U study. Physical Review B, 57(3):1505, jan 1998. ISSN 1550235X. . URL https://journals.aps.org/prb/abstract/10.1103/PhysRevB.57.1505.
```

- [119] Maituo Yu, Shuyang Yang, Chunzhi Wu, and Noa Marom. Machine learning the Hubbard U parameter in DFT+U using Bayesian optimization. *npj*Computational Materials 2020 6:1, 6(1):1–6, nov 2020. ISSN 2057-3960. . URL https://www.nature.com/articles/s41524-020-00446-9.
- [120] D. R. Hamann. Optimized norm-conserving vanderbilt pseudopotentials. Physical Review B - Condensed Matter and Materials Physics, 88:085117, 8 2013. ISSN 10980121. URL https://journals.aps.org/prb/abstract/10.1103/PhysRevB.88.085117.
- [121] G. Kresse and D. Joubert. From ultrasoft pseudopotentials to the projector augmented-wave method. *Physical Review B*, 59(3):1758, jan 1999. ISSN 1550235X. . URL https://journals.aps.org/prb/abstract/10.1103/PhysRevB.59.1758.
- [122] Thom. H. Dunning and P. Jeffrey Hay. Gaussian Basis Sets for Molecular Calculations. *Methods of Electronic Structure Theory*, pages 1–27, 1977. . URL https://link.springer.com/chapter/10.1007/978-1-4757-0887-5_1.
- [123] Joost VandeVondele and Jürg Hutter. Gaussian basis sets for accurate calculations on molecular systems in gas and condensed phases. *Journal of Chemical Physics*, 127(11), sep 2007. ISSN 00219606. . URL /aip/jcp/article/127/11/114105/295855/
 Gaussian-basis-sets-for-accurate-calculations-on.
- [124] G. Kresse and J. Furthmüller. Efficient iterative schemes for ¡i¿ab initio¡/i¿ total-energy calculations using a plane-wave basis set. *Physical Review B*, 54(16): 11169, oct 1996. ISSN 1550235X. . URL https://journals.aps.org/prb/abstract/10.1103/PhysRevB.54.11169.
- [125] G. Kresse and J. Furthmüller. Efficiency of ab-initio total energy calculations for metals and semiconductors using a plane-wave basis set. *Computational Materials Science*, 6(1):15–50, jul 1996. ISSN 0927-0256.

[126] G. Kresse and J. Hafner. ¡i¿Ab initio¡/i¿ molecular dynamics for liquid metals. Physical Review B, 47(1):558, jan 1993. ISSN 01631829. . URL https://journals.aps.org/prb/abstract/10.1103/PhysRevB.47.558.

- [127] G. P. Srivastava and D. Weaire. The theory of the cohesive energies of solids. *Advances in Physics*, 36(4):463–517, jan 1987. ISSN 14606976. . URL https://www.tandfonline.com/doi/abs/10.1080/00018738700101042.
- [128] Kari Laasonen, Alfredo Pasquarello, Roberto Car, Changyol Lee, and David Vanderbilt. Car-Parrinello molecular dynamics with Vanderbilt ultrasoft pseudopotentials. *Physical Review B*, 47(16):10142, apr 1993. ISSN 01631829. . URL

https://journals.aps.org/prb/abstract/10.1103/PhysRevB.47.10142.

- [129] J. S. Lin, A. Qteish, M. C. Payne, and V. Heine. Optimized and transferable nonlocal separable ¡i¿ab initio¡/i¿ pseudopotentials. *Physical Review B*, 47(8): 4174, feb 1993. ISSN 01631829. URL https://journals.aps.org/prb/abstract/10.1103/PhysRevB.47.4174.
- [130] David Vanderbilt. Soft self-consistent pseudopotentials in a generalized eigenvalue formalism. *Physical Review B*, 41(11):7892, apr 1990. ISSN 01631829. . URL https://journals.aps.org/prb/abstract/10.1103/PhysRevB.41.7892.
- [131] M. C. Payne, M. P. Teter, D. C. Allan, T. A. Arias, and J. D. Joannopoulos. Iterative minimization techniques for ¡i¿ab initio¡/i¿ total-energy calculations: molecular dynamics and conjugate gradients. *Reviews of Modern Physics*, 64(4): 1045, oct 1992. ISSN 00346861. URL https://journals.aps.org/rmp/abstract/10.1103/RevModPhys.64.1045.
- [132] R. D. King-Smith, M. C. Payne, and J. S. Lin. Real-space implementation of nonlocal pseudopotentials for first-principles total-energy calculations. *Physical Review B*, 44(23):13063, dec 1991. ISSN 01631829. URL https://journals.aps.org/prb/abstract/10.1103/PhysRevB.44.13063.
- [133] Leonard Kleinman and D. M. Bylander. Efficacious Form for Model Pseudopotentials. *Physical Review Letters*, 48(20):1425, may 1982. ISSN 00319007.

. URL

https://journals.aps.org/prl/abstract/10.1103/PhysRevLett.48.1425.

- [134] Anubhav Jain, Geoffroy Hautier, Charles J. Moore, Shyue Ping Ong, Christopher C. Fischer, Tim Mueller, Kristin A. Persson, and Gerbrand Ceder. A high-throughput infrastructure for density functional theory calculations. Computational Materials Science, 50(8):2295–2310, jun 2011. ISSN 0927-0256.
- [135] Anubhav Jain, Geoffroy Hautier, Charles J. Moore, Shyue Ping Ong, Christopher C. Fischer, Tim Mueller, Kristin A. Persson, and Gerbrand Ceder. A high-throughput infrastructure for density functional theory calculations. Computational Materials Science, 50(8):2295–2310, jun 2011. ISSN 09270256.
- [136] Mark De Berg, Otfried Cheong, Marc Van Kreveld, and Mark Overmars.

 Computational geometry: Algorithms and applications. *Computational Geometry:*Algorithms and Applications, pages 1–386, 2008.
- [137] Atsuyuki Okabe, Barry Boots, Kokichi Sugihara, and Sung Nok Chiu. Spatial tessellations: concepts and applications of voronoi diagrams, with a foreword by dg kendall. *Wiley Series in Probability and Statistics*, page 696, 2000.
- [138] Peter E. Blöchl, O. Jepsen, and O. K. Andersen. Improved tetrahedron method for Brillouin-zone integrations. *Physical Review B*, 49(23):16223, jun 1994. ISSN 01631829. . URL https://journals.aps.org/prb/abstract/10.1103/PhysRevB.49.16223.
- [139] Hendrik J. Monkhorst and James D. Pack. Special points for Brillouin-zone integrations. *Physical Review B*, 13(12):5188, jun 1976. ISSN 01631829. URL https://journals.aps.org/prb/abstract/10.1103/PhysRevB.13.5188.
- [140] M. Methfessel and A. T. Paxton. High-precision sampling for Brillouin-zone integration in metals. *Physical Review B*, 40(6):3616, aug 1989. ISSN 01631829. . URL https://journals.aps.org/prb/abstract/10.1103/PhysRevB.40.3616.
- [141] D. J. Chadi and Marvin L. Cohen. Special Points in the Brillouin Zone. *Physical Review B*, 8(12):5747, dec 1973. ISSN 01631829. . URL https://journals.aps.org/prb/abstract/10.1103/PhysRevB.8.5747.

[142] Pandu Wisesa, Kyle A. McGill, and Tim Mueller. Efficient generation of generalized Monkhorst-Pack grids through the use of informatics. *Physical Review B*, 93(15):155109, apr 2016. ISSN 24699969. . URL https://journals.aps.org/prb/abstract/10.1103/PhysRevB.93.155109.

- [143] Wiley S. Morgan, John E. Christensen, Parker K. Hamilton, Jeremy J. Jorgensen, Branton J. Campbell, Gus L.W. Hart, and Rodney W. Forcade. Generalized regular k-point grid generation on the fly. *Computational Materials Science*, 173: 109340, feb 2020. ISSN 09270256.
- [144] Junwei Lucas Bao and Donald G. Truhlar. Variational transition state theory: theoretical framework and recent developments. *Chemical Society Reviews*, 46 (24):7548–7596, dec 2017. ISSN 14604744. . URL https:

 //pubs.rsc.org/en/content/articlehtml/2017/cs/c7cs00602khttps:

 //pubs.rsc.org/en/content/articlelanding/2017/cs/c7cs00602k.
- [145] H. Bernhard Schlegel. Geometry optimization. Wiley Interdisciplinary Reviews:

 Computational Molecular Science, 1(5):790-809, sep 2011. ISSN 1759-0884. . URL

 https://onlinelibrary.wiley.com/doi/full/10.1002/wcms.34https:

 //onlinelibrary.wiley.com/doi/abs/10.1002/wcms.34https:

 //wires.onlinelibrary.wiley.com/doi/10.1002/wcms.34.
- [146] Vilhjálmur Ásgeirsson, Benedikt Orri Birgisson, Ragnar Bjornsson, Ute Becker, Frank Neese, Christoph Riplinger, and Hannes Jónsson. Nudged Elastic Band Method for Molecular Reactions Using Energy-Weighted Springs Combined with Eigenvector following. *Journal of Chemical Theory and Computation*, 17(8): 4929–4945, aug 2021. ISSN 15499626. URL https://pubs.acs.org/doi/full/10.1021/acs.jctc.1c00462.
- [147] John C. Mauro, Roger J. Loucks, and Jitendra Balakrishnan. A simplified eigenvector-following technique for locating transition points in an energy landscape. *Journal of Physical Chemistry A*, 109(42):9578–9583, oct 2005. ISSN 10895639. . URL https://pubs.acs.org/doi/full/10.1021/jp053581t.

[148] Graeme Henkelman, Blas P. Uberuaga, and Hannes Jónsson. Climbing image nudged elastic band method for finding saddle points and minimum energy paths. *Journal of Chemical Physics*, 113(22):9901–9904, dec 2000. ISSN 00219606. . URL http://aip.scitation.org/doi/10.1063/1.1329672.

- [149] Graeme Henkelman and Hannes Jónsson. Improved tangent estimate in the nudged elastic band method for finding minimum energy paths and saddle points. *Journal of Chemical Physics*, 113(22):9978–9985, dec 2000. ISSN 00219606. . URL http://aip.scitation.org/doi/10.1063/1.1323224.
- [150] Natsuhiko Sugimura, Yoko Igarashi, Reiko Aoyama, and Toshimichi Shibue. Nudged elastic band method and density functional theory calculation for finding a local minimum energy pathway of ¡i¿p¡/i¿-benzoquinone and phenol fragmentation in mass spectrometry. European Journal of Mass Spectrometry, 23 (1):40–44, feb 2017. ISSN 1469-0667. . URL http://journals.sagepub.com/doi/10.1177/1469066716688412.
- [151] HANNES JÓNSSON, GREG MILLS, and KARSTEN W. JACOBSEN. *Nudged* elastic band method for finding minimum energy paths of transitions. World Scientific Pub Co Pte Lt, jun 1998. .
- [152] Naoaki Yabuuchi, Yuta Kawamoto, Ryo Hara, Toru Ishigaki, Akinori Hoshikawa, Masao Yonemura, Takashi Kamiyama, and Shinichi Komaba. A comparative study of LiCoO2 polymorphs: Structural and electrochemical characterization of O2-, O3-, and O4-type phases. *Inorganic Chemistry*, 52(15): 9131–9142, aug 2013. ISSN 00201669. . URL https://pubs.acs.org/doi/full/10.1021/ic4013922.
- [153] Yohan Biecher, Danielle L. Smiley, Marie Guignard, François Fauth, Romain Berthelot, Claude Delmas, Gillian R. Goward, and Dany Carlier. Original Layered OP4-(Li,Na)xCoO2 Phase: Insights on Its Structure, Electronic Structure, and Dynamics from Solid State NMR. *Inorganic Chemistry*, 59(8): 5339–5349, apr 2020. ISSN 1520510X. . URL https://pubs.acs.org/doi/full/10.1021/acs.inorgchem.9b03417.

[154] Sergio Posada-Pérez, Gian Marco Rignanese, and Geoffroy Hautier. Influence of Stacking on H+Intercalation in Layered ACoO2(A = Li, Na) Cathode Materials and Implications for Aqueous Li-Ion Batteries: A First-Principles Investigation.

Chemistry of Materials, 33(17):6942–6954, sep 2021. ISSN 15205002. URL https://pubs.acs.org/doi/full/10.1021/acs.chemmater.1c01887.

- [155] C. Delmas, C. Fouassier, and P. Hagenmuller. Structural classification and properties of the layered oxides. *Physica B+C*, 99(1-4):81–85, jan 1980. ISSN 0378-4363.
- [156] Peng Fei Wang, Ya You, Ya Xia Yin, and Yu Guo Guo. Layered Oxide Cathodes for Sodium-Ion Batteries: Phase Transition, Air Stability, and Performance.

 Advanced Energy Materials, 8(8):1701912, mar 2018. ISSN 1614-6840. . URL https:

```
//onlinelibrary.wiley.com/doi/full/10.1002/aenm.201701912https:
//onlinelibrary.wiley.com/doi/abs/10.1002/aenm.201701912https:
//onlinelibrary.wiley.com/doi/10.1002/aenm.201701912.
```

- [157] Nathan C. Frey, Matthew K. Horton, Jason M. Munro, Sinéad M. Griffin, Kristin A. Persson, and Vivek B. Shenoy. High-throughput search for magnetic and topological order in transition metal oxides. *Science Advances*, 6(50), dec 2020. ISSN 23752548. . URL
 - https://www.science.org/doi/10.1126/sciadv.abd1076.
- [158] Muratahan Aykol, Soo Kim, and C. Wolverton. Van der Waals Interactions in Layered Lithium Cobalt Oxides. *Journal of Physical Chemistry C*, 119(33): 19053–19058, aug 2015. ISSN 19327455. . URL https://pubs.acs.org/doi/full/10.1021/acs.jpcc.5b06240.
- [159] G. Ceder and S. K. Mishra. Stability of orthorhombic and monoclinic-layered LiMnO2. Electrochemical and Solid-State Letters, 2(11):550–552, nov 1999. ISSN 10990062. . URL

```
https://iopscience.iop.org/article/10.1149/1.1390900https://iopscience.iop.org/article/10.1149/1.1390900/meta.
```

[160] Satoshi Matsubara. Native minerals. Encyclopedia of Earth Sciences Series, pages 957–961, 2018. ISSN 1871756X. . URL https://link.springer.com/ referenceworkentry/10.1007/978-3-319-39312-4_317.

- [161] John B. Goodenough. Metallic oxides. *Progress in Solid State Chemistry*, 5(C): 145–399, jan 1971. ISSN 0079-6786.
- [162] A. M. Evans. *Ore geology and industrial minerals: an introduction*. Blackwell Science Ltd, 1992. ISBN 0632029536.
- [163] Kula C. Misra. Understanding Mineral Deposits. *Understanding Mineral Deposits*, 2000. .
- [164] C N R Rao. TRANSITION METAL OXIDES. Annual Rev. Phys Chem., 1989. URL www.annualreviews.org.
- [165] A. C. Scheinost. METAL OXIDES. *Encyclopedia of Soils in the Environment*, 4: 428–438, jan 2005.
- [166] G. Bergerhoff, R. Hundt, R. Sievers, and I. D. Brown. The Inorganic Crystal Structure Data Base. *Journal of Chemical Information and Computer Sciences*, 23(2): 66–69, 1983. ISSN 00952338. URL https://pubs.acs.org/doi/abs/10.1021/ci00038a003.
- [167] W.B. Pearson and G. V. Raynor. Handbook of Lattice Spacings and Structure of Metals. Pergamon Press, 1958. ISBN 9781483213187. URL http://www.sciencedirect.com:5070/book/9781483213187/ a-handbook-of-lattice-spacings-and-structures-of-metals-and-alloys.
- [168] J. Samuel Smart and Selma Greenwald. Crystal Structure Transitions in Antiferromagnetic Compounds at the Curie Temperature. *Physical Review*, 82(1): 113, apr 1951. ISSN 0031899X. . URL https://journals.aps.org/pr/abstract/10.1103/PhysRev.82.113.
- [169] D TAYLOR. Thermal expansion data. I: Binary oxides with the sodium chloride and wurtzite structures, MO. *Transactions and journal of the British Ceramic Society*, 83(1):5–9, 1984. ISSN 0307-7357.

[170] N. G. Schmahl and G. F. Eikerling. Über Kryptomodifikationen des Cu(II)-Oxids. Zeitschrift fur Physikalische Chemie, 62(5-6):268–279, dec 1968. ISSN 09429352. URL https:
//www.degruyter.com/document/doi/10.1524/zpch.1968.62.5_6.268/html.

- [171] Per Söderlind, Olle Eriksson, Börje Johansson, J. M. Wills, and A. M. Boring. A unified picture of the crystal structures of metals. *Nature* 1995 374:6522, 374 (6522):524–525, apr 1995. ISSN 1476-4687. . URL https://www.nature.com/articles/374524a0.
- [172] J. H. Conway and N. J. A. Sloane. *Sphere Packings, Lattices and Groups*, volume 290 of *Grundlehren der mathematischen Wissenschaften*. Springer New York, New York, NY, 1999. ISBN 978-1-4419-3134-4. . URL http://link.springer.com/10.1007/978-1-4757-6568-7.
- [173] Thomas C Hales. A Proof of the Kepler Conjecture. *Annals of Mathematics*, 162 (3):1065–1185, 2005.
- [174] E A Owen, Madoc Jones, and D G Pettifor. Theory of the crystal structures of transition metals. *Journal of Physics C: Solid State Physics*, 3(2):367, feb 1970. ISSN 0022-3719. URL https://iopscience.iop.org/article/10.1088/0022-3719/3/2/018https: //iopscience.iop.org/article/10.1088/0022-3719/3/2/018/meta.
- [175] A.J Bradley and J Thewis. The crystal structure of α-manganese. *Proceedings of the Royal Society of London. Series A, Containing Papers of a Mathematical and Physical Character*, 115(771):456–471, jul 1927. ISSN 0950-1207. . URL https://royalsocietypublishing.org/doi/10.1098/rspa.1927.0103.
- [176] G.D. Preston. CXXV. The crystal structure of β-manganese. The London,
 Edinburgh, and Dublin Philosophical Magazine and Journal of Science, 5(33):
 1207–1225, jun 1928. ISSN 1941-5982. URL
 https://www.tandfonline.com/doi/abs/10.1080/14786440608564570.
- [177] A. T. Dinsdale. SGTE data for pure elements. Calphad, 15(4):317–425, oct 1991.
 ISSN 0364-5916. .

[178] A. Proult and P. Donnadieu. A simple description of the α -manganese (A12) structure derived from defect studies. *Philosophical Magazine Letters*, 72(5): 337–344, 1995. ISSN 13623036.

- [179] Jialiang Wei, Leon Shaw, and Wei Chen. First-Principles Prediction of Na Diffusivity in Doped NaCrO2Layered Cathode Materials with van der Waals Interactions. *Journal of Physical Chemistry C*, 124(23):12239–12248, jun 2020. ISSN 19327455. URL https://pubs.acs.org/doi/full/10.1021/acs.jpcc.0c02274.
- [180] Eric B. Isaacs, Shane Patel, and Chris Wolverton. Prediction of Li intercalation voltages in rechargeable battery cathode materials: Effects of exchange-correlation functional, van der Waals interactions, and Hubbard U.

 Physical Review Materials, 4(6):065405, jun 2020. ISSN 24759953. . URL

 https://journals.aps.org/prmaterials/abstract/10.1103/

 PhysRevMaterials.4.065405.
- [181] R. C. Longo, F. T. Kong, K. C. Santosh, M. S. Park, J. Yoon, D. H. Yeon, J. H. Park, S. G. Doo, and K. Cho. Phase stability of Li-Mn-O oxides as cathode materials for Li-ion batteries: Insights from ab initio calculations. *Physical Chemistry Chemical Physics*, 16(23):11233–11242, may 2014. ISSN 14639076. . URL www.rsc.org/pccp.
- [182] Jeffrey E. Post. Manganese oxide minerals: Crystal structures and economic and environmental significance. *Proceedings of the National Academy of Sciences*, 96(7): 3447–3454, mar 1999. ISSN 00278424. . URL https://www.pnas.org/doi/abs/10.1073/pnas.96.7.3447.
- [183] A. Nicholas Grundy, Bengt Hallstedt, and Ludwig J. Gauckler. Assessment of the Mn-O system. *Journal of Phase Equilibria* 2003 24:1, 24(1):21–39, feb 2003. ISSN 1054-9714. URL https://link.springer.com/article/10.1007/s11669-003-0004-6.
- [184] Yimeng Huang, Yanhao Dong, Sa Li, Jinhyuk Lee, Chao Wang, Zhi Zhu, Weijiang Xue, Yao Li, and Ju Li. Lithium Manganese Spinel Cathodes for

Lithium-Ion Batteries. *Advanced Energy Materials*, 11(2):2000997, jan 2021. ISSN 1614-6840. . URL https:

```
//onlinelibrary.wiley.com/doi/full/10.1002/aenm.202000997https:
//onlinelibrary.wiley.com/doi/abs/10.1002/aenm.202000997https:
//onlinelibrary.wiley.com/doi/10.1002/aenm.202000997.
```

- [185] Bohua Deng, Hiroyoshi Nakamura, and Masaki Yoshio. Capacity fading with oxygen loss for manganese spinels upon cycling at elevated temperatures. *Journal of Power Sources*, 180(2):864–868, jun 2008. ISSN 0378-7753.
- [186] Xiang Gao, Yumi H. Ikuhara, Craig A.J. Fisher, Rong Huang, Akihide Kuwabara, Hiroki Moriwake, Keiichi Kohama, and Yuichi Ikuhara. Oxygen loss and surface degradation during electrochemical cycling of lithium-ion battery cathode material LiMn 2 O 4. *Journal of Materials Chemistry A*, 7(15):8845–8854, apr 2019. ISSN 20507496. . URL https:

 //pubs.rsc.org/en/content/articlehtml/2019/ta/c8ta08083fhttps:

```
//pubs.rsc.org/en/content/articlehtml/2019/ta/c8ta08083fhttps:
//pubs.rsc.org/en/content/articlelanding/2019/ta/c8ta08083f.
```

- [187] D. Carlier, I. Saadoune, L. Croguennec, M. Ménétrier, E. Suard, and C. Delmas. On the metastable O2-type LiCoO2. *Solid State Ionics*, 144(3-4):263–276, dec 2001. ISSN 0167-2738.
- [188] D Carlier, A Van Der Ven, C Delmas, and G Ceder. First-Principles Investigation of Phase Stability in the O2-LiCoO 2 System. *Chemistry of Materials*, 2003. .
- [189] Wenhua Zuo, Xiangsi Liu, Jimin Qiu, Dexin Zhang, Zhumei Xiao, Jisheng Xie, Fucheng Ren, Jinming Wang, Yixiao Li, Gregorio F. Ortiz, Wen Wen, Shunqing Wu, Ming Sheng Wang, Riqiang Fu, and Yong Yang. Engineering Na+-layer spacings to stabilize Mn-based layered cathodes for sodium-ion batteries.

 *Nature Communications 2021 12:1, 12(1):1–11, aug 2021. ISSN 2041-1723. . URL https://www.nature.com/articles/s41467-021-25074-9.
- [190] Sonja Laubach, Stefan Laubach, Peter C. Schmidt, David Ensling, Stefan Schmid, Wolfram Jaegermann, Andreas Thißen, Kristian Nikolowski, and Helmut Ehrenberg. Changes in the crystal and electronic structure of LiCoO2 and

```
LiNiO2 upon Li intercalation and de-intercalation. Physical Chemistry Chemical Physics, 11(17):3278–3289, apr 2009. ISSN 14639076. . URL https://pubs.rsc.org/en/content/articlehtml/2009/cp/b901200ahttps://pubs.rsc.org/en/content/articlelanding/2009/cp/b901200a.
```

- [191] M E Arroyo Y De Dompablo, C Marianetti, A Van Der Ven, and G Ceder.

 Jahn-Teller mediated ordering in layered Li x MO 2 compounds. *Physical Review B*, 2001. .
- [192] F. London. Zur Theorie und Systematik der Molekularkräfte. Zeitschrift für Physik, 63(3-4):245–279, mar 1930. ISSN 14346001. URL https://link.springer.com/article/10.1007/BF01421741.
- [193] Stefan Grimme. Semiempirical GGA-type density functional constructed with a long-range dispersion correction. Journal of Computational Chemistry, 27(15): 1787–1799, nov 2006. ISSN 1096-987X. . URL https://onlinelibrary.wiley.com/doi/full/10.1002/jcc.20495https://onlinelibrary.wiley.com/doi/abs/10.1002/jcc.20495https://onlinelibrary.wiley.com/doi/10.1002/jcc.20495.
- [194] Stefan Grimme, Stephan Ehrlich, and Lars Goerigk. Effect of the damping function in dispersion corrected density functional theory. *Journal of Computational Chemistry*, 32(7):1456–1465, may 2011. ISSN 1096-987X. . URL https://onlinelibrary.wiley.com/doi/full/10.1002/jcc.21759https://onlinelibrary.wiley.com/doi/abs/10.1002/jcc.21759https://onlinelibrary.wiley.com/doi/10.1002/jcc.21759.
- [195] Claude Delmas, Jean Jacques Braconnier, and Paul Hagenmuller. A new variety of LiCoO2 with an unusual oxygen packing obtained by exchange reaction.

 *Materials Research Bulletin, 17(1):117–123, jan 1982. ISSN 0025-5408.
- [196] J. M. Paulsen, C. L. Thomas, and J. R. Dahn. Layered Li-Mn-Oxide with the O2 Structure: A Cathode Material for Li-Ion Cells Which Does Not Convert to Spinel. *Journal of The Electrochemical Society*, 146(10):3560–3565, oct 1999. ISSN 0013-4651. . URL

```
https://iopscience.iop.org/article/10.1149/1.1392514https://iopscience.iop.org/article/10.1149/1.1392514/meta.
```

[197] J. M. Paulsen, C. L. Thomas, and J. R. Dahn. O2 Structure Li2/3Ni1/3Mn23]O2: A New Layered Cathode Material for Rechargeable Lithium Batteries. I. Electrochemical Properties. *Journal of The Electrochemical Society*, 147(3):861, mar 2000. ISSN 1945-7111. . URL

```
https://iopscience.iop.org/article/10.1149/1.1393283https://iopscience.iop.org/article/10.1149/1.1393283/meta.
```

- [198] Brett Ammundsen and Jens Paulsen. Novel Lithium-Ion Cathode Materials
 Based on Layered Manganese Oxides. *Advanced Materials*, 2001. URL
 https://onlinelibrary.wiley.com/terms-and-conditions.
- [199] Shiqi Liu, Boya Wang, Xu Zhang, Shu Zhao, Zihe Zhang, and Haijun Yu.

 Reviving the lithium-manganese-based layered oxide cathodes for lithium-ion batteries. *Matter*, 4(5):1511–1527, may 2021. ISSN 2590-2385.
- [200] E Rossen, J N Reimers, and J R Dahn. Synthesis and Electrochemistry of Spinel LT-LiCoO2 SOLID STATE IOIIICS Synthesis and electrochemistry of spinel LT-LiCoO2. *Solid State Ionics*, 62:53–60, 1993. . URL https://www.researchgate.net/publication/222974659.
- [201] Michael M. Thackeray. Manganese oxides for lithium batteries. *Progress in Solid State Chemistry*, 25(1-2):1–71, jan 1997. ISSN 0079-6786.
- [202] Y. Shao-Horn, S. A. Hackney, A. R. Armstrong, P. G. Bruce, R. Gitzendanner, C. S. Johnson, and M. M. Thackeray. Structural Characterization of Layered LiMnO2 Electrodes by Electron Diffraction and Lattice Imaging. *Journal of The Electrochemical Society*, 146(7):2404–2412, jul 1999. ISSN 0013-4651. . URL https://iopscience.iop.org/article/10.1149/1.1391949/meta.
- [203] A. Robert Armstrong and Peter G. Bruce. Synthesis of layered LiMnO2 as an electrode for rechargeable lithium batteries. *Nature* 1996 381:6582, 381(6582):

```
499-500, 1996. ISSN 1476-4687. . URL https://www.nature.com/articles/381499a0.
```

[204] Miaojun Wang and Alexandra Navrotsky. LiMO 2 (M ¼ Mn, Fe, and Co): Energetics, polymorphism and phase transformation. *Journal of Solid State Chemistry*, 178:1230–1240, 2005. . URL www.elsevier.com/locate/jssc.

- [205] Fumiaki Kuroda, Satoshi Hagiwara, and Minoru Otani. Structural changes in the lithium cobalt dioxide electrode: A combined approach with cluster expansion and Bayesian optimization. *Physical Review Materials*, 7(11):115402, nov 2023. ISSN 24759953. URL https://journals.aps.org/prmaterials/abstract/10.1103/PhysRevMaterials.7.115402.
- [206] Alice J. Merryweather, Quentin Jacquet, Steffen P. Emge, Christoph Schnedermann, Akshay Rao, and Clare P. Grey. Operando monitoring of single-particle kinetic state-of-charge heterogeneities and cracking in high-rate Li-ion anodes. *Nature Materials* 2022 21:11, 21(11):1306–1313, aug 2022. ISSN 1476-4660. URL https://www.nature.com/articles/s41563-022-01324-z.
- [207] Sohrab R. Daemi, Chun Tan, Antonis Vamvakeros, Thomas M.M. Heenan,
 Donal P. Finegan, Marco Di Michiel, Andrew M. Beale, James Cookson, Enrico
 Petrucco, Julia S. Weaving, Simon Jacques, Rhodri Jervis, Dan J.L. Brett, and
 Paul R. Shearing. Exploring cycling induced crystallographic change in NMC
 with X-ray diffraction computed tomography. *Physical Chemistry Chemical Physics*, 22(32):17814–17823, aug 2020. ISSN 14639076. URL https:
 //pubs.rsc.org/en/content/articlehtml/2020/cp/d0cp01851ahttps:
 //pubs.rsc.org/en/content/articlelanding/2020/cp/d0cp01851a.
- [208] Arup Chakraborty, Mudit Dixit, Doron Aurbach, and Dan T. Major. Predicting accurate cathode properties of layered oxide materials using the SCAN meta-GGA density functional. npj Computational Materials 2018 4:1, 4(1):1–9, nov 2018. ISSN 2057-3960. . URL

https://www.nature.com/articles/s41524-018-0117-4.

[209] Yunbing Ran, Zheyi Zou, Bo Liu, Da Wang, Bowei Pu, Penghui Mi, Wei Shi, Yajie Li, Bing He, Ziheng Lu, Xia Lu, Baihai Li, and Siqi Shi. Towards prediction of ordered phases in rechargeable battery chemistry via group–subgroup transformation. *npj Computational Materials* 2021 7:1, 7(1):1–11, nov 2021. ISSN 2057-3960. URL https://www.nature.com/articles/s41524-021-00653-y.

- [210] C. Wolverton and Alex Zunger. First-principles prediction of vacancy order-disorder and intercalation battery voltages in LixCoO2. *Physical Review Letters*, 81(3):606–609, 1998. ISSN 10797114.
- [211] Konstantin Gubaev, Evgeny V. Podryabinkin, Gus L.W. Hart, and Alexander V. Shapeev. Accelerating high-throughput searches for new alloys with active learning of interatomic potentials. *Computational Materials Science*, 156:148–156, jan 2019. ISSN 0927-0256.
- [212] Gus L.W. Hart and Rodney W. Forcade. Generating derivative structures from multilattices: Algorithm and application to hcp alloys. *Physical Review B -Condensed Matter and Materials Physics*, 80(1):014120, aug 2009. ISSN 10980121. . URL https://journals.aps.org/prb/abstract/10.1103/PhysRevB.80.014120.
- [213] Gus L.W. Hart, Lance J. Nelson, and Rodney W. Forcade. Generating derivative structures at a fixed concentration. *Computational Materials Science*, 59:101–107, jun 2012. ISSN 0927-0256.
- [214] Gus L.W. Hart and Rodney W. Forcade. Algorithm for generating derivative structures. *Physical Review B Condensed Matter and Materials Physics*, 77(22): 224115, jun 2008. ISSN 10980121. . URL https://journals.aps.org/prb/abstract/10.1103/PhysRevB.77.224115.
- [215] Michael M. Thackeray, Christopher S. Johnson, John T. Vaughey, N. Li, and Stephen A. Hackney. Advances in manganese-oxide 'composite' electrodes for lithium-ion batteries. *Journal of Materials Chemistry*, 15(23):2257–2267, jun 2005. ISSN 1364-5501. . URL

```
https://pubs.rsc.org/en/content/articlehtml/2005/jm/b417616mhttps://pubs.rsc.org/en/content/articlelanding/2005/jm/b417616m.
```

[216] S. Choi and A. Manthiram. Factors Influencing the Layered to Spinel-like Phase Transition in Layered Oxide Cathodes. *Journal of The Electrochemical Society*, 149 (9):A1157, jul 2002. ISSN 00134651. . URL

```
https://iopscience.iop.org/article/10.1149/1.1497171https://iopscience.iop.org/article/10.1149/1.1497171/meta.
```

- [217] Bud Macaulay and Denis Kramer. The Impact of Lattice Stress on the Layered to Spinel Transformation of Li-Ion Battery Cathode Chemistries. *Journal of The Electrochemical Society*, 171(3):030509, mar 2024. ISSN 1945-7111. URL https://iopscience.iop.org/article/10.1149/1945-7111/ad2d17https://iopscience.iop.org/article/10.1149/1945-7111/ad2d17/meta.
- [218] Ming Shen and Qing Gao. A review on battery management system from the modeling efforts to its multiapplication and integration. *International Journal of Energy Research*, 43(10):5042–5075, aug 2019. ISSN 1099-114X. . URL https://onlinelibrary.wiley.com/doi/full/10.1002/er.4433https://onlinelibrary.wiley.com/doi/abs/10.1002/er.4433https://onlinelibrary.wiley.com/doi/10.1002/er.4433.
- [219] Antoni Szumanowski and Yuhua Chang. Battery management system based on battery nonlinear dynamics modeling. *IEEE Transactions on Vehicular Technology*, 57(3):1425–1432, may 2008. ISSN 00189545.
- [220] Rong Xu, Hong Sun, Luize Scalco de Vasconcelos, and Kejie Zhao. Mechanical and Structural Degradation of LiNi x Mn y Co z O 2 Cathode in Li-Ion Batteries: An Experimental Study. *Journal of The Electrochemical Society*, 164(13): A3333–A3341, nov 2017. ISSN 0013-4651. URL https://iopscience.iop.org/article/10.1149/2.1751713jeshttps://iopscience.iop.org/article/10.1149/2.1751713jes/meta.
- [221] Tianyu Li, Xiao-Zi Yuan, Lei Zhang, Datong Song, Kaiyuan Shi, and Christina Bock. Degradation Mechanisms and Mitigation Strategies of Nickel-Rich

NMC-Based Lithium-Ion Batteries. *Electrochemical Energy Reviews*, 2019. ISSN 2520-8489. URL http://link.springer.com/10.1007/s41918-019-00053-3.

- [222] Jia Yi Wang, Sheng Nan Guo, Xin Wang, Lin Gu, and Dong Su. Structural Degradation of Ni-Rich Layered Oxide Cathode for Li-Ion Batteries. *Journal of Electrochemistry*, 28(2):2108431, feb 2022. ISSN 1006-3471. . URL http://electrochem.xmu.edu.cn/EN/10.13208/j.electrochem.210843.
- [223] Hongyang Li, Aaron Liu, Ning Zhang, Yiqiao Wang, Shuo Yin, Haohan Wu, and Jeff R Dahn. An Unavoidable Challenge for Ni-Rich Positive Electrode Materials for Lithium-Ion Batteries. *Chemistry of Materials*, 2019. . URL https://pubs.acs.org/sharingguidelines.
- [224] V. J. Ovejas and A. Cuadras. Effects of cycling on lithium-ion battery hysteresis and overvoltage. *Scientific Reports*, 9(1):1–9, dec 2019. ISSN 20452322. . URL https://www.nature.com/articles/s41598-019-51474-5.
- [225] Matthew Kristofer Horton, Joseph Harold Montoya, Miao Liu, and Kristin Aslaug Persson. High-throughput prediction of the ground-state collinear magnetic order of inorganic materials using Density Functional Theory. npj Computational Materials 2019 5:1, 5(1):1–11, jun 2019. ISSN 2057-3960. . URL https://www.nature.com/articles/s41524-019-0199-7.
- [226] L G Vanquickenborne, K Pierloot, and D Devoghel. Transition Metals and the Aufbau Principle. *Journal of Chemical Education*, 71(6):469–471, 1994. ISSN 00219584. . URL https://pubs.acs.org/doi/abs/10.1021/ed071p469.
- [227] Al-Moatasem El-Sayed, Matthew B Watkins, Tibor Grasser, and Alexander L Shluger. Effect of electric field on migration of defects in oxides: Vacancies and interstitials in bulk MgO. *Physical Review B*, 98:64102, 2018.
- [228] Jorge Echeverría and Santiago Alvarez. Application of symmetry operation measures in structural inorganic chemistry. *Inorganic Chemistry*, 47(23): 10965–10970, dec 2008. ISSN 00201669. . URL https://pubs.acs.org/doi/pdf/10.1021/ic801264n.

[229] J. B. Goodenough and A. L. Loeb. Theory of Ionic Ordering, Crystal Distortion, and Magnetic Exchange Due to Covalent Forces in Spinels. *Physical Review*, 98 (2):391, apr 1955. ISSN 0031899X. URL https://journals.aps.org/pr/abstract/10.1103/PhysRev.98.391.

[230] Roger G. Burns. *Mineralogical Applications of Crystal Field Theory*. Cambridge University Press, sep 1993. ISBN 9780521430777. . URL

```
https://www.cambridge.org/core/books/
mineralogical-applications-of-crystal-field-theory/
CDF9711F1C9F946772EC5ADE2C896522.
```

- [231] F Aryasetiawan and K Karlsson. Modern theory of orbital magnetic moment in solids. *Journal of Physics and Chemistry of Solids*, 2017. . URL https://doi.org/10.1016/j.jpcs.2017.12.004.
- [232] Wei Yin, Alexis Grimaud, Gwenaelle Rousse, Artem M. Abakumov, Anatoliy Senyshyn, Leiting Zhang, Sigita Trabesinger, Antonella Iadecola, Dominique Foix, Domitille Giaume, and Jean Marie Tarascon. Structural evolution at the oxidative and reductive limits in the first electrochemical cycle of Li1.2Ni0.13Mn0.54Co0.13O2. *Nature Communications* 2020 11:1, 11(1):1–11, mar 2020. ISSN 2041-1723. . URL https://www.nature.com/articles/s41467-020-14927-4.
- [233] Rui Zhang, Chunyang Wang, Peichao Zou, Ruoqian Lin, Lu Ma, Liang Yin, Tianyi Li, Wenqian Xu, Hao Jia, Qiuyan Li, Sami Sainio, Kim Kisslinger, Stephen E. Trask, Steven N. Ehrlich, Yang Yang, Andrew M. Kiss, Mingyuan Ge, Bryant J. Polzin, Sang Jun Lee, Wu Xu, Yang Ren, and Huolin L. Xin. Compositionally complex doping for zero-strain zero-cobalt layered cathodes. Nature 2022 610:7930, 610(7930):67–73, sep 2022. ISSN 1476-4687. . URL https://www.nature.com/articles/s41586-022-05115-z.
- [234] Lucy M Morgan, Mazharul M Islam, Hui Yang, Anisha N Patel, Abir Ghosh, Emma Kendrick, Monica Marinescu, Gregory J Offer, Benjamin J Morgan, M Saiful Islam, Jacqueline Edge, and Aron Walsh. From Atoms to Cells:

Multiscale Modeling of LiNi x Mn y Co z O 2 Cathodes for Li-Ion Batteries. *ACS Energy Lett.*, 10:5, 2024. URL http://pubs.acs.org/journal/aelccp.

- [235] Xian Ming Wu, Run Xiu Li, Shang Chen, Ze Qiang He, and Ming Fei Xu.

 Comparative study of Co, Cr and Al-doped LiMnO2 prepared by ion exchange.

 Bulletin of Materials Science, 31(2):109–113, apr 2008. ISSN 02504707. . URL

 https://link.springer.com/article/10.1007/s12034-008-0019-z.
- [236] P. Suresh, A. K. Shukla, and N. Munichandraiah. Characterization of Zn- and Fe-substituted LiMnO2 as cathode materials in Li-ion cells. *Journal of Power Sources*, 2(161):1307–1313, oct 2006. ISSN 0378-7753. . URL https://www.infona.pl//resource/bwmeta1.element. elsevier-8a55b824-2923-3a43-a1b9-f4e396b94e1d.
- [237] Shikhar Krishn Jha, Harry Charalambous, John S. Okasinski, and Thomas Tsakalakos. Using in operando diffraction to relate lattice strain with degradation mechanism in a NMC battery. *Journal of Materials Science*, 54(3): 2358–2370, feb 2019. ISSN 15734803. URL https://link.springer.com/article/10.1007/s10853-018-3007-8.
- [238] Alice J. Merryweather, Christoph Schnedermann, Quentin Jacquet, Clare P. Grey, and Akshay Rao. Operando optical tracking of single-particle ion dynamics in batteries. *Nature* 2021 594:7864, 594(7864):522–528, jun 2021. ISSN 1476-4687. URL https://www.nature.com/articles/s41586-021-03584-2.
- [239] Pengfei Yan, Jianming Zheng, Meng Gu, Jie Xiao, Ji Guang Zhang, and Chong Min Wang. Intragranular cracking as a critical barrier for high-voltage usage of layer-structured cathode for lithium-ion batteries. *Nature Communications*, 8, jan 2017. ISSN 20411723. . URL /pmc/articles/PMC5241805//pmc/articles/PMC5241805/?report= abstracthttps://www.ncbi.nlm.nih.gov/pmc/articles/PMC5241805/.
- [240] A. Wade, A. V. Llewellyn, T. M. M. Heenan, C. Tan, D. J. L. Brett, Rhodri Jervis, and P. R. Shearing. First Cycle Cracking Behaviour Within Ni-Rich Cathodes

 During High-Voltage Charging. *Journal of The Electrochemical Society*, 170(7):

```
070513, jul 2023. ISSN 1945-7111. . URL

https://iopscience.iop.org/article/10.1149/1945-7111/ace130https:
//iopscience.iop.org/article/10.1149/1945-7111/ace130/meta.
```

- [241] Wangda Li, Hooman Yaghoobnejad Asl, Qiang Xie, and Arumugam Manthiram. Collapse of LiNi1- x- yCoxMnyO2 Lattice at Deep Charge Irrespective of Nickel Content in Lithium-Ion Batteries. *Journal of the American Chemical Society*, 141 (13):5097–5101, apr 2019. ISSN 15205126. . URL https://pubs.acs.org/doi/full/10.1021/jacs.8b13798.
- [242] Aleksandr O. Kondrakov, Holger Geßwein, Kristina Galdina, Lea De Biasi, Velimir Meded, Elena O. Filatova, Gerhard Schumacher, Wolfgang Wenzel, Pascal Hartmann, Torsten Brezesinski, and Jürgen Janek. Charge-transfer-induced lattice collapse in Ni-rich NCM cathode materials during delithiation. *Journal of Physical Chemistry C*, 121(39), 2017. ISSN 19327455. . URL https://pubs.acs.org/doi/full/10.1021/acs.jpcc.7b06598.
- [243] Aleksandr O. Kondrakov, Alexander Schmidt, Jin Xu, Holger Geßwein, Reiner Mönig, Pascal Hartmann, Heino Sommer, Torsten Brezesinski, and Jürgen Janek. Anisotropic Lattice Strain and Mechanical Degradation of High- and Low-Nickel NCM Cathode Materials for Li-Ion Batteries. *Journal of Physical Chemistry C*, 121(6):3286–3294, feb 2017. ISSN 19327455. . URL https://pubs.acs.org/doi/full/10.1021/acs.jpcc.6b12885.
- [244] Mee Kyung Song, Seung Do Hong, and Kyoung Tai No. The Structure of Lithium Intercalated Graphite Using an Effective Atomic Charge of Lithium.

 Journal of The Electrochemical Society, 148(10):A1159, sep 2001. ISSN 00134651..

 URL https://iopscience.iop.org/article/10.1149/1.1402118https://iopscience.iop.org/article/10.1149/1.1402118/meta.
- [245] Klaus A. Moltved and Kasper P. Kepp. The chemical bond between transition metals and Oxygen: Electronegativity, d-Orbital Effects, and Oxophilicity as Descriptors of Metal-Oxygen Interactions. *Journal of Physical Chemistry C*, 123 (30):18432–18444, aug 2019. ISSN 19327455. . URL https://pubs.acs.org/doi/abs/10.1021/acs.jpcc.9b04317.

[246] Nicholas V. Faenza, Nathalie Pereira, David M. Halat, Julija Vinckeviciute, Lejandro Bruce, Maxwell D. Radin, Pinaki Mukherjee, Fadwa Badway, Anna Halajko, Frederic Cosandey, Clare P. Grey, Anton Van Der Ven, and Glenn G. Amatucci. Phase Evolution and Degradation Modes of R3m LixNi1- y-zCoyAlzO2 Electrodes Cycled Near Complete Delithiation. *Chemistry of Materials*, 30(21):7545–7574, nov 2018. ISSN 15205002. URL https://pubs.acs.org/doi/full/10.1021/acs.chemmater.8b02720.

- [247] Yi Pei, Qing Chen, Meiyu Wang, Pengjun Zhang, Qingyong Ren, Jingkai Qin, Penghao Xiao, Li Song, Yu Chen, Wen Yin, Xin Tong, Liang Zhen, Peng Wang, and Cheng Yan Xu. A medium-entropy transition metal oxide cathode for high-capacity lithium metal batteries. *Nature Communications* 2022 13:1, 13(1): 1–13, oct 2022. ISSN 2041-1723. . URL https://www.nature.com/articles/s41467-022-33927-0.
- [248] Tanvir R Tanim, Eric J Dufek, Charles C Dickerson, al, Franziska Friedrich,
 Alexander Kunz, Andreas Jossen, al -Improved Electrochemical Properties, and
 Structural Stability of Overlithiated Li. Understanding the Overlithiation
 Properties of LiNi0.6Mn0.2Co0.2O2 Using Electrochemistry and
 Depth-Resolved X-ray Absorption Spectroscopy. *Journal of The Electrochemical Society*, 167(8):080514, apr 2020. ISSN 1945-7111. . URL
 https://iopscience.iop.org/article/10.1149/1945-7111/ab8a9d/meta.
- [249] Linqin Mu, Ruoqian Lin, Rong Xu, Lili Han, Sihao Xia, Dimosthenis Sokaras, James D. Steiner, Tsu Chien Weng, Dennis Nordlund, Marca M. Doeff, Yijin Liu, Kejie Zhao, Huolin L. Xin, and Feng Lin. Oxygen Release Induced Chemomechanical Breakdown of Layered Cathode Materials. *Nano Letters*, 18 (5):3241–3249, may 2018. ISSN 15306992. URL https://pubs.acs.org/doi/abs/10.1021/acs.nanolett.8b01036.
- [250] A. Van Der Ven and G. Ceder. Lithium diffusion in layered LixCoO2. *Electrochemical and Solid-State Letters*, 3(7):301–304, jul 2000. ISSN 10990062.

```
URL https://iopscience.iop.org/article/10.1149/1.1391130https:
//iopscience.iop.org/article/10.1149/1.1391130/meta.
```

[251] Dongchang Chen, Wang Hay Kan, and Guoying Chen. Understanding Performance Degradation in Cation-Disordered Rock-Salt Oxide Cathodes. *Advanced Energy Materials*, 9(31):1901255, aug 2019. ISSN 1614-6840. . URL https:

```
//onlinelibrary.wiley.com/doi/full/10.1002/aenm.201901255https:
//onlinelibrary.wiley.com/doi/abs/10.1002/aenm.201901255https:
//onlinelibrary.wiley.com/doi/10.1002/aenm.201901255.
```

- [252] Ji Lei Shi, Dong Dong Xiao, Xu Dong Zhang, Ya Xia Yin, Yu Guo Guo, Lin Gu, and Li Jun Wan. Improving the structural stability of Li-rich cathode materials via reservation of cations in the Li-slab for Li-ion batteries. *Nano Research*, 10(12): 4201–4209, dec 2017. ISSN 1998-0124. URL https://www.sciopen.com/article/10.1007/s12274-017-1489-3.
- [253] Hirbod Maleki Kheimeh Sari and Xifei Li. Controllable Cathode–Electrolyte Interface of Li[Ni0.8Co0.1Mn0.1]O2 for Lithium Ion Batteries: A Review.

 Advanced Energy Materials, 9(39):1901597*, oct 2019. ISSN 1614-6840. . URL https:

```
//onlinelibrary.wiley.com/doi/full/10.1002/aenm.201901597https:
//onlinelibrary.wiley.com/doi/abs/10.1002/aenm.201901597https:
//onlinelibrary.wiley.com/doi/10.1002/aenm.201901597.
```

- [254] Guo Rong Hu, Xin Rong Deng, Zhong Dong Peng, and Ke Du. Comparison of AlPO4- and Co3(PO4)2-coated LiNi0.8Co0.2O2 cathode materials for Li-ion battery. *Electrochimica Acta*, 53(5):2567–2573, jan 2008. ISSN 0013-4686.
- [255] Min Gyu Kim and Jaephil Cho. Air stable Al2O3-coated Li2NiO2 cathode additive as a surplus current consumer in a Li-ion cell. *Journal of Materials* Chemistry, 18(48):5880–5887, dec 2008. ISSN 1364-5501. URL https://pubs.rsc.org/en/content/articlehtml/2008/jm/b814161dhttps: //pubs.rsc.org/en/content/articlelanding/2008/jm/b814161d.

[256] Yonghyun Cho, Pilgun Oh, and Jaephil Cho. A new type of protective surface layer for high-capacity ni-based cathode materials: Nanoscaled surface pillaring layer. *Nano Letters*, 13(3):1145–1152, mar 2013. ISSN 15306984. . URL https://pubs.acs.org/doi/full/10.1021/nl304558t.

- [257] J. M. Fernandez-Rodriguez, J. Morales, and J. L. Tirado. Tk and DTA studies of lithium insertion transition metal compounds. *Materials Chemistry and Physics*, 20(2):145–152, sep 1988. ISSN 0254-0584.
- [258] P. N. Kumta, D. Gallet, A. Waghray, G. E. Blomgren, and M. P. Setter. Synthesis of LiCoO2 powders for lithium-ion batteries from precursors derived by rotary evaporation. *Journal of Power Sources*, 72(1):91–98, mar 1998. ISSN 0378-7753.
- [259] M. Antaya, J. R. Dahn, J. S. Preston, E. Rossen, and J. N. Reimers. Preparation and Characterization of LiCoO2 Thin Films by Laser Ablation Deposition. *Journal of The Electrochemical Society*, 140(3):575–578, mar 1993. ISSN 0013-4651. .

 URL https://iopscience.iop.org/article/10.1149/1.2056123https:
 //iopscience.iop.org/article/10.1149/1.2056123/meta.
- [261] PW Tasker. C: Solid State Phys. 12 4977. J. Phys. C: Solid State Phys, 12, 1979.
- [262] Wenhao Sun and Gerbrand Ceder. Efficient creation and convergence of surface slabs. Surface Science, 2013. URL http://dx.doi.org/10.1016/j.susc.2013.05.016.
- [263] Shyue Ping Ong, William Davidson Richards, Anubhav Jain, Geoffroy Hautier, Michael Kocher, Shreyas Cholia, Dan Gunter, Vincent L. Chevrier, Kristin A. Persson, and Gerbrand Ceder. Python Materials Genomics (pymatgen): A

robust, open-source python library for materials analysis. *Computational Materials Science*, 68:314–319, 2013. ISSN 09270256.

- [264] Juarez L F Da Silva, Catherine Stampfl, and Matthias Scheffler. Converged properties of clean metal surfaces by all-electron first-principles calculations. Surface Science, 2005. . URL www.elsevier.com/locate/susc.
- [265] Vincenzo Fiorentini and M. Methfessel. Extracting convergent surface energies from slab calculations. *Journal of Physics Condensed Matter*, 8(36):6525–6529, 1996. ISSN 09538984.
- [266] Nick Woods. On the Nature of Self-Consistency in Density Functional Theory. PhD thesis, University of Cambridge, mar 2018. URL https://arxiv.org/abs/1803.01763v1.
- [267] U Opik and M H L Pryce. Studies of the Jahn-Teller effect. I. A survey of the static problem. *Proceedings of the Royal Society of London. Series A. Mathematical and Physical Sciences*, 238(1215):425–447, 1957. ISSN 0080-4630.
- [268] Isaac B. Bersuker. Modern aspects of the Jahn-Teller effect theory and applications to molecular problems. *Chemical Reviews*, 101(4):1067–1114, apr 2001. ISSN 00092665. URL https://pubs.acs.org/doi/full/10.1021/cr0004411.
- [269] Ralph G Pearson and K Eo -Ek. Concerning Jahn-Teller Effects. *Proceedings of the National Academy of Sciences*, 72(6):2104–2106, jun 1975. ISSN 0027-8424. . URL https://www.pnas.org.
- [270] Soo Kim, Muratahan Aykol, and C. Wolverton. Surface phase diagram and stability of (001) and (111) LiM n2 O4 spinel oxides. *Physical Review B Condensed Matter and Materials Physics*, 92(11):115411, sep 2015. ISSN 1550235X. . URL https://journals.aps.org/prb/abstract/10.1103/PhysRevB.92.115411.
- [271] Liyun Hu, Zhihua Xiong, Chuying Ouyang, Siqi Shi, Yinghua Ji, Minsheng Lei, Zhaoxiang Wang, Hong Li, Xuejie Huang, and Liquan Chen. Ab initio studies on the stability and electronic structure of LiCoO 2 (003) surfaces. *Physical*

Review B - Condensed Matter and Materials Physics, 71(12):125433, mar 2005. ISSN 10980121. . URL

https://journals.aps.org/prb/abstract/10.1103/PhysRevB.71.125433.

- [272] Germain Vallverdu, Marie Minvielle, Nathalie Andreu, Danielle Gonbeau, and Isabelle Baraille. First principle study of the surface reactivity of layered lithium oxides LiMO2 (M = Ni, Mn, Co). *Surface Science*, 649:46–55, jul 2016. ISSN 0039-6028.
- [273] L. Dahéron, H. Martinez, R. Dedryvère, I. Baraille, M. Ménétrier, C. Denage, C. Delmas, and D. Gonbeau. Surface properties of LiCoO2investigated by XPS analyses and theoretical calculations. *Journal of Physical Chemistry C*, 113(14): 5843–5852, apr 2009. ISSN 19327455. URL https://pubs.acs.org/doi/full/10.1021/jp803266w.
- [274] Liang Hong, Linhua Hu, John W. Freeland, Jordi Cabana, Serdar Ögüt, and Robert F. Klie. Electronic Structure of LiCoO 2 Surfaces and Effect of Al Substitution. *Journal of Physical Chemistry C*, 123(14):8851–8858, apr 2019. ISSN 19327455.
- [275] Thomas A. Albright, Jeremy K. Burdett, and Myung Hwan Whangbo. *Orbital Interactions in Chemistry: Second Edition*. Wiley-VCH, 2013. ISBN 9780471080398.
- [276] P. S. Whitfield, I. J. Davidson, L. M.D. Cranswick, I. P. Swainson, and P. W. Stephens. Investigation of possible superstructure and cation disorder in the lithium battery cathode material LiMn1/3Ni1/3Co1/3O2 using neutron and anomalous dispersion powder diffraction. *Solid State Ionics*, 176(5-6):463–471, feb 2005. ISSN 0167-2738.
- [277] Debasish Mohanty, Athena S. Sefat, Jianlin Li, Roberta A. Meisner, Adam J. Rondinone, E. Andrew Payzant, Daniel P. Abraham, David L. Wood, and Claus Daniel. Correlating cation ordering and voltage fade in a lithium–manganese-rich lithium-ion battery cathode oxide: a joint magnetic susceptibility and TEM study. *Physical Chemistry Chemical Physics*, 15(44):

```
19496-19509, oct 2013. ISSN 14639076. . URL https:
//pubs.rsc.org/en/content/articlehtml/2013/cp/c3cp53658khttps:
//pubs.rsc.org/en/content/articlelanding/2013/cp/c3cp53658k.
```

[278] Marine Reynaud and Montse Casas-Cabanas. Order and disorder in NMC layered materials: a FAULTS simulation analysis. *Powder Diffraction*, 32(S1): S213–S220, sep 2017. ISSN 0885-7156. . URL https://www.cambridge.org/core/journals/powder-diffraction/article/order-and-disorder-in-nmc-layered-materials-a-faults-simulation-analysis/482CC1732325F0A10C3B02ABF297AB37.

Chapter 7

Appendices

A Energy differences of the high and low-spin O3-type structures

When investigating the calculated ground state of the Manganese equivalent Goodenough structure $LiMnO_2$ the PBE functional disagrees with the other functionals chosen (PBE+U, PBE+U+D2 and PBE+U+D3.) The PBE functional predicts the Mn in this system to be low-spin, a result that is not observed experimentally and is erroneous. Due to this error, it was decided to determine the relative energies of these high and low-spin structures. This was achieved by initialising the total magnetic moment on the metal site as either high or low spin as according to their d electron configuration (see Table 7.1) and relaxing the structures.

	M ³⁺	High spin	Low spin
	d electrons	configuration	configuration
LiCoO ₂	6	$t_{2g}^5 \ e_g^1$	$t_{2g}^6 e_g^0$
LiNiO ₂	7	$t_{2g}^5 e_g^2$	$t_{2g}^6 e_g^1$
$LiMnO_2$	4	$t_{2g}^3 e_g^1$	$t_{2g}^4\ e_g^0$

TABLE 7.1: Metal d electron and spin state configurations of Goodenough analogue systems.

The on-site magnetic moment was taken from the *VASP* output files and are tabulated in Table 7.2 and suggest that both the high and low spin states have been found. The

on site	magnetic moments /	' uB
	magnetic moments /	PV D

	011.5	2100	ette memerite	, r=		
LiCoO ₂ (LS)						
	PBE	PBE+U	PBE+U+D2	PBE+U+D3		
Li	0.000	0.000	0.000	0.000		
Co	0.000	0.000	0.000	0.000		
O	0.000	0.000	0.000	0.000		
LiCoO ₂ (HS)						
Li	0.008	0.006	0.007	0.007		
Co	2.903	3.093	3.097	3.093		
O	0.454	0.374	0.374	0.376		
		LiN	IiO ₂ (LS)			
Li	0.006	0.005	0.005	0.005		
Ni	0.771	1.421	1.391	1.392		
O	0.080	-0.183	-0.170	-0.171		
LiNiO ₂ (HS)						
Li	0.008	0.002	0.002	0.004		
Ni	1.825	1.848	1.850	1.858		
O	0.489	0.500	0.499	0.498		
LiMnO ₂ (LS)						
Li	0.000	0.000	0.001	0.000		
Mn	1.916	1.986	1.984	1.985		
O	0.023	0.003	0.006	0.005		
LiMnO ₂ (HS)						
Li	0.006	0.005	0.004	0.005		
Mn	3.671	4.076	4.060	4.060		
O	0.065	-0.089	-0.080	-0.081		

TABLE 7.2: Calculated on-site magnetic moments of species within the O3-type structure after geometry optimization. Magnetic moments were initialised at their expected d-configuration.

resulting relative energies can be found in Figure 7.1 where for both Co and Ni, the low spin state is lower energy than the high spin state, with an energy difference > 0.5 eV/f.u. Constrastingly, the Mn system shows the high spin state to be low energy for all functionals utilising the Hubbard U (U=3.9 for Mn). for this system, the PBE functional disagrees significantly with these other functionals. Showing that the high and low spin systems are close in energy (energy barrier < 0.1 eV/f.u.) with the low spin state being the ground state. As a result the PBE functional can be considered erroneous.

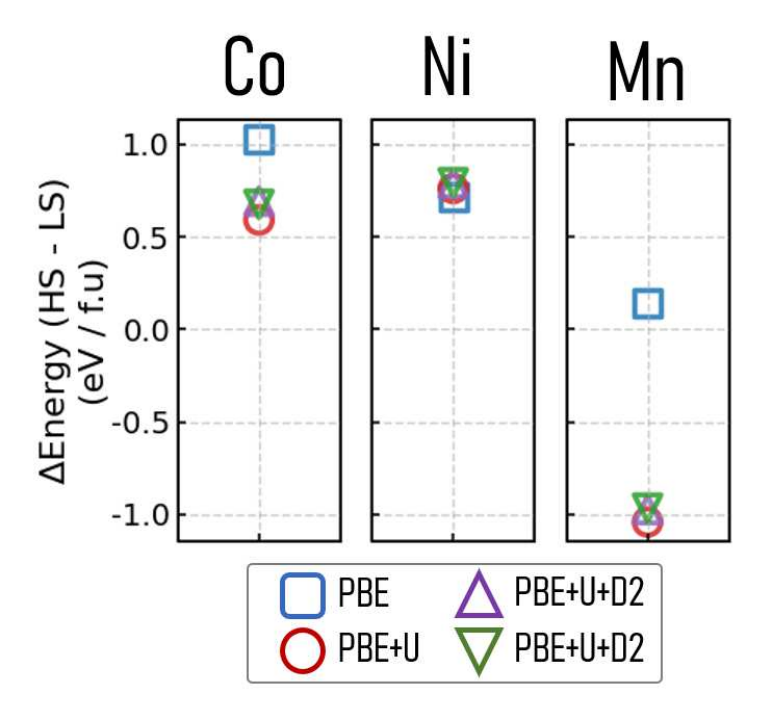


FIGURE 7.1: The Daniell cell is one of the first batteries. Comprised of a Zn electrode and a Cu electrode. Ionic exchange is facilitated through the salt-bridge.